



# TECHNISCHE UNIVERSITÄT MÜNCHEN

Department of Chemistry and Catalysis Research Center  
Chair of Technical Electrochemistry

## **Analysis of Voltage Losses and Degradation Phenomena in PEM Water Electrolyzers**

Maximilian Philipp Bernt

Vollständiger Abdruck der von der Fakultät für Chemie der Technischen Universität  
München zur Erlangung des akademischen Grades eines

Doktors der Naturwissenschaften (Dr. rer. nat.)

genehmigten Dissertation.

Vorsitzender: Prof. Dr. Tom Nilges  
Prüfer der Dissertation: 1. Prof. Dr. Hubert A. Gasteiger  
2. Prof. Dr. Aliaksandr S. Bandarenka

Diese Dissertation wurde am 22.11.2018 bei der Technischen Universität München eingereicht und durch die Fakultät für Chemie am 24.01.2019 angenommen.



# Abstract

The main challenges associated with a large-scale application of proton exchange membrane (PEM) based water electrolysis are the reduction of the iridium loading at the oxygen evolution electrode (anode) to prevent supply constraints as well as the minimization of hydrogen generation costs to increase economic competitiveness while retaining a sufficient system lifetime. These topics are addressed by an optimization of the electrode composition and by a reduction of catalyst loading in the membrane electrode assembly (MEA), accompanied by a rigorous analysis of voltage losses and an investigation of degradation phenomena during an accelerated stress test. First, the influence of ionomer content in anode electrodes with an IrO<sub>2</sub>/TiO<sub>2</sub> catalyst on the electrolyzer performance is investigated. It is shown that by optimizing the ionomer content, voltage losses, e.g., due to mass transport phenomena, can be minimized, thereby enabling high performance at current densities up to 6 A cm<sup>-2</sup>.

In the second part of this thesis, the effect of a reduced catalyst loading is investigated, and we show that a significant reduction of the platinum loading on the hydrogen evolution electrode (cathode) is possible without a decrease in performance. In contrast, lowering the iridium loading on the anode leads to thin, inhomogeneous catalyst layers, resulting in a significant performance drop. Based on these findings, future catalyst material requirements are discussed in the context of a large-scale application of PEM water electrolysis. Finally, the influence of a fluctuating power supply on electrolyzer performance and durability is simulated by an accelerated stress test including load cycles and operation interruptions. It is shown that avoiding current interruptions and resulting open circuit voltage periods is crucial to prevent catalyst dissolution and enable a sufficient long-term stability.



# Kurzfassung

Die wichtigsten Herausforderungen für eine großflächige Anwendung der Protonenaustauschmembran (PEM) basierenden Wasserelektrolyse sind die Reduzierung der Iridiumbelastung der Sauerstoffentwicklungselektrode (Anode) um Versorgungsengpässe zu vermeiden, sowie eine Minimierung der Wasserstofferzeugungskosten um die ökonomische Wettbewerbsfähigkeit zu erhöhen, wobei eine ausreichende Lebensdauer des Systems gewährleistet bleiben muss. Diese Themen werden durch eine Optimierung der Elektrodenstruktur und eine Reduktion der Katalysatorbelastung in der Membran-Elektroden-Einheit (MEA) aufgegriffen, begleitet von einer präzisen Analyse der Spannungsverluste und einer Untersuchung der Degradationsmechanismen während beschleunigten Alterungstests. Zunächst wird der Einfluss des Ionomergehalts in Anodenelektroden mit einem  $\text{IrO}_2/\text{TiO}_2$  Katalysator auf die Leistung des Elektrolyseurs untersucht. Es zeigt sich, dass durch eine Optimierung des Ionomergehalts Spannungsverluste, z.B. durch Massentransportphänomene, minimiert werden können, was eine hohe Leistung bei Stromdichten von bis zu  $6 \text{ A cm}^{-2}$  ermöglicht.

Im zweiten Teil dieser Doktorarbeit wird der Effekt einer reduzierten Katalysatorbelastung untersucht und wir zeigen, dass eine signifikante Reduktion der Platinbelastung auf der Wasserstoffentwicklungselektrode (Kathode) möglich ist ohne die Leistung zu beeinträchtigen. Im Gegensatz dazu führt eine Verringerung der Iridiumbelastung auf der Anode zu dünnen, inhomogenen Elektrodenschichten was einen starken Leistungsverlust zur Folge hat. Basierend auf diesen Ergebnissen werden die Anforderungen an zukünftige Katalysatormaterialien im Kontext einer großflächigen Anwendung der PEM Wasserelektrolyse diskutiert. Abschließend wird der Einfluss einer fluktuierenden Energieversorgung auf die Leistung und Haltbarkeit eines Elektrolyseurs durch einen beschleunigten Alterungstest simuliert, der Lastwechsel und Stillstandphasen beinhaltet. Es wird gezeigt, dass Unterbrechungen des Betriebs und daraus resultierende Phasen bei Leerlaufspannung vermieden werden müssen, um eine Auflösung des Katalysators zu verhindern und eine ausreichende Langzeitstabilität zu ermöglichen.



# Contents

<b>Abstract / Kurzfassung</b>	<b>iii</b>
<b>List of Acronyms</b>	<b>ix</b>
<b>1 Introduction</b>	<b>1</b>
<b>2 Proton Exchange Membrane Water Electrolysis</b>	<b>3</b>
2.1 Materials and Components . . . . .	4
2.1.1 Membrane and Ionomer . . . . .	4
2.1.2 Catalyst Materials . . . . .	8
2.1.3 Porous Transport Layers . . . . .	10
2.1.4 Bipolar Plates . . . . .	11
2.2 Efficiency and Voltage Losses . . . . .	12
2.2.1 Thermodynamics . . . . .	14
2.2.2 Ohmic Losses . . . . .	16
2.2.3 Kinetic Losses . . . . .	19
2.2.4 Transport Losses . . . . .	22
2.3 Operating Conditions . . . . .	25
2.4 Degradation Phenomena . . . . .	29
2.5 Potential of PEM Electrolysis for H <sub>2</sub> Generation . . . . .	33
2.5.1 State-of-the-art Technology and Cost Analysis . . . . .	33
2.5.2 Challenges for Large-Scale Application of PEM Electrolysis . . . . .	36
<b>3 Experimental Methods</b>	<b>41</b>
3.1 Cell Hardware for High Pressure Operation . . . . .	41
3.2 MEA Fabrication . . . . .	46
3.3 Electrochemical Characterization . . . . .	49
3.4 Further Experimental Methods . . . . .	51

<b>4 Results</b>	<b>53</b>
4.1 Influence of Ionomer Content in IrO <sub>2</sub> /TiO <sub>2</sub> Electrodes on PEM Water Electrolyzer Performance . . . . .	53
4.2 Analysis of Voltage Losses in PEM Water Electrolyzers with Low Platinum Group Metal Loadings . . . . .	67
4.3 Impact of Intermittent Operation on Lifetime and Performance of a PEM Water Electrolyzer . . . . .	79
<b>5 Conclusion</b>	<b>93</b>
<b>Bibliography</b>	<b>97</b>
<b>Acknowledgements</b>	<b>115</b>



# List of Acronyms

<b>Abbreviation</b>	<b>Description</b>
AST	accelerated stress test
ATO	antimony doped tin oxide
BET	brunauer-emmett-teller
BEV	battery electric vehicle
BoP	balance of plant
BPP	bipolar plate
CAPEX	capital expenditure
CCM	catalyst coated membrane
CCS	catalyst coated substrate
ECSA	electrochemically active surface area
EIS	electrochemical impedance spectroscopy
FCEV	fuel cell electric vehicle
FRR	fluorine release rate
GDL	gas diffusion layer
HER	hydrogen evolution reaction
HFR	high frequency resistance
HHV	higher heating value
HC	hydrocarbon
LHV	lower heating value
MEA	membrane electrode assembly
MPL	microporous layer
OCV	open circuit voltage
NSTF	nanostructured thin film
OER	oxygen evolution reaction
OPEX	operational expenditure
PEM	proton exchange membrane
PEM-WE	proton exchange membrane water electrolyzer

## Contents

---

PEM-FC	proton exchange membrane fuel cell
PFSA	perfluorosulfonic acid
PGM	platinum group metal
PTFE	polytetrafluoroethylene
PTL	porous transport layer
RH	relative humidity
SEM	scanning electron microscopy
SPE	solid polymer electrolyte
STEM	scanning transmission electron microscopy

# 1 Introduction

Global energy consumption has increased significantly over the past decades to more than  $10^5$  TWh in 2015 and is expected to rise by another 30 % until 2040 ("New Policies Scenario", IEA).<sup>[1]</sup> Since most of the demand is still met by burning fossil fuels, annual carbon dioxide (CO<sub>2</sub>) emissions have increased accordingly, reaching a maximum of 32 Gt in 2015.<sup>[1]</sup> In an effort to reduce these emissions and to curb global warming, the Paris Agreement was passed in 2015 and put into effect on 4 November 2016<sup>[2]</sup> as a replacement of the Kyoto Protocol. The aim of the agreement, which was signed by 195 states, is to keep the global temperature rise below 2°C within this century compared to pre-industrial level and to take efforts to even more strictly limit the increase to 1.5°C.<sup>[2]</sup> Studies show that in principle it is technically and economically possible to reach this ambitious target,<sup>[3]</sup> but that it requires a drastic reduction of CO<sub>2</sub> output with a peak of global emissions no later than 2020 and net-zero emissions being reached by 2050<sup>[4]</sup>. Consequently, a massive and fast transition from fossil fuels to renewable energies in all sectors of energy generation is required. The share of renewable energies in the total primary energy supply is still very low (2.8 % in 2015), but if one were able to maintain the past trend of doubling the installed renewable energy capacity every ca. 5.5 years, a full decarbonization of the entire energy sector could be reached by 2040.<sup>[4]</sup>

In a future energy scenario mainly based on renewable energy sources, means of energy storage will be required due to the intermittent power generation associated with these technologies.<sup>[5]</sup> Even today, with comparably low shares of renewable energies, curtailment is an issue, e.g. in Germany 3.7 TWh of energy had to be curtailed in 2016 causing costs of 370 million €. <sup>[6]</sup> In a scenario with 80 % renewable energies (2050 goal for electricity production in Germany), this value is projected to increase to 56.1 TWh, corresponding to 12.8 % of the total production<sup>[7]</sup>. This emphasizes the need for suitable storage options, ranging from seconds to seasonal time scales. While super-capacitors and batteries can provide energy storage in the range of seconds to days, chemical energy carriers generated from renewable electricity (power to

gas/liquid) are the only viable option for long-term (weeks to months) storage of large amounts of energy.<sup>[5]</sup> Hydrogen generated by water electrolysis could serve as such an energy carrier in the future. Hydrogen can easily be stored as a compressed gas and transferred back to electricity by fuel cells, with the electricity being fed into the power grid in times of low supply while the waste heat of the fuel cell could be used in the heating sector.<sup>[8]</sup> However, the efficiency of this process is comparably low (<50%) and it has to compete with other technologies, such as power-to-heat, which usually present a cheaper option to use excess electricity.<sup>[9]</sup>

A much higher potential for electrolytic hydrogen is related to the transportation sector or industrial applications such as steel manufacturing. The steel industry is responsible for  $\approx 7\%$  of global CO<sub>2</sub> emissions.<sup>[10]</sup> This value could be reduced significantly by replacing carbon used to extract oxygen from the iron oxide by electrolytic hydrogen and first demonstration projects have been started recently.<sup>[10]</sup> The transportation sector consumes  $3.1 \cdot 10^4$  TWh of energy and is responsible for 25% of the global CO<sub>2</sub> emissions.<sup>[11]</sup> To enable a complete decarbonization of the transportation sector, internal combustion engine driven vehicles will have to be replaced by battery electric vehicles (BEVs) and/or fuel cell electric vehicles (FCEVs). While the former ones are more suitable for small-size vehicles and short driving distances, FCEVs will be the choice for larger vehicles and long distances.<sup>[12]</sup> The hydrogen to fuel these vehicles needs to be produced from renewable energy sources in order to enable a CO<sub>2</sub> neutral production chain. Due to its high power density, compact size and flexible operation range, proton exchange membrane (PEM) water electrolysis is a promising technology to supply hydrogen in the future.<sup>[13]</sup> At the moment, however, only a small share of the global hydrogen demand is served by PEM electrolysis due to the relatively high costs associated with this technology.<sup>[14,15]</sup> The aim of this thesis is to investigate the membrane electrode assembly (MEA) of a proton exchange membrane water electrolyzer (PEM-WE) to identify how electrode structure and material parameters influence efficiency and voltage losses, thereby developing strategies to optimize performance and minimize costs. Furthermore, the influence of operating conditions on efficiency and lifetime of PEM-WEs is discussed.

## 2 Proton Exchange Membrane Water Electrolysis

The working principle of a PEM-WE is illustrated in figure 2.1. The MEA is comprised of the electrodes which are attached to both sides of a proton conducting membrane. The membrane separates the gases on anode and cathode and provides electric insulation. The electrodes are typically made with a catalyst material, which besides of catalyzing the electrochemical reactions provides electrical conductivity and high porosity for transport of gas and water, as well as with an ionomer to enable a sufficient proton conductivity within the catalyst layer. The MEA is sandwiched between the porous transport layers (PTLs) which allow water and gas transport to the electrodes, mechanically support the MEA, and provide electrical and thermal conductivity to the bipolar plates (BPPs).

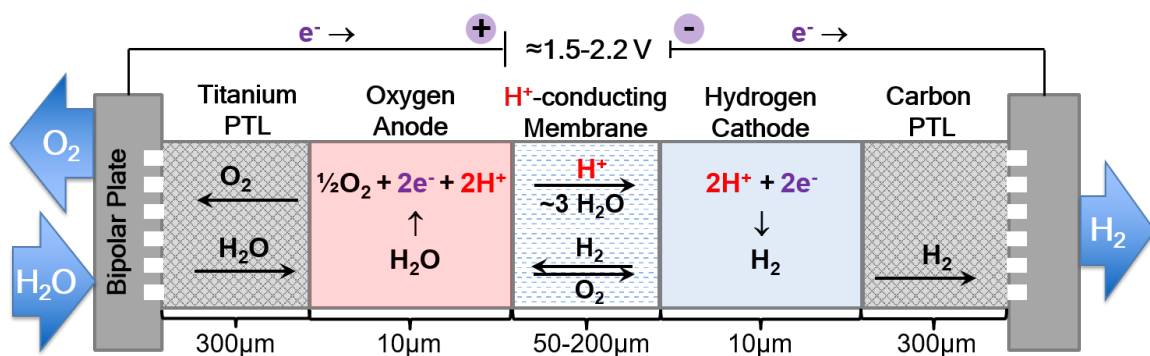
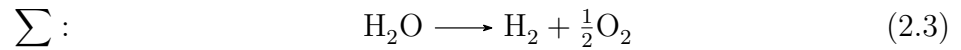
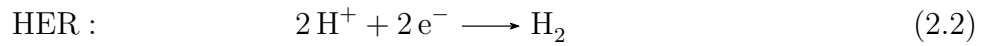
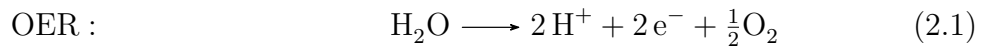


**Figure 2.1:** Schematic illustration of a proton exchange membrane water electrolyzer cell setup (not drawn to scale), including the main cell components and a specification of the relevant electrochemical reactions and transport processes.

During operation, liquid water is supplied to the anode catalyst layer where it is oxidized to protons, electrons, and oxygen (O<sub>2</sub>) which is transported through the PTL to the anode gas outlet. Driven by the electric field, protons move through

the membrane to the cathode where they are reduced to hydrogen ( $\text{H}_2$ ) which is transported through the PTL to the cathode gas outlet. Due to the electro-osmotic drag, water molecules are transported to the cathode along with the protons, enabling a sufficient humidification of the cathode catalyst layer. The overall reaction in a PEM-WE (cf. equation 2.3) is described by the two half-cell reactions on anode (oxygen evolution reaction (OER), cf. equation 2.1) and cathode (hydrogen evolution reaction (HER), cf. equation 2.2).



## 2.1 Materials and Components

In this section, the central components of an electrolyzer stack, namely the membrane electrode assembly (MEA), the porous transport layers (PTLs), and the bipolar plates (BPPs) will be discussed. The MEA is commonly fabricated by deposition of the catalyst layers on the membrane (referred to as catalyst coated membrane (CCM)). In principle, also a deposition of the catalyst on the PTL would be possible (referred to as catalyst coated substrate (CCS)), but this has rarely been reported for PEM electrolysis.<sup>[16]</sup> Details on the manufacturing process of the CCMs used in this work can be found in section 3.2.

### 2.1.1 Membrane and Ionomer

The membrane in a PEM-WE serves as the electrolyte as well as the gas permeation barrier between hydrogen and oxygen compartment. Consequently, it needs to be chemically and mechanically stable under typical operating conditions in a PEM-WE and provide a high proton conductivity as well as a low permeability for the produced gases ( $\text{H}_2$  and  $\text{O}_2$ ). The ionomer which is added to the catalyst during fabrication of the catalyst layer promotes proton transport within the electrode and functions as a binder, giving mechanical stability to the catalyst layer. On the other hand, it reduces the electrical conductivity and porosity of the catalyst layer. Consequently, the amount

of ionomer added to the catalyst layer needs to be adjusted carefully to optimize the performance, which will be discussed in detail in section 4.1. Since membrane and ionomer are usually composed of the same type of material, their properties will be discussed simultaneously in the following.

Perfluorosulfonic acid (PFSA) based materials, such as Nafion<sup>®</sup>, are typically used in state-of-the-art systems due to their excellent chemical and thermal stability, their good mechanical strength, and their high proton conductivity.<sup>[17]</sup> Nafion<sup>®</sup> consists of a polytetrafluoroethylene (PTFE) backbone and ether-linked perfluoro side chains terminating in a sulfonic acid group. The hydration state of the material determines its properties such as proton conductivity and gas permeability. In a PEM-WE, the membrane is exposed to liquid water and, consequently, can be considered fully humidified. However, under certain operating conditions, the water profile across the membrane could change as it has been shown for fuel cells operated at high current densities,<sup>[18–20]</sup> resulting in a local change of the hydration state. In general, the water uptake of a Nafion<sup>®</sup> membrane/ionomer, expressed as weight percent of water ( $WU$ ) is calculated based on the weight of the wet sample,  $w_{\text{wet}}$ , and dry sample,  $w_{\text{dry}}$ :

$$WU [\%] = \frac{w_{\text{wet}} - w_{\text{dry}}}{w_{\text{dry}}} \quad (2.4)$$

Alternatively, the water content of the membrane/ionomer,  $\lambda$ , can be expressed as the number of water molecules per sulfonic acid site and can be related to  $WU$  by

$$\lambda = \frac{WU \cdot EW}{M_{\text{H}_2\text{O}}} \quad (2.5)$$

where  $M_{\text{H}_2\text{O}}$  is the molecular weight of water ( $18 \text{ g mol}^{-1}$ ) and  $EW$  is the equivalent weight which is defined by the quotient of the dry ionomer mass per mole of sulfonic acid ( $\text{g}_{\text{ionomer,dry}} \text{ mol}_{\text{SO}_3\text{H}}^{-1}$ ). Hence, an ionomer with a lower  $EW$  contains a higher density of sulfonic acid groups and, consequently, has a higher proton conductivity.<sup>[21]</sup> Commercial Nafion<sup>®</sup> membranes, which are typically used for electrolysis applications, have an  $EW$  of  $1100 \text{ g mol}^{-1}$ . Due to water uptake, a membrane swells in the in-plane as well as in the through-plane direction; the extend of membrane expansion in a given direction depends on the applied mechanical constraints.

The total increase in volume,  $\Delta V_{\text{memb}}$ , can be expressed as<sup>[22]</sup>

$$\frac{\Delta V_{\text{memb}}}{V_{\text{memb,dry}}} = \frac{M_{\text{H}_2\text{O}} \cdot \rho_{\text{memb,dry}} \cdot \lambda}{\rho_{\text{H}_2\text{O}} \cdot EW} \quad (2.6)$$

where  $M_{\text{H}_2\text{O}}$  is the molecular weight of water,  $\rho_{\text{memb,dry}}$  is the density of the dry membrane ( $\approx 2 \text{ g cm}^{-3}$  for Nafion<sup>[23]</sup>),  $\rho_{\text{H}_2\text{O}}$  is the density of water,  $\lambda$  is the water content, and  $EW$  is the equivalent weight.

The water content of a Nafion membrane immersed in liquid water is higher than that of a membrane exposed to saturated water vapor.<sup>[24,25]</sup> This observation is known as Schroeder's paradox<sup>[26]</sup> and needs to be considered when calculating water uptake and other parameters like proton conductivity or permeability of Nafion<sup>®</sup> membranes for PEM-WE applications. Several studies have shown water contents of Nafion<sup>®</sup> membranes saturated with liquid water, and it was found that the water uptake strongly depends on the pretreatment of the membrane.<sup>[24,25,27]</sup> For membranes which were not pretreated by drying under vacuum or at elevated temperatures, a water content of  $\lambda \approx 21$  was found at 80°C.<sup>[25,28]</sup> However, it is not clear how the hot-pressing process which is typically used for MEA fabrication (section 3.2) affects the water content of the membrane.

The proton conductivity ( $\kappa$ ) of a Nafion<sup>®</sup> membrane is a function of water content and temperature and can be expressed according to Springer et al. by<sup>[18]</sup>

$$\kappa [\text{S cm}^{-1}] = (0.005139\lambda - 0.00326) \exp \left[ 1268 \left( \frac{1}{303} - \frac{1}{T} \right) \right] \quad (2.7)$$

where  $\lambda$  is the water content and  $T$  is the temperature of the membrane (in K). This correlation is in good agreement with other data reported in the literature<sup>[25,29]</sup> and, hence, can be used to approximate ohmic resistances of membranes under PEM-WE conditions. However, the pretreatment of the membrane again needs to be considered, since it influences water content ( $\lambda$ ) as well as conductivity ( $\kappa$ ) of the membrane.

Apart from its proton conductivity, the gas permeability of a membrane is of great importance for PEM-WE applications, since  $\text{H}_2$  is often produced at elevated pressures.<sup>[30]</sup> Permeation of  $\text{H}_2$  from the cathode through the membrane to the anode compartment cannot only reduce the faradaic efficiency of the electrolyzer, but can also lead to the formation of explosive gas mixtures (the lower explosion limit for  $\text{H}_2$  in  $\text{O}_2$  is  $\approx 4\%$ ).<sup>[31]</sup>  $\text{O}_2$  crossover is less critical, since  $\text{O}_2$  is usually produced at ambient pressure



and permeation rates are lower than for H<sub>2</sub>.<sup>[32]</sup> Furthermore, O<sub>2</sub> can get reduced to H<sub>2</sub>O on the cathode catalyst preventing the formation of an explosive gas mixture. This is not the case for H<sub>2</sub> permeating to the anode, since at operating potentials the anode catalyst is not active for hydrogen oxidation.<sup>[33]</sup> Gas permeation rates for Nafion<sup>®</sup> membranes as a function of temperature, relative humidity, and differential pressure have been studied extensively using ex-situ measurement techniques.<sup>[23,34–39]</sup> However, recent studies show that permeation rates are different when measured under actual PEM-WE operating conditions and exhibit a significant dependence on current density.<sup>[40–42]</sup> This phenomenon has been ascribed to a more complex water transport within the membrane during operation,<sup>[17]</sup> generally to a local pressure increase in the catalyst layer or to H<sub>2</sub> super-saturation.<sup>[42]</sup> Furthermore, the influence of structural properties of the catalyst layer and PTL as well as the impact of different cell hardware (applying, e.g., different compressive forces on the MEA) is not well understood yet<sup>[42]</sup> and, consequently, permeation rates have to be measured individually for each test setup.

In state-of-the-art PEM-WEs, relatively thick perfluorosulfonic acid (PFSA) membranes (Nafion<sup>®</sup> 115 or 117 with thicknesses of  $\approx 125$  or  $\approx 175$   $\mu\text{m}$ , respectively) are used because they are mechanically robust and provide a good compromise between ohmic resistance and low gas permeability.<sup>[43]</sup> To reduce ohmic losses, thinner Nafion<sup>®</sup> membranes could be used, however, increased gas crossover would limit PEM-WE operation to lower pressure or higher current densities. Furthermore, chemical degradation leading to membrane thinning would be more critical for thinner membranes. An approach to reduce safety hazards due to high gas crossover is the incorporation of recombination catalysts into the membrane.<sup>[44]</sup> This would prevent the accumulation of H<sub>2</sub> in the anode compartment but could not reduce the faradaic efficiency losses due to gas crossover. Usage of PFSA membranes with lower *EW* or operation at higher temperature could also reduce ohmic losses, but would again result in higher gas crossover and potentially a lower stability. Consequently, hydrocarbon (HC) membranes such as polybenzimidazoles (PBI), poly(ether ether ketones) (PEEK), poly(ether sulfones) (PES), and sulfonated polyphenyl quinoxaline (SPPQ), as well as radiation-grafted membranes are investigated as potential alternatives to PFSA. These types of materials show a much lower gas permeability compared to PFSA membranes and, consequently, a more favorable ratio of ohmic resistance to gas crossover<sup>[45]</sup> but long-term stability still needs to be improved.<sup>[46]</sup>

In summary, thick PFSA based membranes, which are used in state-of-the-art systems to maintain low gas crossover, present a significant contribution to the ohmic losses in a PEM-WE (cf. figure 2.10). Consequently, alternative materials which offer a better ratio of ohmic resistance to gas permeability could significantly improve PEM-WE performance.

### 2.1.2 Catalyst Materials

In general, a good catalyst must provide a high catalytic activity for the respective reaction as well as a high specific surface area to minimize the amount of required material. Furthermore, the material needs to be electrically conductive and stable against corrosion at the respective operating conditions.<sup>[47]</sup> Due to the harsh environment in a PEM-WE the choice of electrocatalysts is limited to platinum group metals (PGMs). Historically, catalyst layers were based on iridium (Ir) for the OER and platinum (Pt) black for the HER, using high metal loadings ( $1 - 5 \text{ mg}_{\text{PGM}} \text{ cm}^{-2}$ ).<sup>[48]</sup> Even today, catalyst loadings are relatively high with  $0.5 - 1.0 \text{ mg}_{\text{Pt}} \text{ cm}^{-2}$  on the cathode and  $\approx 2 \text{ mg}_{\text{Ir}} \text{ cm}^{-2}$  on the anode.<sup>[13]</sup> Due to concerns related to the high costs and the limited availability of PGMs, there have been a lot of efforts to reduce catalyst loadings in recent years.

On the cathode, experience in developing catalysts for PEM fuel cells has led to the replacement of Pt black by platinum nanoparticles supported on carbon black (Pt/C) as the standard catalyst for the HER.<sup>[13]</sup> Due to the extremely fast reaction kinetics of the HER<sup>[49-51]</sup>, overpotentials are relatively small and a significant reduction of the Pt loading is possible without affecting the overall performance (cf. section 4.2). Catalysts consisting of core-shell structures<sup>[52]</sup> or obtained by positioning copper atoms into the subsurface layer of Pt<sup>[53]</sup> show even higher activities and, consequently, could further reduce Pt loadings. Non-noble metal catalysts for the HER have been investigated but, to date, show much lower activities than Pt.<sup>[13]</sup>

On the anode, unsupported Ir or  $\text{IrO}_x$  based catalysts are used in state-of-the-art PEM-WEs.<sup>[13]</sup> Even though, Ir loadings are typically high ( $\approx 2 \text{ mg cm}^{-2}$ ), the kinetic losses due to the slow OER kinetics are still one of the major sources of cell efficiency losses. Consequently, research efforts have been directed towards i) an increase of the intrinsic OER activity of anode catalysts and ii) a reduction of the PGM loading.

The catalytic activities of several PGMs have been characterized by Miles et al., showing that the highest activities towards the OER in acidic media are obtained for Ir

and ruthenium (Ru).<sup>[54]</sup> In a later study, the authors found the lowest overpotentials for RuO<sub>x</sub>,<sup>[55]</sup> which is in agreement with theoretical studies.<sup>[56]</sup> Nevertheless, Ru or RuO<sub>x</sub> is not suitable as an OER catalyst in a PEM-WE since the rate of dissolution and corrosion is unacceptably high.<sup>[57]</sup> Mixed oxides could be a way to find a compromise between the high activity of Ru and the good stability of Ir. Several groups have tested materials like Ir<sub>x</sub>Ru<sub>y</sub>O<sub>2</sub><sup>[58]</sup> or Ir<sub>x</sub>Ru<sub>y</sub>Ta<sub>z</sub>O<sub>2</sub><sup>[59]</sup> and found improved activity compared to pure Ir. However, it remains unclear whether the Ru in the structure is really stabilized and whether Ir-Ru mixed oxides present a valuable alternative to pure Ir.<sup>[60]</sup> The activity of Ir based catalysts itself strongly depends on the oxidation state of the material.<sup>[61]</sup> Reier et al. showed that amorphous IrO<sub>x</sub> prepared at low temperatures provides a higher intrinsic OER activity than more crystalline high temperature IrO<sub>x</sub>, with the best activities obtained at a calcination temperature of 250-350°C.<sup>[62]</sup> In another study, a general trend of decreasing activity and increasing stability for rising temperatures was found and the authors propose a temperature of 400-500°C as the most promising compromise between activity and stability.<sup>[63]</sup>

Besides of increasing the intrinsic OER activity of a catalyst to reduce the kinetic overpotential, research efforts are targeting a reduction of the catalyst loading to overcome issues related to high costs and low availability of Ir. One strategy to improve the mass specific activity (i.e., the activity normalized by the mass of noble metal), is to maximize the noble metal dispersion by supporting thin films or nanoparticles of Ir or IrO<sub>x</sub> on high surface area support materials. However, the high electrochemical potential on the anode side of >1.4 V precludes the use of carbon, since it would oxidize under these conditions.<sup>[64,65]</sup> Titanium dioxide (TiO<sub>2</sub>) is frequently used as a catalyst support<sup>[66,67]</sup> because it represents a stable, commercially available, and inexpensive material.<sup>[68]</sup> However, since TiO<sub>2</sub> itself is not electrically conductive, a relatively high amount of Ir/IrO<sub>x</sub> (>40 %) is required to generate sufficient conductivity by forming a network of Ir/IrO<sub>x</sub> nanoparticles.<sup>[69,70]</sup> The need for a conductive support material to enable low Ir/IrO<sub>x</sub> loadings led to the investigation of different support materials such as TiC or TaC.<sup>[71,72]</sup> However, in the case of TaC the authors found a significant reduction of electrical conductivity of the support material after catalyst synthesis, again requiring high Ir loadings to achieve good conductivity. Antimony doped tin oxide (ATO) has been proposed as another potential support material,<sup>[73,74]</sup> but its long-term stability for PEM electrolysis still needs to be verified. Titanium suboxides present another promising option since they have a higher intrinsic conductivity com-

pared to ATO,<sup>[75,76]</sup> but, again, further research is required to show if this high conductivity can be maintained during prolonged electrolysis operation. Alternative catalyst structures, such as Ir based nanowires,<sup>[77]</sup> nanostructured thin films (NSTFs),<sup>[78]</sup> or core-shell structures<sup>[74,79]</sup> as well as the usage of improved catalyst layer manufacturing techniques, like reactive spray deposition,<sup>[79]</sup> have also been proposed as pathways to achieve lower Ir loadings.

In summary, while the catalyst requirements on the cathode of a PEM-WE are not critical due to the ultra-fast HER kinetics on Pt, a reduction of the kinetic overpotential and the required amount of Ir on the anode is essential to enable high efficiencies and a large-scale application of PEM electrolysis.

### 2.1.3 Porous Transport Layers

The porous transport layer (PTL) in a PEM-WE needs to promote gas/water transport from/to the catalyst layer through its pore space as well as the transport of heat and charge between electrode and BPP through its solid structure.<sup>[43]</sup> Additionally, it needs to mechanically support the MEA, especially when the electrolyzer is operated at differential pressure.<sup>[80]</sup> Consequently, PTLs should combine a high porosity with good mechanical stability, while being electrically and thermally conductive.<sup>[13]</sup> On the cathode of a PEM-WE, carbon based materials such as papers or cloths can be used, similar to those in fuel cells. However, due to different conditions in an electrolyzer compared to a fuel cell (e.g., higher pressure), requirements for a PTL to provide an optimum in performance might be different. On the anode, carbon based materials would corrode due to the high potential and therefore PTLs are typically fabricated from titanium (Ti) in the form of sintered porous media, expanded screen mesh, or felt (unwoven fabric).<sup>[81]</sup> Nano-manufacturing techniques, like electron beam melting or photochemical machining of Ti foils, have also been introduced to fabricate thin PTLs with tunable porosity.<sup>[82,83]</sup> In general, porosity and pore size distribution of a PTL have been found to be the most relevant structural parameters influencing PEM-WE performance.<sup>[81,84–87]</sup> Hwang et al. tested Ti felts with different fiber diameters as PTL in a reversible fuel cell and found the best performance in electrolysis mode for the smallest fiber diameter of 20  $\mu\text{m}$ .<sup>[88]</sup> Since pure Ti felts have a relatively large pore size, Ti powder was added to change pore size and porosity.<sup>[81,89]</sup> Ito et al. found that electrolysis performance increased with decreasing pore size, while porosity

did not have a significant effect as long as it exceeded 50%.<sup>[81]</sup> For sintered Ti PTLs, porosity should lie in the 30-50% range and an optimum pore size of 12-13  $\mu\text{m}$  was proposed.<sup>[84]</sup> Suermann et al. investigated electrolyzer performance for PTLs with different pore sizes and found an increased high frequency resistance (HFR) for the coarsest material, which was attributed to the interfacial resistance between PTL and catalyst layer.<sup>[90]</sup> The contact between catalyst layer (nano-level) and PTL (micro-level) generally seems to play an important role, and in the case of PEM fuel cells it led to the addition of microporous layers (MPLs) to gas diffusion layers (GDLs).<sup>[13]</sup> Consequently, the development of MPLs that could be applied onto Ti-based PTLs in order to smooth the contact between the layers could lead to significant improvements in performance, especially for thin catalyst layers (cf. section 4.2). Lettenmeier et al. developed pore-graded PTLs with smaller pore sizes at the catalyst layer/PTL interface via vacuum plasma spraying and showed similar or slightly improved performance compared to conventional sintered Ti PTLs, which can be seen as a first step into this direction.<sup>[91,92]</sup>

In summary, due to their manifold functions, PTLs play a very important but still not well investigated role in PEM-WEs. Better understanding of the performance determining parameters of PTLs as well as new developments in terms of materials and PTL structure could play an important role in optimizing PEM-WE performance.

### 2.1.4 Bipolar Plates

Bipolar plates (BPP) separate the single cells in a PEM-WE stack. They need to be mechanically stable to provide structure to the cell and allow uniform compression inside the stack. Additionally, high electrical and thermal conductivity are essential requirements. While graphite composites are well-established materials for BPPs in proton exchange membrane fuel cells (PEM-FCs),<sup>[93,94]</sup> significant corrosion was observed under PEM-WE operating conditions.<sup>[95]</sup> Due to its excellent strength, low electrical resistivity, high thermal conductivity and low permeability,<sup>[13]</sup> Ti is used as a standard material for BPPs in PEM-WEs despite of its high costs.<sup>[96]</sup> However, Ti can develop a passive oxide layer during PEM electrolysis operation, leading to an increased contact resistance.<sup>[13]</sup> Consequently, coatings of gold (Au) or Pt are often added to the Ti base material to lower the electrical contact resistance between BPP and PTL as well as to improve durability.<sup>[95,97]</sup> However, adding precious metal coatings on an already ex-

pensive base material increases the BPP costs even further.<sup>[96]</sup> Cheaper base materials such as stainless steel or carbon-based composites with a protective coating to prevent corrosion could be used as a low cost alternative.<sup>[98]</sup> Langemann et al. tested Au and TiN coatings on stainless steel and found an improved stability compared to the pure stainless steel substrate.<sup>[96]</sup> However, minor imperfections in the coatings resulted in a corrosion of the substrate material. Gago et al. introduced the deposition of a thin layer of Ti ( $\approx 50 \mu\text{m}$ ) via vacuum plasma spraying on a stainless steel substrate as an approach to reduce BPP costs.<sup>[99]</sup> However, long-term stability was only achieved when adding an additional Pt coating.<sup>[91,100]</sup> Alternative manufacturing techniques for BPPs, such as 3D printing, have also been introduced as a possibility to lower costs.<sup>[101]</sup>

BPPs for PEM-WEs often have a flow-field based on a channel structure to distribute the reactant water evenly over the active area and remove product gases.<sup>[43]</sup> BPPs without flow-fields that only rely on the PTLs to distribute water are also used, but typically cannot supply the water evenly for large cell areas.<sup>[13]</sup> Amongst different flow-field designs, parallel channels have shown a higher performance compared to serpentine patterns due to a better water distribution and a lower pressure drop.<sup>[102]</sup> However, even parallel channel structures were shown to result in non-uniform water flow rate and temperature distributions over the active area,<sup>[103–105]</sup> and improved flow-field designs might lead to a better flow uniformity.<sup>[106]</sup>

In summary, BPPs are a major cost contributor to the PEM-WE stack (cf. figure 2.8) and, hence, replacement of Ti by low cost alternative materials is essential to reduce PEM-WE stack costs. Improved flow-field designs to provide a uniform water distribution in the cell will become more important with increasing active areas.

## 2.2 Efficiency and Voltage Losses

The measured cell voltage,  $E_{\text{cell}}$ , of a PEM-WE can be defined by adding the contributions of various voltage losses to the reversible cell voltage,  $E_{\text{rev}}$ , (note that current, potentials, and overpotentials are taken as positive values):

$$E_{\text{cell}} = E_{\text{rev}} + i \cdot (R_{\text{memb}} + R_{\text{el}}) + |\eta_{\text{HER}}| + \eta_{\text{OER}} + i \cdot (R_{\text{H}^+, \text{cath}}^{\text{eff}} + R_{\text{H}^+, \text{an}}^{\text{eff}}) + \eta_{\text{mt}} \quad (2.8)$$

where  $i$  is the electrolyzer current.  $R_{\text{memb}}$  and  $R_{\text{el}}$  are the ohmic resistance of the membrane and the electrical resistance (sum of contact resistances between BPPs and

PTLs as well as between PTLs and electrodes and bulk PTL resistances), respectively.  $\eta_{\text{HER}}$  and  $\eta_{\text{OER}}$  are the kinetic overpotentials of the HER and OER, while  $R_{\text{H}^+, \text{cath}}^{\text{eff}}$  and  $R_{\text{H}^+, \text{an}}^{\text{eff}}$  represent the proton transport resistance in the respective catalyst layers.  $\eta_{\text{mt}}$  describes additional losses related to mass transport phenomena. The voltage losses for an MEA based on a Nafion<sup>®</sup> 212 membrane operated at 80°C and ambient pressure are shown exemplarily in figure 2.2 (anode: IrO<sub>2</sub>/TiO<sub>2</sub>, 2 mg<sub>Ir</sub> cm<sup>-2</sup>; cathode: Pt/C, 0.35 mg<sub>Pt</sub> cm<sup>-2</sup>).

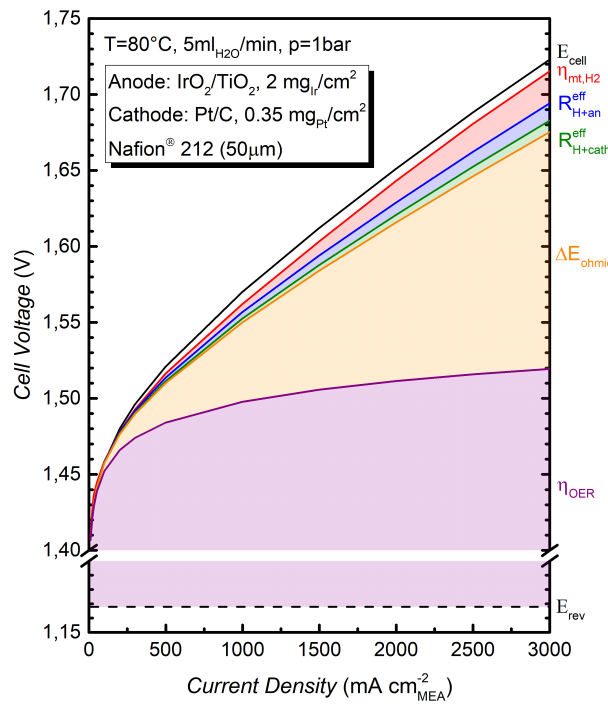


**Figure 2.2:** Contributions of various voltage losses to overall cell voltage. The reversible cell voltage is given by the dashed black line and the purple area represents the OER kinetic losses (y-axis is intercepted between 1.2 V and 1.4 V for better visualization of other losses). Ohmic losses are given by the orange area, and losses due to proton conduction resistance in the cathode and anode electrodes are shown by the green and blue areas, respectively. The red area represents the losses due to H<sub>2</sub> mass transport and the full black line gives the cell voltage measured at ambient pressure (80°C, 5 ml<sub>H<sub>2</sub>O</sub> min<sup>-1</sup>). The white space between the full black line and the red line represents unaccounted voltage losses, which could originate from mass transport phenomena on the anode. Catalyst loadings are 2 mg<sub>Ir</sub> cm<sup>-2</sup> on the anode and 0.35 mg<sub>Pt</sub> cm<sup>-2</sup> on the cathode; ≈50 μm thick Nafion<sup>®</sup> 212 membrane. Reproduced from reference.<sup>[107]</sup>

### 2.2.1 Thermodynamics

According to thermodynamics, the reaction enthalpy,  $\Delta H$ , defines the total energy needed for the electrochemical splitting of water.

$$\Delta H = \Delta G + T \cdot \Delta S \quad (2.9)$$

where  $\Delta G$  is the Gibbs free energy of the reaction,  $T$  is the temperature, and  $\Delta S$  is the change in entropy of the system. At standard conditions (298 K, 1 bar), the Gibbs free energy  $\Delta G^0$  is 237 kJ/mol. This represents the minimum electrical work needed for splitting water at the corresponding theoretical cell potential

$$E_{\text{rev}}^0 = \left| -\frac{\Delta G^0}{nF} \right| = 1.23 \text{ V} \quad (2.10)$$

where  $n$  is the number of transferred electrons in the reaction ( $n=2$  for reaction 2.1) and  $F$  is the Faraday constant ( $96485 \text{ As mol}^{-1}$ ). The thermoneutral potential,  $E_{\text{tn}}^0$ , is defined as the potential at which water electrolysis can be conducted without the production or consumption of heat, i.e., where a thermally insulated electrolyzer would operate at constant temperature.

$$E_{\text{tn}}^0 = \left| -\frac{\Delta H^0}{nF} \right| = 1.48 \text{ V} \quad (2.11)$$

Here,  $\Delta H^0$  is the reaction enthalpy at standard conditions ( $\Delta H^0=286 \text{ kJ mol}^{-1}$ ).

The reversible cell voltage,  $E_{\text{rev}}$ , is a function of temperature and activity of the species involved in the reaction and can be calculated for reaction 2.3 by

$$E_{\text{rev}} = E_{\text{rev}}^0 + \frac{RT}{2F} \ln \left( \frac{a_{\text{H}_2} \cdot (a_{\text{O}_2})^{\frac{1}{2}}}{a_{\text{H}_2\text{O}}} \right) \quad (2.12)$$

where the temperature dependence of the standard reversible potential,  $E_{\text{rev}}^0$ , can be calculated as<sup>[108]</sup>

$$E_{\text{rev}}^0 = 1.2291 \text{ V} - 0.0008456 \text{ V} \cdot (T - 298.15 \text{ K}) \quad (2.13)$$

For liquid water, the activity of water,  $a_{\text{H}_2\text{O}}$ , is one, while the activities of the gaseous



species,  $a_{\text{H}_2}$  and  $a_{\text{O}_2}$ , are represented by the ratio of their partial pressures to the standard pressure of 1 bar. Consequently,  $E_{\text{rev}}$  can be expressed as

$$E_{\text{rev}} = E_{\text{rev}}^0 + \frac{RT}{2F} \ln \left[ \left( \frac{p_{\text{H}_2}}{1 \text{ bar}} \right) \cdot \left( \frac{p_{\text{O}_2}}{1 \text{ bar}} \right)^{\frac{1}{2}} \right] \quad (2.14)$$

where  $p_{\text{H}_2}$  and  $p_{\text{O}_2}$  are the partial pressure of  $\text{H}_2$  and  $\text{O}_2$ , respectively. At the typical measurement conditions of  $80^\circ\text{C}$  and ambient pressure used in most of this work, the saturation pressure of  $\text{H}_2\text{O}$  is  $0.47 \text{ bar}_a$ , resulting in  $p_{\text{H}_2}=p_{\text{O}_2}=0.53 \text{ bar}_a$ . This yields a reversible cell voltage  $E_{\text{rev}}=1.17 \text{ V}$ .

In a real system, the cell voltage is of course higher as a result of the contributions of different overpotentials as described in equation 2.8. To determine the voltage efficiency,  $\eta_v$ , of an electrolyzer, the theoretically required amount of energy for the reaction, i.e., the reaction enthalpy  $\Delta H^0$ , has to be divided by the actual electrical energy input determined from the operating cell potential  $E_{\text{cell}}$ .

$$\eta_v = \left| \frac{-\Delta H^0}{2 \cdot F \cdot E_{\text{cell}}} \right| \quad (2.15)$$

The voltage efficiency can be calculated based on the higher heating value (HHV) of  $\text{H}_2$  or on the lower heating value (LHV) of  $\text{H}_2$ . The HHV corresponds to the reaction enthalpy from liquid water to gaseous hydrogen and is commonly used to calculate the efficiency ( $\eta_{\text{HHV}}$ ) if  $\text{H}_2$  is utilized chemically or if one aims to consider the heat balance of the electrolyzer. The efficiency based on the LHV ( $\eta_{\text{LHV}}$ ), on the other hand, is used when the product  $\text{H}_2$  is used energetically (e.g., transformation to electrical energy with a fuel cell) in an application which does not benefit from the condensing enthalpy of water ( $\Delta H_{\text{vap}}^0=44 \text{ kJ mol}^{-1}$ ). A way to characterize the efficiency of an electrolyzer independent of the further utilization of the produced  $\text{H}_2$  is to state the amount of electrical energy required to produce a certain amount of hydrogen in  $\text{kWh kg}^{-1}(\text{H}_2)$  or  $\text{kWh Nm}^{-3}(\text{H}_2)$  (at atmospheric pressure and  $0^\circ\text{C}$ ). An overview of the respective values is given in table 2.1.

To determine the overall efficiency of an electrolyzer, not only the voltage efficiency,  $\eta_v$ , has to be considered but also losses due to permeation of  $\text{H}_2$  and  $\text{O}_2$  through the membrane. This is expressed by the faradaic efficiency,  $\eta_F$ , which depends on the used materials (membrane material and thickness), the operating conditions (pressure,

**Table 2.1:** Enthalpy of the water splitting reaction in different units for water being in liquid state (HHV) and water being in gaseous state (LHV) as well as the corresponding thermoneutral voltage  $E_{\text{tn}}^0$ ; ( $\text{Nm}^3$  at atmospheric pressure and  $0^\circ\text{C}$ ).

	$\Delta H^0$			$E_{\text{tn}}^0$
	$\text{kJ mol}^{-1}$	$\text{kWh kg}^{-1}$	$\text{kWh Nm}^{-3}$	V
higher heating value (HHV)	286	39.7	3.54	1.48
lower heating value (LHV)	242	33.6	3.00	1.25

temperature), and the current density at which the electrolyzer is operated. In this work, the term efficiency usually refers to the efficiency of an electrolyzer single cell or stack. To determine the overall efficiency of an electrolyzer system, also balance of plant (BoP) components such as pumps, heaters, and power electronics need to be considered.

### 2.2.2 Ohmic Losses

The measured cell potential,  $E_{\text{cell}}$ , is comprised of the reversible cell voltage,  $E_{\text{rev}}$ , as well as several overpotentials as expressed in equation 2.8. Ohmic losses in an electrolyzer can be divided into ionic losses due to the proton transport resistance of the membrane,  $R_{\text{memb}}$ , and losses due the electrical resistance contributions within the cell,  $R_{\text{el}}$ . The total ohmic resistance of a single cell is typically quantified by the high frequency resistance,  $R_{\text{HFR}}$ , which can be accessed via electrochemical impedance spectroscopy (EIS).

$$R_{\text{HFR}} = R_{\text{memb}} + R_{\text{el}} \quad (2.16)$$

To deconvolute the contributions of  $R_{\text{memb}}$  and  $R_{\text{el}}$  to the total ohmic resistance,  $R_{\text{HFR}}$  can be measured for MEAs with membranes of different thickness, as shown in figure 2.3. Since  $R_{\text{el}}$  is independent of membrane thickness, while  $R_{\text{memb}}$  is expected to scale linearly with the actual membrane thickness, the contributions of both can be determined by a linear regression of the data points:

$$R_{\text{HFR}} = \frac{1}{\kappa_{\text{memb}}} \cdot t_{\text{memb,wet}} + R_{\text{el}} \quad (2.17)$$

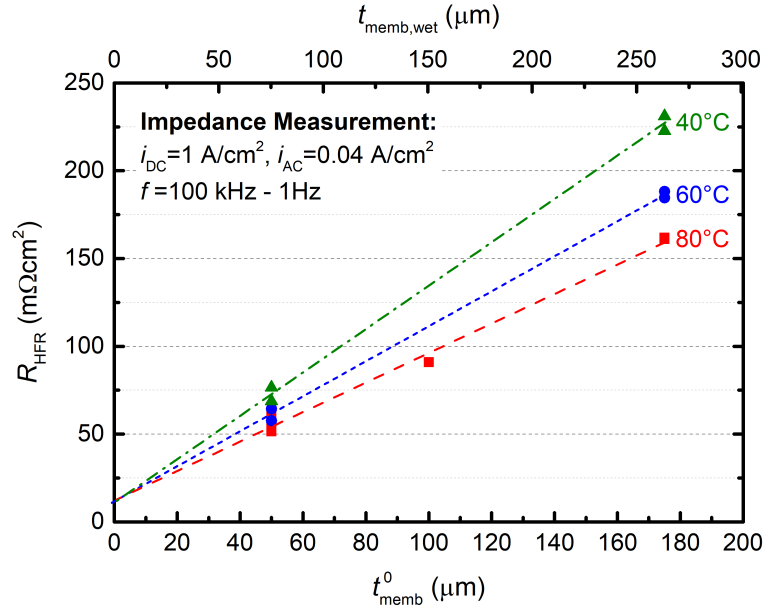


**Figure 2.3:** High frequency resistance,  $R_{\text{HFR}}$ , as a function of the membrane thickness determined at operating temperatures of 40°C (green triangles), 60°C (blue circles) and 80°C (red squares). The lower x-axis shows the nominal membrane thickness at 25 °C and 50% relative humidity,  $t_{\text{memb}}^0$ , while the upper x-axis represents the actual membrane thickness in the electrolyzer,  $t_{\text{memb,wet}}$ .  $R_{\text{HFR}}$  was determined from the x-axis intercept in a Nyquist plot for an electrochemical impedance measurement performed at a DC current density of 1 A cm<sup>-2</sup> and a perturbation current of 0.04 A cm<sup>-2</sup> in a frequency range of 100 kHz to 1 Hz. From the slope of a linear regression (dashed/dotted lines) the membrane conductivity can be determined, while the y-axis intercept corresponds to the electrical resistance.

To determine the correct values for the ionic conductivity of the membrane,  $\kappa_{\text{memb}}$ , in S cm<sup>-1</sup>, the actual thickness of the membrane in the electrolyzer,  $t_{\text{memb,wet}}$ , needs to be used in equation 2.17 instead of the nominal membrane thickness,  $t_{\text{memb}}^0$ , at 25°C and 50% relative humidity (RH). The difference between the two arises from the swelling of the membrane in the electrolyzer, i.e., in the presence of liquid water at elevated temperatures (cf. section 2.1.1). In general, it is expected that the membrane swells in the in-plane as well as in the through-plane direction. However, since the edges of the membrane are compressed between the gaskets of the cell hardware, a significant expansion in the in-plane direction is not expected and it is assumed that swelling only occurs in the through-plane direction.

Consequently, the increase in membrane thickness,  $\Delta t_{\text{memb}}$ , equals the total volume increase,  $\Delta V_{\text{memb}}$  and the thickness of the membrane in equilibrium with liquid water,  $t_{\text{memb,wet}}$ , can be expressed according to equation 2.6 as

$$t_{\text{memb,wet}} = t_{\text{memb,dry}} \left( 1 + \frac{M_{\text{H}_2\text{O}} \cdot \rho_{\text{memb,dry}} \cdot \lambda}{\rho_{\text{H}_2\text{O}} \cdot EW} \right) \quad (2.18)$$

where  $M_{\text{H}_2\text{O}}$  is the molecular weight of water,  $\rho_{\text{memb,dry}}$  is the density of the dry membrane ( $\approx 2 \text{ g cm}^{-3}$  for Nafion<sup>®</sup>),  $\rho_{\text{H}_2\text{O}}$  is the density of water,  $\lambda$  is the water content and  $EW$  is the equivalent weight. Based on a nominal thickness,  $t_{\text{memb}}^0$ , of  $50 \mu\text{m}$  for a Nafion<sup>®</sup> 212 membrane at  $25^\circ\text{C}$  and  $50\%$  RH ( $\lambda=3.7$ ,  $\rho_{\text{H}_2\text{O}}=1.0 \text{ g cm}^{-3}$ ), the dry membrane thickness,  $t_{\text{memb,dry}}$ , is  $45 \mu\text{m}$ . At a temperature of  $80^\circ\text{C}$  in equilibrium with water ( $\lambda=21$ <sup>[25,28]</sup>) the actual membrane thickness,  $t_{\text{memb,wet}}$ , is  $50\%$  higher than the nominal membrane thickness, i.e., that measured at  $25^\circ\text{C}$  and  $50\%$  RH. A water content of  $\lambda=21$  is also assumed for the measurements at  $40^\circ\text{C}$  and  $60^\circ\text{C}$ , which were performed after the experiment at  $80^\circ\text{C}$ , since it was found that equilibrium hydration attained at a given temperature tends to be maintained at lower temperatures.<sup>[25,28]</sup> The calculated values for  $R_{\text{el}}$  and  $\kappa_{\text{memb}}$  based on the actual membrane thickness  $t_{\text{memb,wet}}$  are shown in table 2.2 for different temperatures.

**Table 2.2:** Electrical resistance,  $R_{\text{el}}$ , and membrane conductivity,  $\kappa_{\text{memb}}$ , for different temperatures obtained from a linear regression of  $R_{\text{HFR}}$  measured for various membrane thicknesses according to equation 2.17 and equation 2.18 for  $\lambda=21$ .

Temperature	$R_{\text{el}}$	$\kappa_{\text{memb}}$
$^\circ\text{C}$	$\text{m}\Omega\text{cm}^2$	$\text{S cm}^{-1}$
40	$11 \pm 6$	$122 \pm 5$
60	$11 \pm 4$	$151 \pm 5$
80	$13 \pm 3$	$181 \pm 7$

The ionic conductivity of the membrane,  $\kappa_{\text{memb}}$ , calculated based on  $t_{\text{memb,wet}}$  agrees well with the correlation by Springer et al.<sup>[18]</sup> (cf. equation 2.7) and other experimentally determined values.<sup>[25,29]</sup> The electrical resistance obtained from the y-axis intercept in figure 2.3 is similar for all measured temperatures (cf. table 2.2). This

electrical resistance is considered to arise mainly from the contact resistance between PTL and flow-field,<sup>[22]</sup> which can be measured externally with a setup shown in section 4.1. For the cell hardware and the PTLs used in this work, a total electrical resistance of  $\approx 12 \text{ m}\Omega\text{cm}^2$  was estimated based on the external contact resistance measurement, which is in good agreement with the values shown in table 2.2.

### 2.2.3 Kinetic Losses

The kinetic overpotential or activation overpotential is the result of irreversible processes within an electrochemical reaction. It is commonly described by the Butler-Volmer equation:

$$i_{+/-} = i_0 \cdot rf \cdot \left[ \exp\left(\frac{\alpha_a \cdot F}{R \cdot T} \cdot \eta\right) - \exp\left(-\frac{\alpha_c \cdot F}{R \cdot T} \cdot \eta\right) \right] \quad (2.19)$$

where  $i_{+/-}$  is the current of a half-cell reaction and  $\eta$  is the overpotential, which has a positive sign for an anodic and a negative sign for a cathodic reaction.  $i_0$  is the exchange current density, a kinetic reaction rate constant, which depends on the specific electrocatalyst, and  $rf$  is the electrode roughness factor, which relates the real surface area of the catalyst to the geometric area of the electrode (in units of  $\text{cm}^2_{\text{surface}}/\text{cm}^2_{\text{electrode}}$ ).  $\alpha_a$  and  $\alpha_c$  are the transfer coefficients of the anodic and the cathodic reaction, describing the symmetry of the energy barrier and the number of exchanged electrons in the rate determining step. Furthermore,  $F$  is the Faraday constant,  $T$  is the temperature and  $R$  is the gas constant. In the following, the kinetic overpotentials for the HER on the cathode,  $\eta_{\text{HER}}$ , and the OER on the anode,  $\eta_{\text{OER}}$ , of a PEM-WE will be discussed.

### Kinetics of the Hydrogen Evolution Reaction

Due to the fast reaction kinetics of the HER on Pt<sup>[49-51]</sup> and the small resulting overpotential, the Butler-Volmer equation can be linearized and  $\eta_{\text{HER}}$  can be expressed as<sup>[109]</sup>

$$\eta_{\text{HER}} = i_{\text{HER}} \cdot R_{\text{K,HER}} \quad (2.20)$$

where  $i_{\text{HER}}$  is the current of the HER (cathodic current:  $i_{\text{HER}} < 0$ ) and

$$R_{\text{K,HER}} = \frac{RT}{(\alpha_a + \alpha_c) \cdot F \cdot rf \cdot i_{0,\text{HER}}} \quad (2.21)$$

Here,  $\alpha_a$  and  $\alpha_c$  are the transfer coefficients and  $i_{0,\text{HER}}$  is the exchange current density of the HER at the respective operating temperature. The roughness factor,  $rf$ , can be determined from the Pt loading,  $L_{\text{Pt}}$ , and the electrochemically active surface area,  $A_{\text{Pt,el}}$ :

$$rf = L_{\text{Pt}} \cdot A_{\text{Pt,el}} \quad (2.22)$$

It was found that for carbon supported platinum catalysts the HER/HOR kinetics are linear up to  $\approx 500 \text{ A mg}_{\text{Pt}}^{-1}$ <sup>[110]</sup> making equations 2.20 and 2.21 a valid assumption for all operational current densities and catalyst loadings discussed in this work. The resulting HER overpotential,  $\eta_{\text{HER}}$ , is calculated for different catalyst loadings in section 4.2 and is typically small enough to be considered negligible compared to other voltage losses.

### Kinetics of the Oxygen Evolution Reaction

The kinetics of the OER in a PEM-WE are much slower compared to the HER, causing a significant activation overpotential,  $\eta_{\text{OER}}$ .<sup>[47]</sup> For large overpotentials, one of the terms in equation 2.19 becomes negligible and the Butler-Volmer equation can be simplified to the so-called Tafel equation

$$i_{\text{OER}} = i_0 \cdot rf \cdot \exp\left(\frac{\alpha_a \cdot F}{R \cdot T} \cdot \eta_{\text{OER}}\right) \quad (2.23)$$

In this case, the kinetic overpotential of the OER can be expressed as

$$\eta_{\text{OER}} = \frac{2.303 \cdot R \cdot T}{\alpha_a \cdot F} \cdot \log\left(\frac{i_{\text{OER}}}{i_{0,\text{OER}} \cdot rf}\right) = b \cdot \log\left(\frac{i_{\text{OER}}}{i_{0,\text{OER}} \cdot rf}\right) \quad (2.24)$$

where  $b$  is referred to as the Tafel slope, representing the overpotential increase required for a 10x increase in current. The Tafel slope can be extracted from experimental data by a linear regression of the iR-free cell voltage when plotted on a logarithmic current scale as shown in figure 2.4.

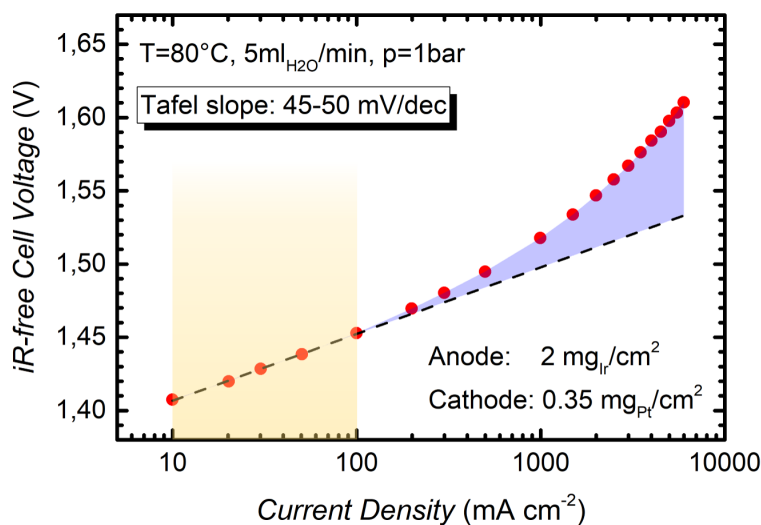


**Figure 2.4:** Ambient pressure Tafel plot of the *iR*-free cell voltage vs. the logarithm of the current density for an MEA with standard catalyst loadings measured at 80°C (anode: IrO<sub>2</sub>/TiO<sub>2</sub>, 2 mg<sub>Ir</sub> cm<sup>-2</sup>; cathode: Pt/C, 0.35 mg<sub>Pt</sub> cm<sup>-2</sup>; ≈50 μm thick Nafion<sup>®</sup> 212 membrane). The Tafel slope is obtained from a linear fit of the values between 10-100 mA cm<sup>-2</sup> (indicated in yellow), i.e., from the region where transport losses can be neglected. The remaining voltage losses after subtraction of ohmic and kinetic losses, which can be attributed to transport phenomena, (cf. section 2.2.4), are indicated by the light purple area.

For small current densities (a range of 10-100 mA cm<sup>-2</sup> was chosen here), voltage losses due to proton transport in the electrodes or mass transport are negligible and the *iR*-free cell voltage follows a linear behavior, thus expressing the pure OER kinetics (under the assumption that the HER overpotential is negligible). A linear fit in this region yields a Tafel slope of 45-50 mV dec<sup>-1</sup> for the IrO<sub>2</sub>/TiO<sub>2</sub> catalyst used in this work. This is in good agreement with the values reported by Matsumoto and Sato for sputtered and thermally prepared IrO<sub>2</sub><sup>[111]</sup>, and with that by Reier et al. for amorphous iridium oxide on a titanium substrate.<sup>[62]</sup> Suermann et al., on the other hand, report Tafel slopes of 70 mV dec<sup>-1</sup> or higher for an iridium-based catalyst similar to the one used in this work.<sup>[112]</sup> However, it is likely that these high apparent Tafel slopes do not actually represent the pure OER kinetics but are influenced by additional voltage losses. A similar effect on the apparent Tafel slope was shown for increased mass transport resistance in the cathode of a PEM-WE<sup>[113]</sup> as well as for an inhomogeneous anode catalyst layer leading to additional voltage losses (cf. section 4.2). Consequently, higher than expected Tafel slopes can be seen as a hint towards additional voltage losses that have not been accounted for in the analysis.

As shown in figure 2.4, the  $iR$ -free cell voltage follows the expected Tafel behavior up to  $\approx 200 \text{ mA cm}^{-2}$  and deviates for higher current densities. The difference between the Tafel line (dashed black line in figure 2.4) and the measured  $iR$ -free cell voltage (red points in figure 2.4) represents the remaining voltage losses due to transport phenomena which will be discussed in the following section.

### 2.2.4 Transport Losses

Voltage losses related to transport phenomena,  $E_{\text{tr}}$ , can be expressed by subtracting ohmic and kinetic losses from the measured cell voltage:

$$E_{\text{tr}} = E_{\text{cell}} - E_{\text{rev}} - i \cdot (R_{\text{memb}} + R_{\text{el}}) - |\eta_{\text{HER}}| - \eta_{\text{OER}} = i \cdot (R_{\text{H}^+, \text{cath}}^{\text{eff}} + R_{\text{H}^+, \text{an}}^{\text{eff}}) + \eta_{\text{mt}} \quad (2.25)$$

The remaining losses can be divided into overpotentials due to the proton transport resistance in the catalyst layers and an overpotential due to mass transport phenomena, which can include water transport to the active sites as well as transport of the evolved gases from the active sites to the gas outlet of the cell.

#### Proton Transport Resistance of the Cathode

Due to the fast kinetics (cf. section 2.2.3), the HER will occur preferably very near the electrode/membrane interface, and losses due to proton transport within the electrode will be small.<sup>[114]</sup> The effective proton transport resistance of the cathode,  $R_{\text{H}^+, \text{cath}}^{\text{eff}}$ , can be calculated based on the charge transfer resistance,  $R_{\text{K,HER}}$ , and the sheet resistance for proton transport,  $R_{\text{H}^+, \text{cath}}$ , according to<sup>[109]</sup>

$$\frac{R_{\text{H}^+, \text{cath}}}{R_{\text{H}^+, \text{cath}}^{\text{eff}}} = \frac{\beta}{\left( \frac{e^\beta + e^{-\beta}}{e^\beta - e^{-\beta}} - \frac{1}{\beta} \right)} \quad (2.26)$$

where  $\beta$  is given by

$$\beta = \left( \frac{R_{\text{H}^+, \text{cath}}}{R_{\text{K,HER}}} \right)^{1/2} \quad (2.27)$$

The sheet resistance for proton transport,  $R_{\text{H}^+, \text{cath}}$ , can be determined by EIS using a one-dimensional transmission-line model.<sup>[22,115]</sup> Liu et al. used this method to measure  $R_{\text{H}^+, \text{cath}}$  of Pt/C-based catalyst layers for different ionomer/carbon ratios, relative humidities, electrode thicknesses, ionomer equivalent weights and carbon sup-



port materials.<sup>[22,116,117]</sup> For the Pt catalyst supported on a Vulcan-type carbon and an ionomer/carbon ratio of 0.6 used in this work, a resistivity  $\rho_{\text{H}^+, \text{cath}} = 25 \Omega \text{cm}$  is obtained at typical operating conditions of  $80^\circ \text{C}$  in the presence of liquid water.<sup>[22]</sup> From this value  $R_{\text{H}^+, \text{cath}}$  can be calculated:

$$R_{\text{H}^+, \text{cath}} = \rho_{\text{H}^+, \text{cath}} \cdot t_{\text{cath}} \quad (2.28)$$

where  $t_{\text{cath}}$  is the electrode thickness of the cathode. A detailed calculation of these values for different catalyst loadings can be found in section 4.2.

### Proton Transport Resistance of the Anode

The effective proton transport resistance of the anode,  $R_{\text{H}^+, \text{an}}^{\text{eff}}$ , can be calculated from the sheet resistance for proton transport,  $R_{\text{H}^+, \text{an}}$  as<sup>[118]</sup>

$$R_{\text{H}^+, \text{an}}^{\text{eff}} = \frac{R_{\text{H}^+, \text{an}}}{3 + \zeta} \quad (2.29)$$

where  $\zeta$  is a correction factor which accounts for the effect of a reduced catalyst utilization in the anode.  $\zeta$  is a function of the ratio of the sheet resistance for proton transport to the kinetic resistance.

$$\frac{i \cdot R_{\text{H}^+, \text{an}}}{b} \quad (2.30)$$

where  $i$  is the current density,  $R_{\text{H}^+, \text{an}}$  the sheet resistance for proton transport and  $b$  the Tafel slope. For small values of  $i \cdot R_{\text{H}^+, \text{an}}/b$ , the catalyst utilization approaches 100% and the correction factor,  $\zeta$ , goes to zero. The sheet resistance for proton transport in the Ir-based anode,  $R_{\text{H}^+, \text{an}}$ , could in principle be determined by EIS analogous to the transmission line analysis used for PEM fuel cell cathodes<sup>[22,115]</sup> and first attempts to do this were shown by Babic et al.<sup>[119]</sup> In this work,  $R_{\text{H}^+, \text{an}}$  was estimated with the correlation introduced by Liu et al.<sup>[22]</sup>

$$R_{\text{H}^+, \text{an}} = \frac{t_{\text{an}}}{\kappa \cdot V_{\text{ion, wet}}/\tau} \quad (2.31)$$

Here,  $t_{\text{an}}$  is the electrode thickness,  $\kappa$  is the conductivity of the ionomer,  $V_{\text{ion, wet}}$  is the volume fraction of ionomer in the electrode equilibrated with liquid water, and

$\tau$  is the tortuosity of the ionomer phase in the electrode. The conductivity of the ionomer is assumed to be similar to the conductivity of the membrane,  $\kappa_{\text{memb}}$ , and  $t_{\text{an}}$  as well as  $V_{\text{ion,wet}}$  can be determined from cross-sectional SEM images of the MEAs (cf. section 4.1). The tortuosity of the ionomer phase,  $\tau$ , is the only unknown parameter which needs to be estimated from the literature values for Pt/C based electrodes.<sup>[22]</sup> A detailed calculation of  $R_{\text{H}^+, \text{an}}$  for electrodes with different ionomer contents can be found in section 4.1.

### Mass Transport Resistance

The nature and origin of mass transport losses in PEM-WEs are to date not well-understood, which is related to the complex nature of the two-phase flow of liquid water and gas.<sup>[90]</sup> In general, the mass transport resistance should depend on the structure (i.e., thickness, porosity, pore size) of the catalyst layer and the PTL as well as the flow-field features. Suermann et al. showed that for current densities above  $1 \text{ A cm}^{-2}$ , mass transport losses contribute to 20-25% of the total overpotential<sup>[120]</sup> and concluded that the two-phase flow at the anode plays a critical role.<sup>[112]</sup> This is in strong contradiction to the results obtained in this work where mass transport losses contribute only  $\approx 30 \text{ mV}$  to the total overpotential at  $3 \text{ A cm}^{-2}$  (cf. figure 2.2). The largest fraction of this overpotential ( $\approx 20 \text{ mV}$ ) can be explained by a mass transport resistance in the cathode catalyst layer and it was shown by Rheinlaender et al., that this contribution can increase to about 50 mV for a higher ionomer content, i.e., a lower porosity of the catalyst layer.<sup>[113]</sup> This illustrates that optimization of catalyst layers is critical to reduce mass transport losses in PEM-WEs, and that with an optimized electrode structure and suitable PTLs the contribution of mass transport losses to the cells overpotential is almost negligible even at relatively high current densities (cf. figure 2.2).

## 2.3 Operating Conditions

Apart from improving materials and components, optimization of operating conditions is crucial to ensure a high efficiency and lifetime of a PEM-WE. In this section, the influence of temperature and pressure on the performance of a PEM-WE is discussed.

### Temperature

Typical operating temperatures of state-of-the-art PEM-WEs are in a range of 50-80°C.<sup>[15]</sup> In general, higher temperatures lead to an improved performance due to a higher ionic conductivity of the membrane and faster reaction kinetics resulting in lower ohmic and kinetic overpotentials. Figure 2.5 shows polarization curves along with the HFR obtained for an MEA with a Nafion<sup>®</sup> 117 membrane ( $\approx 175\ \mu\text{m}$ ) and catalyst loadings of  $1.2\ \text{mg}_{\text{Ir}}\ \text{cm}^{-2}$  and  $0.3\ \text{mg}_{\text{Pt}}\ \text{cm}^{-2}$ , respectively. Measurements were performed at temperatures of 40°C, 60°C, to 80°C.

The difference in cell voltage between 40°C and 80°C is  $\approx 160\ \text{mV}$  at a current density of  $1\ \text{A}\ \text{cm}^{-2}$  and increases to more than  $250\ \text{mV}$  at  $3\ \text{A}\ \text{cm}^{-2}$ . This difference is the result of a 50% increase of membrane conductivity from 40°C and 80°C (cf. table 2.2), resulting in a reduction of the HFR by  $\approx 70\ \text{m}\Omega\ \text{cm}^2$  at  $1\ \text{A}\ \text{cm}^{-2}$ . For higher current densities, the HFR values slightly decrease, which can be explained by an increase of the temperature in the MEA due to the produced waste heat and, hence, a lower ionic resistance. This effect is most pronounced for the lowest temperature of 40°C because of a higher total membrane resistance. Apart from the reduced ohmic resistance at higher temperature, a reduced kinetic overpotential is responsible for a difference of  $\approx 90\ \text{mV}$  when increasing the operating temperature from 40°C to 80°C (estimated from the difference in *iR*-free cell voltage at the lowest measured current density of  $10\ \text{mA}\ \text{cm}^{-2}$ ). Reduced proton transport resistances in the electrodes as well as changes in mass transport resistance might also have an effect at higher current densities, but their influence on the overall performance is expected to be comparably small. This analysis shows that increasing the operating temperature of a PEM-WE can significantly improve the performance.

However, high temperatures lead to an increase of the gas permeability<sup>[27]</sup> and a decrease of the mechanical stability of the membrane,<sup>[43]</sup> and might result in an accelerated degradation rate (cf. section 2.4). Along with stability issues with ion-exchange

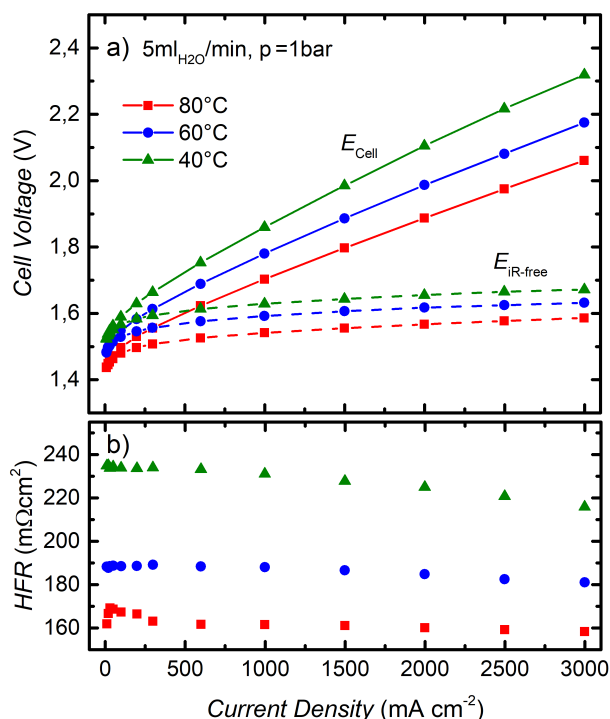


**Figure 2.5:** a) Ambient pressure polarization curves measured for an MEA with a Nafion<sup>®</sup> 117 membrane and catalyst loadings of  $1.2 \text{ mg}_{\text{Ir}} \text{ cm}^{-2}$  ( $\text{IrO}_2/\text{TiO}_2$ ) and  $0.3 \text{ mg}_{\text{Pt}} \text{ cm}^{-2}$  ( $\text{Pt}/\text{C}$ ) at operating temperatures of  $40^\circ\text{C}$  (green),  $60^\circ\text{C}$  (blue), and  $80^\circ\text{C}$  (red). Full lines represent the measured cell voltage, while dashed lines give the cell voltage corrected by HFR. b) Corresponding HFR.

resins at  $>60^\circ\text{C}$ , which are used to maintain the purity of the process water, these are the reasons why in today's commercial PEM-WE systems the temperature usually does not exceed  $60\text{--}70^\circ\text{C}$ .<sup>[43]</sup> Nevertheless, alternative membrane materials with good mechanical and gas barrier properties at elevated temperatures, such as short side-chain PFSA membranes,<sup>[121,122]</sup> could enable operation at higher temperatures in the future.

## Pressure

Typical operating pressures of commercial PEM-WEs are in a range of  $20\text{--}50 \text{ bar}$ ,<sup>[15,123]</sup> but also higher pressures up to  $350 \text{ bar}$  have been demonstrated.<sup>[98]</sup> Pressurized electrolysis is beneficial compared to ambient pressure operation because it could allow direct storage of  $\text{H}_2$  without subsequent mechanical compression and it also reduces

the effort for gas drying due to the lower water content at higher pressure.<sup>[124]</sup> However, high-pressure operation leads to more demanding material requirements, imposes additional safety precautions, and reduces the faradaic efficiency due to a higher gas permeation through the membrane, especially critical at small current densities. Pressurized PEM-WEs can be operated at balanced pressure (similar pressure on hydrogen and oxygen sides) or differential pressure (only hydrogen being pressurized). While balanced pressure reduces mechanical stress on the components compared to differential pressure, it requires a high pressure water pump, handling of high pressure O<sub>2</sub>, and leads to a reduced purity of H<sub>2</sub> due to an increased O<sub>2</sub> permeation rate.<sup>[43]</sup> Several studies investigated the influence of operating pressure and mode (balanced vs. differential) on the overall system efficiency. Depending on the desired delivery pressure of H<sub>2</sub>, an optimum was found for a pressure of 30 - 45 bar<sup>[30]</sup> with differential pressure operation being more efficient than balanced pressure operation.<sup>[125]</sup> Newer studies suggest that by reducing the energy demand for the gas drying process, the optimum operating pressure is shifted to values below 20 bar.<sup>[124,126]</sup>

In this work, operating pressures of up to 30 bar will be investigated. Figure 2.6 shows polarization curves along with the HFR recorded at ambient pressure ( $p_{\text{cath}} = p_{\text{an}} = 1\text{bar}_a$ ), differential pressure of 29 bar ( $p_{\text{cath}} = 30\text{bar}_a$ ,  $p_{\text{an}} = 1\text{bar}_a$ ), and balanced pressure of 30 bar ( $p_{\text{cath}} = p_{\text{an}} = 30\text{bar}_a$ ). It can be observed that the cell voltage increases for high pressure operation compared to ambient pressure. The HFR is similar for all measurements with slightly lower values at high current densities and balanced pressure of 30 bar. An increase of cell voltage with pressure is expected due to the pressure dependency of the reversible cell voltage and can be calculated according to equation 2.14. At the applied operating temperature of 80°C, the saturation pressure of water is 0.47 bar<sub>a</sub>. Consequently, the partial pressure of H<sub>2</sub> and O<sub>2</sub> can be obtained by subtracting 0.47 bar from the total pressure in the cathode/anode compartment. For the given cathode pressures of 1 and 30 bar<sub>a</sub> this yields H<sub>2</sub> partial pressures of 0.53 and 29.53 bar, which results in a Nernstian voltage shift of 61 mV at 80°C (cf. equation 2.14). Assuming that all other voltage losses are independent of the cathode pressure, the expected iR-free cell voltage at a differential pressure of 30 bar can be calculated by adding the Nernstian shift to the measured data at ambient pressure. This theoretically expected iR-free cell voltage is compared to the measured data in Figure 2.7a. It can be observed that the measured iR-free cell voltage very well matches the expected behavior up to a current density of  $\approx 200\text{mA cm}^{-2}$ . For higher current densities the

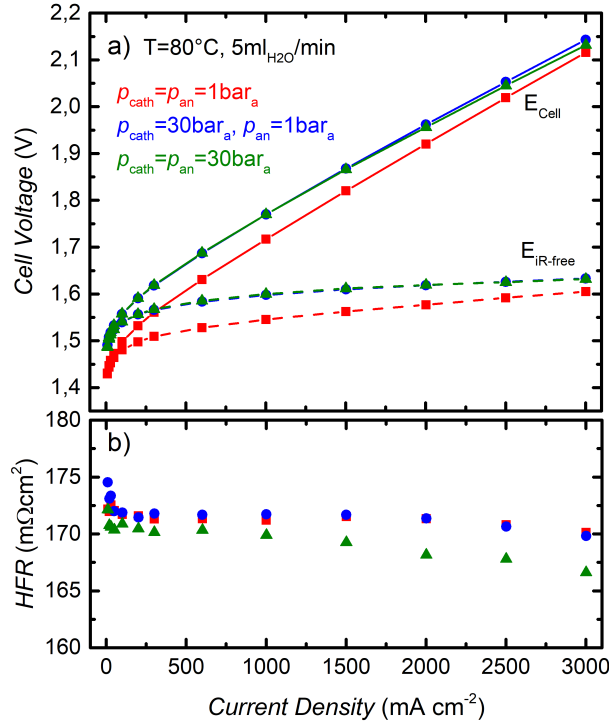


**Figure 2.6:** a) Polarization curves at  $80^\circ\text{C}$  measured for an MEA with a Nafion<sup>®</sup> 117 membrane and catalyst loadings of  $1.2 \text{ mg}_{\text{Ir}} \text{ cm}^{-2}$  ( $\text{IrO}_2/\text{TiO}_2$ ) and  $0.3 \text{ mg}_{\text{Pt}} \text{ cm}^{-2}$  ( $\text{Pt}/\text{C}$ ) at ambient pressure (red), differential pressure of 29 bar (blue), and balanced pressure of 30 bar<sub>a</sub> (green). Full lines represent the measured cell voltage, while dashed lines give the cell voltage corrected by HFR. b) Corresponding HFR.

actual performance is better than expected from the projected values. The difference is indicated by the light blue area in Figure 2.7a. This better than expected performance at high current density and high  $\text{H}_2$  pressure can be explained by a hydrogen mass transport overpotential due to a pressure gradient between the cathode catalyst layer and the flow-field channel, which has a much larger effect at ambient pressure than at high pressure (cf. section 4.1 for detailed analysis).

When the oxygen anode is also pressurized to 30 bar<sub>a</sub>, an additional increase of the reversible cell voltage of 30 mV is expected according to equation 2.14 (cf. dotted green line in figure 2.7b). This increase, however, is not observed in the measured polarization curve at balanced pressure of 30 bar, which is basically identical to the curve measured at differential pressure of 30 bar (cf. figure 2.6). Consequently, the increase of  $E_{\text{rev}}$  must be compensated by the reduction of another overpotential due

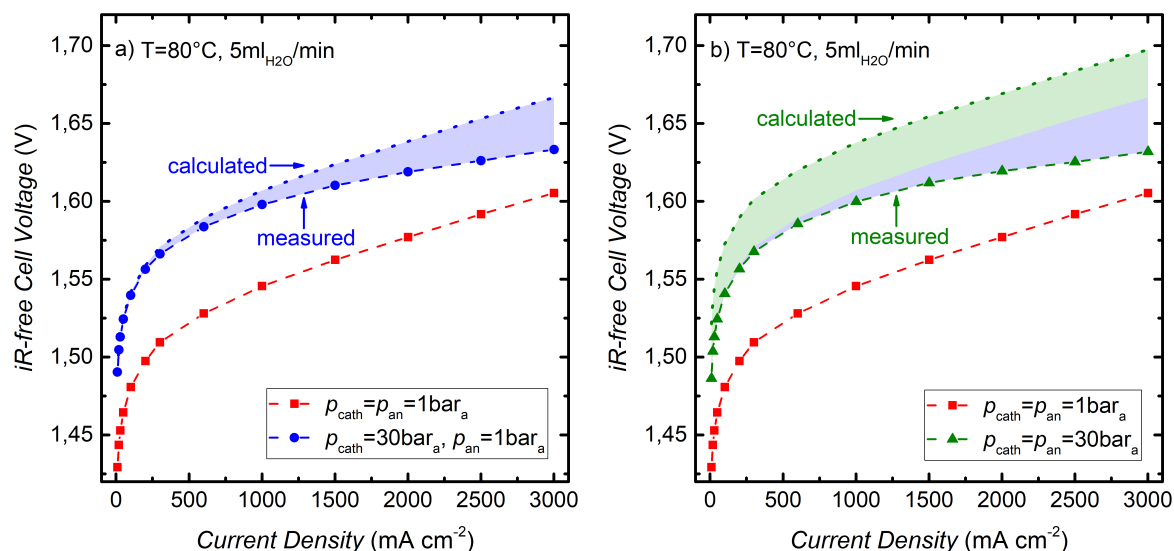


**Figure 2.7:** a) iR-free cell voltage at 80°C for ambient pressure (red symbols with dashed line) and differential pressure of 30 bar (blue symbols with dashed line). The dotted blue line represents the theoretically expected voltage based on the Nernstian voltage shift as calculated from equation 2.14 (i.e., 61 mV). The light blue area indicates the difference between calculated and measured data. b) iR-free cell voltage at 80°C for ambient pressure (red symbols with dashed line) and balanced pressure of 30 bar (green symbols with dashed line). The dotted green line represents the theoretically expected voltage based on the Nernstian voltage shift as calculated from equation 2.14 (i.e., 91 mV). The light blue (same as in figure 2.7a) and light green areas indicate differences between calculated and measured data due to effects related to H<sub>2</sub> and O<sub>2</sub> pressure, respectively. This analysis is based on the data shown in figure 2.6.

to the elevated O<sub>2</sub> pressure (cf. light green area in figure 2.7). A similar behavior has been observed in literature<sup>[84,112,127,128]</sup> and was explained by either a higher apparent exchange current density for the OER<sup>[112]</sup> or by an improved mass transport in the porous structures due to lower gas volumes and/or smaller gas bubbles.<sup>[127,129]</sup>

## 2.4 Degradation Phenomena

Sufficient lifetime is a key factor for commercialization of PEM-WEs with a DOE target for component replacement as high as 10 years.<sup>[130]</sup> A lifetime of 60,000 hours has been demonstrated for a commercial stack design by Proton OnSite with a relatively low degradation rate of 4 μV h<sup>-1</sup>, while an improved system showed no measurable performance decay over more than 40,000 hours.<sup>[131]</sup> Even longer lifetimes of >100,000 hours

have been demonstrated for PEM-WEs used for naval O<sub>2</sub> generation.<sup>[132]</sup> However, these systems were operated at (quasi-)stationary conditions and relatively low temperatures and current densities (e.g., 50°C and 1.3 A cm<sup>-2</sup> for Proton OnSite test). Furthermore, thick membranes (Nafion<sup>®</sup> N1110, thickness of 254 μm, *EW*=1100) and high catalyst loadings (10 mg cm<sup>-2</sup> total PGM loading) were used.<sup>[131]</sup> Application of PEM-WEs for means of energy storage in a future energy scenario mainly based on renewable sources might result in frequent load cycles (accompanied by variations of temperature and pressure) and possible start-stop events, which could accelerate degradation processes. Additionally, cost reduction will result in thinner membranes, lower catalyst loadings, and operation at elevated current density and pressure, which could further increase degradation rates. In this section, degradation mechanism of the central components of a PEM-WE are discussed.

### Membrane and Ionomer

Membrane and ionomer can degrade due to thermal, mechanical, and/or chemical stress. Chemical degradation of PFSA ionomers occurs due to radical induced attack leading to a gradual decomposition of the polymer.<sup>[133–136]</sup> O<sub>2</sub> permeating through the membrane to the cathode reacts with atomic hydrogen chemisorbed on the surface of the platinum catalyst to form hydrogen peroxide (H<sub>2</sub>O<sub>2</sub>) and peroxy radicals (HO<sub>2</sub>•), which can decompose into highly reactive nucleophilic radicals (HO•).<sup>[133]</sup> The chemical degradation then occurs generally by an attack of non-fluorinated end groups by the HO• radical.<sup>[137]</sup> At dry operating conditions, also the R-CF<sub>2</sub>-SO<sub>3</sub>H-group can be attacked and decomposed to R-CF<sub>2</sub>• from where the chain unzipping continues in a similar manner.<sup>[136]</sup> In PEM-WEs, the formation of H<sub>2</sub>O<sub>2</sub> and the resulting membrane degradation is expected to occur predominantly at the cathode, since the Ir-based anode catalyst is in the oxide form during operation, suppressing the recombination of H<sub>2</sub> and O<sub>2</sub>.<sup>[135]</sup> Degradation of the membrane and ionomer can be quantified by measuring the fluorine release rate (FRR) and/or the membrane thickness.<sup>[138,139]</sup> While membrane thinning due to chemical attack will first result in a performance increase due to a lower ohmic resistance, it will lead to increased gas permeation and, ultimately, cell failure due to formation of pin holes.<sup>[140]</sup> Chemical degradation of the membrane and ionomer can be accelerated by introduction of cationic contaminations from the feed water or parts of the cell hardware. Transition metal cations such as Fe<sup>3+</sup> and



$\text{Cu}^{2+}$  can promote the chemical decomposition of hydrogen peroxide to radicals, which accelerates membrane thinning.<sup>[133]</sup>

Furthermore, cations can exchange with protons in the PFSA material resulting in a decreased proton conductivity. The performance loss due to this cation poisoning is reversible as shown by Sun et al., who could restore the initial performance of a contaminated MEA by treating the membrane with sulfuric acid.<sup>[141]</sup> Stability of the membrane to mechanical stress is of great importance as well, especially for operation at elevated pressure.<sup>[142]</sup> Creep failure under the cell stack loads at high operating pressure is a problem, especially for thin membranes.<sup>[98]</sup> Ayers et al. showed a significant improvement in lifetime for thin reinforced PFSA membranes compared to standard PFSA membranes due to their better mechanical stability.<sup>[98]</sup> Operating conditions can have a significant influence on membrane degradation as well. High gas pressure can lead to an increased FRR<sup>[135]</sup> and a higher risk of mechanical failure. Increasing the temperature will lead to faster chemical degradation with FRRs increasing approximately by two orders of magnitude with a temperature increase from 55 to 150°C<sup>[143]</sup>. Additionally, softening of the membrane material at high temperatures makes it more vulnerable to mechanical stress.<sup>[43]</sup>

## Catalyst Layer

Degradation of the catalyst layer can occur due to dissolution or agglomeration of the catalyst as well as by catalyst surface blocking by metal ions.<sup>[142]</sup> Dissolution of the Ir-based catalyst on the anode of a PEM-WE depends on the oxidation state of Ir,<sup>[63]</sup> and a possible degradation mechanism was proposed by Kasian et al.<sup>[144]</sup> Furthermore, dissolution of Ir seems to be accelerated by high current densities (i.e., high potentials) or during load cycling. Lettenmeier et al. observed diffusion of dissolved iridium into the membrane during operation at high current density<sup>[145]</sup> and Xu showed spherical agglomerates of Ir nanoparticles in the membrane after load cycling between 1.4- 2.0 V.<sup>[146]</sup> In section 4.3, the influence of different accelerated stress test (AST) protocols on MEA degradation is studied, and Ir dissolution and redeposition in the membrane is observed for MEAs cycled between operating potentials (>1.4 V) and open circuit voltage (OCV) periods. Dissolution of the Ir catalyst should in general lead to a lower OER activity due to a reduced electrochemically active surface area (ECSA). This effect is often masked by the high catalyst loadings used in PEM-

WEs,<sup>[147]</sup> but would lead to a more significant performance decay for low Ir-loadings. Agglomeration of catalyst particles was observed on the Pt cathode<sup>[148,149]</sup> along with a migration and detachment from the carbon support.<sup>[150]</sup> The contribution of this effect to the cell degradation was, however, found to be insignificant, which is consistent with the above discussed high HER activity of Pt.

Finally, cationic contaminations originating from the feed water or cell components can occupy ion exchange sites of the ionomer in the catalyst layer, resulting in an increase of the charge transfer resistance.<sup>[142]</sup> Rakousky et al. claim to observe this reduced activity due to a contamination of the anode with titanium species.<sup>[149]</sup>

### **Porous Transport Layer and Bipolar Plate**

At anodic potentials in a PEM-WE, the surface of titanium based BPPs and PTLs is passivated by a thin oxide film. For prolonged operation at high potentials, this passivation can lead to a significant increase of the contact resistance between PTL and BPP as shown by Rakousky et al.<sup>[149]</sup> Noble metal coatings are frequently used to prevent passivation, but add significant cost to the system.<sup>[100,149]</sup> Corrosion of titanium at typical anode potentials is in general not expected, but could occur due to the presence of fluoride ions originating from membrane/ionomer decomposition.<sup>[142]</sup> On the cathode, H<sub>2</sub> embrittlement could lead to cracking and mechanical failure of titanium based BPPs, however, it has been shown that H<sub>2</sub> uptake can be eliminated by applying a nitride coating.<sup>[131]</sup>

In summary, many different degradation processes can take place in PEM-WEs. However, quantification of these effects is challenging due to long lifetimes for state-of-the-art materials (>10,000 h) under standard operating conditions (constant load). Furthermore, comparison of literature results regarding degradation is difficult due to varying operating conditions and test protocols. Consequently, standardized AST protocols need to be developed to trigger specific degradation mechanisms in order to study durability of new materials in a reasonable time frame. ASTs can further be used to investigate the influence of different operating conditions, such as increased temperature, pressure, and intermittent operation on PEM-WE lifetime. An AST to simulate the effect of recurring OCV periods on the long-term performance of MEAs based on a Nafion<sup>®</sup> 212 membrane operated at 80°C was developed and results are shown in section 4.3.

## 2.5 Potential of PEM Electrolysis for H<sub>2</sub> Generation

In this section, the potential of PEM-WEs for H<sub>2</sub> generation is analyzed in comparison to other technologies and the challenges which need to be overcome to enable a large-scale application of the technology are discussed.

### 2.5.1 State-of-the-art Technology and Cost Analysis

PEM water electrolysis was first introduced in the 1960s by General Electric.<sup>[48]</sup> Up to now, PEM-WEs are established only in relatively small niche markets, such as laboratory hydrogen generators, O<sub>2</sub> supply for submarines, and some other industrial applications with system sizes in the range of 0.1 - 100 kW.<sup>[43,123]</sup> Considering this relatively small market and the specific requirements, PEM-WE systems have been designed to provide good reliability and robustness, rather than optimized cost-efficiency. The development of PEM-WEs in the MW-range has started recently and systems are available today from several companies.<sup>[15]</sup> First plants for large-scale H<sub>2</sub> production for energy storage and power-to-gas applications have been installed (e.g., the 6 MW power-to-gas plant in Mainz (Germany)<sup>[151]</sup> or the 6 MW PEM-WE at the voestalpine steel plant in Linz (Austria)<sup>[10]</sup>). Since these systems will be in competition to other H<sub>2</sub> production technologies, optimization of H<sub>2</sub> generation costs has become more important.

As the main competitor, alkaline water electrolysis is a more mature technology with several plants in the multi-MW size already installed in the 20th century.<sup>[152]</sup> The main difference to PEM-WE is that a liquid electrolyte (20-30 % KOH) is used instead of a proton exchange ionomer. This results in limited current densities of  $\approx 0.25 - 0.45 \text{ A cm}^{-2}$  for current commercial systems (cf. table 2.3).<sup>[15]</sup> However, research towards using thinner separators is ongoing<sup>[153]</sup> and current densities of up to  $2 \text{ A cm}^{-2}$  might be possible in the future.<sup>[154]</sup> Other disadvantages of the alkaline technology are a low partial load range, lower operating pressures with a restriction to balanced pressure operation, and the need to handle large amounts of KOH.<sup>[123]</sup> PEM-WE provides a more compact system design with much higher power densities. State-of-the-art PEM-WEs are operated at current densities of  $\approx 1 - 2 \text{ A cm}^{-2}$  (cf. table 2.3) and values of up to  $20 \text{ A cm}^{-2}$  have been shown in laboratory tests.<sup>[78]</sup> Additionally, PEM-WEs allow fast start-up and dynamic operation, as well as differential pressure operation,

eliminating the need for handling of high pressure O<sub>2</sub>.<sup>[13]</sup> The main drawback of PEM technology is the limitation to noble-metal catalysts and titanium based BPPs and PTLs due to the highly corrosive environment. As a result of these more expensive materials and the much smaller-scale production volume of PEM-WEs, current investment costs are almost a factor 2 higher compared to alkaline systems.<sup>[15,155]</sup> A detailed comparison of the most relevant technical specifications of commercial alkaline and PEM water electrolyzers can be found in table 2.3. Other electrolysis technologies, namely solid oxide electrolysis and anion exchange membrane electrolysis are still in an early research stage and are not discussed.

**Table 2.3:** Technical specifications of commercial PEM and alkaline water electrolyzers.<sup>[15]</sup>

<b>Specifications</b>		<b>PEM</b>	<b>Alkaline</b>
Cell Temperature	(°C)	50 - 80	60 - 90
Pressure	(bar)	20 - 50	10 - 30
Current Density	(A cm <sup>-2</sup> )	1.0 - 2.0	0.25 - 0.45
System Efficiency	(% <sub>LHV</sub> )	46 - 60	51 - 60
	(kWh kg <sub>H<sub>2</sub></sub> <sup>-1</sup> )	56 - 73	56 - 66
System Cost	(€ kW <sup>-1</sup> )	1400 - 2100	800 - 1500

The total costs for H<sub>2</sub> production from electrolysis are determined by system costs (capital expenditure, CAPEX) and operating expenditure (OPEX) which is dominated by the price of electricity. A breakdown of PEM-WE system costs shows that the stack is the biggest cost contributor with ≈60% (cf. figure 2.8).<sup>[155]</sup> This share is expected to increase even further for larger systems due to a reduced contribution of balance of plant (BoP) costs.<sup>[79]</sup> About half of the stack costs are related to BPPs and another 17% are added by PTLs. However, due to advanced manufacturing techniques, scale-up and automation, as well as new materials, a significant cost reduction is expected for these components.<sup>[131]</sup> While the parts of the MEA, namely catalysts and membrane, are only responsible for 13% of the stack costs at the moment (c.f figure 2.8), this fraction is expected to increase as other parts become cheaper.

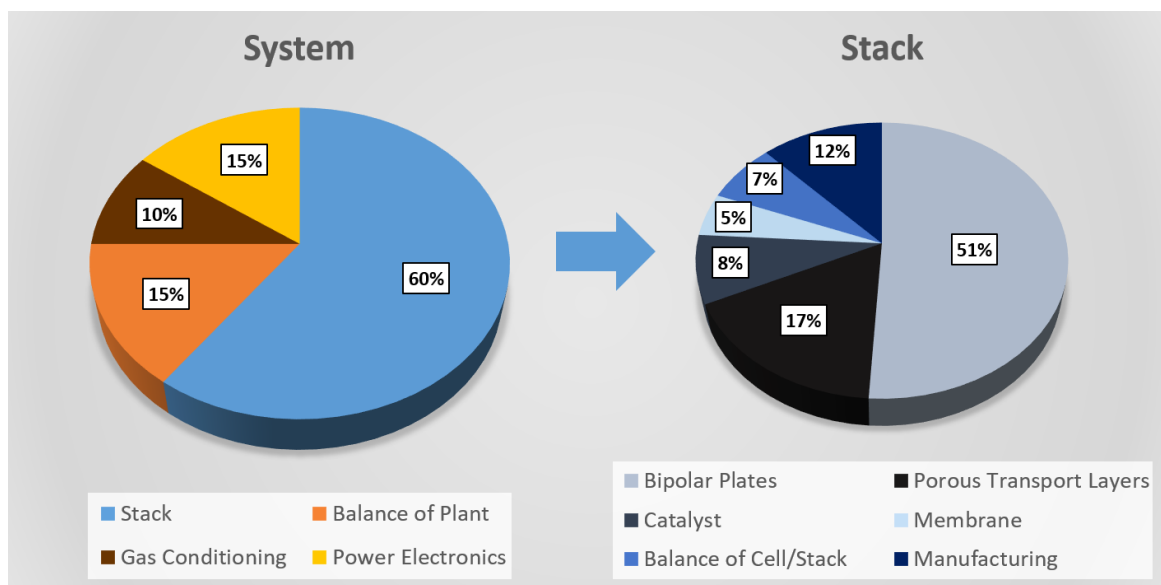


**Figure 2.8:** Cost breakdown for system and stack of a PEM-WE; redrawn based on the data presented in references.<sup>[43,155]</sup>

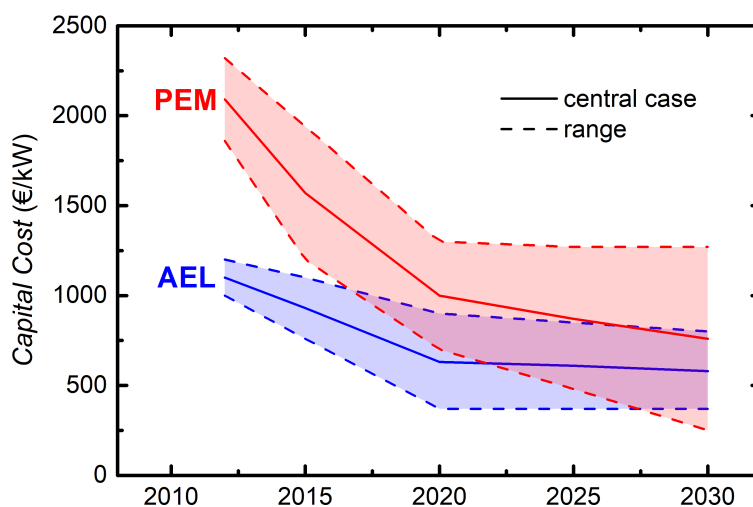


**Figure 2.9:** Projected system cost development for PEM and alkaline water electrolyzers. Full lines represent the central case scenario, while dashed lines indicate the possible range between best and worst case scenario (data from reference<sup>[155]</sup>). Values include power electronics, system control, and gas drying; they do not include grid connection, external compression, external purification, and hydrogen storage.

According to the cost projection presented by Bertuccioli et al., capital costs for PEM-WEs should be close to  $1200 \text{ €kW}^{-1}$  in 2018 and are expected to drop to  $\approx 760 \text{ €kW}^{-1}$  in 2030, reaching similar values as alkaline water electrolyzers (cf. figure 2.9).<sup>[155]</sup> Taking into account the higher operational flexibility of PEM-WEs, experts expect a commercial advantage compared to alkaline technology.<sup>[156]</sup> Total  $\text{H}_2$  production costs are expected to drop from  $4\text{-}8 \text{ €kg}_{\text{H}_2}^{-1}$  to  $2.5\text{-}4 \text{ €kg}_{\text{H}_2}^{-1}$  in 2030 (best case scenario).<sup>[155]</sup> This value, however, depends strongly on the assumed cost of electricity which is an element of great uncertainty.

### 2.5.2 Challenges for Large-Scale Application of PEM Electrolysis

An important consideration for the envisaged large-scale application of PEM water electrolyzers in renewable energy generation/storage are the supply constraints for the PGM based catalysts. On the cathode, the Pt loadings can be reduced significantly without a negative impact on performance and, hence, Pt supply is not considered to be a limiting factor (cf. section 4.2). A concern is the availability of Ir for the anode catalyst, since Ir is one of the rarest materials on earth, with an estimated annual production of only  $\approx 4$  tons.<sup>[43]</sup> Consequently, a significant reduction of the Ir loading will be necessary to ensure a sufficient supply of Ir for PEM-WE installations in the multi-GW scale. In section 4.2, it is shown that an Ir loading of  $\approx 0.05 \text{ mg}_{\text{Ir}} \text{ cm}^{-2}$  (in contrast to today's typical loadings of  $1\text{-}2 \text{ mg}_{\text{Ir}} \text{ cm}^{-2}$ ) will be required to meet the target value for Ir-specific power density of  $\approx 0.01 \text{ g}_{\text{Ir}} \text{ kW}^{-1}$ , necessary for a large-scale application of PEM electrolysis. To maintain an electrode thickness of at least  $4 \text{ }\mu\text{m}$  (minimum thickness for homogeneous catalyst layer; cf. section 4.2), catalysts with a significantly lower packing density ( $\approx 80 \text{ }\mu\text{m} (\text{mg}_{\text{Ir}} \text{ cm}^{-2})^{-1}$ ) compared to state-of-the-art materials, will be required. While availability of Ir will become an issue in the future when PEM-WE installations reach the multi-GW scale, at the moment a significant market penetration of PEM electrolysis is still hindered by the high  $\text{H}_2$  generation costs, which are not affected significantly by the noble metal costs (cf. figure 2.8).<sup>[14]</sup> Even with the predicted values of  $2.5\text{-}4 \text{ €kg}_{\text{H}_2}^{-1}$  in 2030, electrolytic  $\text{H}_2$  will be more expensive than  $\text{H}_2$  produced from conventional sources, e.g., by steam reforming of methane.<sup>[152,155]</sup> Consequently, research must be focused on the reduction of  $\text{H}_2$  generation costs to improve the competitiveness of PEM electrolysis in the near future.

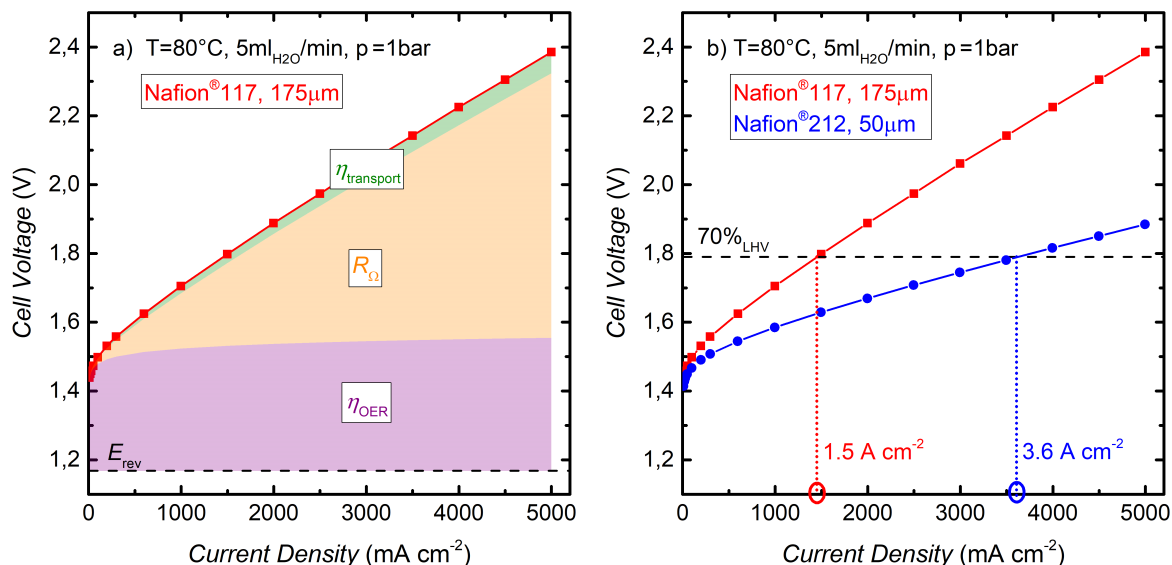


**Figure 2.10:** a) Ambient pressure polarization curves measured for an MEA with a Nafion<sup>®</sup> 117 membrane and catalyst loadings of  $1.2 \text{ mg}_{\text{Ir}} \text{ cm}^{-2}$  and  $0.3 \text{ mg}_{\text{Pt}} \text{ cm}^{-2}$  (same MEA as in figure 2.5) at a temperature of  $80^\circ\text{C}$  (red). The dashed black line gives the reversible cell voltage, while the light purple area represents the kinetic overpotential, the light orange area the ohmic overpotential, and the light green area the overpotentials due to proton and mass transport. b) Ambient pressure polarization curves for the MEA shown in figure 2.10a compared to an MEA with similar catalyst loadings but a thinner Nafion<sup>®</sup> 212 membrane ( $50 \mu\text{m}$ ). The dashed black line represents a voltage efficiency of 70% based on the lower heating value of H<sub>2</sub> and the current density at which this efficiency is reached is marked in figure 2.10b (efficiency losses due to gas permeation are not included in the analysis).

Aiming at a reduction of the CAPEX, bipolar plates and PTLs offer a great potential for cost optimization, since they account for 2/3 of the stack costs (cf. figure 2.8). Advanced manufacturing techniques, scale-up and automation, as well as development of new materials are promising possibilities for a significant cost reduction of these components. Apart from reducing material costs for stack components, increasing the current density can be a way to lower H<sub>2</sub> generation costs by reducing the total cell area required to achieve a given target H<sub>2</sub> production rate. Figure 2.10 shows a polarization curve of a state-of-the-art MEA with a Nafion<sup>®</sup> 117 membrane ( $175 \mu\text{m}$ ), which would be operated at a maximum current density of  $1\text{-}2 \text{ A cm}^{-2}$  in a commercial electrolyzer today.<sup>[15]</sup> At higher current densities the cell voltage increases significantly due to the high ohmic resistance of the membrane, leading to a lower efficiency. An analysis of the contributions of different voltage losses shows that at the highest current density of  $5 \text{ A cm}^{-2}$  more than 60% of the total overpotential

are due to ohmic losses. Since the electrical resistance represents only a small fraction of the ohmic resistance (cf. table 2.2), reducing the ionic membrane resistance offers the largest potential to improve high current density performance. The result of reducing the membrane thickness to only 50  $\mu\text{m}$  by using a Nafion<sup>®</sup> 212 instead of the Nafion<sup>®</sup> 117 is shown in figure 2.10b. At a desired voltage efficiency of 70 % based on the lower heating value (LHV) of  $\text{H}_2$ , the current density increases by a factor of  $\approx 2.5$  for the MEA with the thin membrane. This increase of the stack's  $\text{H}_2$  output translates directly into a CAPEX reduction by a factor of  $\approx 2.5$  while the same efficiency is retained. From this example, it becomes clear that minimizing the membrane thickness offers the biggest leverage for cost reduction. Of course, issues like an increased waste heat flux at high current densities need to be considered. Furthermore, the implementation of thin membranes can be problematic due to lower mechanical stability and increased gas permeation rates, especially in the context of operation at elevated pressure ( $\approx 30$  bar). Optimization of structural components in the cell hardware to ensure sufficient mechanical support, as well as mitigation strategies for  $\text{H}_2$  permeation or the development of membranes with an improved (i.e., lowered) ratio of gas permeability to ionic conductivity will be required to ensure safe operation with a sufficient load-following range.

In order to minimize the OPEX, components such as MEA and PTL need to be optimized in terms of efficiency, which requires a detailed understanding of the factors which influence PEM-WE performance. In section 4.1, a detailed analysis of the contributions of different voltage losses is presented and it is shown that losses due to proton and mass transport can be minimized by optimization of the electrode composition. Catalyst materials with a higher activity, especially on the anode, could contribute to an improved efficiency by reducing the kinetic overpotentials. In addition, the development of microporous layers for PTLs could improve the performance by providing a smooth interface to the catalyst layer, which is important especially for thin catalyst layers with a potentially lower in-plane electrical conductivity (cf. section 4.2).

Apart from the optimization of materials, operation at elevated temperature is a way to boost performance due to a lower membrane resistance and increased catalytic activity. Another way to reduce operating costs could be an adaptation of the electrolyzer operating strategy to fluctuating power costs. This would of course require a dynamic operation and a lower capacity utilization, i.e., a lower number of operating



hours translating into a higher share of system costs.

Besides of Ir supply constraints and the need for cost reduction, long-term durability is the third big challenge in PEM electrolysis. This topic is especially important in the context of intermittent operation including load cycling and possible start-stop events (cf. section 4.3). Furthermore, the impact of new cost-optimized components, such as thin membranes and low catalyst loading electrodes, as well as of more demanding operating conditions, such as high current densities and elevated temperatures, on system lifetime is unknown. Consequently, a better understanding of different degradation mechanisms and how they are influenced by material properties and operating conditions is essential to ensure sufficient lifetime for future systems. For this purpose, standardized accelerated stress test (AST) protocols need to be designed to enable degradation tests within a reasonable time frame and to allow a comparison of results between different research groups. A short summary of the main challenges for a large-scale application of PEM electrolysis is given below:

- Development of improved catalyst materials which allow a significant reduction of Ir loading to prevent Ir supply constraints.
- Reduction of H<sub>2</sub> generation costs by low-cost stack components (BPP, PTL), operation at high current densities, optimized efficiency due to thin membranes, more active catalysts, optimized MEAs and PTLs, and elevated operating temperature, as well as cost-optimized operating strategies.
- Design of AST protocols to gain better understanding of degradation mechanisms and to study the influence of new materials and operating conditions on PEM-WE lifetime.



## 3 Experimental Methods

In this chapter, the experimental methods used in this work will be presented. This includes a description of the cell hardware, along with instructions for cell assembly, details on MEA fabrication, electrochemical measurement techniques, and further experimental methods for MEA characterization.

### 3.1 Cell Hardware for High Pressure Operation

A schematic drawing of the high-pressure cell hardware developed within the course of this thesis is presented in figure 3.1. It comprises aluminum end plates (cf. (1) in figure 3.1) with a thickness of 25 mm, which are compressed by M8 screws fixed with a torque of 20 Nm. Copper current collectors (cf. (3) in figure 3.1) are separated from the end plates by a 2 mm thick interlayer of Gylon<sup>®</sup> (Type 3545, 2 mm thick, Garlock<sup>®</sup>, ENPRO Industries Inc., USA; cf. (2) in figure 3.1) to provide electric insulation and a more uniform pressure distribution. The MEA (cf. (7) in figure 3.1), along with PTLs (cf. (6) and (8) in figure 3.1) and PTFE gaskets (cf. (5) in figure 3.1), is placed between gold coated titanium plates (cf. (4) in figure 3.1) with a single serpentine flow field, providing an active area of 5 cm<sup>2</sup>. A more detailed description of these components along with information on the gold coating process and measurements of the electrical contact resistance between PTLs and flow-fields can be found in section 4.1. This section, on the other hand, will focus on the sealing properties and the assembly of the MEA in the cell hardware.

#### Sealing Properties

Gaskets made from PTFE foil are used for sealing of the cell hardware. To ensure gas tightness during high pressure operation, a uniform compressive force on the gaskets as well as a smooth, defect-free surface are essential. The pressure distribution on the sealing area can be measured with a pressure sensitive film (Prescale, Fujifilm), which is placed between flow-fields and PTFE gaskets as shown in the bottom-left panel of

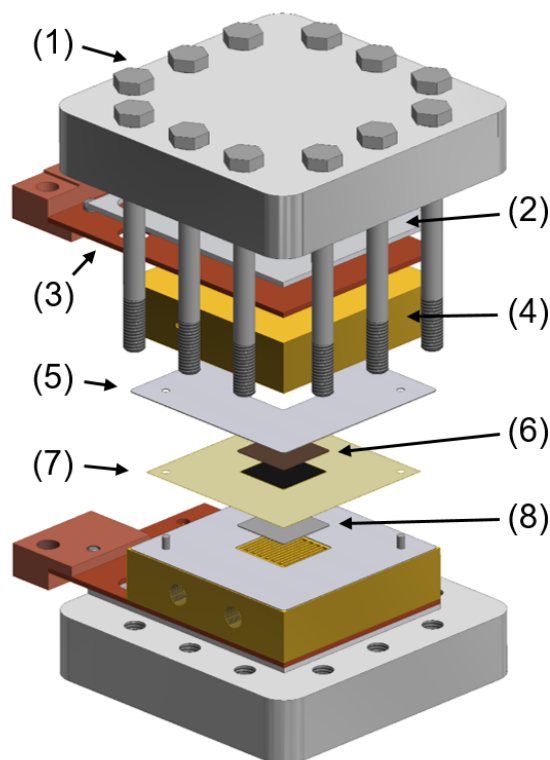


**Figure 3.1:** Schematic drawing of the 5 cm<sup>2</sup> high-pressure electrolysis cell: (1) aluminum end plate, (2) 2 mm Gylon<sup>®</sup> layer, (3) copper current collector, (4) gold coated titanium flow-fields, (5) PTFE gaskets, (6) carbon PTL, (7) MEA, and (8) titanium PTL.

figure 3.2. A non-uniform pressure distribution on the flow field plates is obtained in the absence of a Gylon<sup>®</sup> interlayer between end plates and current collectors (cf. top-left panel in figure 3.2). After addition of the Gylon<sup>®</sup> interlayer, the pressure distribution is more homogeneous, as shown in the top-center panel in figure 3.2. However, imprints of the milling process are still visible on the flow-fields and the surface is very rough as can be seen in the SEM image (cf. bottom-center panel in figure 3.2). Consequently, the titanium flow-fields were mechanically polished on a polishing machine (Buehler Beta) with SiC grinding paper in three subsequent steps starting with a course (P320), followed by an intermediate (P1000), and finished with a fine (P2000) grade grinding paper. As a result, a very smooth surface (cf. bottom-right panel in figure 3.2) and a very homogeneous pressure distribution (cf. top-right panel in figure 3.2) were obtained. After these modifications, the cell showed excellent

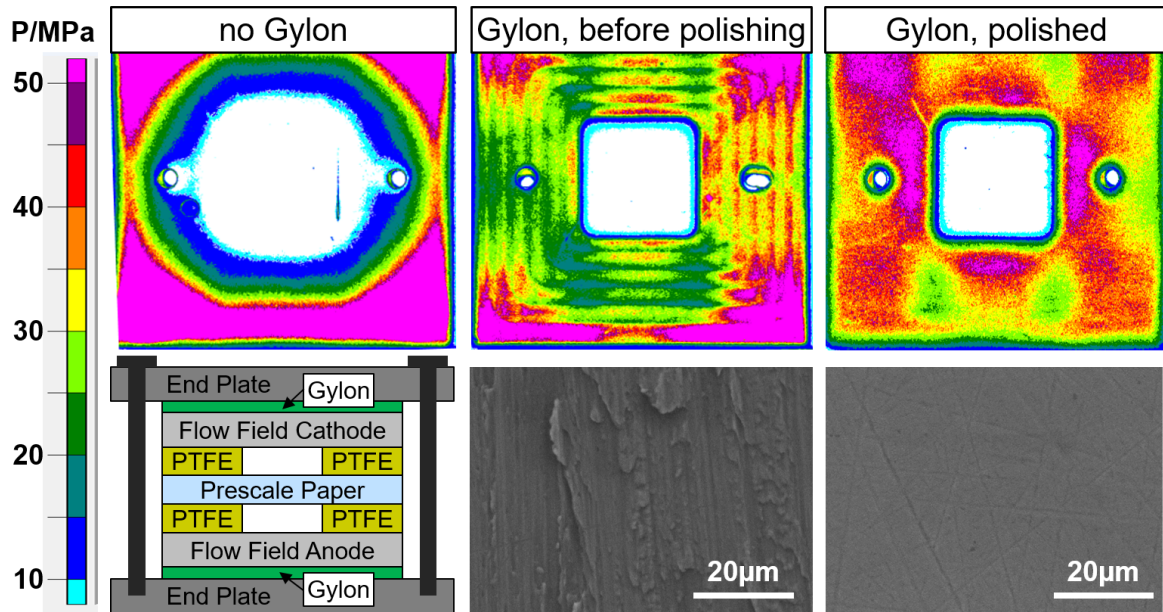


**Figure 3.2:** Bottom-left: Schematic drawing of the assembly used to measure the pressure distribution on the sealing area with a pressure sensitive film (Prescale, Fujifilm). Top-left: Pressure distribution for flow-fields without a Gylon<sup>®</sup> interlayer. Center: Pressure distribution (top) and SEM image of flow-field surface (bottom) before polishing but with a Gylon<sup>®</sup> interlayer. Right: Pressure distribution (top) and SEM image of flow-field surface (bottom) after polishing with a Gylon<sup>®</sup> interlayer.

sealing properties in a leak test conducted with helium gas at a pressure of 50 bar (cf. section 4.1). These results illustrate the importance of the Gylon<sup>®</sup> interlayer and of a smooth flow-field surface to achieve a uniform compressive force on the gaskets and, consequently, reliable sealing at high pressure.

## Cell Assembly

This section will focus on the assembly of the components in the cell hardware, including a calculation of the carbon PTL compression and the resulting compressive force on the active area of the MEA. Figure 3.3 shows a schematic illustration of the cell assembly. The MEA is sandwiched between a carbon PTL (TGP-H-120 from Toray, Japan, no MPL) with a thickness of  $370 \pm 10 \mu\text{m}$  on the cathode and a sintered titanium PTL (from Mott Corporation, USA) with a thickness of  $280 \pm 10 \mu\text{m}$  on the anode. This sandwich is placed between the flow-field plates and the compression of

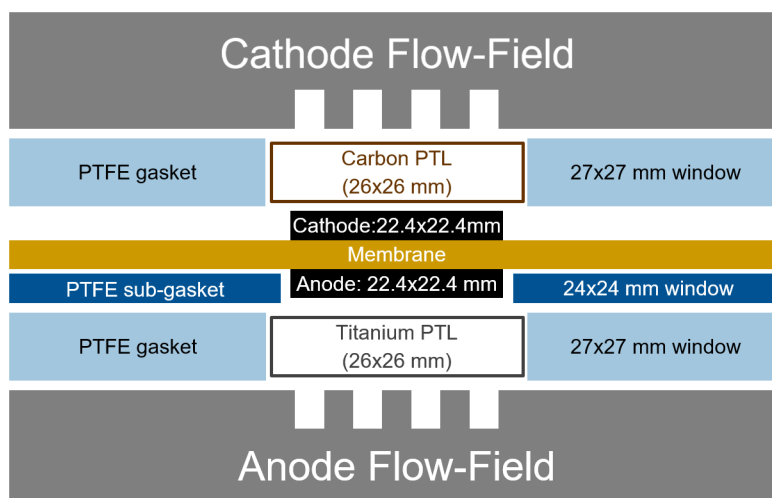


**Figure 3.3:** Schematic illustration of cell assembly (not drawn to scale) including dimensions of components.

the carbon PTL (the titanium PTL can be considered comparably incompressible) is adjusted by the thickness of the gaskets. In the standard configuration used in this work, PTFE gaskets with a nominal thickness of  $300\ \mu\text{m}$  (measured thickness:  $315\pm 10\ \mu\text{m}$ ) are used on anode and cathode. An additional PTFE sub-gasket with a thickness of  $10\ \mu\text{m}$  is added on the anode to cover the edges of the titanium PTL and reduce the risk of ohmic shorting of the membrane. After assembling the components between the flow-fields, these are placed between the end plates along with copper current collectors and the Gylon<sup>®</sup> interlayers (at least one of the Gylon<sup>®</sup> sheets needs to be replaced after each test to ensure uniform compression), as shown in figure 3.1. The screws are tightened to a final torque of 20 Nm in several steps. First, the screws are fixed using an open-end wrench and little force in a diagonal manner (numbers at screws indicate sequence). During this process, the compressible Gylon<sup>®</sup> layer can settle, which will loosen the screws again. Several rounds of tightening will be necessary until the Gylon<sup>®</sup> has fully settled and the screws don't become loose any more. After that, a torque wrench is used to further tighten the screws in several steps (5 Nm - 10 Nm - 15 Nm - 20 Nm) to reach the final torque of 20 Nm.

The thickness of the compressed carbon PTL ( $t_{\text{C-PTL}}$ ) in the final cell assembly can be calculated from the thickness of the gaskets ( $t_{\text{gasket}}$ ), the sub-gasket ( $t_{\text{sub-gasket}}$ ), the titanium PTL ( $t_{\text{Ti-PTL}}$ ) which is essentially incompressible compared to the soft

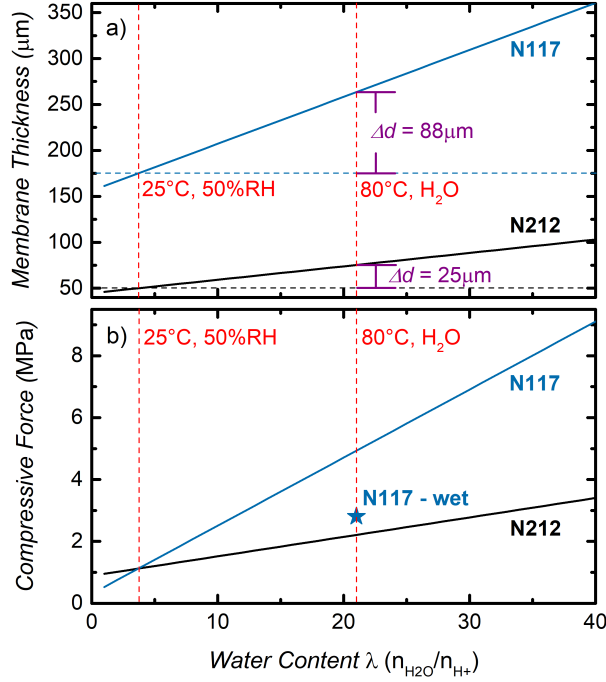


**Figure 3.4:** a) Membrane thickness as a function of water content,  $\lambda$ , for a Nafion<sup>®</sup> 212 membrane (black line) and a Nafion<sup>®</sup> 117 membrane (blue line).  $\Delta d$  gives the increase of membrane thickness for an increase in water content from  $\lambda=3.7$  ( $25^\circ\text{C}$ , 50% RH) to  $\lambda=21$  ( $80^\circ\text{C}$ , liquid water), as indicated by the red dashed lines. b) Compressive force on the active area as a function of water content, as determined from the stress/strain curve in reference.<sup>[157]</sup> The blue star indicates the compressive force at  $\lambda=21$  for a Nafion<sup>®</sup> 117 membrane which has been immersed into liquid water at  $25^\circ\text{C}$  for 1 h ( $\lambda=13$ ) before cell assembly. It is assumed that for the membranes assembled in the cell hardware, swelling occurs only in the through-plane (i.e., thickness) direction.

carbon PTL, and the electrodes ( $t_{\text{an}}$ ,  $t_{\text{cath}}$ ):

$$t_{\text{C-PTL}} = (2 \cdot t_{\text{gasket}} + t_{\text{sub-gasket}}) \cdot 0.97 - t_{\text{Ti-PTL}} - t_{\text{an}} - t_{\text{cath}} \quad (3.1)$$

Here, a compression of the PTFE gaskets of 3% is assumed (determined by an external measurement, where several PTFE gaskets are compressed between the flow fields in a cell hardware and the change in thickness is measured). For electrode thicknesses of  $10 \mu\text{m}$ , the carbon PTL is compressed to a thickness  $t_{\text{C-PTL}}=321 \mu\text{m}$  ( $\approx 13\%$  compression) corresponding to a compressive stress of  $\approx 1 \text{ MPa}$  based on the stress/strain curve of this material.<sup>[157]</sup>

However, the actual compression will be higher since swelling of the membrane due to water uptake at operating conditions needs to be considered (cf. equation 2.18). The effect of water uptake on the membrane thickness and the resulting compressive force on the active area is shown in figure 3.4 for a Nafion<sup>®</sup> 212 and Nafion<sup>®</sup> 117 membrane. It is assumed that the membrane is assembled under ambient atmospheric conditions at 25°C and 50% RH ( $\lambda=3.7$ ) and that swelling can only occur in the through-plane (i.e., thickness) direction. At typical operating conditions of 80°C in liquid water ( $\lambda=21$ ), the membrane thickness increases by  $\approx 50\%$  (cf. figure 3.4a), resulting in a compressive force of  $\approx 2.2$  MPa for Nafion<sup>®</sup> 212 and of  $\approx 5$  MPa for Nafion<sup>®</sup> 117. In general, increasing the compressive force results in a lower electrical contact resistance (cf. section 4.1). However, the high compressive force in the case of Nafion<sup>®</sup> 117 (corresponding to a compression of the carbon PTL of  $\approx 37\%$ )<sup>[157]</sup> could press the carbon PTL into the flow-field structure and lead to ohmic shorting or mechanical failure of the cell. To reduce the compressive force, one could either adjust the thickness of the PTFE gaskets or assemble an already pre-swollen membrane. The calculated compressive force for an MEA based on a Nafion<sup>®</sup> 117 membrane which was immersed in liquid water at 25°C for 1 hour ( $\lambda=13$ )<sup>[28]</sup> prior to cell assembly is  $\approx 2.8$  MPa (cf. blue star in figure 3.4b), which is closer to the value obtained with a Nafion<sup>®</sup> 212 membrane. In conclusion, this shows that membrane swelling can have a significant impact on the compressive force on the MEA and, consequently, needs to be taken into account for cell assembly.

## 3.2 MEA Fabrication

In this section, the MEA fabrication process is described, including the preparation of inks, the coating process, and the hot-pressing of catalyst coated membranes (CCMs).

### Ink fabrication

Since catalyst powders used for ink fabrication can ignite upon contact with alcohol, special care must be taken when handling these materials. Mixing of catalyst powders should in general occur under inert atmosphere and all residues of catalyst powder need to be wetted with water after use and disposed in a self-extinguishing metal waste container. Furthermore, a lab coat, nitrile gloves and a respiratory mask (class



FFP3) must be worn when working with catalyst powders. Inks are made by mixing catalyst powder, solvents, and ionomer solution in capped HDPE bottles with a size of 8 ml for ink volumes of 1 - 2 ml and 15 ml for an ink volume of 5 ml. A small funnel is formed from weighing paper to facilitate the addition of catalyst powder into the HDPE bottle. The weight of the catalyst is determined by weighing the bottle before and after addition of the material. Then, de-ionized (DI) water (18 M $\Omega$ cm) is added to the catalyst powder, followed by the addition of the solvent (2-propanol, purity  $\geq 99.9\%$  or acetone, purity  $\geq 99.9\%$ , from Sigma Aldrich, Germany). For the standard anode catalyst (IrO<sub>2</sub>/TiO<sub>2</sub> with 75 wt% iridium; Elyst Ir75 0480 from Umicore, Germany) this step can occur under ambient air. For the cathode catalysts (45.8 wt% Pt/C, TEC10V50E and 4.8 wt% Pt/C, TEC10V05E from Tanaka, Kikinzoku Kogyo, Japan) and other Ir-based catalyst materials, catalyst powder and solvent need to be transferred into a nitrogen purged glovebox for mixing in order to prevent ignition. After that, the bottle with catalyst and solvent is removed from the glovebox and the amount of added solvent is controlled by weighing. Finally, Nafion<sup>®</sup> ionomer solution (20 wt% ionomer; D2021 from IonPower, USA) and ZrO<sub>2</sub> grinding balls (5 mm diameter,  $\approx 16.5$  g for 15 ml bottle and  $\approx 8$  g for 8 ml bottle) are added to the other components. The bottle is closed and the lid of the bottle is wrapped with Parafilm<sup>®</sup> to avoid unscrewing of the cap. The bottle is then placed on a roller mill for 24 h at a rotation rate of 180 rpm to achieve a homogeneous suspension.

### Coating Process

Inks are coated by the Mayer-rod technique onto a 25  $\mu$ m thick ETFE foil (FP361025 from Goodfellow, UK) or a 50  $\mu$ m thick PTFE foil (from Angst+Pfister, Germany). The latter one is preferred because it is easier to handle while showing similar coating quality. The foil is cleaned with isopropanol on both sides and fixed on a glass plate with adhesive tape. To avoid coating inhomogeneities, it is crucial to remove all dust and air bubbles beneath the foil and to ensure that the surface is perfectly flat with no wrinkles. The film thickness of the coating and the resulting catalyst loading can be controlled by using Mayer-rods (K Bar, RK PrintCoat Instruments Ltd) with different sizes. The appropriate Mayer-rod is placed on the coating machine (without additional weights but touching the PTFE foil) and the ink is added right in front of the Mayer-rod using a disposable plastic pipette. A coating speed setting of 1-2 is chosen on

### 3 Experimental Methods

---

the machine (K Control Coater, RK PrintCoat Instruments Ltd) to distribute the ink homogeneously on the PTFE foil. The glass plate with the coating is removed from the machine and dried in air, followed by drying at 80°C in an oven. The coating rod is cleaned right after usage to remove ink residue while the ink is still wet. After drying, decals with a size of 5 cm<sup>2</sup> are cut from the coating using a cutting die, which is placed in an automated hydraulic press (Collin P200 PM, Collin GmbH). During cutting, the coating side should face the blades.

#### **MEA Hot-Pressing**

MEAs are prepared by hot-pressing of the electrodes onto a Nafion<sup>®</sup> membrane. Decals are first dried at 80°C for at least one hour and then weighed using a microbalance ( $\pm 15 \mu\text{g}$ ; Mettler Toledo XPE105DR). Two sheets of Kapton<sup>®</sup> (8 x 8 cm, 25  $\mu\text{m}$  thick) are wiped with isopropanol and placed on a clean glass plate. The surface of the Kapton<sup>®</sup> foil is cleaned with compressed air to remove dust or other contaminations. The anode decal is also dusted-off with compressed air and placed on the Kapton<sup>®</sup> foil with the electrode side facing upwards. Next, the two protective foils are removed from the membrane (Nafion<sup>®</sup> 212 only, no protective foil for Nafion<sup>®</sup> 117) and one side of the membrane is labeled to identify anode and cathode after hot-pressing. The membrane (size: 7 x 7 cm) is then placed onto the anode decal, followed by putting the cathode decal on top of the membrane with the electrode side facing the membrane. It is important to ensure that the membrane is flat without wrinkles and that anode and cathode decal are aligned exactly. The second Kapton<sup>®</sup> sheet is then placed on top and remaining air bubbles between the Kapton<sup>®</sup> sheets and the membrane are removed. Finally, the sandwich comprising membrane, decals, and Kapton<sup>®</sup> sheets is placed between two sheets (size: 7 x 7 cm) of Gylon<sup>®</sup> (Type 3545, 2 mm thick, Garlock<sup>®</sup>, ENPRO Industries Inc.) as pressure leveling layer and two metal plates. This assembly is hot-pressed for 3 min at 155°C at a pressure of 2.5 MPa. The temperature is above the glass transition temperature of Nafion<sup>®</sup>, which allows the polymer to flow and create a good connection between electrode and membrane. After the hot-pressing step, the Kapton<sup>®</sup> layers are removed to peel off the decals. By weighing these decals without catalyst layer and comparing with the initial weight, the mass of the catalyst layer can be determined. From the ink composition, the PGM loadings ( $\text{mg}_{\text{Pt}} \text{cm}^{-2}$  or  $\text{mg}_{\text{Ir}} \text{cm}^{-2}$ ) can be calculated. The CCM can then be covered by the Kapton<sup>®</sup> sheets

to avoid contamination and stored in a plastic bag. Assembly of the MEA in the cell hardware was already described in section 3.1.

### 3.3 Electrochemical Characterization

Electrochemical characterization of MEAs is performed with an automated test station from Greenlight Innovation using the Emerald automation software. The test station is equipped with a Reference 3000 potentiostat and a 30 A booster from Gamry. Due to recurring connectivity problems between potentiostat and automation software causing frequent system shutdowns, a different potentiostat (BioLogic VSP 300, 20 A booster) was used for the long-term experiments presented in section 4.3. The operating temperature is controlled by heating rods which are mounted into the end plates and two fans which are placed at each side of the cell. The actual cell temperature is measured by thermocouples situated in the flow-fields close to the active area. The pressure can be adjusted on anode and cathode individually from 1 - 30 bar using a back pressure regulator. During operation, pre-heated water can be fed to the anode (and if required to the cathode) at a rate of up to  $10 \text{ ml min}^{-1}$ . The product gas at the anode outlet can be diluted with nitrogen (up to 200 nccm) to prevent the formation of an explosive gas mixture, due to  $\text{H}_2$  permeation into the anode compartment. On the cathode, the cell can be purged with  $\text{N}_2$  or  $\text{H}_2$  gas. Prior to electrochemical characterization, a warm-up step under  $\text{N}_2$  atmosphere is performed to reach the desired operating temperature.

#### Polarization Curves and Impedance Spectroscopy

Electrochemical characterization of the MEA is started by a conditioning step where the current is ramped up to  $1 \text{ A cm}^{-2}$  and held for 30 min. Subsequently, galvanostatic polarization curves are recorded in a current range from 0.01 to  $6 \text{ A cm}^{-2}$ . Each current step is held for 5 min before recording the cell voltage (averaged over 10 s) to ensure stabilization. Due to slight changes in performance during the first two polarization curves, these are typically considered part of the conditioning process and are not included in the data analysis. After this extended conditioning process, the performance of the cell is very reproducible and further experiments can be conducted. Galvanostatic AC impedance measurements are carried out to determine the high frequency resistance (HFR) for each step of a polarization curve. A frequency range of 100 kHz -

1 Hz is used and the amplitude of the current perturbation is chosen for each step to obtain a sufficient signal to noise ratio, while keeping the perturbation small enough to ensure a linear system response. The HFR is then obtained from the high-frequency intercept with the real axis in a Nyquist plot.

### Cyclic Voltammetry

Cyclic voltammograms (CVs) of the IrO<sub>2</sub>/TiO<sub>2</sub> anode electrode are recorded at a scan rate of 50 mV s<sup>-1</sup> at 80°C. The working electrode (anode) is flushed with liquid water at a flow rate of 5 ml min<sup>-1</sup>, while the counter electrode (cathode) is purged with dry H<sub>2</sub> at a rate of 50 ml min<sup>-1</sup> to ensure a stable reference potential. A CV of the IrO<sub>2</sub>/TiO<sub>2</sub> catalyst used in this work is shown in figure 3.5.

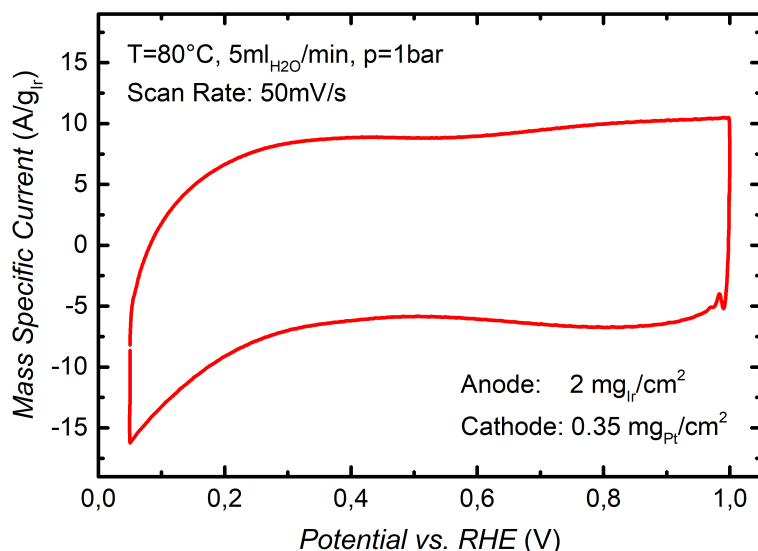


**Figure 3.5:** Ambient pressure cyclic voltammogram (CV) of IrO<sub>2</sub>/TiO<sub>2</sub> based anode with an Ir loading of 2.0 mg<sub>Ir</sub> cm<sup>-2</sup> (cathode: Pt/C, 0.35 mg<sub>Pt</sub> cm<sup>-2</sup>, Nafion<sup>®</sup> 212 membrane). The mass-specific current is plotted vs. the applied potential. The CV was recorded at a scan rate of 50 mV s<sup>-1</sup> at 80°C. H<sub>2</sub>O was supplied to the anode at 5 ml min<sup>-1</sup>, and dry H<sub>2</sub> was supplied to the cathode at 50 ml min<sup>-1</sup>.

For the IrO<sub>2</sub>/TiO<sub>2</sub> electrode, only capacitive currents can be seen which is typical for a thermally prepared, crystalline IrO<sub>2</sub>.<sup>[63]</sup> From an integration of the CV, the voltammetric charge can be determined which is a measure for the number of active sites available for the OER. By normalizing this voltammetric charge by the mass of iridium, it can be used to compare the electrochemically active surface area (ECSA)

of different electrodes. Using this method, a reduced catalyst utilization for inhomogeneous electrodes (cf. section 4.2) or electrodes with a too high ionomer content (cf. section 4.1) could be shown. Furthermore, CVs can reveal information about the surface morphology and oxidation state of the catalyst (cf. section 4.3) and can, therefore, be a valuable method to track changes in the catalyst surface composition/chemistry during experiments.

## 3.4 Further Experimental Methods

Apart from electrochemical measurements, other characterization techniques have been applied, which will be described in the following.

### **N<sub>2</sub>-Sorption**

To evaluate the surface area of catalyst materials, N<sub>2</sub> physisorption at 77 K is performed with a Quantachrome Autosorb-iQ instrument. Prior to the measurement, the catalyst powder samples are degassed for 6 h at 200°C. The specific surface area is calculated by the Brunauer-Emmett-Teller (BET) method using the ASiQwin program.

### **Scanning Electron Microscopy**

Scanning electron microscopy (SEM) is used to analyze catalyst layers and MEA cross-sections. To obtain top-view images of a catalyst layer, a small piece is cut from an MEA and fixed on a plane sample holder using a carbon tape. Cross-sections of MEAs are prepared either by cryo-fracturing in liquid nitrogen, or by embedding small pieces of MEAs in room-temperature curing epoxy resin (EpoThin 2 resin and hardener, Buehler Ltd.). Remaining gas bubbles are removed from the epoxy resin by lowering the pressure in a desiccator, followed by hardening at 40°C over night. The sample surface is then ground with SiC paper in two steps (grade P320 and P1200, from Buehler, Germany) and subsequently polished with 9 μm diamond polishing agent. Images are recorded either with a JEOL JCM-6000Plus NeoScope scanning electron microscope at an accelerating voltage of 15 kV or, for higher resolution, with a JEOL JSM-7500F scanning electron microscope. For the latter, the accelerating voltage can be varied between 1-15 kV to obtain images with different surface sensitivity

and resolution. The electrode thickness was determined by measurements at 10–15 different locations of an MEA cross-section to account for local inhomogeneity.

#### **Scanning Transmission Electron Microscopy**

Scanning transmission electron microscopy (STEM) was performed at EPLF (Lausanne, Switzerland) to visualize iridium particles in the membrane after the AST described in section 4.3. For this purpose, cross-sectional lamellae of pristine and tested MEAs were prepared by focused ion beam milling (Zeiss NVision 40). Small areas of the lamella were thinned for transmission electron microscopy (TEM). A spherical aberration corrected TEM (FEI Titan Themis 60-300) equipped with a high brightness gun source operated at 200 kV was used for STEM analysis. During the measurement, the current was kept as low as possible to avoid electron induced damage. High-angle annular dark field-STEM (HAADF-STEM) images of the interface between the IrO<sub>2</sub>/TiO<sub>2</sub> catalytic layer and the Nafion<sup>®</sup> membrane were recorded as well as energy dispersive spectroscopy (STEM-EDS) elemental maps of iridium and oxygen.

#### **Contact Resistance Measurements**

The electrical contact resistance between PTL and flow-field was determined using the setup described in section 4.1. For the measurement, the PTL is placed between two flow-fields and two copper plates. A thin Kapton foil (25 μm) is used to ensure that there is no electrical contact between the flow-fields, except through the PTL. The compressive force on the PTL is regulated by an automated hydraulic press (Collin P200 PM, Collin GmbH). A current is applied to the copper plates and the voltage drop across the flow-fields is measured.

## 4 Results

In this chapter, the journal articles comprising this PhD thesis are presented. In section 4.1, the influence of ionomer content in an IrO<sub>2</sub>/TiO<sub>2</sub> anode electrode on PEM-WE performance is investigated, providing the basis for a detailed analysis of the contributions of different voltage loss terms to the total overpotential. In section 4.2, the effect of different catalyst loadings (and resulting electrode thicknesses) is studied to gain better understanding of the performance limiting factors for low-loading electrodes. Furthermore, the required reduction of Ir loading to enable large-scale application of PEM electrolysis along with the required developments for catalyst materials are discussed. Finally, in section 4.3, an accelerated stress test (AST) protocol simulating intermittent operation of a PEM-WE is introduced and the effect of recurring open circuit voltage (OCV) periods on PEM-WE durability is analyzed.

### 4.1 Influence of Ionomer Content in IrO<sub>2</sub>/TiO<sub>2</sub> Electrodes on PEM Water Electrolyzer Performance

The article "Influence of Ionomer Content in IrO<sub>2</sub>/TiO<sub>2</sub> Electrodes on PEM Water Electrolyzer Performance"<sup>[107]</sup> was submitted in April 2016 and published as an open access article in the *JES Focus Issue on Electrolysis for Increased Renewable Energy Penetration* of the peer-reviewed *Journal of the Electrochemical Society* in August 2016, distributed under the terms of the Creative Commons Attribution 4.0 License (CC BY). This paper was presented by Maximilian Bernt at the 229<sup>th</sup> Meeting of The Electrochemical Society (May 2016) in San Diego, USA (abstract number: # I03-1418). The permanent web link to the article is <http://jes.ecsdl.org/content/163/11/F3179>.

In this publication, an in-house designed 5 cm<sup>2</sup> active area, single-cell PEM-WE test hardware is presented, which is suitable for differential pressure operation up to

30 bar and shows state-of-the-art performance. Utilizing this cell hardware, the influence of different ionomer contents in the IrO<sub>2</sub>/TiO<sub>2</sub> anode electrode ( $\approx 2 \text{ mg}_{\text{Ir}} \text{ cm}^{-2}$ ) of a PEM-WE MEA (based on a Nafion<sup>®</sup> 212 membrane) is investigated and the impact on various voltage losses is discussed. The best performance, with a cell voltage of 1.57 V at 1 A cm<sup>-2</sup> and less than 2 V at 6 A cm<sup>-2</sup>, was obtained for an ionomer content of 11.6 wt%, corresponding to a wet-ionomer volume fraction of  $\approx 35\%$  and a remaining electrode void volume fraction of also  $\approx 35\%$ , as determined from SEM cross-sections. For lower ionomer contents the performance decreases, which can be explained by a lower proton conductivity within the anode catalyst layer. On the other hand, for higher ionomer contents the void volume in the catalyst layer is filled with ionomer to an increasing degree. This results in a lower catalyst utilization due electric insulation of parts of the electrode, an increased electrical contact resistance due to the formation of an ionomer film at the electrode/PTL interface, and an additional overpotential due to O<sub>2</sub> transport from the catalyst layer to the flow-field. This was shown by an analysis of i) ohmic losses determined by the high-frequency resistance, ii) the kinetic overpotential of the OER quantified by a Tafel analysis, and iii) losses due to proton transport in the catalyst layers. The kinetic overpotential of the HER was shown to be negligible for the catalyst loading of  $\approx 0.35 \text{ mg}_{\text{Pt}} \text{ cm}^{-2}$ . For the optimized anode composition, the remaining mass transport losses account to  $\approx 30 \text{ mV}$  at a current density of 3 A cm<sup>-2</sup>. The largest fraction ( $\approx 20 \text{ mV}$ ) of this overpotential can be explained by a mass transport resistance on the hydrogen cathode induced by a pressure gradient between catalyst layer and flow-field caused by the capillary pressure of water in a slightly hydrophilic cathode electrode.

### Author contributions

M.B. and H.G. developed the high pressure cell design. M.B. prepared membrane electrode assemblies, performed physical characterization and electrochemical testing, evaluated experimental results, and wrote the manuscript. H.G. and M.B. discussed the experimental results and revised the manuscript.





## Influence of Ionomer Content in IrO<sub>2</sub>/TiO<sub>2</sub> Electrodes on PEM Water Electrolyzer Performance

Maximilian Bernt<sup>a,b,z</sup> and Hubert A. Gasteiger<sup>b,\*</sup>

<sup>a</sup>Bayerisches Zentrum für angewandte Energieforschung, 85748 Garching, Germany

<sup>b</sup>Chair of Technical Electrochemistry, Department of Chemistry and Catalysis Research Center, Technische Universität München, 85748 Garching, Germany

In this study, the influence of ionomer content in IrO<sub>2</sub>/TiO<sub>2</sub> anode electrodes for a proton exchange membrane (PEM) electrolyzer is investigated (Nafion 212 membrane; 2.0 mg<sub>Ir</sub> cm<sup>-2</sup> / 0.35 mg<sub>Pt</sub> cm<sup>-2</sup> (anode/cathode)) and the contributions of ohmic losses, kinetic losses, proton transport losses in the electrodes, and mass transport losses to the overall cell voltage are analyzed. Electrolysis tests are performed with an in-house designed high pressure electrolyzer cell at differential pressure up to 30 bar. The best performance is obtained for an ionomer content of 11.6 wt% and a cell voltage of 1.57 V at 1 A cm<sup>-2</sup> and less than 2 V at 6 A cm<sup>-2</sup> (ambient pressure, 80°C). Performance losses at lower ionomer contents are the result of a higher proton conduction resistance. For higher ionomer contents, on the other hand, performance losses can be related to a filling of the electrode void volume by ionomer, leading to a higher O<sub>2</sub> mass transport resistance, an increased electronic contact resistance, and the electronic insulation of parts of the catalyst by ionomer. At high pressure operation, the performance corrected by the shift of the Nernst voltage increases with H<sub>2</sub> pressure and we propose a new explanation for this effect.

© The Author(s) 2016. Published by ECS. This is an open access article distributed under the terms of the Creative Commons Attribution 4.0 License (CC BY, <http://creativecommons.org/licenses/by/4.0/>), which permits unrestricted reuse of the work in any medium, provided the original work is properly cited. [DOI: 10.1149/2.023161jes] All rights reserved.

Manuscript submitted April 15, 2016; revised manuscript received August 8, 2016. Published August 25, 2016. This was Paper 1418 from the San Diego, California, Meeting of the Society, May 29–June 2, 2016. *This paper is part of the JES Focus Issue on Electrolysis for Increased Renewable Energy Penetration.*

In the course of the transition from fossil-based to renewable energy sources, hydrogen technology has gained considerable attention during the past decades. Proton exchange membrane (PEM) electrolyzers are well suited to be coupled with intermittent energy sources such as wind and solar and could provide electrolytic hydrogen for long-term energy storage or fuel cell mobility. At the moment, the large-scale application of PEM electrolyzers is still hindered by their high capital costs.<sup>1,2</sup> One attempt to overcome this challenge is to increase the H<sub>2</sub> output by operating an electrolyzer at current densities much higher than the values typically reported in the literature (1–2 A cm<sup>-2</sup>).<sup>2</sup> Recent publications have shown that current densities of 5 A cm<sup>-2</sup> and higher are possible.<sup>3,4</sup> Another factor that can be economically beneficial is the operation at high pressure because it allows direct storage of H<sub>2</sub> without subsequent mechanical compression. However, high-pressure operation leads to more demanding materials requirements, imposes additional safety precautions, and reduces the faradaic efficiency due to a higher gas permeation through the membrane.<sup>5,6</sup> It was reported that an operating pressure of 30–45 bar could be a good compromise,<sup>7</sup> with differential pressure operation ( $p_{O_2} \approx$  ambient pressure) being more efficient than balanced pressure operation ( $p_{O_2} \approx p_{H_2}$ ).<sup>8</sup> However, increasing the current density and the operating pressure of an electrolyzer will increase the cell voltage, leading to a lower overall voltage efficiency and thus higher operating costs. Since the latter are, along with the capital costs, one of the main cost drivers for large-scale applications,<sup>9</sup> minimizing cell voltage at high current densities and pressures is essential for economic competitiveness. Therefore, a careful analysis of the various voltage loss contributions is necessary to identify how material parameters and operating conditions influence PEM electrolyzer performance, and how the MEA (membrane electrode assembly) can be modified to minimize the overall cell voltage.

The difference between the measured cell voltage and the reversible cell voltage comprises kinetic losses, ohmic losses, losses associated with proton transport in the electrodes, and mass transport losses. The hydrogen evolution reaction (HER) kinetics on platinum, which is typically used as cathode catalyst in PEM electrolyzers have been shown to be very fast, so that high reaction rates can be obtained

at very low overpotentials.<sup>10–13</sup> On the other hand, the kinetics for the oxygen evolution reaction (OER) on the anode are orders of magnitude slower, so that substantial overpotentials are observed even with iridium based catalysts, which are usually used because they provide the best compromise between activity and stability.<sup>14</sup> One strategy to improve their mass specific activity (i.e., the activity normalized by the mass of noble metal), is to maximize the noble metal dispersion by supporting thin films or nanoparticles of iridium (oxide) on high surface area support materials like TiC,<sup>15</sup> TaC,<sup>16</sup> TiO<sub>2</sub><sup>17</sup> or Ti.<sup>18</sup> Another approach is to increase the intrinsic activity of the OER catalyst, and several modifications were examined like fluorine doped iridium oxide,<sup>19</sup> Ir<sub>x</sub>Ru<sub>y</sub>O<sub>2</sub><sup>20</sup> and Ir<sub>x</sub>Ru<sub>y</sub>Ta<sub>z</sub>O<sub>2</sub>.<sup>21</sup>

The ohmic resistance of an electrolyzer includes the electronic contact resistance, mostly between the bipolar plate flow-fields and the porous transport layer (PTL) as well as the membrane's proton conduction resistance. To reduce the contact resistance and increase the durability of the flow-fields, Au or TiN coatings are often applied to titanium-based flow-fields.<sup>22,23</sup> The resistance of the membrane can account for significant voltage losses, especially under operation at high current densities. It can be reduced by employing thinner membranes, but this adjustment increases the hydrogen permeation (often referred to as "crossover") through the membrane, leading to a lower faradaic efficiency, particularly at high operation pressure and low current densities.

The influence of proton conduction resistance in the electrodes has been studied for PEM fuel cells<sup>24–27</sup> and could also play a role in PEM electrolysis, especially when the content of the proton conducting ionomer in the electrodes is low. So far, only few studies have examined the effect of ionomer content in the electrodes on PEM electrolyzer performance.<sup>28,29</sup> They showed a significant influence of ionomer content on the electrolyzer performance, which was attributed to changes in the catalyst/ionomer interfacial resistance and/or catalyst layer resistance. However, only current densities up to 1.5 A cm<sup>-2</sup> were discussed and a complete understanding of the effect is still missing.

Finally, mass transport resistances can add significant voltage losses as reported by Suermann et al., who performed an analysis of the voltage losses for a PEM electrolysis cell at operating pressures ranging from 1–100 bar.<sup>3</sup> In contrast to what would generally be expected, they did not observe a significant increase of cell

\*Electrochemical Society Fellow.

<sup>z</sup>E-mail: maximilian.bernt@tum.de

voltage with pressure. This unexpected behavior was also reported in other studies,<sup>5,6</sup> but a satisfying explanation of the phenomenon is still missing.

In this work, the influence of the MEA's ionomer content in the anode electrode layer on electrolyzer performance is investigated, and the various voltage losses which contribute to the overall performance loss are quantified. We also introduce a new small active-area (5 cm<sup>2</sup>) single-cell electrolyzer cell design for high pressure operation, with which we study the effect of varying hydrogen pressure (1–30 bar<sub>a</sub>) on the electrolysis performance under differential pressure conditions ( $p_{O_2}$  = ambient pressure).

## Experimental

**Membrane electrode assembly (MEA) preparation and cell assembly.**—MEAs with an active area of 5 cm<sup>2</sup> were prepared by a decal transfer method. For the hydrogen cathode electrodes, platinum supported on Vulcan XC72 carbon (46.7 wt% Pt/C; TEC10V50E from Tanaka, Japan) was used as catalyst. For the oxygen anode, IrO<sub>2</sub> supported on TiO<sub>2</sub> (IrO<sub>2</sub>/TiO<sub>2</sub> with 75 wt% iridium; Elyst Ir75 0480 from Umicore, Germany) was used. Catalyst inks were prepared from catalyst powder, 2-propanol (purity ≥ 99.9%, from Sigma Aldrich), de-ionized (DI) water (18 MΩ cm) and Nafion ionomer solution (20 wt% ionomer; D2021 from IonPower, USA). ZrO<sub>2</sub> grinding balls (5 mm diameter) were added and the components were mixed for 24 hours using a roller mill to achieve a homogenous suspension. The ink was then coated onto ETFE foil (25 μm thick, FP361025 from Goodfellow, UK) utilizing a Mayer-rod coating machine. After drying, the electrodes were hot-pressed onto a Nafion 212 membrane (50 μm thick; from Quintech, Germany) for 3 min at 155°C at a pressure of 2.5 MPa. The catalyst loading was determined by weighing the ETFE decals before and after the decal transfer step, using a microbalance (± 1 μg; from Mettler Toledo, Germany). For the hydrogen cathode electrodes the loading was  $0.35 \pm 0.05 \text{ mg}_{Pt} \text{ cm}_{MEA}^{-2}$  and the ionomer to carbon weight ratio was fixed at 0.6/1. The ionomer content of the oxygen anode electrodes was varied between 2.2 and 28.0 wt% relative to the total weight of the electrode. The anode catalyst loading was  $2.00 \pm 0.25 \text{ mg}_{Ir} \text{ cm}_{MEA}^{-2}$  for the electrodes with an ionomer content between 3.9–28.0 wt% and  $1.46 \pm 0.10 \text{ mg}_{Ir} \text{ cm}_{MEA}^{-2}$  for the sample with 2.2 wt% ionomer. Sintered titanium (from Mott Corporation, USA) with a porosity of ~50% and a thickness of  $280 \pm 10 \mu\text{m}$  as well as a carbon fiber paper (TGP-H-120T from Toray, no MPL, 20 wt% PTFE) with a thickness of  $370 \pm 10 \mu\text{m}$  were used as porous transport layers (PTL) at the anode and at the cathode, respectively. The MEA was placed between the PTLs and sealed with virgin PTFE foil. Sealings with an appropriate thickness were chosen to achieve a 25% compression of the carbon PTL. (under the applied compression, the titanium PTL can be considered incompressible).

**Physical characterization.**—Cross-sectional scanning electron microscopy (SEM) measurements were performed with a JEOL JCM-6000Plus NeoScope scanning electron microscope at an accelerating voltage of 15 kV to determine electrode thickness. MEA cross-sections were prepared by cryo-fracturing MEAs in liquid nitrogen. 5 values for the electrode thickness were measured at three different locations to account for inhomogeneities in the electrode thickness. High resolution SEM images were taken with a JEOL JSM-7500F scanning electron microscope with an accelerating voltage of 1 kV. The Brunauer-Emmett-Teller (BET) surface area was determined by adsorption of liquid nitrogen on the catalyst powder with a Quantachrome Autosorb-iQ after outgasing for 6 hours at 200°C.

**Electrochemical characterization.**—Tests were performed on an automated test station from Greenlight Innovation equipped with a potentiostat and booster (Reference 3000 and 30 A booster, Gamry). All measurements were done at 80°C cell temperature; deionized (DI) water was pre-heated to 80°C and fed to the anode side of the electrolysis cell at a rate of 5 ml min<sup>-1</sup>. Polarization curves were recorded at hydrogen pressures between 1–30 bar<sub>a</sub> absolute pressure. The oxy-

gen side was always kept at ambient pressure. For the high pressure tests, the product gas at the anode side of the cell was diluted with nitrogen (100 nccm) to prevent the development of an explosive gas mixture which otherwise could be formed by the permeation of H<sub>2</sub> through the membrane into the anode compartment. After a warm-up step under N<sub>2</sub> atmosphere to reach the desired temperature, the cell was conditioned by ramping the current to 1 A cm<sup>-2</sup> and holding this value for 30 min. Subsequently, galvanostatic polarization curves were recorded at current densities starting at 0.01 and increasing to 6 A cm<sup>-2</sup>. Each current step was held for 5 min, before recording the cell voltage to ensure stabilization. A slight improvement in cell performance was typically observed for the first two polarization curves, while it remained constant afterwards. Consequently, the first two polarization curves can be regarded as an additional conditioning step and were not included in the data analysis shown here. AC impedance measurements in a range of 10 Hz–20 kHz with current perturbations of ±200 mA were carried out at each current step to determine the high frequency resistance (HFR), which was obtained from the high-frequency intercept of the Nyquist plot with the real axis. CVs of the IrO<sub>2</sub>/TiO<sub>2</sub> anode electrode were recorded at a scan rate of 50 mV s<sup>-1</sup> at 80°C. The anode working electrode was flushed with H<sub>2</sub>O at a flow rate of 5 ml min<sup>-1</sup>, while the cathode counter electrode was purged with dry H<sub>2</sub> at 50 ml min<sup>-1</sup>.

**Ohmic loss correction.**—To identify the contribution of different kinds of voltage losses, polarization curves were first corrected by the HFR, which is considered to be the sum of the membrane resistance  $R_{memb}$  and the electronic resistance (sum of contact resistances between flow-fields and PTLs and bulk PTL resistances),  $R_{el}$ . To validate this correlation,  $R_{el}$  and  $R_{memb}$  were measured separately:  $R_{el}$  as described in the next section and  $R_{memb}$  by a conductivity measurement. For the latter, a piece of Nafion 212 membrane was assembled in an in-plane conductivity cell (BekkTech, USA) and placed in liquid water at 80°C. The conductivity was determined from the HFR measured via AC impedance spectroscopy after immersing the membrane in water for more than 20 h to ensure that the membrane is fully hydrated.<sup>30</sup>

## Electrolyzer Cell Hardware

The electrolyzer cell design used in this study is presented in Fig. 1. The cell consists of aluminum end plates (s. (1) in Fig. 1), which are compressed by 12 M8 screws. In order to regulate the temperature during experiments, heating rods are mounted into the end plates and two fans are placed at each side of the cell. The cell temperature is measured by two thermocouples situated in the center of the two flow-fields. Copper current collectors (s. (3) in Fig. 1) are used to connect the power supply cables to the cell. Between the end plates and the current collectors, 2 mm thick Gylon (type 3545, from Garlock, USA; s. (2) in Fig. 1) patches are placed for electronic insulation of the end plate from the rest of the cell. The Gylon also provides a more equal distribution of the compressive force on the sealing and the active-area of the cell. Single serpentine flow-fields with an area of 5 cm<sup>2</sup> were machined into the titanium blocks (8×8×2 cm). The width and depth of the channels are 1 mm, while the width of the lands is 0.7 mm. NPT threads for the gas connections are directly machined into the titanium blocks. Dielectric fittings (SS-4-DE-6, from Swagelok, Germany) are connected to these NPT threads to prevent ohmic shorting between anode and cathode flow-fields. The MEA (s. (7) in Fig. 1) is placed between the flow-fields (s. (4) in Fig. 1) with the carbon PTL (s. (6) in Fig. 1) on the hydrogen cathode and the titanium PTL (s. (8) in Fig. 1) on the oxygen anode side. Gaskets punched from virgin PTFE foil (from Reichelt, Germany) are used for sealing (s. (5) in Fig. 1).

A thin gold coating was applied to the titanium plates to reduce the contact resistance between PTL and flow-field as well as to improve the corrosion resistance of the flow-field. Prior to Au deposition, the surface of the titanium flow-fields was mechanically polished on a polishing machine (Buehler Beta) with SiC grinding paper. Besides allowing a better adhesion of gold on the titanium plate, the

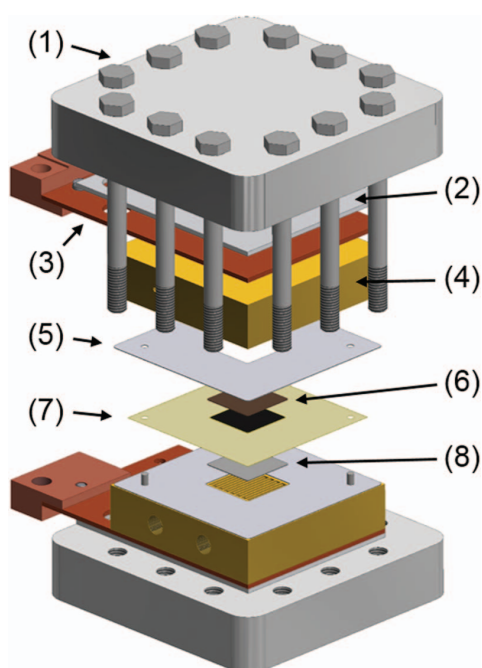


**Figure 1.** Schematic drawing of the 5 cm<sup>2</sup> high pressure electrolysis cell: (1) aluminum end plate, (2) 2 mm Gylon layer, (3) copper current collector, (4) gold coated titanium flow-fields, (5) PTFE gaskets, (6) carbon PTL, (7) MEA, and (8) titanium PTL.

polishing step is essential to achieve a good sealing, especially at high gas pressure. After polishing, the titanium blocks were cleaned by ultrasonication in a mixture of DI water and isopropanol and by boiling them in DI water for several hours. The flow-fields were then dipped into a diluted hydrofluoric acid solution (2.5% HF in DI water) for 30 seconds to remove the oxide layer from the surface; subsequently they were washed in DI water. A gold layer with a nominal thickness of 300 nm was deposited on the surface via thermal evaporation.

The sealing of the cell was studied by measuring the pressure distribution on the sealing area. For this purpose, a pressure sensitive film (Prescale, Fujifilm) was placed in the middle of a sandwich comprised of the set of flow-fields and PTFE gaskets, as used in the actual experiments. When the screws connecting the two endplates were tightened with a torque of 20 Nm, a uniform pressure distribution on the sealing area was obtained, indicating an average compressive force of  $\approx 40$  MPa. To verify the gas-tightness of the sealing, a leak test was performed by filling the cell with helium at a pressure of 50 bar, with the other gas connection ports of the cell being closed off. Subsequently, the valve at the gas inlet of the cell was closed and the pressure inside the cell was monitored with a pressure gauge attached to the dead-ended gas-outlet of the cell. The He pressure was monitored and remained stable over 20 hours, indicating a leak rate below 0.005 nccm, which is negligible compared to the lowest examined rate of H<sub>2</sub> production ( $\approx 0.35$  nccm at 0.01 A cm<sup>-2</sup>). Consequently, at operating pressures up to 30 bar<sub>a</sub>, we did not detect a leak of H<sub>2</sub> by the H<sub>2</sub> sensors placed close to the cell. This confirms an excellent sealing of the cell also under real operating conditions with H<sub>2</sub> at 30 bar<sub>a</sub> and temperatures of 80°C.

The right level of compression of the PTLs is essential to ensure both a low contact resistance between the PTLs and the flow-fields as well as a sufficiently high porosity of the carbon fiber paper based cathode PTL. To determine the compressive force applied to the active-area of the MEA, a pressure sensitive paper was placed between the

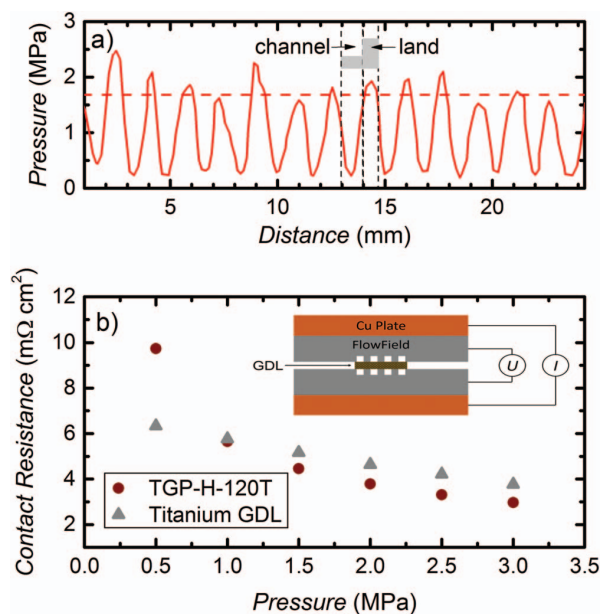


**Figure 2.** a) Pressure distribution for 5 cm<sup>2</sup> flow-field with a titanium and a carbon PTL at a compressive force resulting in a carbon paper strain of 25%. b) Contact resistance of one flow-field/PTL interface for carbon paper and titanium PTL vs. compressive force on the PTL, whereby the compression is obtained by dividing the applied force by the land area of the flow-field plates. The inset shows the setup for the contact resistance measurement.

titanium and the carbon PTLs, and this sandwich was placed between the flow-fields together with the PTFE gaskets. The total thickness of the latter was chosen to result in a compressive strain of  $\approx 25\%$  of the carbon paper (the titanium PTL is essentially incompressible under the applied compression). The pressure distribution over the active-area determined from the pressure sensitive paper is shown in Fig. 2a. The average pressure calculated over the entire “land” area is  $\approx 1.7$  MPa (s. dashed line in Fig. 2a). The resulting contact resistance between PTLs and flow-fields was measured with the setup shown in the inset of Fig. 2b: a PTL was placed between the flow-fields, which were compressed between two copper plates by an automatic platen press (Dr. Collin P 200 PM); here, the pressure is referred to the force applied by the press divided by the total land area of the flow-field. Since most of the applied compressive force lies on the land area (s. Fig. 2a), the obtained pressure should represent the actual pressure on the land area with sufficient accuracy. A current of 3 A was applied via the copper plates and the voltage drop between the flow fields was measured. The corresponding resistance is then the sum of contact resistances between PTL and both flow-fields in addition to the bulk resistance of the PTL, which is  $\approx 2$  m $\Omega$  cm<sup>2</sup> for the carbon PTL (manufacturer information) and considered negligible for the titanium PTL. The contact resistance between one flow-field/PTL interface,  $R_C$  (i.e., half of total resistance–bulk resistance) measured at an average compressive force of 1.5 MPa with the carbon PTL decreased significantly from  $\approx 30$  m $\Omega$  cm<sup>2</sup> for the bare titanium flow-fields (data not shown) to  $\approx 5$  m $\Omega$  cm<sup>2</sup> for the Au coated flow-field (s. circular symbols in Fig. 2b). At the same compressive force, the resistance of the titanium PTL between the Au-coated titanium plates is also  $\approx 5$  m $\Omega$  cm<sup>2</sup> (s. triangular symbols in Fig. 2b). Thus, for an average pressure of 1.7 MPa on the lands, i.e., the pressure obtained for 25% strain of the carbon PTL (s. Fig. 2a), the total electronic resistance (i.e. the sum of the contact resistances for one flow-field/titanium PTL interface, one flow-field/carbon PTL interface and the carbon PTL bulk resistance) is  $\approx 12$  m $\Omega$  cm<sup>2</sup>.



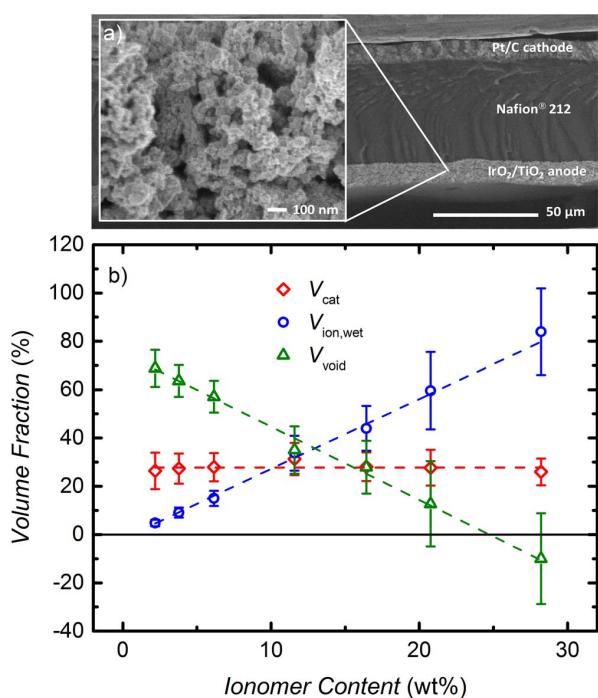


**Figure 3.** a) SEM image of an MEA cross-section. The inset shows a higher resolution SEM image of the IrO<sub>2</sub>/TiO<sub>2</sub> anode electrode. b) Electrode volume fractions versus ionomer content for the IrO<sub>2</sub>/TiO<sub>2</sub> catalyst,  $V_{\text{cat}}$  (red diamonds), the ionomer equilibrated with liquid water at 80°C,  $V_{\text{ion,wet}}$  (blue circles), and for the remaining electrode void volume,  $V_{\text{void}}$  (green triangles). These were determined by measuring the thickness and the areal weight of the anode electrodes.

## Results

**Electrode thickness and ionomer volume fraction.**—Fig. 3a shows an exemplary SEM image of an MEA cross-section determined after the electrochemical measurements, employed to quantify electrode thickness. All Pt/C electrodes with a loading of  $0.35 \pm 0.05 \text{ mg}_{\text{Pt}} \text{ cm}^{-2}$  (corresponding to a carbon loading of  $0.40 \pm 0.06 \text{ mg}_{\text{C}} \text{ cm}^{-2}$ ) had a thickness of  $10 \pm 1 \mu\text{m}$ . This is in agreement with the expected electrode thickness of  $28 \pm 2 \mu\text{m}$  for a carbon loading of  $1 \text{ mg}_{\text{C}} \text{ cm}^{-2}$ .<sup>26</sup> The thickness of the IrO<sub>2</sub>/TiO<sub>2</sub> electrodes ranged from 8–12  $\mu\text{m}$ , depending on the exact catalyst loading. From the catalyst loading,  $L_{\text{cat}}$ , the anode electrode thickness,  $t_{\text{an}}$ , and the average catalyst density,  $\rho_{\text{cat}} = 9.5 \text{ g cm}^{-2}$ , the catalyst volume fraction,  $V_{\text{cat}}$ , can be calculated:

$$V_{\text{cat}} = \frac{L_{\text{cat}}}{\rho_{\text{cat}} \cdot t_{\text{an}}} \quad [1]$$

The average catalyst density was calculated based on the assumption that the catalyst consists of iridium(IV)oxide and titanium(IV)oxide. With the weight percentages of the components (86.9 wt% IrO<sub>2</sub> and 13.1 wt% TiO<sub>2</sub>) and the density of the materials ( $11.7 \text{ g cm}^{-3}$  for IrO<sub>2</sub> and  $4.23 \text{ g cm}^{-3}$  for TiO<sub>2</sub> (rutile)) the average catalyst density can be calculated. As shown in Fig. 3b,  $V_{\text{cat}}$  is about 28% for all IrO<sub>2</sub>/TiO<sub>2</sub> based anode electrodes (s. red diamonds in Fig. 3b), yielding an electrode void volume of 72% in the absence of ionomer (i.e., for 0 wt% ionomer). The empty pores are partially filled by the ionomer which is incorporated into the electrode structure; its volume fraction in the electrode can then be calculated by:

$$V_{\text{ion,dry}} = \frac{L_{\text{ion}}}{\rho_{\text{ion}} \cdot t_{\text{an}}} \quad [2]$$

where  $L_{\text{ion}}$  is the loading of ionomer in the electrode,  $\rho_{\text{ion}} = 2.1 \text{ g cm}^{-3}$  is the ionomer density, and  $V_{\text{ion,dry}}$  corresponds to the volume of the dry ionomer. Swelling of the ionomer under operating conditions (80°C, liquid water) must be considered when calculating the actual ionomer volume fraction,  $V_{\text{ion,wet}}$ , which is about a factor of 1.8 higher compared to the dry ionomer volume.<sup>27</sup> The ionomer volume fraction in equilibrium with liquid water at 80°C,  $V_{\text{ion,wet}}$ , is shown by the blue circles in Fig. 3b, while the remaining void volume in the electrode,  $V_{\text{void}}$ , is shown by the green triangles in Fig. 3b. Error bars represent one standard deviation based on the variation of the measured electrode thickness. Note that the same analysis was applied previously to PEM fuel cell MEAs.<sup>31</sup>

For an ionomer content increasing from 2.2–28.0 wt% relative to the total electrode weight, the wet ionomer volume fraction in the electrode increases from 5–84%. The remaining void volume is obtained by subtraction of  $V_{\text{cat}}$  and  $V_{\text{ion,wet}}$  from the total electrode volume, i.e., from 100%. Hence, for an ionomer content of 20–25 wt%, the electrode void volume will be essentially completely filled with ionomer. Finally, using the BET surface area of the IrO<sub>2</sub>/TiO<sub>2</sub> catalyst of  $31 \text{ m}^2 \text{ g}_{\text{cat}}^{-1}$ , the effective ionomer film thickness on the catalyst surface can be calculated assuming a uniform ionomer film over the total catalyst surface, which then results in nominal ionomer film thicknesses increasing from  $\approx 0.6$  to  $\approx 11 \text{ nm}$  as the ionomer content increases from 2.2 to 28.0 wt%. The assumption of a homogeneous ionomer film is only valid if the pore size in the electrode is much larger than the nominal film thickness. From the inset in Fig. 3a it can be seen that the pores in the IrO<sub>2</sub>/TiO<sub>2</sub> electrode range from  $\approx 10$  to  $\approx 100 \text{ nm}$ . Even smaller pores might be present as well, but could not be identified from the SEM image. Consequently, the assumption of a uniform ionomer film thickness might not be applicable, especially for samples with a high ionomer content.

### Electrolysis performance: influence of ionomer content.

Steady-state polarization curves at 80°C and ambient pressure are shown in Fig. 4a for MEAs with an anode ionomer content of 3.9, 11.6, and 28.0 wt%. The best performance is obtained for the intermediate ionomer content of 11.6 wt%, with  $V_{\text{ion,wet}} \approx V_{\text{void}} \approx 35\%$  (s. Fig. 3b). Here, a cell voltage of 1.57 V is measured at a current density of  $1 \text{ A cm}^{-2}$ , and even at  $6 \text{ A cm}^{-2}$  the cell voltage stays clearly below 2 V (s. blue circles in Fig. 4a). For the sample with 3.9 wt% ionomer (s. red diamonds in Fig. 4a), the performance decreases only slightly, while for the sample with 28 wt% ionomer (s. green squares in Fig. 4a), the cell voltage is significantly higher, which is partly due to a higher HFR (s. below). In Fig. 4b, the cell voltages corrected by the HFR (iR-free) are plotted for all MEAs. Again, the best performance can be observed for the sample with 11.6 wt% ionomer (s. blue circles in Fig. 4b), while the cell voltage increases when the ionomer content either decreases or increases with respect to this value.

For high current densities, the amount of heat produced at the MEA can reach up to  $\approx 3 \text{ W cm}^{-2}$  and since the temperature is not measured directly at the membrane but in the flow-fields, a significant difference between the actual MEA temperature and the measured value can be expected, estimated to be  $\approx 6^\circ\text{C}$  at  $6 \text{ A cm}^{-2}$ . Consequently, all further analysis is carried out only for current densities up to  $3 \text{ A cm}^{-2}$ , where the maximum heat production is  $< 1 \text{ W cm}^{-2}$ , resulting in a reasonably small temperature difference of less than  $2^\circ\text{C}$ .

A more detailed analysis of the influence of ionomer content on cell performance is given in Fig. 5, where the iR-free cell voltages at three fixed current densities ( $0.1 / 1.0 / 3.0 \text{ A cm}^{-2}$ ) are plotted against ionomer content. A minimum iR-free cell voltage is observed at 11.6 wt% for all current densities (Fig. 5a), increasing for both lower and higher ionomer content as could already be seen in Fig. 4b. However, the maximum difference in iR-free cell voltage is only  $\approx 50 \text{ mV}$  at  $3 \text{ A cm}^{-2}$ . Fig. 5b shows the HFR for the different current densities vs. the ionomer content. It can be seen that the HFR is almost constant for all MEAs with an ionomer content up to  $\approx 16 \text{ wt\%}$ , with a value of  $52.5 \pm 1.5 \text{ m}\Omega \text{ cm}^2$ . Considering that the HFR should be the sum of  $R_{\text{memb}}$  and  $R_{\text{el}}$ , this HFR-value can be compared with the independently measured values for  $R_{\text{memb}}$  and  $R_{\text{el}}$ .

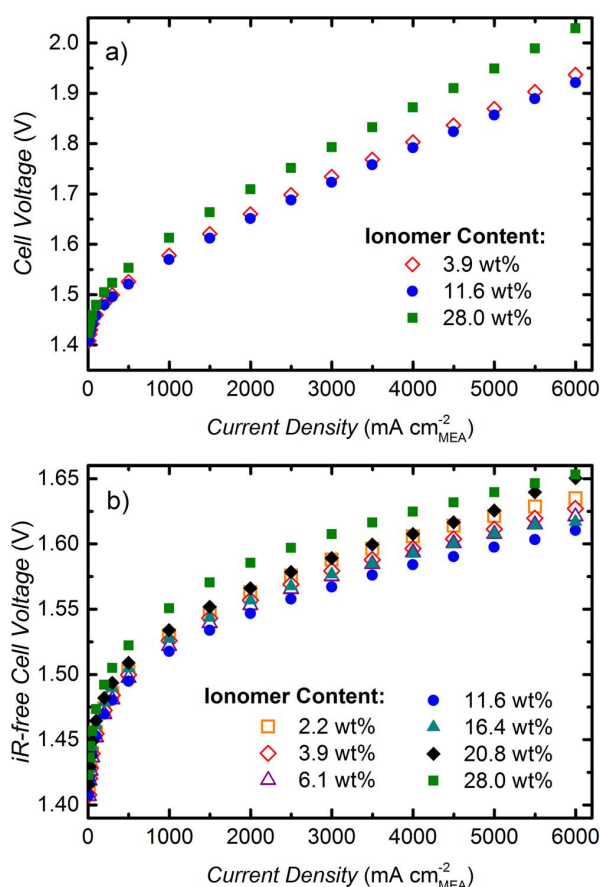


**Figure 4.** Ambient pressure polarization curves ( $80^{\circ}\text{C}$ ,  $5\text{ ml H}_2\text{O min}^{-1}$ ) for MEAs with different anode ionomer loadings (in weight percent relative to total mass of electrode) using a  $\approx 50\text{ }\mu\text{m}$  thick Nafion 212 membrane: a) measured cell voltage; b) cell voltage corrected by HFR. Anode and cathode catalyst loadings are  $0.35 \pm 0.05\text{ mgPt cm}_{\text{MEA}}^{-2}$  and  $2.00 \pm 0.25\text{ mgIr cm}_{\text{MEA}}^{-2}$ , respectively.

In the applied cell configuration with an average compressive force of 1.7 MPa on the flow-field lands (s. Fig. 2a),  $R_{\text{el}}$  is  $\approx 12\text{ m}\Omega\text{ cm}^2$  as described earlier. For the Nafion 212 membrane, a conductivity of  $142\text{ mS cm}^{-1}$  was measured at  $80^{\circ}\text{C}$  in liquid water, which is in agreement with the values reported in literature.<sup>32–36</sup> The thickness of the membrane, assembled in the cell, is between  $\approx 58\text{--}77\text{ }\mu\text{m}$ . The lower value is obtained if the volume expansion due to exposure to water occurs isotropically, whereas the higher value was calculated according to Liu et al., making the assumption that the volume expansion only occurs in the through-plane direction.<sup>25</sup> This leads to a membrane resistance  $R_{\text{memb}}$  of  $\approx 41\text{--}54\text{ m}\Omega\text{ cm}^2$ . The sum of  $R_{\text{el}}$  and  $R_{\text{memb}}$  therefore is predicted to range in between  $53\text{--}66\text{ m}\Omega\text{ cm}^2$ . Comparing these values to the measured HFR ( $52.5 \pm 1.5\text{ m}\Omega\text{ cm}^2$ ), the agreement between measured and predicted HFR is very good, if one assumes an isotropic volume expansion of the membrane.

At an ionomer content of  $\approx 20\text{ wt}\%$ , the HFR increases significantly to  $\approx 63\text{ m}\Omega\text{ cm}^2$  and stays at this value for even higher ionomer contents. The sudden increase of the HFR coincides quite well with the predicted complete filling of the electrode void volume for an ionomer content of approximately  $>20\text{ wt}\%$  (s. green triangles in Fig. 3b). This suggests that in the case when the ionomer volume exceeds the void volume between the catalyst particles, an electronically insulating film of residual ionomer forms at the electrode/PTL interface, leading to a higher contact resistance and thus to a higher HFR. The increase in  $iR$ -

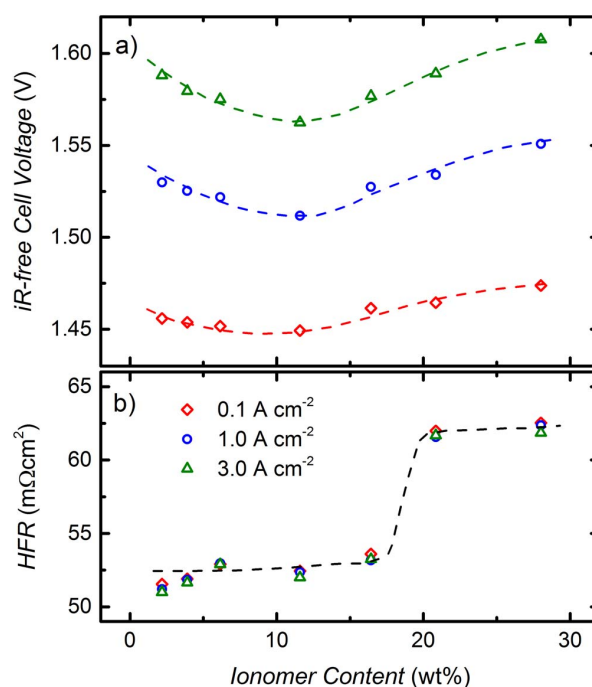


**Figure 5.** a) Ambient pressure cell voltage corrected by HFR,  $E_{iR\text{-free}}$ , at current densities of  $0.1\text{ A cm}^{-2}$ ,  $1.0\text{ A cm}^{-2}$  and  $3.0\text{ A cm}^{-2}$  ( $80^{\circ}\text{C}$ ,  $5\text{ ml H}_2\text{O min}^{-1}$ ) as a function of anode ionomer content (in weight percent relative to total mass of electrode). b) Corresponding HFR.

free cell voltage in this case is likely related to an additional electronic insulation of parts of the catalyst particles, leading to higher kinetic overpotentials and thus higher  $iR$ -free cell voltages.

To ensure reproducibility of the results, three different MEAs with the optimum ionomer content of  $11.6\text{ wt}\%$  were tested. The anode catalyst loading was between  $2.00\text{--}2.20\text{ mgIr cm}_{\text{MEA}}^{-2}$  and the cathode catalyst loading was  $0.35 \pm 0.05\text{ mgPt cm}_{\text{MEA}}^{-2}$  for the three samples. For current densities up to  $3\text{ A cm}^{-2}$  the electrochemical measurements showed excellent reproducibility, with differences in cell voltage of less than  $10\text{ mV}$ , Tafel Slopes between  $45\text{--}47\text{ mV dec}^{-1}$  and HFRs of  $52\text{--}55\text{ m}\Omega\text{ cm}^2$ .

**High pressure electrolysis.**—High pressure electrolysis tests were carried out with the MEA with the above found optimal anode ionomer content of  $11.6\text{ wt}\%$ . Polarization curves were recorded at differential pressure conditions, with a cathode pressure  $p_{\text{cath}}$  of 3, 10, and  $30\text{ bar}_a$ , while the anode pressure was kept at  $1\text{ bar}_a$ . Before and after the differential pressure tests, a polarization curve was recorded at ambient pressure conditions ( $p_{\text{cath}} = p_{\text{an}} = 1\text{ bar}_a$ ) to ensure that no degradation had occurred during the differential pressure tests. The recorded cell voltages before and after the differential pressure tests were identical within a range of  $\pm 2\text{ mV}$ . The polarization curves at different hydrogen pressures are shown in Fig. 6. The cell voltage increases with increasing operating pressure, and at the highest shown current density of  $3\text{ A cm}^{-2}$ , an increase of the cathode pressure from ambient pressure to  $30\text{ bar}_a$  results in an increase in cell voltage of  $<50\text{ mV}$  (s. Fig. 6a), which is at least qualitatively consistent with other data in the literature.<sup>1</sup> Since the HFR is essentially independent of pressure (data not shown), a similar gain in  $E_{iR\text{-free}}$  is observed (s. Fig. 6b). The fact that the differences between the curves in Fig. 6 are decreasing with increasing current density is addressed in more detail in the Discussion section.

In the Discussion section, we will now analyze the various voltage loss terms as a function of the ionomer content in the anode electrode of the MEA, seeking to explain the origin of the increasing cell voltage

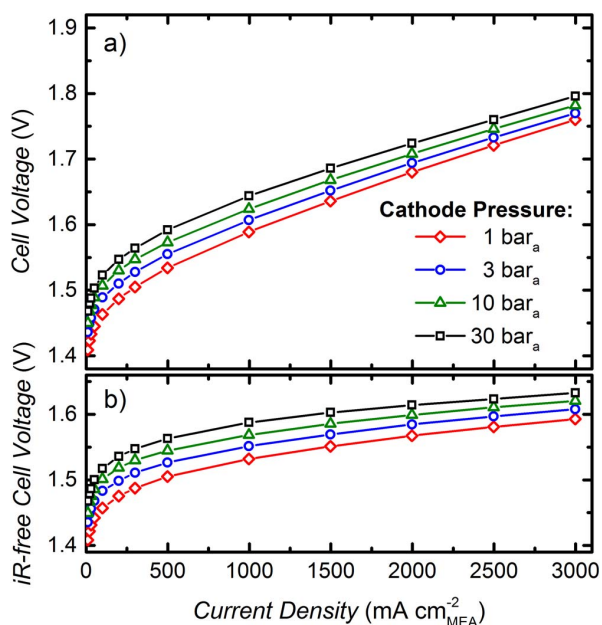


**Figure 6.** Polarization curves for MEAs at hydrogen cathode pressures of 1–30 bar<sub>a</sub> (80°C, 5 ml<sub>H<sub>2</sub>O</sub> min<sup>-1</sup>) while keeping the oxygen anode at ambient pressure: a) measured cell voltage; b) cell voltage corrected by HFR. Anode and cathode catalyst loadings are 0.35 ± 0.05 mg<sub>Pt</sub> cm<sub>MEA</sub><sup>-2</sup> and 2.00 ± 0.25 mg<sub>Ir</sub> cm<sub>MEA</sub><sup>-2</sup>, respectively; ≈50 μm thick Nafion 212 membrane.

at ionomer contents above and below the experimentally determined optimum value. In addition, we will provide an explanation for the reported decrease in mass transport resistance with increasing operating pressure.<sup>3</sup>

### Discussion

In the following, the contribution of the different voltage losses to the total overpotential and the influence of the operating pressure will be discussed. The overall electrolysis cell voltage can be defined by adding the voltage loss terms to the reversible cell voltage:

$$E_{\text{cell}} = E_{\text{rev}} + i \cdot (R_{\text{memb}} + R_{\text{el}}) + \eta_{\text{HER}} + \eta_{\text{OER}} + i \cdot (R_{\text{H}^+, \text{an}}^{\text{eff}} + R_{\text{H}^+, \text{cath}}^{\text{eff}}) + \eta_{\text{mt}} \quad [3]$$

where  $E_{\text{rev}}$  is the reversible cell voltage, which is a function of temperature and pressure, and  $R_{\text{memb}}$  and  $R_{\text{el}}$  are the ohmic resistance of the membrane and the electronic resistance, respectively.  $\eta_{\text{HER}}$  and  $\eta_{\text{OER}}$  are the kinetic overpotentials for the HER and the OER, while  $R_{\text{H}^+, \text{an}}^{\text{eff}}$  and  $R_{\text{H}^+, \text{cath}}^{\text{eff}}$  represent the effective proton transport resistance in the respective electrodes. Finally,  $\eta_{\text{mt}}$  describes additional losses which can be related to mass transport. For ambient pressure operation, the effect of H<sub>2</sub> and O<sub>2</sub> crossover is small compared to the other losses and can be neglected.<sup>37</sup> For simplicity, voltages are treated as positive values, even though in a strict thermodynamic view, they would have negative values for an electrolyzer.

At a temperature of 80°C, the saturation pressure of H<sub>2</sub>O is 0.47 bar<sub>a</sub>, so that for ambient pressure operation of the cell (1 bar<sub>a</sub>), the partial pressures of hydrogen in the cathode and of oxygen in the anode are  $p_{\text{H}_2} = 0.53 \text{ bar}_a$  and  $p_{\text{O}_2} = 0.53 \text{ bar}_a$ , respectively.  $E_{\text{rev}}$ , which is a function of temperature and activity of the species involved in the reaction can then be calculated for the cell reaction of H<sub>2</sub>O<sub>liquid</sub> → H<sub>2</sub> + 0.5 O<sub>2</sub> by:

$$E_{\text{rev}} = E_{\text{rev}}^0 + \frac{RT}{2F} \ln \left[ \frac{a(\text{H}_2) \cdot \sqrt{a(\text{O}_2)}}{a(\text{H}_2\text{O})} \right] \quad [4]$$

where the temperature dependence of the standard reversible potential,  $E_{\text{rev}}^0$ , can be obtained from Reference<sup>38</sup> as:

$$E_{\text{rev}}^0 = 1.2291 \text{ V} - 0.0008456 \text{ V} \cdot (T - 298.15 \text{ K}) \quad [5]$$

For liquid water, the activity of water,  $a(\text{H}_2\text{O})$ , is one, while the activity of the gaseous species is represented by the ratio of their partial pressure to the standard pressure of 1 bar<sub>a</sub>. Thus, at ambient pressure and 80°C,  $a(\text{H}_2) = a(\text{O}_2) = \frac{0.53 \text{ bar}_a}{1 \text{ bar}_a}$ , which yields a reversible cell voltage of  $E_{\text{rev}} = 1.168 \text{ V}$  (first term on the right-hand side of Eq. 3). As discussed in the previous section, the ohmic loss can be corrected for by subtracting the product of current density and HFR from the measured cell voltage (second term on the right-hand side of Eq. 3).

**Voltage losses at the H<sub>2</sub> cathode.**—For the calculation of  $\eta_{\text{HER}}$ , the Butler-Volmer equation can be linearized due to the fast reaction kinetics.<sup>10</sup> The overpotential can then be defined as:<sup>31</sup>

$$\eta_{\text{HER}} = i \cdot R_{\text{K,HER}} \quad [6]$$

where

$$R_{\text{K,HER}} = \frac{RT}{2F \cdot L_{\text{Pt}} \cdot A_{\text{Pt,el}} \cdot i_{0,\text{HER}}} \quad [7]$$

With an exchange current density of  $i_{0,\text{HER}} = 250 \text{ mA cm}_{\text{metal}}^{-2}$  at 80°C,<sup>12</sup> a cathode catalyst loading of  $L_{\text{Pt}} = 0.35 \text{ mg}_{\text{Pt}} \text{ cm}^{-2}$ , and an electrochemically active surface area of  $A_{\text{Pt,el}} = 60 \text{ m}^2 \text{ g}_{\text{Pt}}^{-1}$ <sup>31</sup> for the catalyst used in this study,  $R_{\text{K,HER}}$  equates to 0.29 mΩ cm<sup>2</sup>, which results in an  $\eta_{\text{HER}}$  value of less than 1 mV even at a current density of 3 A cm<sup>-2</sup>. Thus, the kinetic overpotential for the HER,  $\eta_{\text{HER}}$ , can be neglected in the further analysis.

On the other hand, the effective proton transport resistance for the hydrogen cathode can be calculated following the approach described by Gu et al.:<sup>31</sup>

$$\frac{R_{\text{H}^+, \text{cath}}^{\text{eff}}}{R_{\text{H}^+, \text{cath}}} = \frac{1}{\beta} \cdot \left( \frac{e^\beta + e^{-\beta}}{e^\beta - e^{-\beta}} - \frac{1}{\beta} \right) \quad [8]$$

where

$$\beta = \left( \frac{R_{\text{H}^+, \text{cath}}}{R_{\text{K,HER}}} \right)^{1/2} \quad [9]$$

Here, the sheet resistance for proton transport in a Pt/C electrode,  $R_{\text{H}^+, \text{cath}}$ , can be calculated from the reported sheet resistivity of ≈25 Ω cm for a Pt/Vulcan electrode with an I/C-ratio of 0.6/1 at 80°C and a relative humidity of 122% (i.e., in the presence of liquid water)<sup>25</sup> and the electrode thickness of ≈10 μm (s. Experimental section), equating to a proton conduction sheet resistance of  $R_{\text{H}^+, \text{cath}} \approx 25 \text{ m}\Omega \text{ cm}^2$ . Together with the above determined charge transfer resistance ( $R_{\text{K,HER}} \approx 0.29 \text{ m}\Omega \text{ cm}^2$ ), this yields a  $\beta$ -value of ≈9 (s. Eq. 9). Thus, the effective proton transport resistance,  $R_{\text{H}^+, \text{cath}}^{\text{eff}}$ , calculated by Eq. 8 is ≈2.5 mΩ cm<sup>2</sup>, which would result in very small voltage loss of ≈7 mV at 3 A cm<sup>-2</sup>.

**Voltage losses at the O<sub>2</sub> anode.**—The overpotential for the OER can be determined from a Tafel fit of the data in Fig. 4, as shown in Fig. 7, where the iR-free cell voltage is plotted on a logarithmic current scale. The Tafel slope was determined in the 10–100 mA cm<sup>-2</sup> region, where the behavior is approximately linear and the effects of proton and mass transport resistances can be neglected. The Tafel slopes are between 45–50 mV dec<sup>-1</sup> (see Table I), which is reasonably consistent with the values of 40–56 mV dec<sup>-1</sup> reported by Matsumoto and Sato for sputtered and thermally prepared IrO<sub>2</sub>,<sup>39</sup> and with 40–45 mV dec<sup>-1</sup> reported by Reier et al.<sup>40</sup> for amorphous iridium oxide on a titanium substrate. In analogy to the quantification of the activity for the oxygen reduction reaction (ORR) in PEM fuel cells, where the activity of different catalysts is benchmarked at an iR-free cell voltage of 0.9 V, due to the negligible transport resistances at the low current densities at this voltage,<sup>41</sup> we here propose to quantify the activity of OER catalysts at an iR-free cell voltage of 1.45 V. At this potential, the current density is large enough to neglect the effect of



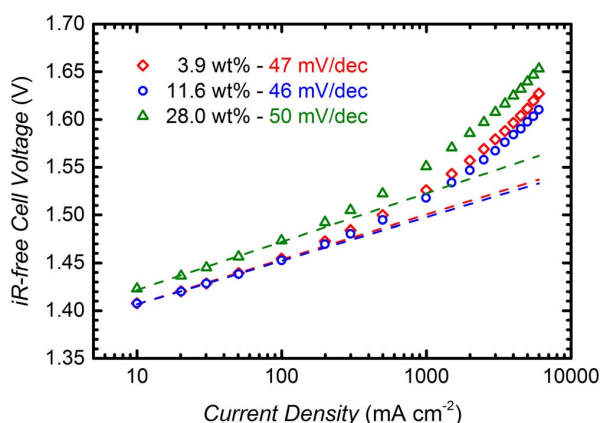


**Figure 7.** Ambient pressure Tafel plot of the  $iR$ -free voltage data from Fig. 4 ( $80^\circ\text{C}$ ,  $5 \text{ ml}_{\text{H}_2\text{O}} \text{ min}^{-1}$ ) for different anode ionomer loadings (in weight percent relative to total mass of electrode). The Tafel slope is obtained from a linear fit of the values between  $10$ – $100 \text{ mA cm}^{-2}$ . Anode and cathode catalyst loadings are  $0.35 \pm 0.05 \text{ mg}_{\text{Pt}} \text{ cm}_{\text{MEA}}^{-2}$  and  $2.00 \pm 0.25 \text{ mg}_{\text{Ir}} \text{ cm}_{\text{MEA}}^{-2}$ , respectively;  $\approx 50 \mu\text{m}$  thick Nafion 212 membrane.

ohmic shorting, but still small enough to largely exclude the influence of mass transport resistances. The respective values for the current density at  $1.45 \text{ V}_{iR\text{-free}}$  and for the mass-specific current densities (in units of  $\text{A g}_{\text{Ir}}^{-1}$ ) are given in Table I.

Considering that the anode and cathode catalyst loadings are essentially identical for the three MEAs shown in Fig. 7, one would expect a superposition of the Tafel lines in the kinetically controlled region, i.e., at low current densities. One explanation for the clearly higher value of  $\eta_{\text{OER}}$  for the MEA with an anode ionomer content of 28 wt% (s. green triangles in Fig. 7) might be a lower electrochemically active surface area (ECSA) compared to the other samples. For oxide based catalysts, the number of active sites available for the OER is typically related to the voltammetric charge  $q$  obtained from integration of a cyclic voltammogram (CV),<sup>42–44</sup> assuming that the number of active sites for the OER is proportional to the voltammetric charge. The CVs for the samples with 3.9, 11.6, and 28.0 wt% ionomer recorded at a scan rate of  $50 \text{ mV s}^{-1}$  are shown in Fig. 8, whereby the voltammetric current is normalized by the mass of iridium. Quite clearly, the voltammetric charge for the samples with 3.9 and 11.6 wt% ionomer is very similar, while it is significantly lower for an ionomer content of 28.0 wt%. The values of the mass normalized voltammetric charge or mass specific charge,  $q^*$ , obtained from an integration of the CVs between  $0.05$ – $1.00 \text{ V}$  are shown for all examined MEAs in the last column of Table I. The substantially lower mass specific capacity,  $q^*$ , of the MEA with 28 wt% ionomer ( $155 \text{ C g}_{\text{Ir}}^{-1}$ ; s. Table I) compared to the 3.9 and 11.6 wt% ionomer containing MEAs ( $294 \text{ C g}_{\text{Ir}}^{-1}$ ; s.

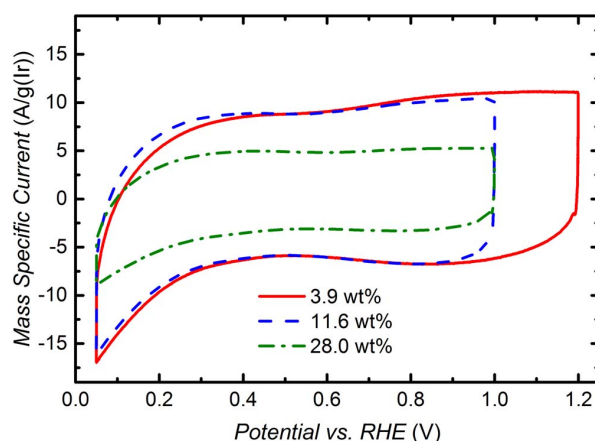


**Figure 8.** Ambient pressure cyclic voltammograms (CV) of  $\text{IrO}_2/\text{TiO}_2$  based anodes with different ionomer contents (in weight percent relative to total mass of electrode). The mass-specific current is plotted vs. the applied potential. CVs were recorded at a scan rate of  $50 \text{ mV/s}$  at  $80^\circ\text{C}$ .  $\text{H}_2\text{O}$  was supplied to the anode at  $5 \text{ ml}_{\text{H}_2\text{O}} \text{ min}^{-1}$ , and dry  $\text{H}_2$  was supplied to the cathode at  $\sim 50 \text{ ml min}^{-1}$ .

Table I) can only be explained by a lower catalyst utilization in the former electrode. This, we believe, is due to the electronic insulation of parts of the catalyst by the ionomer, which occurs when the electrode void volume approaches zero (s. green triangles in Fig. 3b). This is in agreement with the findings of Xu et al., who also observed a decrease in the mass specific capacity at high ionomer content.<sup>29</sup> Assuming that  $q^*$  is directly proportional to the active sites for the OER, the differences in  $\eta_{\text{OER}}$  in the Tafel region would be related to:

$$\Delta\eta_{\text{OER}} = b \cdot \log\left(\frac{q_1^*}{q_2^*}\right) \quad [10]$$

With a Tafel slope of  $b \approx 47 \text{ mV dec}^{-1}$  and the values for  $q_1^* = 294 \text{ C g}_{\text{Ir}}^{-1}$  and  $q_2^* = 155 \text{ C g}_{\text{Ir}}^{-1}$  for the MEAs with 11.6 wt% and 28.0 wt% ionomer, respectively, the predicted value for  $\Delta\eta_{\text{OER}}$  is  $\approx 13 \text{ mV}$ , which is in excellent agreement with the shift of the  $iR$ -free cell voltage observed in Fig. 7. Consequently, when normalizing the mass specific activity (evaluated at  $1.45 \text{ V}_{iR\text{-free}}$ ; s. Table I) of the  $\text{IrO}_2/\text{TiO}_2$  catalysts by their mass specific capacity, the resulting capacity normalized activity averaged over all MEAs is  $138 \pm 6 \text{ mA C}^{-1}$ , i.e., essentially identical for all MEAs tested here. In summary, part of the lower performance at high ionomer content is due to the electronic insulation of some of the catalyst particles by the ionomer. Therefore, the effect of ionomer void volume filling must be considered when conducting kinetic experiments.

**Table I.** Estimated values for the proton conduction sheet resistance of different anode electrodes,  $R_{\text{H}^+, \text{an}}$  (at  $80^\circ\text{C}$  in contact with liquid water), determined by Eq. 11 and assuming  $\tau = 0.7$ – $1.5$ ,  $\sigma = 142 \text{ mS cm}^{-1}$ , and using  $V_{\text{ion, wet}}$  from Fig. 3b. Furthermore, kinetic parameters and mass specific capacity for the  $\text{IrO}_2/\text{TiO}_2$  OER catalyst in MEAs with different ionomer content: i) geometric current density and mass specific current density (in  $\text{A g}_{\text{Ir}}^{-1}$ ) at an  $iR$ -free potential of  $1.45 \text{ V}$ ; ii) Tafel slope for the OER; and, iii) mass specific capacity ( $\text{C g}_{\text{Ir}}^{-1}$ ) determined by cyclic voltammetry between  $0.05$  and  $1.0 \text{ V}$ .

Ionomer Content (wt%)	$R_{\text{H}^+, \text{an}}$ ( $\text{m}\Omega \text{ cm}^2$ )	$I$ at $E_{iR\text{-free}} = 1.45 \text{ V}$		Tafel Slope ( $\text{mV dec}^{-1}$ )	CV Charge ( $\text{C g}_{\text{Ir}}^{-1}$ )
		( $\text{mA cm}^{-2}$ )	( $\text{A g}_{\text{Ir}}^{-1}$ )		
2.2	80–171	67.2	46.1	47	-
3.9	49–106	69.0	38.9	47	294
6.1	33–71	78.1	39.0	45	272
11.6	14–30	90.1	42.9	46	294
16.4	11–23	63.9	32.6	45	232
20.8	9–18	54.9	26.7	49	194
28.0	6–13	38.7	20.1	50	155

To quantify the overpotential due to proton transport in the anode, first the electrode sheet resistance for proton conduction has to be determined, which in principle can be calculated from:<sup>25</sup>

$$R_{\text{H}^+, \text{an}} = \frac{t_{\text{an}}}{\sigma \cdot V_{\text{ion, wet}}/\tau} \quad [11]$$

where  $t_{\text{an}}$  is the electrode thickness,  $\sigma$  is the conductivity of the ionomer,  $V_{\text{ion, wet}}$  is the ionomer volume fraction in the liquid water equilibrated electrode, and  $\tau$  is the apparent tortuosity of the ionomer phase in the electrode. The electrode thickness and ionomer volume fraction were determined from the cross-sectional SEM images as shown before (s. Fig. 3). The conductivity of the ionomer is assumed to be the same as that for the Nafion 212 membrane (142 mS cm<sup>-1</sup> at 80°C in contact with liquid water) because of the essentially identical equivalent weight (EW). The apparent tortuosity was determined previously for a Pt/C electrode and turned out to be between 0.7–1.5 for a temperature of 80°C and a relative humidity of 122%.<sup>27</sup> In a first approximation, we assume that the ionomer phase tortuosity of the IrO<sub>2</sub>/TiO<sub>2</sub> electrode is in the same range as that obtained for the Pt/C catalyst. The so calculated minimum and maximum values for  $R_{\text{H}^+, \text{an}}$  are shown in Table I.

From the estimated sheet resistances for proton conduction,  $R_{\text{H}^+, \text{an}}$  (s. Table I), the effective proton conduction resistance in the anode electrode,  $R_{\text{H}^+, \text{an}}^{\text{eff}}$ , can be calculated from:<sup>45</sup>

$$R_{\text{H}^+, \text{an}}^{\text{eff}} = \frac{R_{\text{H}^+, \text{an}}}{3 + \zeta} \quad [12]$$

where  $\zeta$  is a correction factor which accounts for the effect of a reduced catalyst utilization, and which is a function of the dimensionless ratio of the proton conduction sheet resistance over the kinetic resistance:<sup>45</sup>

$$\frac{i \cdot R_{\text{H}^+, \text{an}}}{b} \quad [13]$$

where  $i$  is the current density,  $R_{\text{H}^+, \text{an}}$  the proton transport resistance and  $b$  the Tafel slope.

From the above analysis, it is now possible to quantify all of the voltage loss terms on the right-hand side of Eq. 3, with the exception of the mass transport term,  $\eta_{\text{mt}}$  (last term on the right-hand side of Eq. 3). The magnitude of the latter can be estimated by subtracting all the known voltage loss terms from the reversible cell voltage, as will be shown in the following section.

**Discussion of additional voltage losses.**—The fraction of the total overpotential which is not due to ohmic (determined by the HFR) and OER kinetic losses (the HER kinetic losses are only on the order of 1 mV; see above) can be determined from the difference between the Tafel line (s. dashed lines in Fig. 7) and the  $iR$ -free cell voltage (s. Fig. 4b). This remaining overpotential for the samples with 3.9, 11.6 and 28.0 wt% ionomer is plotted in Fig. 9 (red diamonds), along with the voltage loss contributions from proton conduction resistance in the anode and cathode electrodes. The additional undefined mass transport losses remaining after the subtraction of the proton conduction related voltage losses in the cathode electrode (green areas in Fig. 9) and in the anode electrode (blue areas in Fig. 9) are visualized by the red area in Fig. 9.

Let us first examine the analysis for the MEA with the anode electrode with a low ionomer content of 3.9 wt% shown in Fig. 9a. For this MEA, the anode void volume is  $\approx 65\%$  (s. Fig. 3b), so that one would expect little voltage losses due to O<sub>2</sub> and H<sub>2</sub>O transport resistances. This can be examined by summing up the contributions from the proton conduction induced voltage losses in the cathode (green area in Fig. 9a) and in the anode (blue area in Fig. 9a), whereby the uncertainty in the latter is indicated by the blue dashed lines in Fig. 9a. Indeed, as expected, the unassigned voltage losses range between only  $\approx 5$  and  $\approx 20$  mV at 3 A cm<sup>-2</sup>, as is indicated by the voltage difference between the blue dashed lines and the red line in Fig. 9a. As we will explain in the next section, these losses are likely due to an overpotential caused by the pressure buildup of gaseous

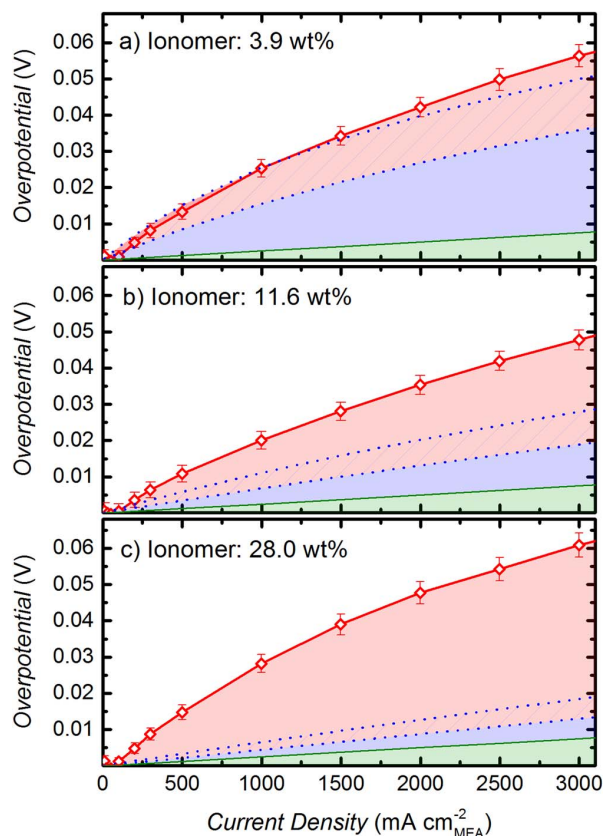


**Figure 9.** Remaining overpotential after subtraction of ohmic and kinetic losses for three MEAs with different ionomer content (red diamonds and red line) for polarization curves obtained at 80°C and ambient pressure (data from Figs. 4 and 7). The overpotential due to proton conduction resistance on the cathode is represented by the green area, corresponding to 2.5 mΩ cm<sup>2</sup> (s. text). The overpotential due to proton conduction resistance on the anode is represented by the blue area, whereby the dotted blue lines give the lower and upper limit for  $R_{\text{H}^+, \text{an}}^{\text{eff}}$ , determined from Eq. 12 and using the  $R_{\text{H}^+, \text{an}}$  values given in Table I.

hydrogen in the cathode electrode, which we estimate to be on the order of  $\approx 20$  mV at 3 A cm<sup>-2</sup>.

For the MEA with the optimum ionomer content of 11.6 wt% in the anode, the unassigned voltage losses at 3 A cm<sup>-2</sup> range from  $\approx 20$  to  $\approx 30$  mV (s. difference between the blue dashed lines and the red line in Fig. 9b). For this MEA, the void volume in the electrode ( $\approx 35\%$ , s. Fig. 3b) is only roughly one half of that the above discussed MEA with an ionomer content of 3.9 wt%, so that an additional O<sub>2</sub> and/or H<sub>2</sub>O transport resistance induced voltage loss of  $\approx 10$ –15 mV seems reasonable.

Finally, the unassigned voltage losses for the MEA with 28.0 wt% ionomer in the anode electrode range between  $\approx 40$ –45 mV at 3 A cm<sup>-2</sup> (s. difference between the blue dashed lines and the red line in Fig. 9c). While approximately 20 mV may be caused by the above mentioned additional losses at the cathode, we believe that the remaining losses are largely due to oxygen transport resistances originating from the strong diffusion barrier imposed by a completely ionomer filled anode electrode (s. Fig. 3b). In this case it is conceivable that the local O<sub>2</sub> pressure at the electrode increases, which in turn would increase the reversible cell potential according to the Nernst Equation by  $\Delta E_{\text{rev}}$ , equating to a mass transport induced overpotential,  $\eta_{\text{mt}}$ :

$$\eta_{\text{mt}} = \Delta E_{\text{rev}} = \frac{RT}{4F} \ln \left[ \frac{p_{\text{O}_2, \text{cat}}}{p_{\text{O}_2, \text{channel}}} \right] \quad [14]$$



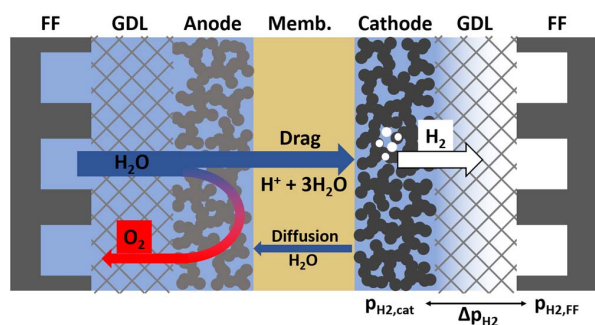


**Figure 10.** Scheme illustrating the H<sub>2</sub>O transport mechanisms in an electrolyzer. H<sub>2</sub>O is supplied to the anode catalyst layer and partly consumed by the H<sub>2</sub>O electrolysis reaction. Additionally, H<sub>2</sub>O is transported through the membrane to the cathode catalyst layer by electro-osmotic drag and expelled into the cathode flow-field by the evolving hydrogen gas and/or returned to the anode by pressure-driven back-diffusion through the membrane back to the anode. The partial pressure of O<sub>2</sub> and H<sub>2</sub> inside the electrodes is expected to be higher than the gas pressure in the flow-field.

where  $p_{O_2,cat}$  and  $p_{O_2,channel}$  are the partial pressures of O<sub>2</sub> in the electrode and in the flow-field channel, respectively. For a perfectly crack-free ionomer filling of the anode electrode, the produced O<sub>2</sub> must be removed by permeation through the ionomer phase. The required O<sub>2</sub> partial pressure in the catalyst layer,  $p_{O_2,cat}$ , to support O<sub>2</sub> permeation at a rate equivalent to the O<sub>2</sub> generation rate can then be calculated by:<sup>46</sup>

$$\Delta p = p_{O_2,cat} - p_{O_2,channel} = \frac{t_{eff} \cdot \Phi_{O_2}}{K_{O_2}} \quad [15]$$

where  $t_{eff}$  is the effective permeation path,  $\Phi_{O_2}$  represents the oxygen generation rate (i.e.,  $\Phi_{O_2} = \frac{i}{4F}$ ), and  $K_{O_2}$  is the permeability of O<sub>2</sub> in the Nafion ionomer. As a first approximation,  $t_{eff}$  is assumed to be half of the anode electrode thickness (i.e.  $t_{eff} = \frac{t_{an}}{2}$ ). For  $K_{O_2}$ , a value of  $2 \cdot 10^{-13} \frac{\text{mol cm}}{\text{s cm}^2 \text{ kPa}}$  is estimated for our electrode, based on the permeability of Nafion 212 at the given operating conditions (80°C, liquid water).<sup>46</sup> With these parameters, a pressure gradient  $\Delta p$  of up to  $\approx 200$  bar would be required at 3 A cm<sup>-2</sup>, resulting in an overpotential  $\eta_{mt}$  of  $\approx 45$  mV (based on Eq. 14, with 0.53 bar<sub>a</sub> O<sub>2</sub> in the flow-field channel at ambient pressure and 80°C). On the other hand, the expected loss due to an O<sub>2</sub> partial pressure gradient is more on the order of  $\approx 20$ –25 mV (s. above), which would correspond to a much lower value of  $\Delta p \approx 10$  bar. For this reason, we believe that the main path for oxygen removal from the electrode is not permeation but convective transport through cracks or pinholes in the ionomer layer within the electrode, even for electrodes with nominally zero void volume.

Mass transport on the H<sub>2</sub> side could play a role for all MEAs in the case of water flooding of the cathode catalyst layer, as illustrated in Fig. 10. At high current densities, the transport of H<sub>2</sub>O to the cathode by electro-osmotic drag can become quite significant, with drag coefficients under electrolyzer operating conditions in the range of 2.5–3.2.<sup>47</sup> The H<sub>2</sub>O dragged to the cathode will be removed by a combination of pressure-driven back-diffusion through the membrane to the anode and water expulsion into the cathode flow-field by the evolving H<sub>2</sub> gas. If the contact angle inside the cathode catalyst layer is  $< 90^\circ$  (i.e., if the cathode electrode is hydrophilic), the H<sub>2</sub> pressure inside the cathode electrode must reach the capillary pressure,  $p_{cap}$ , in order to push the water out of the electrode pores. The capillary pressure can be estimated by:

$$p_{cap} = \frac{2\gamma_{H_2O} \cos \theta}{r_{cap}} \quad [16]$$

with the surface tension of water  $\gamma_{H_2O}$ , the capillary radius  $r_{cap}$ , and the water contact angle in the electrode  $\theta$ . The surface tension of

water,  $\gamma_{H_2O}$ , at 80°C is 0.0626 N m<sup>-1</sup>, and  $r_{cap}$  is  $\approx 25$  nm for an average pore diameter in the cathode catalyst layer of  $\approx 50$  nm.<sup>31</sup> With these values, the capillary pressure  $p_{cap}$  would range from 0–25 bar for contact angles ranging from 90 to 0° (at contact angles  $> 90^\circ$ , no H<sub>2</sub> pressure buildup would be required for the expulsion of water from the cathode electrode). Unfortunately, the exact value for  $\theta$  is difficult to measure, as the contact angle of membranes and ionomer bonded electrodes depends on the hydration state and the history of the electrode. Yu et al. investigated the contact angle of membranes and of catalyst layers composed of Pt/C and ionomer by the sessile drop method and by environmental scanning electron microscopy.<sup>48</sup> For a Nafion membrane they observed a decrease of the contact angle from initially 93.9° to 87.8° after extended contact with liquid water. For the catalyst layer of new MEAs, they found contact angles of  $\approx 145^\circ$ , while it decreased to 33–98° for aged catalyst layers, most likely due to the gradual oxidation of the carbon support surface. We believe that the actual contact angle of conditioned and water soaked cathode electrodes is likely equal to the contact angle of the ionomer (i.e., of the Nafion membrane), which would suggest a contact angle of  $\approx 87.8^\circ$ , equating to a capillary pressure of  $p_{cap} \approx 2$  bar<sub>a</sub>. Further insights on this can be gained by the following analysis of the electrolyzer performance versus hydrogen pressure under differential pressure conditions (i.e., the anode compartment remaining at ambient pressure).

**High pressure electrolysis.**—Since only the H<sub>2</sub> side of the cell is pressurized, the activities of H<sub>2</sub>O and O<sub>2</sub> are not affected by the high pressure operation on the H<sub>2</sub> side. Consequently, the shift of the reversible cell voltage  $\Delta E_{rev}$  compared to ambient pressure operation ( $p_{H_2} = 0.53$  bar<sub>a</sub>) can be calculated by:

$$\Delta E_{rev} = \frac{RT}{2F} \ln \left[ \frac{p_{H_2}}{0.53 \text{ bar}_a} \right] \quad [17]$$

For the maximum cathode pressure  $p_{cath} = 30$  bar<sub>a</sub> ( $p_{H_2} = 29.53$  bar<sub>a</sub>), the cell voltage should be shifted by  $\Delta E_{rev} = 60.9$  mV at 80°C. In Fig. 11, the iR-free cell voltages are plotted for the measurements at a cathode pressure between 1–30 bar<sub>a</sub>. The curves were corrected by  $\Delta E_{rev}$  to exclude the pressure induced shift of the reversible cell voltage from the analysis. Assuming that  $\Delta E_{rev}$  is the only factor influencing the performance, the curves should lie on top of each other. For current densities of  $\approx 200$  mA cm<sup>-2</sup> this is in fact the case. At smaller current densities, the pressure fluctuated due to the low gas flow, which can explain some fluctuations of the cell voltages. In general, however, in this current range the cell voltage at high pressure seems to be slightly lower than expected. This can be explained by the H<sub>2</sub> crossover through the membrane. For a H<sub>2</sub> permeability of  $3 \cdot 10^{-9} \frac{\text{mol m}}{\text{m}^2 \text{ s bar}}$ ,<sup>49</sup> the H<sub>2</sub> crossover current at a cathode pressure of 30 bar<sub>a</sub> is  $\approx 30$  mA cm<sup>-2</sup>. Consequently, for small current densities, the H<sub>2</sub> flux to the anode is in the range of the O<sub>2</sub> production. Since H<sub>2</sub> does not react with O<sub>2</sub> at the anode but accumulates,<sup>50</sup> its presence effectively lowers the O<sub>2</sub> partial pressure at the anode, which leads to a reduction of  $E_{rev}$  according to Eq. 4. This, of course, is an undesirable operating condition, as significant concentrations of H<sub>2</sub> build up in the O<sub>2</sub> compartment.

While the dilution effect of crossover H<sub>2</sub> becomes negligible at current densities of  $> 300$  mA cm<sup>-2</sup>, the cell voltage for high pressure operation gets increasingly lower than expected from  $\Delta E_{rev}$ , i.e., the electrolyzer performance at high pressure actually improves when corrected for  $\Delta E_{rev}$  (s. black squares at 30 bar<sub>a</sub> vs. red diamonds at 1 bar<sub>a</sub> in Fig. 11). This can be seen more clearly in the inset of Fig. 11, which shows the difference between the  $\Delta E_{rev}$ -corrected voltage at any given pressure referenced to that at 30 bar<sub>a</sub>, clearly indicating a maximum improvement of  $\approx 20$  mV at 3 A cm<sup>-2</sup> when raising the H<sub>2</sub> pressure from 1 to 30 bar<sub>a</sub>. Therefore, high pressure operation of the H<sub>2</sub> cathode must result in a reduction of one of the voltage loss terms. A similar phenomenon has been observed in other studies and was ascribed to a reduction of the size of produced gas bubbles at high pressure<sup>5,6</sup> or to improved OER kinetics, inferred from a lower

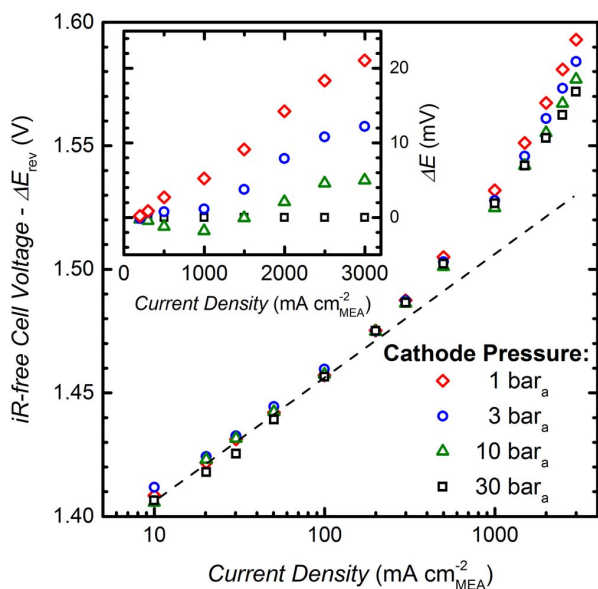


**Figure 11.** IR-free cell voltages corrected by  $\Delta E_{\text{rev}}$  (s. Eq. 17) for measurements at a total cathode pressure ranging from 1 to 30 bar<sub>a</sub> (80°C, 5 ml<sub>H<sub>2</sub>O</sub> min<sup>-1</sup>). The black dashed line indicates the average Tafel slope for all measurements ( $\approx 50$  mV dec<sup>-1</sup>). The inset shows the difference between the data at any given pressure and the data at 30 bar<sub>a</sub>, i.e.  $\Delta E \equiv (E_{\text{iR-free}} - \Delta E_{\text{rev}})_{\text{X bar}_a} - (E_{\text{iR-free}} - \Delta E_{\text{rev}})_{30 \text{ bar}_a}$ . Anode and cathode catalyst loadings are  $0.35 \pm 0.05$  mg<sub>Pt</sub> cm<sub>MEA</sub><sup>-2</sup> and  $2.00 \pm 0.25$  mg<sub>Ir</sub> cm<sub>MEA</sub><sup>-2</sup>, respectively; the anode ionomer content is 11.6 wt%;  $\approx 50$   $\mu\text{m}$  thick Nafion 212 membrane.

apparent Tafel slope at high pressure.<sup>3</sup> However, in these studies the O<sub>2</sub> side of the cell was also pressurized (balanced pressure), in contrast to the experiments in our study which were carried out at differential pressure conditions. Consequently, in our measurements, the OER kinetics and the O<sub>2</sub> mass transport should not change, suggesting that high H<sub>2</sub> pressure must affect some so far not addressed voltage loss on the H<sub>2</sub> side of the electrolysis cell. We believe that its most likely origin is a mass transport overpotential on the cathode caused by an increased partial pressure of H<sub>2</sub> in the cathode catalyst layer,  $p_{\text{H}_2, \text{cat}}$ . This is illustrated by assuming a difference in H<sub>2</sub> partial pressure between the cathode catalyst layer and the flow-field channel of  $p_{\text{H}_2, \text{cat}} - p_{\text{H}_2, \text{channel}} \approx 2$  bar<sub>a</sub>, similar to the capillary pressure  $p_{\text{cap}} \approx 2$  bar<sub>a</sub> calculated by Eq. 16 with a contact angle of 87.8° and an average pore radius of 25 nm. The corresponding mass transport overpotential at pressures of either 1 or 30 bar<sub>a</sub> in the H<sub>2</sub> flow-field would be:

$$\eta_{\text{mt}}(p_{\text{cath}} = 1 \text{ bar}_a) = \frac{RT}{2F} \ln \left[ \frac{2.53 \text{ bar}_a}{0.53 \text{ bar}_a} \right] = 24 \text{ mV} \quad [18]$$

$$\eta_{\text{mt}}(p_{\text{cath}} = 30 \text{ bar}_a) = \frac{RT}{2F} \ln \left[ \frac{31.53 \text{ bar}_a}{29.53 \text{ bar}_a} \right] = 1 \text{ mV} \quad [19]$$

From this exemplary calculation it becomes clear that the overpotential due to H<sub>2</sub> mass transport would be much larger at ambient pressure than at high pressure if the contact angle in the cathode electrode is  $< 90^\circ$ . The above estimated decrease of  $\eta_{\text{mt}}$  with increasing pressure would be expected to be most pronounced at high current densities, where a possible bypass of hydrogen through partially flooded pores would become more unlikely, thus leading to a gradual increase of the difference between the 1 and 30 bar<sub>a</sub> voltage shown in the inset of Fig. 11. The overall difference of  $\approx 20$  mV at 3 A cm<sup>-2</sup> (s. inset of Fig. 11), which is clearly caused by the hydrogen cathode performance corresponds, we believe, to the unassigned mass transport losses in Fig. 9a and to a large extent to those in Fig. 9b.

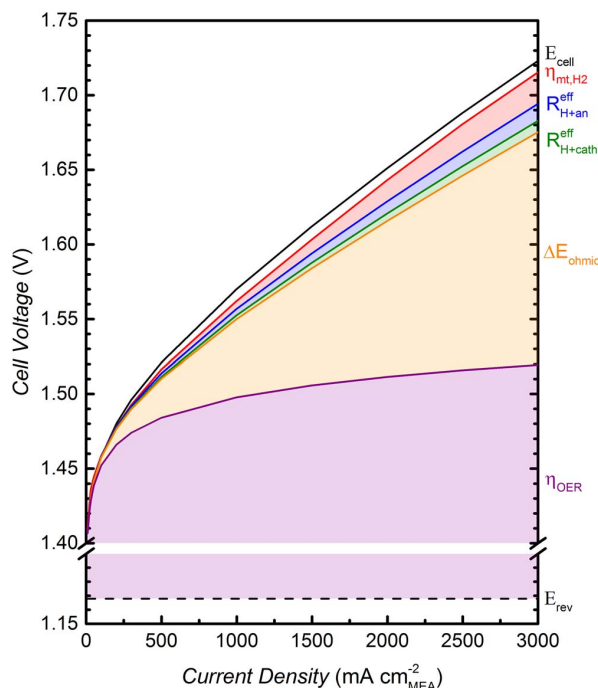


**Figure 12.** Contributions of various voltage losses to overall cell voltage. The reversible cell voltage is given by the dashed black line and the purple area represents the OER kinetic losses (y-axis is intercepted between 1.2 V and 1.4 V for better visualization of other losses). Ohmic losses are given by the orange area, and losses due to proton conduction resistance in the cathode and anode electrodes are shown by the green and blue areas, respectively. The red area represents the losses due to H<sub>2</sub> mass transport and the full black line gives the cell voltage measured at ambient pressure (80°C, 5 ml<sub>H<sub>2</sub>O</sub> min<sup>-1</sup>). Anode and cathode catalyst loadings are  $0.35 \pm 0.05$  mg<sub>Pt</sub> cm<sub>MEA</sub><sup>-2</sup> and  $2.00 \pm 0.25$  mg<sub>Ir</sub> cm<sub>MEA</sub><sup>-2</sup>, respectively; the anode ionomer content is 11.6 wt%;  $\approx 50$   $\mu\text{m}$  thick Nafion 212 membrane.

A summary of the contributions of the various voltage losses to the overall cell voltage is given in Fig. 12. For the MEA with the optimum ionomer content of 11.6 wt% in the anode. The highest overpotentials are due to the OER kinetic losses determined by a Tafel analysis, which account for  $\approx 350$  mV at 3 A cm<sup>-2</sup> (s. purple area in Fig. 12) and the ohmic losses calculated from the HFR, which account for  $\approx 155$  mV at 3 A cm<sup>-2</sup> (s. orange area in Fig. 12). The losses due to proton conduction resistance in the cathode and anode electrodes add up to  $\approx 20$  mV at 3 A cm<sup>-2</sup> (s. green and blue area in Fig. 12). For the calculation of the proton conduction resistance in the anode electrode the lower limit of  $R_{\text{H}^+, \text{an}}^{\text{eff}}$  is used (s. Fig. 9). The overpotential for H<sub>2</sub> mass transport is calculated from the difference between the data at 1 bar<sub>a</sub> and the data at 30 bar<sub>a</sub> as shown in the inset in Fig. 11, which results in  $\approx 20$  mV at 3 A cm<sup>-2</sup>. The remaining losses account for less than 10 mV at 3 A cm<sup>-2</sup> and can likely be attributed to O<sub>2</sub> mass transport.

## Conclusions

In this study, we present a new small-scale single-cell electrolyzer cell design for differential pressure operation up to 30 bar, showing state-of-the-art performance. The influence of the ionomer content in the oxygen electrode based on a TiO<sub>2</sub>-supported IrO<sub>2</sub> catalyst ( $\approx 2.0$  mg<sub>Ir</sub> cm<sup>-2</sup>) was analyzed, and an optimum of the electrolysis performance was found at an ionomer content of 11.6 wt%, corresponding to an electrode void volume fraction of  $\approx 35\%$  and a wet-ionomer volume fraction of also  $\approx 35\%$ .

Below the optimum ionomer content, the performance decreases, which can be related largely to voltage losses due to an increasingly limiting proton conductivity in the anode electrode. On the other hand, above the optimum ionomer content, the void volume filling of the anode by ionomer (equilibrated with liquid water) leads to additional overpotentials from O<sub>2</sub> gas transport from the electrode to the flow-field channel, to an increase of the electronic contact resistance due to an ionomer film buildup at the anode electrode / porous transport layer interface, and to the electronic insulation of a fraction of the catalyst by the ionomer.

This was demonstrated by deconvoluting the overall voltage losses into: i) ohmic losses (quantified by the high-frequency resistance); ii) kinetic losses for the oxygen evolution reaction (OER) quantified by a Tafel analysis; and, iii) proton conduction losses in the anode and cathode electrodes. The kinetic losses for the hydrogen evolution reaction (HER) were shown to be negligible on the carbon-supported Pt cathode ( $\approx 0.35 \text{ mg}_{\text{Pt}}/\text{cm}^2$ ). The extent of residual mass transport losses was determined by the difference between the reversible cell voltage corrected for the above described voltage losses and the measured electrolyzer voltage. For the optimum anode composition, a smaller fraction of the thus quantified transport losses ( $< 30 \text{ mV}$  at  $3 \text{ A cm}^{-2}$ ) is due to O<sub>2</sub> transport in the anode electrode, while a larger fraction is due to additional voltage losses at the H<sub>2</sub> cathode (i.e., beyond negligible HER kinetic losses and minor losses due to proton conduction resistance in the cathode).

The origin of the latter was revealed by analyzing the electrolyzer performance as a function of hydrogen pressure, while keeping the anode at ambient pressure (i.e., differential pressure operation). While one would expect the increase in electrolyzer potential with increasing hydrogen pressure to follow the Nernstian potential shift, the observed increase in electrolyzer potential was actually lower, i.e., the performance at high hydrogen pressure was better than predicted by the Nernst equation. Our analysis suggests that this is due to a substantial hydrogen pressure gradient between the cathode electrode and the flow-field channel, caused by the capillary pressure of water in a slightly hydrophilic cathode electrode and resulting in a hydrogen mass transport overpotential.

### Acknowledgments

This work was funded by the Bavarian Ministry of Economic Affairs and Media, Energy and Technology through the project ZAE-ST (storage technologies). Seed-funding by the Bavarian State Ministry of Education and Culture, Science and Art through TUM's Munich School of Engineering in the framework of the "Energy Valley Bavaria" project is gratefully acknowledged. We thank Courtney Mittelsteadt (Giner Inc., Boston, USA) for the insight into electrolyzer testing, Marcel Schmidt and Marc Schönberger (TUM chemistry department workshop) as well as Svetoslav Koynov (Walther-Schottky-Institut, TUM) for their help with the cell design, Maximilian Möckl for the inspiring discussions, and Thomas Mittermeier, Armin Siebel and Yelena Gorlin for reviewing the paper. The electron microscopy was accomplished at the WACKER-Chair of Molecular Chemistry of the TUM with the assistance of Katia Rodewald.

### References

1. K. E. Ayers, E. B. Anderson, C. B. Capuano, B. D. Carter, L. T. Dalton, G. Hanlon, J. Manco, and M. Niedzwiecki, *ECS Trans.*, **33**(1), 3 (2010).
2. M. Carmo, D. L. Fritz, J. Mergel, and D. Stolten, *Int. J. Hydrogen Energy*, **38**, 4901 (2013).
3. M. Suermann, T. J. Schmidt, and F. N. Büchi, *ECS Trans.*, **69**(17), 1141 (2015).
4. K. A. Lewinski, D. F. van der Vliet, and S. M. Luopa, *ECS Trans.*, **69**(17), 893 (2015).
5. S. A. Grigoriev, P. Millet, S. V. Korobtsev, V. I. Porembkiy, M. Pepic, C. Etievant, C. Puyenchet, and V. N. Fateev, *Int. J. Hydrogen Energy*, **34**, 5986 (2009).
6. S. A. Grigoriev, V. I. Porembkiy, S. V. Korobtsev, V. N. Fateev, F. Auprêtre, and P. Millet, *Int. J. Hydrogen Energy*, **36**, 2721 (2011).
7. F. Marangio, M. Pagani, M. Santarelli, and M. Cali, *Int. J. Hydrogen Energy*, **36**, 7807 (2011).
8. B. Bensmann, R. Hanke-Rauschenbach, I. K. Peña Arias, and K. Sundmacher, *Electrochim. Acta*, **110**, 570 (2013).
9. C. K. Mittelsteadt, *ECS Trans.*, **69**(17), 205 (2015).
10. K. C. Neyerlin, W. Gu, J. Jorne, and H. A. Gasteiger, *J. Electrochem. Soc.*, **154**, B631 (2007).
11. J. Durst, A. Siebel, C. Simon, F. Hasche, J. Herranz, and H. A. Gasteiger, *Energy Environ. Sci.*, **7**, 2255 (2014).
12. J. Durst, C. Simon, F. Hasche, and H. A. Gasteiger, *J. Electrochem. Soc.*, **162**, F190 (2015).
13. W. Sheng, H. A. Gasteiger, and Y. Shao-Horn, *J. Electrochem. Soc.*, **157**, B1529 (2010).
14. E. Fabbri, A. Haberer, K. Waltar, R. Kötz, and T. J. Schmidt, *Catal. Sci. Tech.*, **4**, 3800 (2014).
15. L. Ma, S. Sui, and Y. Zhai, *Int. J. Hydrogen Energy*, **34**, 678 (2009).
16. J. Polonský, P. Mazúr, M. Paidar, E. Christensen, and K. Bouzek, *Int. J. Hydrogen Energy*, **39**, 3072 (2014).
17. P. Mazúr, J. Polonský, M. Paidar, and K. Bouzek, *Int. J. Hydrogen Energy*, **37**, 12081 (2012).
18. C. Rozain, E. Mayousse, N. Guillet, and P. Millet, *Appl. Catal. B Environ.*, **182**, 123 (2016).
19. K. S. Kadakia, P. H. Jampani, O. I. Velikokhatnyi, M. K. Datta, S. K. Park, D. H. Hong, S. J. Chung, and P. N. Kumta, *J. Power Sources*, **269**, 855 (2014).
20. S. Siracusano, N. Van Dijk, E. Payne-Johnson, V. Baglio, and A. S. Arico, *Appl. Catal. B Environ.*, **164**, 488 (2015).
21. A. Marshall, S. Sunde, M. Tsyppkin, and R. Tunold, *Int. J. Hydrogen Energy*, **32**, 2320 (2007).
22. H. Y. Jung, S. Y. Huang, P. Ganesan, and B. N. Popov, *J. Power Sources*, **194**, 972 (2009).
23. M. Langemann, D. L. Fritz, M. Mu, and D. Stolten, *Int. J. Hydrogen Energy*, **40**, 11385 (2015).
24. C. Boyer, S. Gambaureze, O. Velev, S. Srinivasan, and A. J. Appleby, *Electrochim. Acta*, **43**, 3703 (1998).
25. Y. Liu, M. W. Murphy, D. R. Baker, W. Gu, C. Ji, J. Jorne, and H. A. Gasteiger, *J. Electrochem. Soc.*, **156**, B970 (2009).
26. Y. Liu, C. Ji, W. Gu, D. R. Baker, J. Jorne, and H. A. Gasteiger, *J. Electrochem. Soc.*, **157**, B1154 (2010).
27. Y. Liu, C. Ji, W. Gu, J. Jorne, and H. A. Gasteiger, *J. Electrochem. Soc.*, **158**, B614 (2011).
28. L. Ma, S. Sui, and Y. Zhai, *Int. J. Hydrogen Energy*, **34**, 678 (2009).
29. W. Xu and K. Scott, *Int. J. Hydrogen Energy*, **35**, 12029 (2010).
30. G. Alberti, R. Narducci, and M. Sganappa, *J. Power Sources*, **178**, 575 (2008).
31. W. Gu, D. R. Baker, Y. Liu, and H. A. Gasteiger, in *Handbook of Fuel Cells*, Vol. 6, W. Vielstich, H. A. Gasteiger, and H. Yokokama, Editors, p. 631, Chap. 43, John Wiley & Sons, Chichester, UK (2009).
32. T. A. Zawodzinski, T. E. Springer, J. Davey, R. Jester, C. Lopez, J. Valeria, and S. Gottesfeld, *J. Electrochem. Soc.*, **140**, 1981 (1993).
33. K. Scott, W. Taama, and J. Cruickshank, *J. Power Sources*, **65**, 159 (1997).
34. R. W. Kopitzke, C. A. Linkous, H. R. Anderson, and G. L. Nelson, *J. Electrochem. Soc.*, **147**, 1677 (2000).
35. F. Marangio, M. Santarelli, and M. Cali, *Int. J. Hydrogen Energy*, **34**, 1143 (2009).
36. H. Ito, T. Maeda, A. Nakano, and H. Takenaka, *Int. J. Hydrogen Energy*, **36**, 10527 (2011).
37. C. K. Mittelsteadt and H. Liu, in *Handbook of Fuel Cells*, Vol. 5, W. Vielstich, H. A. Gasteiger, and H. Yokokama, Editors, p. 345, Chap. 23, John Wiley & Sons, Chichester, UK (2009).
38. S. G. Bratsch, *J. Phys. Chem. Ref. Data*, **18**, 1 (1989).
39. Y. Matsumoto and E. Sato, *Mater. Chem. Phys.*, **14**, 397 (1986).
40. T. Reier, D. Teschner, T. Lunkenbein, A. Bergmann, S. Selve, R. Kraehnert, R. Schlögl, and P. Strasser, *J. Electrochem. Soc.*, **161**, F876 (2014).
41. H. A. Gasteiger, S. S. Kocha, B. Sompalli, and F. T. Wagner, *Appl. Catal. B Environ.*, **56**, 9 (2005).
42. G. Lodi, E. Sivieri, A. Debattisti, and S. Trasatti, *J. Appl. Electrochem.*, **8**, 135 (1978).
43. S. Ardizzone, G. Fregonara, and S. Trasatti, *Electrochim. Acta*, **35**, 263 (1990).
44. C. Rozain, E. Mayousse, N. Guillet, and P. Millet, *Appl. Catal. B Environ.*, **182**, 153 (2016).
45. K. C. Neyerlin, W. Gu, J. Jorne, A. Clark, and H. A. Gasteiger, *J. Electrochem. Soc.*, **154**, B279 (2007).
46. J. Zhang, H. A. Gasteiger, and W. Gu, *J. Electrochem. Soc.*, **160**, F616 (2013).
47. M. Doyle and G. Rajendran, in *Handbook of Fuel Cells: Fundamentals, Technology, and Applications*, Vol. 3, W. Vielstich, A. Lamm, and H. A. Gasteiger, Editors, Chap. 34, p. 18, John Wiley & Sons, New York (2003).
48. H. M. Yu, C. Ziegler, M. Oszcipok, M. Zobel, and C. Hebling, *Electrochim. Acta*, **51**, 1199 (2006).
49. B. Bensmann, R. Hanke-Rauschenbach, and K. Sundmacher, *Int. J. Hydrogen Energy*, **39**, 49 (2014).
50. M. Schalenbach, M. Carmo, D. L. Fritz, J. Mergel, and D. Stolten, *Int. J. Hydrogen Energy*, **38**, 14921 (2013).



## 4.2 Analysis of Voltage Losses in PEM Water Electrolyzers with Low Platinum Group Metal Loadings

In this section the article "Analysis of Voltage Losses in PEM Water Electrolyzers with Low Platinum Group Metal Loadings"<sup>[158]</sup> is presented, which was submitted in January 2018 and accepted for publication in *The Journal of the Electrochemical Society* in March 2018 as an open access article, distributed under the terms of the Creative Commons Attribution 4.0 License (CC BY). This paper was presented by Maximilian Bernt at the 231<sup>st</sup> Meeting of The Electrochemical Society (May 2017) in New Orleans, USA (abstract number: # I01-1382). The permanent web link to the article is <http://jes.ecsdl.org/content/165/5/F305>.

In this study, we investigate the influence of catalyst loading on the performance of a PEM-WE using commercial Pt/C catalysts for the HER and IrO<sub>2</sub>/TiO<sub>2</sub> for the OER in MEAs based on a 50 μm Nafion<sup>®</sup> 212 membrane. The loading on the cathode can be reduced from 0.30 mg<sub>Pt</sub> cm<sup>-2</sup> to 0.025 mg<sub>Pt</sub> cm<sup>-2</sup> without any negative impact on performance, due to the fast reaction kinetics of the HER. On the anode, the Ir loading was varied between 0.20-5.41 mg<sub>Ir</sub> cm<sup>-2</sup> and an optimum in performance at operational current densities ( $\geq 1$  A cm<sup>-2</sup>) was found for a catalyst loading of 1-2 mg<sub>Ir</sub> cm<sup>-2</sup>, corresponding to an electrode thickness of  $\approx 4-8$  μm. For higher catalyst loadings ( $> 2$  mg<sub>Ir</sub> cm<sup>-2</sup>, electrode thickness  $> 10$  μm) a slightly lower kinetic overpotential for the OER is obtained, however, cell voltage and HFR increase at high current densities. This is attributed to a water transport resistance through the thicker catalyst layer, resulting in a reduced water content at the membrane/anode interface and, consequently, a lower membrane conductivity. On the other hand, catalyst loadings  $< 0.5$  mg<sub>Ir</sub> cm<sup>-2</sup> lead to very thin ( $< 2$  μm) and, consequently, inhomogeneous catalyst layers with a poor electrical in-plane conductivity. In combination with the coarse structure of the Ti PTL this leads to a poor anode catalyst utilization and an associated higher HFR. We demonstrate that this effect can be mitigated by incorporating a PTL modified with a microporous layer.

Finally, the impact of these results regarding possible Ir-supply constraints for a large-scale application of PEM electrolysis is discussed. It is shown that with the commercial IrO<sub>2</sub>/TiO<sub>2</sub> catalyst used in this study the target value for the Ir-specific

power density of  $0.01 \text{ g}_{\text{Ir}} \text{ kW}^{-1}$  at a voltage efficiency of  $70\%_{\text{LHV}}$  cannot be reached due to performance losses at low catalyst loadings or, more precisely, for thin electrodes. This emphasizes the need to develop catalyst materials with a reduced packing density, so that electrodes with a sufficient thickness ( $\approx 4\text{-}8 \mu\text{m}$ ) at Ir loadings of only  $\approx 0.05 \text{ mg}_{\text{Ir}} \text{ cm}^{-2}$  can be fabricated.

### **Author contributions**

M.B. fabricated membrane electrode assemblies, performed physical characterization as well as electrochemical testing, and evaluated experimental results. A.S. and M.B. wrote the manuscript. All authors discussed the experimental results and revised the manuscript.





## Analysis of Voltage Losses in PEM Water Electrolyzers with Low Platinum Group Metal Loadings

Maximilian Bernt,<sup>1,2,\*</sup> Armin Siebel,<sup>1,2,\*</sup> and Hubert A. Gasteiger<sup>2,\*\*</sup>

<sup>1</sup>Bayerisches Zentrum für angewandte Energieforschung, 85748 Garching, Germany

<sup>2</sup>Chair of Technical Electrochemistry, Department of Chemistry and Catalysis Research Center, Technical University of Munich, 85748 Garching, Germany

In this study, the influence of catalyst loading on the performance of a proton exchange membrane (PEM) water electrolyzer is investigated (Nafion 212 membrane; IrO<sub>2</sub>/TiO<sub>2</sub> (anode) and Pt/C (cathode)). Due to the fast kinetics of the hydrogen evolution reaction (HER) on platinum (Pt), the Pt loading on the cathode can be reduced from 0.30 mg<sub>Pt</sub> cm<sup>-2</sup> to 0.025 mg<sub>Pt</sub> cm<sup>-2</sup> without any negative effect on performance. On the anode, the iridium (Ir) loading was varied between 0.20–5.41 mg<sub>Ir</sub> cm<sup>-2</sup> and an optimum in performance at operational current densities ( $\geq 1$  A cm<sup>-2</sup>) was found for 1–2 mg<sub>Ir</sub> cm<sup>-2</sup>. At higher Ir loadings, the performance decreases at high current densities due to insufficient water transport through the catalyst layer whereas at Ir loadings <0.5 mg<sub>Ir</sub> cm<sup>-2</sup> the catalyst layer becomes inhomogeneous, which leads to a lower electrochemically active area and catalyst utilization, resulting in a significant decrease of performance. To investigate the potential for a large-scale application of PEM water electrolysis, the Ir-specific power density (g<sub>Ir</sub> kW<sup>-1</sup>) for membrane electrode assemblies (MEAs) with different catalyst loadings is analyzed as a function of voltage efficiency, and the consequences regarding catalyst material requirements are discussed.

© The Author(s) 2018. Published by ECS. This is an open access article distributed under the terms of the Creative Commons Attribution 4.0 License (CC BY, <http://creativecommons.org/licenses/by/4.0/>), which permits unrestricted reuse of the work in any medium, provided the original work is properly cited. [DOI: 10.1149/2.0641805jes]



Manuscript submitted January 22, 2018; revised manuscript received March 15, 2018. Published March 28, 2018. This was Paper 1382 presented at the New Orleans, Louisiana, Meeting of the Society, May 28–June 1, 2017.

PEM water electrolysis could provide electrolytic hydrogen for large-scale energy storage and mobility in a future energy scenario based on renewable energy sources. Currently, only a small share of the global hydrogen demand is served by PEM electrolysis due to the relatively high costs associated with this technology.<sup>1,2</sup> Overall H<sub>2</sub> costs are influenced by operating costs, which are governed by electricity prices and the efficiency of the electrolyzer, as well as system costs. According to a 2014 report by the EU's FCHJU, 70–90% of the projected long-term costs for H<sub>2</sub> production via PEM water electrolysis are due to the cost of electricity, so that significant improvements of the overall H<sub>2</sub> production efficiency are desired, proposing a 2030 target of 64–76%<sub>LHV</sub> (based on the lower heating value of hydrogen, LHV).<sup>1</sup> For currently installed systems (size typically in the kW– to MW–range),<sup>1–3</sup> the contribution of catalyst costs to the total system costs are comparably small ( $\approx 5\%$ ).<sup>1,4,5</sup> Consequently, high platinum group metal (PGM) loadings (several mg<sub>PGM</sub> cm<sub>MEA</sub><sup>-2</sup>), namely mostly platinum (Pt) to catalyze the hydrogen evolution reaction (HER) and iridium (Ir) to catalyze the oxygen evolution reaction (OER), are used to ensure good performance and lifetime.<sup>6</sup> However, as the PEM electrolyzer stack power is being increased to the MW-scale, the contribution of balance-of-plant costs is predicted to be much lower, and catalyst costs will become a major cost contributor.<sup>3</sup>

An equally important consideration for the envisaged large-scale application of PEM water electrolyzers in renewable energy generation/storage are the supply constraints for Ir and Pt.<sup>1</sup> While the fast HER kinetics of Pt<sup>7,8</sup> at the hydrogen cathode suggest that a reduction of the Pt loading would not significantly affect the electrolyzer performance, this is not the case for the oxygen anode, owing to the much slower OER kinetics on iridium oxide surfaces. Hence, a growing concern in the context of large-scale PEM water electrolysis applications is the availability of Ir, which is one of the rarest materials on earth with an estimated annual production of only  $\approx 4$  tons.<sup>4</sup> In a recent study by Babic et al., the authors estimate that if 25% of the annually produced Ir were to be used for PEM water electrolysis and considering that current PEM water electrolyzers require  $\approx 0.5$  g<sub>Ir</sub> kW<sup>-1</sup>, the annual PEM water electrolyzer installation would be limited to 2 GW/year.<sup>4</sup>

This currently estimated maximum Ir-supply limited annual PEM water electrolyzer installation capacity may be compared to the water

electrolysis capacity which would be needed, for example, if a large fraction of the currently used fossil fuels in the transportation sector were to be replaced by hydrogen. The worldwide fossil energy demand for transportation is currently 10<sup>20</sup> Joule<sup>9</sup> and, assuming that this demand would have to be supplied by H<sub>2</sub>, this would equal to an annual production of 700 Mt<sub>H<sub>2</sub></sub> (based on the H<sub>2</sub> higher heating value (HHV) of 285.8 kJ/mol). At the above mentioned long-term electrolyzer efficiency of  $\approx 70\%$  <sub>LHV</sub> (corresponding to a cell voltage of  $\approx 1.79$  V), this corresponds to an average electric power of  $\approx 3800$  GW. Taking into account that electrolyzers would be coupled to fluctuating renewable energy sources and could not run permanently at full load, the required world-wide installed electrolyzer power would be approximately three-fold higher, i.e.,  $\approx 12000$  GW (assuming, e.g., an average production power of roughly one third of its peak power available from wind farms).<sup>1</sup> From this example, it becomes clear that an installed capacity on the order of  $\approx 150$  GW/year would be necessary to completely decarbonize the mobility sector by the end of this century. Even when assuming that 50% of the Ir production could be used for PEM water electrolysis, this would require a  $\approx 50$ -fold reduction of today's Ir-specific power density down to  $\approx 0.01$  g<sub>Ir</sub> kW<sup>-1</sup> while maintaining a high efficiency. Whether this is feasible based on the OER activity of current Ir-based catalyst will be the focus of this study.

In general, it is possible to reduce the Ir-specific power density by reducing the catalyst loading as well as by increasing the current density. However, both will result in an increase of cell voltage and, consequently, a lower efficiency. Therefore, the final catalyst loading as well as the operating point (i.e., the current density) will be dictated by Ir price and availability.<sup>10</sup> Different approaches to reduce Ir loadings are reported in the literature, e.g., maximizing the noble metal dispersion by supporting thin films or nanoparticles of iridium (oxide) on high surface area support materials like TiC,<sup>11</sup> TaC,<sup>12</sup> TiO<sub>2</sub>,<sup>13</sup> or nano-structured thin films (NSTF),<sup>14</sup> whereby for the latter it was shown that high performance is possible even at Ir loadings <0.5 mg<sub>Ir</sub> cm<sup>-2</sup>.<sup>14</sup> Fabrication of core-shell catalysts and usage of improved catalyst layer manufacturing techniques like reactive spray deposition have also been proposed as pathways to achieve low Ir loadings.<sup>3</sup> However, most catalysts used in these studies are experimental materials and not yet commercially available. Additionally, there are only few studies which systematically analyze the effect of Ir loading on the performance and the voltage losses of an electrolyzer,<sup>15,16</sup> suggesting that loadings as low as 0.1 mg<sub>Ir</sub> cm<sup>-2</sup> can deliver high performance and durability.

\*Electrochemical Society Student Member.

\*\*Electrochemical Society Fellow.

<sup>†</sup>E-mail: [maximilian.bernt@tum.de](mailto:maximilian.bernt@tum.de)

In this study, we present a detailed investigation of the influence of widely ranging cathode and anode catalyst loadings on electrolyzer performance for in-house prepared MEAs with typical commercial catalyst materials, viz., carbon-supported platinum (Pt/C) and IrO<sub>2</sub>-coated titanium (IrO<sub>2</sub>/TiO<sub>2</sub>). We identify the optimum in performance depending on current density and analyze the occurring voltage losses. Furthermore, we address the question whether it is possible to reach the above outlined target values for the Ir-specific power density ( $\approx 0.01 \text{ g}_{\text{Ir}} \text{ kW}^{-1}$ ) with today's state-of-the-art catalysts.

## Experimental

**Membrane electrode assembly (MEA) preparation and cell assembly.**—5 cm<sup>2</sup> MEAs were prepared by a decal transfer method. Platinum supported on Vulcan XC72 carbon with two different metal loadings (45.8 wt% Pt/C, TEC10V50E and 4.8 wt% Pt/C, TEC10V05E from Tanaka, Kikinzoku Kogyo, Japan) was used as catalyst for the hydrogen evolution reaction at the cathode. For the oxygen evolution anode, IrO<sub>2</sub> supported on TiO<sub>2</sub> (IrO<sub>2</sub>/TiO<sub>2</sub> with 75 wt% iridium; Elyst Ir75 0480 from Umicore, Germany) was used. Suspensions were prepared by mixing catalyst powder, a solvent (either 2-propanol, purity  $\geq 99.9\%$  or acetone, purity  $\geq 99.9\%$ , from Sigma Aldrich, Germany), de-ionized (DI) water (18 M $\Omega$  cm) and Nafion ionomer solution (1100 EW, 20 wt% ionomer; D2021 from IonPower, USA) for 24 hours using a roller mill (rotating at 180 rpm). To achieve a homogenous suspension, ZrO<sub>2</sub> grinding beads (5 mm diameter) were added to 2–5 ml of the ink dispersion contained in a 8 ml polypropylene bottle.

The resulting catalyst ink was then coated onto a thin plastic foil (25  $\mu\text{m}$  thick ETFE (FP361025 from Goodfellow, UK) or 50  $\mu\text{m}$  thick PTFE (from Angst+Pfister, Germany)) using a Mayer-rod coating machine. After drying, electrodes with an active area of 5 cm<sup>2</sup> were punched from the coatings and hot-pressed onto a Nafion 212 membrane (50  $\mu\text{m}$  thick; from Quintech, Germany) for 3 min at 155°C at a pressure of 2.5 MPa. The catalyst loading was determined by weighing the ETFE/PTFE decals before and after the decal transfer step, using a microbalance ( $\pm 15 \mu\text{g}$ ; Mettler Toledo XPE105DR). For the cathode electrodes with an ionomer to carbon weight ratio of 0.6/1, the loadings were  $0.30 \pm 0.05 \text{ mg}_{\text{Pt}} \text{ cm}_{\text{MEA}}^{-2}$  (45.8 wt% Pt/C) and  $0.025 \pm 0.007 \text{ mg}_{\text{Pt}} \text{ cm}_{\text{MEA}}^{-2}$  (4.8 wt% Pt/C), respectively; the electrode thicknesses, calculated from the average packing density of the resulting Vulcan carbon supported catalyst layers ( $22 \pm 4 \mu\text{m} (\text{mg}_{\text{Vulcan}} \text{ cm}^{-2})^{-1}$ ),<sup>17</sup> were very similar, viz.,  $\approx 8 \mu\text{m}$  for the high-loaded and  $\approx 11 \mu\text{m}$  for the low-loaded cathode. For the anode, the solid content of the inks as well as the wet-film thickness of the coatings was varied to obtain catalyst loadings between 0.20–5.41  $\text{mg}_{\text{Ir}} \text{ cm}_{\text{MEA}}^{-2}$ , while the ionomer content was kept at 11.6 wt% relative to the total weight of the electrode (shown to yield the optimum performance in our earlier study).<sup>18</sup>

Sintered titanium (from Mott Corporation, USA) with a porosity of  $\approx 50\%$  and a thickness of  $280 \pm 10 \mu\text{m}$  as well as a carbon fiber paper (TGP-H-120T without MPL, 20 wt% PTFE; from Toray, Japan) with a thickness of  $370 \pm 10 \mu\text{m}$  were used as porous transport layers (PTL) at the anode and at the cathode, respectively. The MEA and PTLs were placed between the flow fields of the electrolyzer test cell and sealed with virgin PTFE gaskets. Sealings with an appropriate thickness were chosen to achieve  $\approx 25\%$  compression of the carbon PTL (under the applied compression, the titanium PTL is considered incompressible). Details of the cell hardware and the cell assembly are described elsewhere.<sup>18</sup>

**Physical characterization.**—Cross-sectional scanning electron microscopy (SEM) samples were prepared by embedding MEAs (after electrochemical characterization) in room-temperature curing epoxy. The sample surface was ground with SiC paper in two steps (grade P320 and P1200, from Buehler, Germany) and subsequently polished with 9  $\mu\text{m}$  diamond polishing agent. SEM analysis was performed with a JEOL JSM-7500F scanning electron microscope at an accelerating voltage of 5–15 kV. The electrode thickness was measured

at 10–15 different locations of an MEA cross-section to account for local inhomogeneity of the electrode thickness.

**Electrochemical characterization.**—An automated test station from Greenlight Innovation, equipped with a potentiostat and booster (Reference 3000 and 30 A booster, Gamry), was used for electrochemical characterization of the MEAs. The cell temperature was fixed to 80°C and deionized (DI) water was pre-heated to 80°C and fed to anode and cathode of the electrolysis cell at a rate of 5 ml min<sup>-1</sup>. Polarization curves were recorded at pressures ranging from 1–30 bar absolute pressure (bar<sub>a</sub>). The product gas at the anode outlet was diluted with nitrogen (200 nccm) to prevent the formation of an explosive gas mixture, which can be produced by the permeation of H<sub>2</sub> through the membrane into the anode compartment, especially at high pressure and low current densities.

After a warm-up step under N<sub>2</sub> atmosphere, the cell was conditioned at 1 A cm<sup>-2</sup> for 30 min. Subsequently, galvanostatic polarization curves were recorded in a current range from 0.01 to 6 A cm<sup>-2</sup>. At each current, the cell voltage was averaged over 10 s after 5 min equilibration time. The first two polarization curves were considered part of the conditioning process and were thus not included in the data analysis. Galvanostatic AC impedance measurements between 100 kHz – 1 Hz were carried out after each polarization step. The amplitude of the current perturbation was chosen for each step to obtain a sufficient signal to noise ratio, while keeping the perturbation small enough to ensure a linear system response. The high-frequency resistance (HFR) was obtained from the high-frequency intercept of the Nyquist plot with the real axis. All polarization curves and corresponding HFR values reported in this work represent an average of three consecutive measurements for a single MEA. The standard deviation of the three measurements was evaluated and included as error bars in all figures (note that for most samples the standard deviation is too small to be visible in the graphs).

Cyclic voltammograms (CVs) of the IrO<sub>2</sub>/TiO<sub>2</sub> anode electrode were recorded at the beginning of a test, using a scan rate of 50 mV s<sup>-1</sup> at 80°C. The anode working electrode was flushed with H<sub>2</sub>O at a flow rate of 5 ml min<sup>-1</sup>, while the cathode counter electrode was purged with dry H<sub>2</sub> at 50 ml min<sup>-1</sup>. Except for the CV test, it was ensured that the cell potential did not drop below  $\approx 1.3 \text{ V}$  during the entire test in order to prevent a reduction of the IrO<sub>2</sub> on the anode, as this was shown to lead to a change in activity and Tafel slope.<sup>19</sup>

## Results and Discussion

**Platinum loading in cathode catalyst layer.**—To study the influence of the Pt loading on the cathode, two MEAs with Pt loadings of 0.30  $\text{mg}_{\text{Pt}} \text{ cm}^{-2}$  (red curve in Fig. 1) and 0.025  $\text{mg}_{\text{Pt}} \text{ cm}^{-2}$  (blue curve in Fig. 1) were tested. The different loadings were obtained by using Pt/C catalysts with Pt metal loadings of 45.8 wt% and 4.8 wt% while keeping the electrode thickness of both samples similar ( $\approx 8 \mu\text{m}$  for the high loaded and  $\approx 11 \mu\text{m}$  for the low loaded cathode). For these experiments, the Ir loading on the anode was kept constant for both MEAs ( $\approx 1.6 \text{ mg}_{\text{Ir}} \text{ cm}^{-2}$ ). Polarization curves including the measured cell voltage,  $E_{\text{cell}}$ , as well as the iR-free cell voltage,  $E_{\text{iR-free}}$ , are shown in Fig. 1, together with the corresponding HFR values. Obviously, the cell voltage is very similar for both MEAs (cf. Fig. 1a). The slightly higher cell voltage at high current densities for the MEA with low Pt loading (amounting to  $\approx 20 \text{ mV}$  at 6 A cm<sup>-2</sup>) may be partially due to its higher overpotential for the HER and proton transport resistance in the catalyst layer, but may also partially be caused by the slightly higher HFR obtained for this cell (58 vs. 53 m $\Omega$  cm<sup>2</sup>; Fig. 1b), resulting in the observation that the iR-free cell voltage (dashed line in Fig. 1a) is almost identical for both MEAs, i.e., for both high and low cathode loadings. Tafel slopes – obtained from a linear fit of the iR-free cell voltage for current densities between 10–100 mA cm<sup>-2</sup> – are also identical within the experimental error for both samples (47–48 mV dec<sup>-1</sup>, cf. inset in Fig. 1a).

The expected overpotentials for HER kinetics and cathode proton transport can be calculated as shown in our previous work<sup>18</sup> (cf.



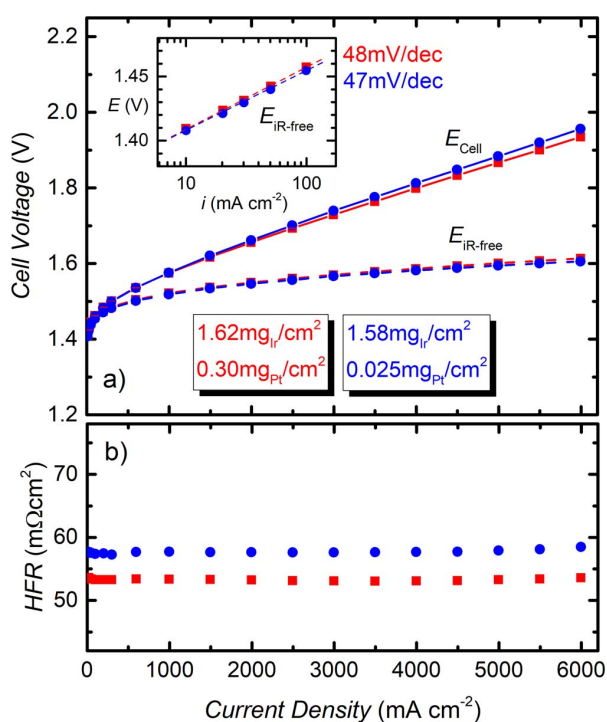


**Figure 1.** a) Ambient pressure polarization curves ( $80^{\circ}\text{C}$ ,  $5 \text{ mlH}_2\text{O min}^{-1}$ ) of MEAs with different cathode catalyst loadings (red:  $0.30 \text{ mg}_{\text{Pt}} \text{ cm}_{\text{MEA}}^{-2}$  with  $45.8 \text{ wt}\%$  Pt/C; blue:  $0.025 \text{ mg}_{\text{Pt}} \text{ cm}_{\text{MEA}}^{-2}$  with  $4.8 \text{ wt}\%$  Pt/C) and with standard anode Ir loadings ( $\approx 1.6 \text{ mg}_{\text{Ir}} \text{ cm}_{\text{MEA}}^{-2}$ ) using a  $\approx 50 \mu\text{m}$  thick Nafion 212 membrane. The full lines represent the measured cell voltage, the dashed lines give the cell voltage corrected by the HFR. The inset shows a Tafel plot of the iR-free cell voltages, with the Tafel slope values obtained from a linear fit between  $10$ – $100 \text{ mA cm}^{-2}$ . b) HFR-values vs. current density obtained by electrochemical impedance spectroscopy.

Appendix for detailed calculation) and result in an overall difference of  $\approx 7.5 \text{ m}\Omega \text{ cm}^2$  between high-loaded and low-loaded cathode. This would amount to a cell voltage difference of  $\approx 45 \text{ mV}$  at  $6 \text{ A cm}^{-2}$  (assuming a similar HFR for both MEAs), which is close to the observed value ( $\approx 20 \text{ mV}$  at  $6 \text{ A cm}^{-2}$ ). The HFR difference of  $\approx 5 \text{ m}\Omega \text{ cm}^2$  between high-loaded and low-loaded cathodes is observed systematically for all tested samples. Here it should be mentioned, however, that the difference in the measured HFR values ( $\approx 10\%$ ) is close to within our estimated experimental accuracy for this measurement. Furthermore, we cannot exclude that the HFR values obtained from the x-axis intercept in a Nyquist plot are affected by the different HER overpotentials for high-loaded and low-loaded cathodes, i.e. that the different HER semi-circles (which occur at rather high frequencies) in the Nyquist plot distort the determination of the HFR. However, since the expected difference for HER kinetics and proton transport ( $\approx 7.5 \text{ m}\Omega \text{ cm}^2$ ) is on the same order as the observed HFR difference ( $\approx 5 \text{ m}\Omega \text{ cm}^2$ ) between the two MEAs, we cannot reliably deconvolute these differences, but can clearly state that ultra-low cathode Pt loadings produce minor performance differences (on the order of  $10 \text{ mV}$ ) within typical operating current densities ( $< 3 \text{ A cm}^{-2}$ ).

Consequently, we can consider the beginning-of-life performance of a PEM water electrolyzer operated at  $80^{\circ}\text{C}$  as essentially independent of the cathode Pt loading down to  $\approx 0.025 \text{ mg}_{\text{Pt}} \text{ cm}^{-2}$ . By extension, this implies that the apparent Tafel slope determined from the inset in Fig. 1a corresponds to the Tafel slope for the OER on the  $\text{IrO}_2/\text{TiO}_2$  catalyst, in agreement with the value determined in our earlier publication.<sup>18</sup> Catalyst degradation during prolonged operation could, of course, be more severe for lower cathode loadings and

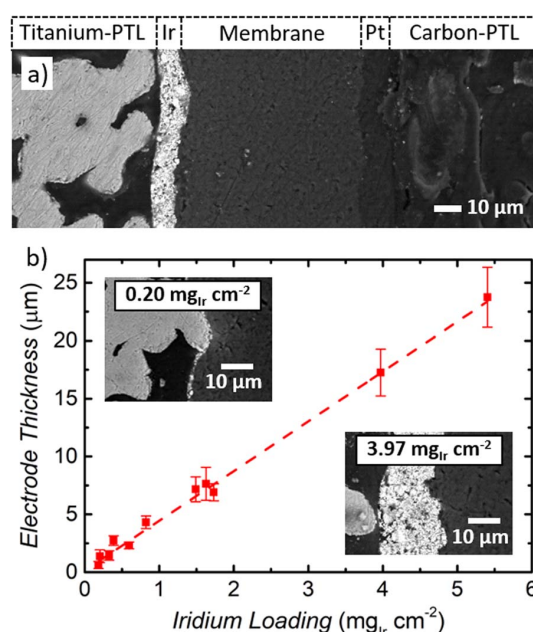


**Figure 2.** a) Cross-sectional SEM image of an MEA with an Ir loading of  $1.58 \text{ mg}_{\text{Ir}} \text{ cm}^{-2}$  and Pt loading of  $0.025 \text{ mg}_{\text{Pt}} \text{ cm}^{-2}$ . From left to right: anode PTL (titanium sinter), anode electrode composed of  $\text{IrO}_2/\text{TiO}_2$  catalyst and ionomer,  $50 \mu\text{m}$  thick Nafion 212 membrane, cathode electrode composed of  $4.8 \text{ wt}\%$  Pt/C and ionomer, cathode PTL (carbon paper). b) Electrode thickness determined from 10–15 individual measurements on cross-sectional SEM images vs. iridium loading determined from the areal weight of the anode electrodes; the dashed line is a linear regression line of anode thickness ( $t_{\text{anode}}$ ) vs. iridium loading ( $L_{\text{Ir}}$ ), yielding  $t_{\text{anode}} = 4.3 \pm 0.3 \mu\text{m} (\text{mg}_{\text{Ir}} \text{ cm}^{-2})^{-1} \cdot L_{\text{Ir}}$ . The insets show SEM images of an MEA with a low Ir loading ( $0.20 \text{ mg}_{\text{Ir}} \text{ cm}^{-2}$ , electrode thickness  $\approx 1 \mu\text{m}$ ) and a high Ir loading ( $3.97 \text{ mg}_{\text{Ir}} \text{ cm}^{-2}$ ,  $\approx 17 \mu\text{m}$ ).

hence, the influence of catalyst loading on the long-term performance requires further investigation. In our example, the final Pt loading of  $0.025 \text{ mg}_{\text{Pt}} \text{ cm}^{-2}$  is almost two orders of magnitude lower than the standard Ir loading of  $\approx 1.6 \text{ mg}_{\text{Ir}} \text{ cm}^{-2}$ , indicating that the main challenges toward a substantial reduction of noble metal loading remain at the anode of the electrolyzer. Consequently, the rest of our study will focus on the influence of the Ir anode loading on PEM electrolyzer performance.

**Iridium loading in anode catalyst layer.**—The commercial state-of-the-art catalyst for the anode used in this study has a fixed Ir metal content of  $75 \text{ wt}\%$  and hence, adjusting the iridium loading in the range of  $0.20$ – $5.41 \text{ mg}_{\text{Ir}} \text{ cm}^{-2}$  was accompanied by a variation of the anode electrode thickness. Thus, for each MEA, cross-sectional SEM micrographs were recorded (cf. Fig. 2a, where it is exemplarily shown for an MEA with the standard Ir loading of  $\approx 1.6 \text{ mg}_{\text{Ir}} \text{ cm}^{-2}$ ), from which the electrode thickness as a function of Ir loading was determined (cf. Fig. 2b). As one would expect, the anode thickness scales linearly with the catalyst loading (from  $\approx 1$ – $25 \mu\text{m}$ ), corresponding to an effective packing density of  $4.3 \pm 0.3 \mu\text{m} (\text{mg}_{\text{Ir}} \text{ cm}^{-2})^{-1}$  (cf. Fig. 2b). Error bars represent the standard deviation for 10–15 measurements on each electrode. The insets in Fig. 2b exemplarily show the SEM images of two extreme Ir loadings ( $0.20 \text{ mg}_{\text{Ir}} \text{ cm}^{-2}$  vs.  $3.97 \text{ mg}_{\text{Ir}} \text{ cm}^{-2}$ ), which will be relevant to the further analysis below.

Polarization curves at ambient pressure and  $80^{\circ}\text{C}$  were recorded for all MEAs. In order to facilitate the direct comparison of the performance at various Ir loadings, the iR-free cell voltage,  $E_{\text{iR-free}}$ , at three current densities is displayed as a function of Ir loading in Fig. 3. Here,  $E_{\text{iR-free}}$  is defined as the cell voltage,  $E_{\text{cell}}$ , corrected by the measured HFR, which represents the sum of the membrane resistance,

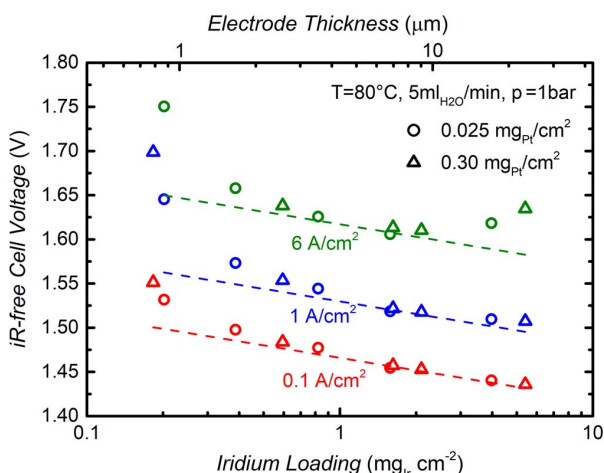


**Figure 3.** Ambient pressure cell voltage corrected by HFR,  $E_{iR-free}$ , at current densities of 0.1 A cm<sup>-2</sup>, 1.0 A cm<sup>-2</sup> and 6.0 A cm<sup>-2</sup> (80°C, 5 ml<sub>H<sub>2</sub>O</sub> min<sup>-1</sup>) as a function of anode iridium loading. The dashed lines represent the expected iR-free cell voltage based on the performance of the MEAs with standard Ir loadings ( $\approx 1.6$  mg<sub>Ir</sub> cm<sub>MEA</sub><sup>-2</sup>), assuming that only the OER overpotential changes with Ir loading (Tafel slope:  $\approx 47$  mV dec<sup>-1</sup>). MEAs with low Pt loadings ( $\approx 0.025$  mg<sub>Pt</sub> cm<sub>MEA</sub><sup>-2</sup>) are represented by circles, MEAs with high Pt loadings ( $\approx 0.30$  mg<sub>Pt</sub> cm<sub>MEA</sub><sup>-2</sup>) are shown by triangles.

$R_{memb}$ , and the electronic resistance,  $R_{el}$ :

$$E_{iR-free} \equiv E_{cell} - i \cdot (R_{memb} + R_{el}) \\ = E_{rev} + \eta_{HER} + \eta_{OER} + i \cdot (R_{H^+,an}^{eff} + R_{H^+,cath}^{eff}) + \eta_{mt} \quad [1]$$

The right-hand-side of Eq. 1 shows the reversible cell voltage,  $E_{rev}$ , to which all other voltage loss terms are added (note that current, potentials, and overpotentials are taken as positive values here): i)  $\eta_{HER}$  and  $\eta_{OER}$  are the kinetic overpotentials for the HER and the OER; ii)  $R_{H^+,an}^{eff}$  and  $R_{H^+,cath}^{eff}$  represent the effective proton transport resistance in anode and cathode catalyst layer, respectively; and iii)  $\eta_{mt}$  represents any residual mass transport resistance(s) (for examples see Reference 18).

For the smallest current density (0.1 A cm<sup>-2</sup>; red symbols), mass transport  $\eta_{mt}$  and proton transport ( $R_{H^+,an}^{eff} + R_{H^+,cath}^{eff}$ ) can be considered negligible, so that the iR-free potential shown in Fig. 3 should be exclusively governed by the OER kinetics (HER kinetics can be neglected as discussed in the previous section). In this case, at constant H<sub>2</sub>/O<sub>2</sub> partial pressures and temperature, and under the assumption that the OER can be described by simple Tafel kinetics, one would expect that  $E_{iR-free}$  should be described by:

$$E_{iR-free} \propto TS \cdot \log(i) - TS \cdot \log(i_{0(OER)} \cdot A_{Ir,el} \cdot L_{Ir}) \quad [2]$$

where  $TS$  is the Tafel slope for the OER,  $i_{0(OER)}$  is the OER exchange current density,  $A_{Ir,el}$  is the specific surface area of the anode catalyst, and  $L_{Ir}$  is the iridium catalyst loading. Thus, when using the same anode catalyst (i.e.,  $A_{Ir,el} = \text{constant}$ ) and for constant current density, Eq. 2 yields:

$$\left( \frac{\partial E_{iR-free}}{\partial \log L_{Ir}} \right)_{A_{Ir,el}, i, T, p_{O_2}, p_{H_2}} = -TS \quad [3]$$

With an intrinsic OER Tafel slope of  $TS \approx 47$  mV dec<sup>-1</sup> (see inset in Fig. 1a), at a low and constant current density, a plot of  $E_{iR-free}$  vs. the logarithm of the iridium loading of each MEA should follow a straight line with a slope of 47 mV dec<sup>-1</sup>. This expected trend for  $E_{iR-free}$  vs.  $\log(L_{Ir})$  at 0.1 A cm<sup>-2</sup> is indicated by the dashed red line in Fig. 3, demonstrating that the measured data points follow the prediction very well, down to a catalyst loading of  $\approx 0.5$  mg<sub>Ir</sub> cm<sup>-2</sup>. However, for lower Ir loadings,  $E_{iR-free}$  is higher than expected for an OER kinetics controlled regime, indicating additional voltage loss

contributions even at such low current density, the origin of which will be discussed in the next Section.

In general, Eqs. 2 and 3 are not expected to be valid at a current density of 1 A cm<sup>-2</sup>, where transport related resistances, particularly related to proton conduction in the anode and H<sub>2</sub> mass transport resistances in the cathode, become appreciable (amounting to a total of  $\approx 20$  mV, as shown in our previous work).<sup>18</sup> However, if these resistances were to be independent of the Ir loading (as expected, e.g., for resistances caused by the H<sub>2</sub> cathode), one would still expect the same 47 mV dec<sup>-1</sup> slope of  $E_{iR-free}$  vs.  $\log(L_{Ir})$  at 1 A cm<sup>-2</sup>, but offset from the 0.1 A cm<sup>-2</sup> line by a bit more than 47 mV. However, except for a narrow range of Ir loadings ( $\approx 0.8$ –2.0 mg<sub>Ir</sub> cm<sup>-2</sup>), this is not the case (see blue symbols in Fig. 3). Most noteworthy, as the Ir loading and thus the anode catalyst layer thickness decreases, the magnitude of additional transport related losses increases ( $> 100$  mV at the lowest loading of 0.2 mg<sub>Ir</sub> cm<sup>-2</sup>), even though one would expect rather the opposite, as thinner electrodes would have lower ( $i \cdot R_{H^+,an}^{eff}$ ) losses.

At the highest current density of 6 A cm<sup>-2</sup> (green symbols in Fig. 3), the presence of additional resistances at low Ir loadings is also apparent, but now pronounced transport related losses can also be observed at high Ir loadings (at  $\approx 4$  and 5.4 mg<sub>Ir</sub> cm<sup>-2</sup>), suggesting a different anode loading (or thickness) dependent transport resistance. Based on the analysis in Fig. 3, transport related voltage losses are minimized and optimal cell performance is obtained for Ir loadings in the range of  $\approx 1$ –2 mg<sub>Ir</sub> cm<sup>-2</sup> with anode electrode thicknesses of  $\approx 4$ –8  $\mu$ m. It should be mentioned at this point, that some of the MEAs shown in Fig. 3 have cathode electrodes with a high Pt loading (triangles), while others have low Pt loadings (circles). As expected from our earlier analysis of different Pt loadings (see the previous section), the Pt loading does not influence the performance. The effects leading to an increase of cell voltage at very low and high Ir loadings, associated with very thin and very thick electrodes, are discussed in more detail in the following sections.

**High iridium loadings.**—The polarization curve of an MEA with a high Ir loading (3.97 mg<sub>Ir</sub> cm<sup>-2</sup>; brown lines/symbols) is compared to a standard MEA in Fig. 4a (1.58 mg<sub>Ir</sub> cm<sup>-2</sup>; blue lines/symbols). At low current densities, i.e., in the kinetic region,  $E_{iR-free}$  is slightly lower for the sample with a high Ir loading (cf. inset in Fig. 4a). This is expected due to the higher electrochemically active surface area compared to the standard Ir loading. An estimation based on a simple Tafel equation (cf. Eq. 3) predicts a difference of  $\approx 19$  mV, which is very close to the experimentally observed value ( $\approx 15$  mV, cf. dashed red line in Fig. 3). At high current densities, on the other hand, the cell voltage of an MEA with high Ir loading is higher than for the standard MEA. This indicates additional voltage losses due to mass- and/or proton transport, which are expected to become more prominent in a  $\approx 2.5$ -fold thicker electrode ( $\approx 7$  vs.  $\approx 17$   $\mu$ m, cf. Fig. 2). The effective proton transport resistance,  $R_{H^+,an}^{eff}$ , and the corresponding voltage loss can be estimated as shown in more detail in a previous study.<sup>18</sup> From this calculation, one would expect an additional penalty of  $\approx 15$  mV at 6 A cm<sup>-2</sup> for the MEA with a high Ir loading (3.97 mg<sub>Ir</sub> cm<sup>-2</sup>) compared to the standard MEA (1.58 mg<sub>Ir</sub> cm<sup>-2</sup>). This, however, can only partly explain the difference between measured and expected iR-free cell voltage considering the difference in OER overpotential ( $\approx 31$  mV, cf. green symbols and dashed line in Fig. 3), which indicates that a different additional mass transport resistance must be involved.

Insights into this phenomenon can be gained by examining the HFR, particularly its strong increase with current density for the high-loaded/thick anode electrode (cf. Fig. 4b). This is in stark contrast to the standard MEA with a lower anode loading and a thinner anode electrode, for which the HFR is essentially independent of current density. Moreover, if there were a dependency of the HFR on current density, one would expect the HFR to rather decrease with increasing current density, as a concomitant increase in heat production could result in a local temperature increase at the electrode/membrane interface, leading to a higher ionic conductivity of the membrane.<sup>20</sup>

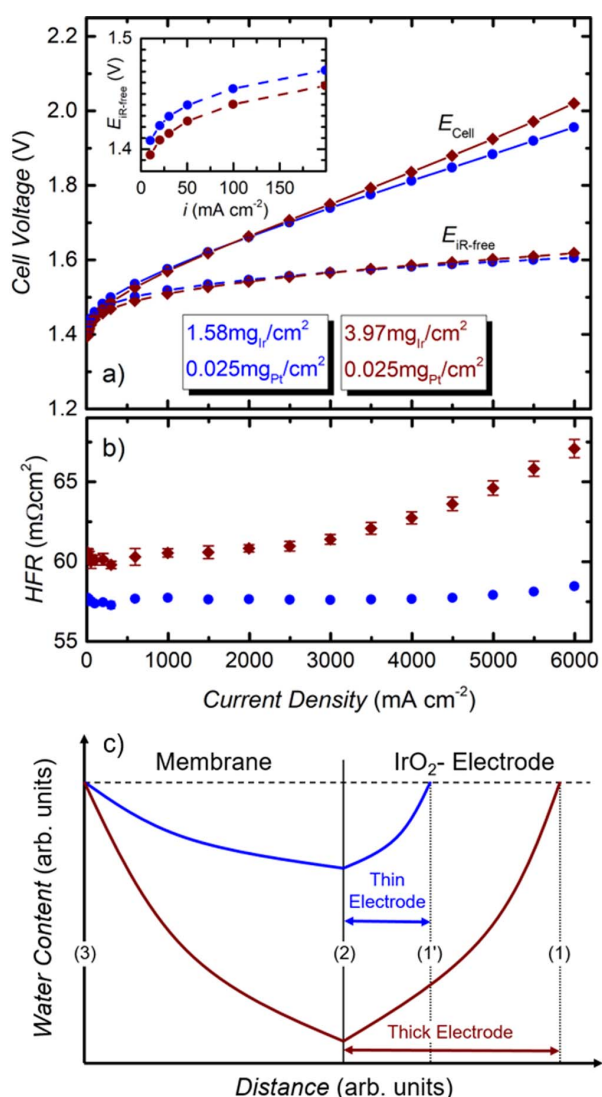


**Figure 4.** a) Ambient pressure polarization curves ( $80^{\circ}\text{C}$ ,  $5 \text{ mL H}_2\text{O min}^{-1}$ ) for an MEA with a high Ir loading ( $3.97 \text{ mgIr cm}^{-2}$ , with a thickness of  $\approx 17 \mu\text{m}$ ) compared to the MEA with standard loading ( $1.58 \text{ mgIr cm}^{-2}$ , with a thickness of  $\approx 7 \mu\text{m}$ ), both using a  $\approx 50 \mu\text{m}$  thick Nafion 212 membrane and  $0.025 \text{ mgPt cm}^{-2}$  cathodes. The full lines represent the measured cell voltage, the dashed lines give the cell voltage corrected by HFR ( $E_{iR\text{-free}}$ ). The inset shows a magnification of the  $iR\text{-free}$  cell voltage at small current densities. b) Corresponding HFR values. c) Qualitative sketch of the water concentration profile within the membrane and the anode catalyst layer for the two anode electrodes with different thicknesses, marking: (1) anode/PTL interface for the thick anode electrode, (1') anode/PTL interface for the thin anode electrode, (2) membrane/anode electrode interface, and, (3) cathode electrode/membrane interface.

Nevertheless, in this case it would also be expected for the low-loaded anode. As the HFR represents the sum of electronic contact resistance and membrane resistance, either of these factors could be responsible for the observed HFR increase with current density. However, since the contact resistance should be independent of the applied current, the only logical explanation is that this effect is related to the membrane resistance. A similar increase of the HFR for high current densities was previously observed for PEM fuel cells when comparably thick membranes ( $\geq 50 \mu\text{m}$ ) were used.<sup>21,22</sup> Springer et al. showed that this HFR increase is related to a change of the water profile across the

membrane when increasing the current density,<sup>21</sup> owing to the electroosmotic water drag rate from anode to cathode which is roughly proportional to the current density: at high current densities, the water flux due to electroosmotic drag is too high to be compensated by back diffusion of water from cathode to anode, resulting in a lower water content in the anode-near region of the membrane and, consequently, an increase of the HFR.<sup>21</sup>

Based on these findings, we propose a similar model for our electrolyzer MEA to explain the increase of HFR with current density for thick (high-loaded) anode electrodes. A qualitative water profile across the membrane and anode catalyst layer is illustrated in Fig. 4c for a thin and a thick anode electrode, respectively. In the case of an electrolyzer, excess liquid water is supplied to the anode, so that we can always assume an equally high water content at the anode/PTL interface ((1) and (1') in Fig. 4c), independent of current density. The amount of water transported to the membrane/anode interface ((2) in Fig. 4c) is then controlled by the thickness of the electrode, which acts as a diffusion barrier for water transport. In principle, liquid water transport across the anode electrode should be rather rapid within the free void volume of the electrode ( $\approx 35\%$  void volume fraction for the  $11.6 \text{ wt\%}$  ionomer containing anode),<sup>18</sup> but with increasing current density, the void volume will likely be filled more and more by  $\text{O}_2$ , thereby gradually limiting water transport to the ionomer phase (its volume fraction is also  $\approx 35\%$ ).<sup>18</sup> Once the latter becomes dominating, the water transport resistance through the thick anode electrode ( $\approx 17 \mu\text{m}$ ) should of course be higher than for the thin electrode ( $\approx 7 \mu\text{m}$ ), and water transport toward the membrane is slower. At the same time, with increasing current density, the water transport from anode to cathode ((3) in Fig. 4c) due to electroosmotic drag (drag coefficient of  $2.4\text{--}3.4$ )<sup>23,24</sup> increases and at some point cannot be compensated by the comparably slow water transport through the thick anode electrode anymore. This would lead to a lower water content in the anode-near region of the membrane and, consequently, an increase of the membrane resistance. This could very well explain why the HFR for the MEA with a high Ir loading ( $3.97 \text{ mgIr cm}^{-2}$ ) starts to increase significantly for current densities above  $3 \text{ A cm}^{-2}$  while it is constant up to  $6 \text{ A cm}^{-2}$  for the MEA with standard Ir loading ( $1.58 \text{ mgIr cm}^{-2}$ ).

Assuming this hypothesis to be correct, a decrease of the oxygen volume fraction within the anode electrode by increasing the oxygen pressure should either increase the current density above which an increase of the HFR is observed or even eliminate this effect. The latter is indeed observed in Fig. 5, comparing polarization curves for the MEA with an Ir loading of  $3.97 \text{ mgIr cm}^{-2}$  at ambient pressure (brown lines/symbols) and balanced pressure ( $p_{\text{H}_2} = p_{\text{O}_2}$ ) of  $30 \text{ bar}_a$  (green lines/symbols). Interestingly, at high pressure, the HFR does no longer increase with current density (Fig. 5b). Instead, even a slight decrease is observed at high current densities, as would be expected due to a local increase of temperature with current (see above). This shows that the increase of operating pressure on the anode improves the water transport through the anode electrode, preventing a decrease of the water content in the anode-near region of the membrane. This effect is clearly related to the higher anode pressure, because a similar behavior was not observed when only the cathode was pressurized (data not shown). Thus, at high operating pressure, a lower volume fraction of  $\text{O}_2$  gas in the pores of the catalyst layer and/or smaller  $\text{O}_2$  bubbles seem to be clearly beneficial for the transport of water.<sup>25,26</sup> However, the two-phase flow inside the catalyst layer is a very complex topic and more research is required to fully understand the phenomena.<sup>27</sup>

**Low iridium loadings.**—The polarization curve of an MEA with a low Ir loading ( $0.20 \text{ mgIr cm}^{-2}$ , with  $\approx 1 \mu\text{m}$  thickness; orange lines/symbols) is shown in Fig. 6, again compared to a standard MEA ( $1.58 \text{ mgIr cm}^{-2}$ , with  $\approx 7 \mu\text{m}$  thickness; blue lines/symbols). The cell voltage of the MEA with low Ir loading is significantly higher than for the standard MEA, which can be partly explained by an increase of the HFR (30–40%), compared to the standard MEA (cf. Fig. 6b). However, even for the HFR-corrected cell voltage there is a difference of  $\approx 150 \text{ mV}$  already at  $1 \text{ A cm}^{-2}$ , which is much higher than the



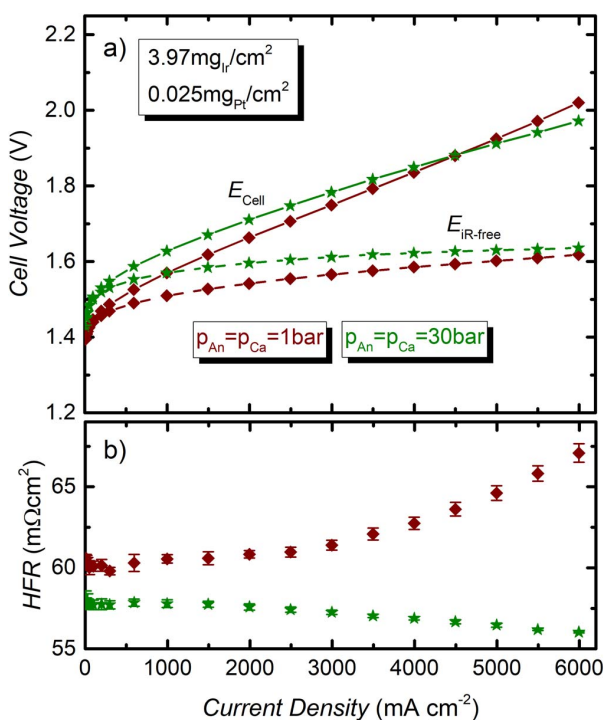


**Figure 5.** a) Polarization curves ( $80^{\circ}\text{C}$ ,  $5 \text{ mlH}_2\text{O min}^{-1}$ ) for an MEA with a  $\approx 17 \mu\text{m}$  thick anode with an Ir loading of  $3.97 \text{ mg}_{\text{Ir}} \text{ cm}_{\text{MEA}}^{-2}$  (cathode:  $0.025 \text{ mg}_{\text{Pt}} \text{ cm}_{\text{MEA}}^{-2}$ ), operated at balanced pressures of 1 bar (brown) and 30 bar (green), respectively. The full lines represent the measured cell voltage, the dashed lines give the cell voltage corrected by HFR. b) Corresponding HFR.

expected increase of the kinetic OER overpotential of  $\approx 42 \text{ mV}$  as calculated from Eq. 3. This clearly shows that additional voltage loss terms must be considered for MEAs with low-loaded and thin anodes.

In order to gain more insights into the behavior at low current densities, Tafel slopes were determined from a fit of the linear region between  $10\text{--}100 \text{ mA cm}^{-2}$  (cf. Fig. 7). For the MEAs with standard Ir loading ( $1.58 \text{ mg}_{\text{Ir}} \text{ cm}^{-2}$ ) and high Ir loading ( $3.97 \text{ mg}_{\text{Ir}} \text{ cm}^{-2}$ ), the Tafel slopes are similar ( $47 \text{ mV dec}^{-1}$  vs.  $45 \text{ mV dec}^{-1}$ ) and the difference in  $E_{\text{IR-free}}$  at low current densities ( $\approx 15 \text{ mV}$ ) is as expected from Eq. 3. At low Ir loading, on the other hand, there is a difference in  $E_{\text{IR-free}}$  of  $\approx 55 \text{ mV}$  compared to the standard MEA, even at the lowest current density ( $0.01 \text{ A cm}^{-2}$ ). This is higher than what would be expected from the OER kinetics ( $\approx 42 \text{ mV}$ ), indicating additional voltage losses even at such low current densities. The difference in  $E_{\text{IR-free}}$  grows with increasing current density, which is also reflected by a significantly higher apparent Tafel slope of  $68 \text{ mV dec}^{-1}$  for the MEA with the low Ir loading. Apart from a change of the OER reaction mechanism, which we consider utterly unlikely, since it is the same catalyst operating at almost the same potential, this discrepancy could point toward additional voltage losses even at very low current densities. Consequently, for the MEA with a  $\approx 1 \mu\text{m}$  thin low-loaded anode, the Tafel slope does no longer represent the pure OER kinetics in contrast to the MEAs with higher Ir loading. In fact, for Ir loadings  $> 1 \text{ mg}_{\text{Ir}} \text{ cm}^{-2}$ , all Tafel slopes are between  $45\text{--}50 \text{ mV dec}^{-1}$  (cf. Fig. 7b), which is consistent with the results for an Ir loading of  $\approx 2 \text{ mg}_{\text{Ir}} \text{ cm}^{-2}$  from our previous study<sup>18</sup> as well as with literature values obtained with model electrodes.<sup>28,29</sup> For Ir loadings  $< 1 \text{ mg}_{\text{Ir}} \text{ cm}^{-2}$ , on the other hand, the apparent Tafel slope increases significantly.

The reasons for the additional voltage losses leading to an increase of the apparent Tafel slopes can be explained in terms of the electrode structure for low Ir loadings. Fig. 8a shows a cross-sectional SEM

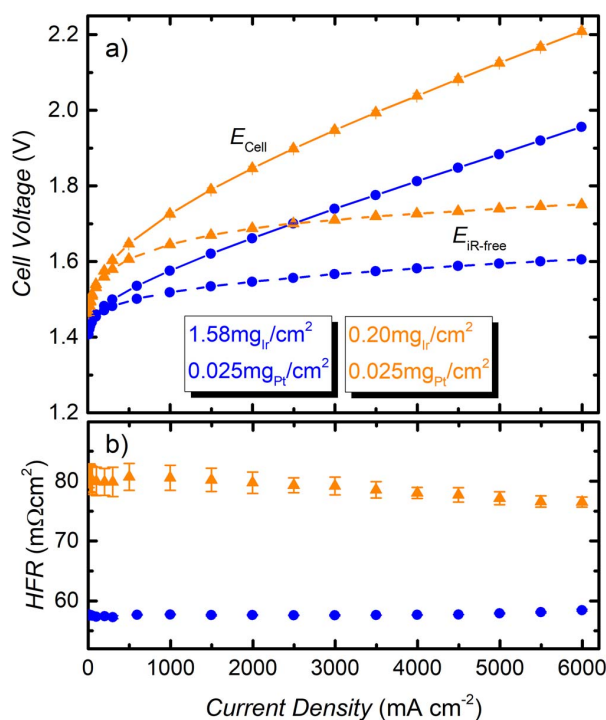


**Figure 6.** a) Ambient pressure polarization curves ( $80^{\circ}\text{C}$ ,  $5 \text{ mlH}_2\text{O min}^{-1}$ ) for an MEA with a low Ir loading ( $0.20 \text{ mg}_{\text{Ir}} \text{ cm}_{\text{MEA}}^{-2}$ , with a thickness of  $\approx 1 \mu\text{m}$ ) compared to the MEA with standard loadings ( $1.58 \text{ mg}_{\text{Ir}} \text{ cm}_{\text{MEA}}^{-2}$ , with a thickness of  $\approx 7 \mu\text{m}$ ), both using a  $\approx 50 \mu\text{m}$  thick Nafion 212 membrane and a cathode loading of  $0.025 \text{ mg}_{\text{Pt}} \text{ cm}_{\text{MEA}}^{-2}$ . The full lines represent the measured cell voltage, the dashed lines give the cell voltage corrected by HFR. b) Corresponding HFR.

image of an anode electrode with a low Ir loading ( $0.20 \text{ mg}_{\text{Ir}} \text{ cm}^{-2}$ ). The nominal electrode thickness for this loading is only  $\approx 1 \mu\text{m}$ , leading to a non-uniform catalyst layer (cf. Fig. 8a). The reason for this inhomogeneity is related to the catalyst material itself which has typical structure sizes in the range of  $0.1\text{--}1 \mu\text{m}$  (cf. Fig. 8b). It is rather obvious that it is not possible to make a uniform  $\approx 1 \mu\text{m}$  thick catalyst layers when single catalyst particles are already on the same length scale. The result is an inhomogeneous catalyst layer, as evidenced by the top-view SEM image (Fig. 8b) of a  $0.20 \text{ mg}_{\text{Ir}} \text{ cm}^{-2}$  anode coated onto a Nafion membrane, where dark areas indicate  $\mu\text{m}$ -sized regions without any catalyst particles. However, since the free membrane patches in between the catalyst layer are of a dimension (on the order of  $0.5\text{--}2 \mu\text{m}$ ) which is more than an order of magnitude smaller than the thickness of the membrane, this cannot directly explain the higher HFR (see orange symbols in Fig. 6b).

Instead, we believe that the anomalously high HFR is related to the large pore sizes of the Ti PTL ( $10\text{--}50 \mu\text{m}$  pores) in combination with the low in-plane electronic conductivity of an inhomogeneous, non-contiguous anode catalyst layer, as outlined in the following. From Fig. 8a it becomes clear that due to the large structures of the PTL, not all parts of the catalyst layer are in direct electronic contact with the PTL, thus requiring in-plane electron conduction over distances of several tens of micrometers within the catalyst layer to enable the OER. For a thick and therefore contiguous catalyst layer (Fig. 8c), high in-plane electronic conductivity is provided by the good electronic conductivity of  $\text{IrO}_2$ . On the other hand, for a very thin and non-contiguous catalyst layer, the resistance for electron transport within the layer is expected to increase if electronic contact is not maintained throughout the entire catalyst layer, which in fact is evident from Fig. 8b. Therefore, segments of the low-loaded

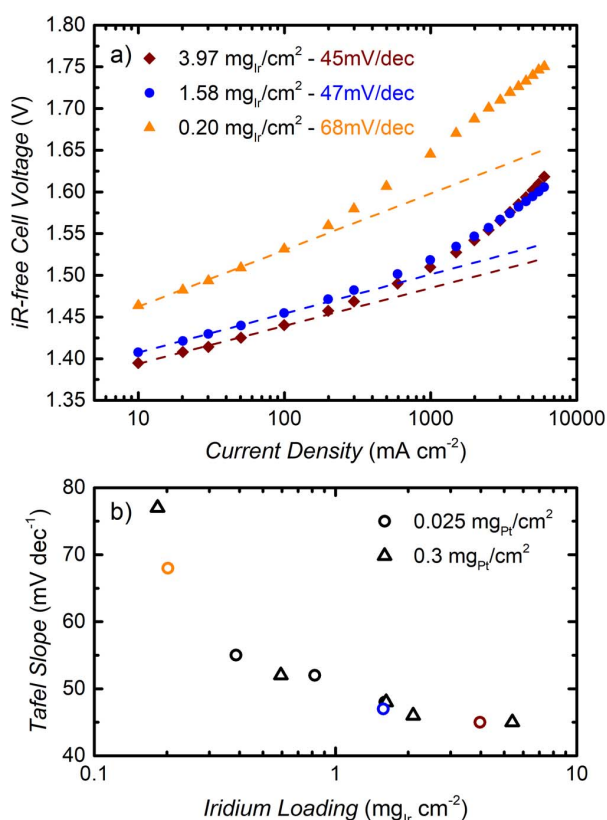


**Figure 7.** a) Ambient pressure Tafel plot of the  $iR$ -free cell voltage ( $80^\circ\text{C}$ ,  $5 \text{ ml}_{\text{H}_2\text{O}} \text{ min}^{-1}$ ) for different anode Ir loadings and thicknesses:  $0.20 \text{ mg}_{\text{Ir}} \text{ cm}_{\text{MEA}}^{-2}$  ( $\approx 1 \mu\text{m}$  thickness),  $1.58 \text{ mg}_{\text{Ir}} \text{ cm}_{\text{MEA}}^{-2}$  ( $\approx 7 \mu\text{m}$  thickness), and  $3.97 \text{ mg}_{\text{Ir}} \text{ cm}_{\text{MEA}}^{-2}$  ( $\approx 17 \mu\text{m}$  thickness). The Tafel slope is obtained from a linear fit of the values between  $10$ – $100 \text{ mA cm}^{-2}$ . b) Tafel slopes as a function of anode iridium loading. MEAs with low cathode loadings ( $\approx 0.025 \text{ mg}_{\text{Pt}} \text{ cm}_{\text{MEA}}^{-2}$ ) are represented by circles, MEAs with high cathode loadings ( $\approx 0.30 \text{ mg}_{\text{Pt}} \text{ cm}_{\text{MEA}}^{-2}$ ) are shown by triangles; the membrane was a  $\approx 50 \mu\text{m}$  thick Nafion 212.

anode catalyst layers with sizes comparable to the Ti PTL pore size ( $10$ – $50 \mu\text{m}$ ) will have poor or no electronic connection with the Ti PTL (see Fig. 8d), and will thus not participate in the OER. Furthermore, the fraction of inactive anode catalyst segments will increase with increasing current density (i.e., the catalyst utilization will decrease), resulting in the observed apparent increase of the Tafel slope. Under this hypothesis, the observed higher HFR for thin anodes (see orange symbols in Fig. 6b) is simply a consequence of the fact that the size of these electronically poorly connected patches are on the order of the thickness of the membrane.

This hypothesis can be probed by cyclic voltammetry (CV) as shown in our previous study,<sup>18</sup> where the mass normalized voltammetric charge,  $q^*$  (the sum of the absolute values of the anodic and cathodic charges), is used as a measure for the electrochemically active surface area.<sup>15,30,31</sup> Fig. 9a shows cyclic voltammograms of the anode electrode of the standard MEA with a  $\approx 7 \mu\text{m}$  thick anode (solid blue line) and the MEA with the  $\approx 1 \mu\text{m}$  thick low-loaded anode (dashed yellow line). Since the mass-specific current is plotted on the y-axis, one would expect similar voltammetric charges for both MEAs, independent of Ir loading. However,  $q^*$ , obtained by integration of the area under the CV, is  $\approx 35\%$  lower for the MEA with the low Ir loading, clearly showing a lower catalyst utilization for the thin, inhomogeneous and non-contiguous anode catalyst layer. Voltammetric charges,  $q^*$ , for all tested MEAs are shown in Fig. 9b. Here, it is readily observed that for Ir loadings  $< 0.5 \text{ mg}_{\text{Ir}} \text{ cm}^{-2}$ ,  $q^*$

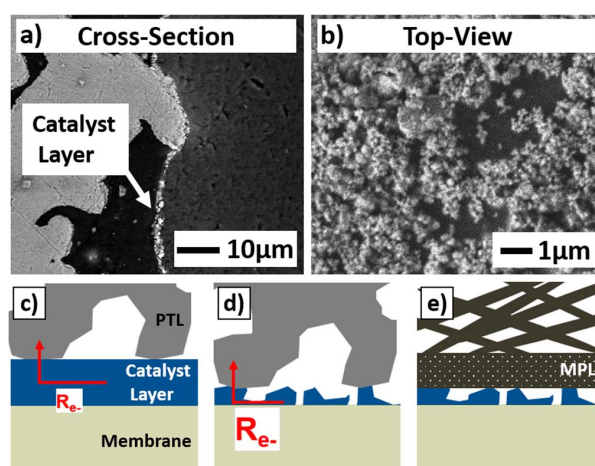


**Figure 8.** a) Cross-sectional SEM image of a  $\approx 1 \mu\text{m}$  thin anode catalyst layer with low Ir loading ( $0.20 \text{ mg}_{\text{Ir}} \text{ cm}_{\text{MEA}}^{-2}$ ). b) Top-view SEM image of the catalyst layer. Scheme illustrating the electronic transport within an anode catalyst layer and to the PTL for c) a homogeneous catalyst layer (Ir loading  $> 1 \text{ mg}_{\text{Ir}} \text{ cm}_{\text{MEA}}^{-2}$ ) and d) a thin, inhomogeneous catalyst layer (Ir loading  $< 0.50 \text{ mg}_{\text{Ir}} \text{ cm}_{\text{MEA}}^{-2}$ ). e) Replacement of Ti PTL by a carbon PTL with microporous layer (MPL) which has an effective pore size on the order of  $0.1 \mu\text{m}$ .

decreases significantly. As discussed before, we attribute this lower catalyst utilization to an insufficient in-plane electronic conductivity of the thin non-contiguous anode catalyst layer in combination with the large porous structure of the Ti PTL.

In order to prove this hypothesis, we replaced the Ti PTL with a carbon fiber paper, coated with a carbon-black based microporous layer (MPL) facing the anode catalyst layer, with the aim to improve the electronic contact with all segments of the anode electrode (cf. Fig. 8e). The pore size of the MPL is on the order of  $0.1 \mu\text{m}$ , and thus much smaller than that of the Ti PTL ( $10$ – $50 \mu\text{m}$ ). Using the carbon fiber paper with MPL, the CV of the MEA with low Ir loading (dotted purple line in Fig. 9a) now enlarges significantly, and its  $q^*$  value increases dramatically (see purple triangle in Fig. 9b) and reaches a value comparable to that of MEAs with Ir loadings  $> 1 \text{ mg}_{\text{Ir}} \text{ cm}^{-2}$ . This clearly supports our hypothesis that thin non-contiguous anode catalyst layers are characterized by a lower catalyst utilization, resulting from the combination of a large-pore PTL and an insufficient in-plane conductivity of the anode catalyst layer. It is important to note that this effect occurs already at very small absolute current densities during a CV measurement ( $\approx \pm 1.5 \text{ mA cm}^{-2}$  for the  $0.2 \text{ mg}_{\text{Ir}} \text{ cm}^{-2}$  anode shown in Fig. 9a). Since the in-plane electronic resistance within the catalyst layer will have a stronger effect at higher current densities (i.e., causing an even lower catalyst utilization), it is consistent with the observed disproportionately large increase of  $E_{iR\text{-free}}$  with current density for the MEA with low Ir loading (cf. Fig. 7a), the consequence of which is an apparently higher Tafel slope for MEAs with thin low-loaded anodes (cf. Fig. 7b). Ultimately, the application of a truly microporous MPL (pore size of  $< 1 \mu\text{m}$ ) could improve the performance of thin catalyst layers. Since the carbon paper would not be stable under OER conditions, a Ti PTL with MPL would be required and a beneficial effect of such a MPL has already been shown in the literature.<sup>32</sup>

**Iridium requirements for large-scale PEM electrolysis.**—Finally, we would like to discuss the implications of our analysis regarding the Ir requirements for a large-scale application of PEM electrolysis. As outlined in the Introduction section, there are several criteria which must be met: i) high cell voltage efficiency to minimize electricity cost (opex), with a 2030 target of  $\approx 70 \%$   $\text{LHV}$  ( $\equiv 1.79 \text{ V}$  cell voltage); ii) high current densities to minimize the investment cost (capex); and

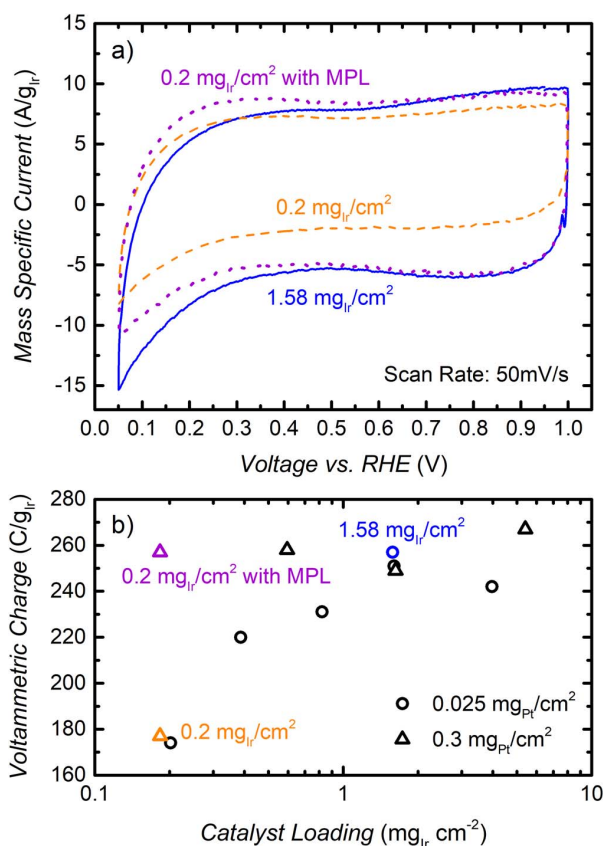


**Figure 9.** a) Ambient pressure cyclic voltammograms (CV) of  $\text{IrO}_2/\text{TiO}_2$  based anodes with different Ir loadings:  $0.20 \text{ mg}_{\text{Ir}} \text{ cm}_{\text{MEA}}^{-2}$  ( $\approx 1 \mu\text{m}$  thickness) and  $1.58 \text{ mg}_{\text{Ir}} \text{ cm}_{\text{MEA}}^{-2}$  ( $\approx 7 \mu\text{m}$  thickness). The mass-specific current is plotted vs. the applied potential. CVs were recorded at a scan rate of  $50 \text{ mV s}^{-1}$  at  $80^\circ\text{C}$ .  $\text{H}_2\text{O}$  was supplied to the anode at  $5 \text{ ml}_{\text{H}_2\text{O}} \text{ min}^{-1}$ , and dry  $\text{H}_2$  was supplied to the cathode at  $50 \text{ ml}_{\text{H}_2} \text{ min}^{-1}$ . b) Voltammetric charge,  $q^*$ , obtained from integration of the absolute values of the currents of the CVs as a function of anode iridium loading. MEAs with low cathode loadings ( $\approx 0.025 \text{ mg}_{\text{Pt}} \text{ cm}_{\text{MEA}}^{-2}$ ) are represented by circles, MEAs with high cathode loadings ( $\approx 0.30 \text{ mg}_{\text{Pt}} \text{ cm}_{\text{MEA}}^{-2}$ ) are shown by triangles.

iii) Ir-specific power densities of  $\approx 0.01 \text{ g}_{\text{Ir}} \text{ kW}^{-1}$  to meet the iridium supply constraints for large-scale implementation. This means that the iridium loadings must be minimized while maintaining high current density at low electrolyzer cell voltages, whereby it is unclear whether this requirement can be met with the OER activity of currently known  $\text{IrO}_2$ -based anode catalysts.

The Ir-specific power density vs. current density shown in Fig. 10b is obtained from the measured polarization curves (cf. Fig. 10a) by dividing the anode Ir loading by the product of cell voltage and current density. The current density and Ir-specific power density at which the cell voltage efficiency corresponds to  $70\%_{\text{LHV}}$  ( $\equiv 1.79 \text{ V}$ ) is marked in Fig. 10b by the intersection of the dashed black line with the line representing each of the measured anode loadings (cathode Pt loadings are either  $0.30$  or  $0.025 \text{ mg}_{\text{Pt}} \text{ cm}^{-2}$ ). For conventionally used Ir loadings of  $\approx 1.6 \text{ mg}_{\text{Ir}} \text{ cm}^{-2}$  (blue and red lines in Fig. 10), the cell voltage efficiency target of  $70\%_{\text{LHV}}$  ( $\equiv 1.79 \text{ V}$ ) is met at a current density of  $\approx 3.6 \text{ A cm}^{-2}$  and an Ir-specific power density of  $\approx 0.25 \text{ g}_{\text{Ir}} \text{ kW}^{-1}$ . Quite clearly, this is still more than an order of magnitude higher than the target value of  $0.01 \text{ g}_{\text{Ir}} \text{ kW}^{-1}$  that we consider necessary for a large-scale decarbonization of the transportation sector by means of electrolytic hydrogen, even though ohmic losses were already minimized by using a thin membrane ( $\approx 50 \mu\text{m}$ ). Obviously, a significant

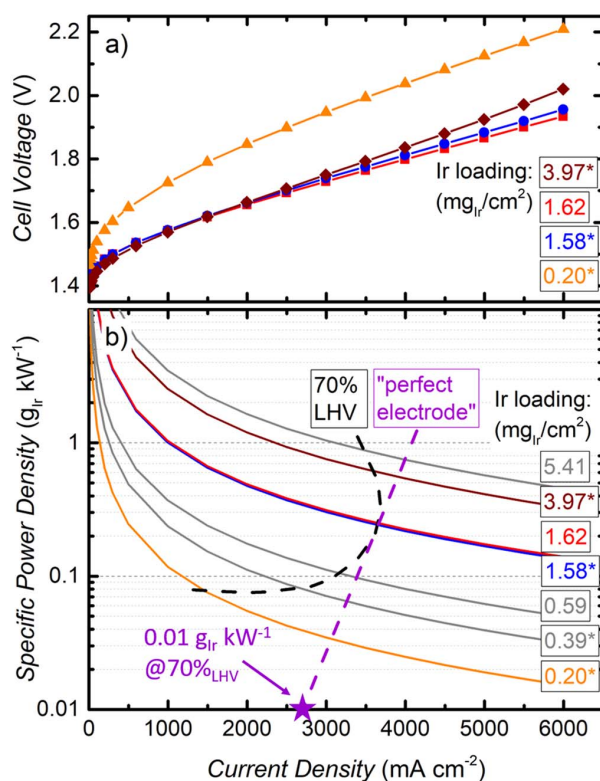


**Figure 10.** a) Ambient pressure polarization curves for different Ir anode loadings at  $80^\circ\text{C}$  ( $5 \text{ ml}_{\text{H}_2\text{O}} \text{ min}^{-1}$ ) with cathode loadings of either  $\approx 0.30 \text{ mg}_{\text{Pt}} \text{ cm}_{\text{MEA}}^{-2}$  or  $\approx 0.025 \text{ mg}_{\text{Pt}} \text{ cm}_{\text{MEA}}^{-2}$  (curves with low cathode loadings are marked by an asterisk at the anode loading label). b) Ir-specific power density as a function of current density for MEAs with different Ir loadings ( $0.20$ – $5.41 \text{ mg}_{\text{Ir}} \text{ cm}_{\text{MEA}}^{-2}$ ). The black dashed line indicates an electrolyzer efficiency of  $70\%_{\text{LHV}}$ , corresponding to a cell voltage of  $1.79 \text{ V}$ . The purple dashed line indicates an electrolyzer efficiency of  $70\%_{\text{LHV}}$  based on the performance of the MEAs with standard Ir loadings ( $\approx 1.6 \text{ mg}_{\text{Ir}} \text{ cm}_{\text{MEA}}^{-2}$ ) and assuming that only the overpotential of the OER changes with Ir loading (Tafel slope:  $\approx 47 \text{ mV dec}^{-1}$ ), i.e., that HFR, proton and mass transport are similar for all MEAs and no additional losses occur for lower or higher Ir loadings. The purple star marks the target value of  $0.01 \text{ g}_{\text{Ir}} \text{ kW}^{-1}$  at an efficiency of  $70\%_{\text{LHV}}$ .

reduction of the Ir anode loading is required to reach the ambitious targets outlined above. If requiring a cell voltage efficiency of  $70\%_{\text{LHV}}$ , the minimum Ir-specific power density that can be reached with MEAs prepared in this work is  $\approx 0.08 \text{ g}_{\text{Ir}} \text{ kW}^{-1}$ , which was obtained for the lowest loaded anode with  $0.2 \text{ mg}_{\text{Ir}} \text{ cm}^{-2}$  (marked by the intersection of the orange line with the dashed black line in Fig. 10b) at a rather low current density of  $\approx 1.5 \text{ A cm}^{-2}$ .

Even though the lowest achieved Ir-specific power density is still 8-fold above the desired target, the poor performance of the low-loaded anode is not due to insufficient OER kinetics, but, as discussed above, caused by the inability to prepare such thin anode catalyst layers that are homogenous and contiguous, at least with the anode catalyst used in this study. While we have not been able to overcome this difficulty, one can still conduct a thought-experiment of how an  $\text{IrO}_2$ -based catalyst would perform at low loadings, if one were able to make a “perfect” homogenous and contiguous electrode that would have equally low transport resistances and HFR-values, as are observed for anodes with an optimal thickness between  $4$ – $8 \mu\text{m}$  (here corresponding to a loading of  $1$ – $2 \text{ mg}_{\text{Ir}} \text{ cm}^{-2}$ ; see Fig. 3). This thought-experiment can be conducted in the following manner based on the polarization curve with anode and cathode loadings of



1.58 mg<sub>Ir</sub> cm<sup>-2</sup> and 0.025 mg<sub>Pt</sub> cm<sup>-2</sup>, respectively (blue line in Fig. 10a): i) calculating the difference in OER overpotential for lower Ir loadings by means of Eq. 3 using a Tafel slope of 47 mV dec<sup>-1</sup>; ii) upshifting the polarization curve obtained for the MEA with the 1.58/0.025 mg<sub>Pt</sub> cm<sup>-2</sup> (anode/cathode) loading by the calculated OER overpotential difference; iii) determining the current density of the upshifted curve at a cell voltage of 1.79 V (≡70 %<sub>LHV</sub>); and iv) dividing the assumed Ir loading by the resulting power density at 1.79 V and plotting the thus calculated Ir-specific power density vs. current density for different hypothetical Ir loadings. The thus projected Ir-specific power density vs. current density relationship for a “perfect” electrode at a cell voltage of 1.79 V is shown by the dashed purple line in Fig. 10b. It is based on the assumption that the HFR, as well as proton- and mass transport losses for the ≈7 μm thick standard MEA (with 1.58 mg<sub>Ir</sub> cm<sup>-2</sup> and 0.025 mg<sub>Pt</sub> cm<sup>-2</sup>) can be maintained constant independent of the Ir anode catalyst loading, i.e., that the Ir loading only affects the kinetic OER overpotential (cf. Eq. 3).

The “perfect” electrode projection (purple line in Fig. 10b) reveals that a Ir-specific power density of 0.01 g<sub>Ir</sub> kW<sup>-1</sup> at 1.79 V could be reached with an IrO<sub>2</sub>-based anode catalyst at a current density of ≈2.7 A cm<sup>-2</sup> (x-axis intercept of the purple dashed line in Fig. 10b), i.e., at a power density of ≈5 W cm<sup>-2</sup>. This, in turn, means that a catalyst with the same OER kinetics as the IrO<sub>2</sub>/TiO<sub>2</sub> catalyst used here, incorporated at a loading of ≈0.05 mg<sub>Ir</sub> cm<sup>-2</sup> (the product of 0.01 g<sub>Ir</sub> kW<sup>-1</sup> and ≈5 W cm<sup>-2</sup>) into a “perfect” electrode, would in principle be able to meet the target of 0.01 g<sub>Ir</sub> kW<sup>-1</sup> at 1.79 V. “Perfect” electrode in this context implies a homogeneous and contiguous electrode, which would not be possible for the IrO<sub>2</sub>/TiO<sub>2</sub> catalyst used in this work, because the corresponding anode thickness of ≈0.2 μm (based on its here measured packing density of 4.3 ± 0.3 μm (mg<sub>Ir</sub> cm<sup>-2</sup>)<sup>-1</sup>) could not be realized. The ideal thickness for a ≈0.05 mg<sub>Ir</sub> cm<sup>-2</sup> anode would rather be on the order of ≈4–8 μm (based on Fig. 3), which translates into an extremely low packing density of ≈80–160 μm (mg<sub>Ir</sub> cm<sup>-2</sup>)<sup>-1</sup>.

In fuel cell electrodes, such low packing densities are commonly used and are realized by supporting Pt nanoparticles on a highly structured carbon support; e.g., the packing density of a 15 wt% Pt/Vulcan catalyst is ≈125 μm (mg<sub>Pt</sub> cm<sup>-2</sup>)<sup>-1</sup> (based on 22 μm (mg<sub>C</sub> cm<sup>-2</sup>)<sup>-1</sup> · (15/85 mg<sub>Pt</sub> · mg<sub>C</sub><sup>-1</sup>)<sup>-1</sup>).<sup>17</sup> For an OER catalyst, however, this would require the deposition of Ir nanoparticles on a similarly high-structured support with sufficient electronic conductivity and stability at the high anodic potentials of an electrolyzer anode (precluding the use of carbon). Examples for this might include Ir nanoparticles deposited on, e.g., antimony-doped tin oxide (ATO).<sup>33,34</sup> In the absence of a suitable conductive oxide support, IrO<sub>2</sub> catalyst structures with a porosity of ≈99% (corresponding to ≈85 μm (mg<sub>Ir</sub> cm<sup>-2</sup>)<sup>-1</sup>) would be required.

In summary, this illustrates that a large-scale application of PEM electrolysis is in principle feasible with Ir based catalysts. However, advanced catalyst concepts, viz., Ir or IrO<sub>2</sub> nanoparticles on conductive and oxidatively stable supports or Ir/IrO<sub>2</sub> aerogels with extremely high void volume would be necessary to fabricate homogeneous and contiguous catalyst layers at Ir loadings of ≈0.05 mg<sub>Ir</sub> cm<sup>-2</sup>. Concerning the Pt cathode catalyst, loadings of 0.025 mg<sub>Pt</sub> cm<sup>-2</sup> are possible without significant performance loss, which at a power density of ≈5 W cm<sup>-2</sup> equates to only 0.005 g<sub>Pt</sub> kW<sup>-1</sup>. Assuming an annual installation capacity of ≈150 GW (cf. Introduction section), this translates into a Pt consumption of less than 1 ton/year, which should not be limiting considering the ≈50-fold higher mining rate of Pt compared to Ir. While this analysis is based on the beginning-of-life performance of electrolyzer MEAs, it must be noted that it is still an open question as to whether sufficient durability can be obtained with such low catalyst loadings.

Finally, it needs to be stressed that our projections above present an extreme example based on the assumption that hydrogen were to solely replace fossil fuels in the transportation sector and that all hydrogen would be produced by PEM electrolysis. In reality, other technologies (e.g. battery electric vehicles) will also take a significant share of

vehicle propulsion systems in the future. Furthermore, alkaline electrolysis is a well-established technology and will likely continue to play an important role in electrolytic hydrogen production.<sup>35</sup> After all, while the final application might not actually require a specific power density as low as 0.01 g<sub>Ir</sub> kW<sup>-1</sup>, our work revealed that this ambitious target could be met with Ir-based catalysts if incorporated in an appropriate electrode structure.

## Conclusions

In this study, we presented an analysis of the influence of catalyst loading on the performance of a PEM electrolyzer using commercial Pt/C catalysts for the hydrogen evolution reaction (HER) and IrO<sub>2</sub>/TiO<sub>2</sub> for the oxygen evolution reaction (OER) in in-house prepared membrane electrode assemblies (MEAs) based on a 50 μm Nafion 212 membrane. We showed that the Pt loading on the cathode has only a minor effect on the performance due to its high HER activity and that a reduction from 0.30 mg<sub>Pt</sub> cm<sup>-2</sup> to 0.025 mg<sub>Pt</sub> cm<sup>-2</sup> is possible without significant performance losses.

The Ir loading giving the best overall performance was found to be ≈1–2 mg<sub>Ir</sub> cm<sup>-2</sup>, which corresponds to an anode electrode thickness of ≈4–8 μm. For thicker electrodes (>10 μm, Ir loading >2 mg<sub>Ir</sub> cm<sup>-2</sup>), an increase of cell voltage and HFR at high current densities was observed, which we attribute to the high water transport resistance through a thick catalyst layer, leading to a low water content in the membrane near the membrane/anode interface and an associated drop in membrane conductivity. On the other hand, for very thin anode electrodes (<2 μm, Ir loading <0.5 mg<sub>Ir</sub> cm<sup>-2</sup>), the electrolyzer performance decreases drastically due to the inhomogeneous non-contiguous character of such thin catalyst layers, resulting in poor anode catalyst utilization and an associated higher HFR value. We have demonstrated that this effect can be mitigated by incorporating a porous transport layer (PTL) modified with a microporous layer.

Finally, we have evaluated the performance at various Ir loadings in the context of Ir-specific power requirements for large-scale applications, which we argue to be at or below ≈0.01 g<sub>Ir</sub> kW<sup>-1</sup> at 70 %<sub>LHV</sub> (≡1.79 V cell voltage). With the commercial IrO<sub>2</sub>/TiO<sub>2</sub> anode catalyst used in this study, it is not possible to reach this target value due to performance losses at low catalyst loadings or, more precisely, for thin electrodes. However, our analysis shows that the intrinsic OER activity of Ir-based catalysts would be sufficient to reach ≈0.01 g<sub>Ir</sub> kW<sup>-1</sup> at 1.79 V, if the packing density of iridium in the electrode can be reduced, so that ≈4–8 μm thick electrodes with an Ir loading of only ≈0.05 mg<sub>Ir</sub> cm<sup>-2</sup> can be made. This shows that catalyst morphology/structure may be equally important as its OER activity.

## Acknowledgments

This work was funded by the Bavarian Ministry of Economic Affairs and Media, Energy and Technology through the project ZAE-ST (storage technologies) as well as by the German Federal Ministry of Education and Research (BMBF) in the framework of the Kopernikus P2X project (funding number 03SFK2V0). We thank Matthias Singer for electrode preparation as well as Alexandra Weiß and Maximilian Möckl for reviewing the paper. The electron microscopy was accomplished at the WACKER-Chair of Molecular Chemistry of the TUM with the assistance of Katia Rodewald.

## Appendix

The expected kinetic overpotential for the hydrogen evolution reaction (HER),  $\eta_{\text{HER}}$ , for the different Pt loadings can be estimated via linearization of the Butler-Volmer equation.<sup>36,37</sup>

$$\eta_{\text{HER}} = i \cdot R_{\text{K,HER}} \quad [\text{A1}]$$

where

$$R_{\text{K,HER}} = \frac{RT}{(\alpha_a + \alpha_c) \cdot F \cdot L_{\text{Pt}} \cdot A_{\text{Pt,el}} \cdot i_{0,\text{HER}}} \quad [\text{A2}]$$

With an HER exchange current density of  $i_{0,HER} = 250 \text{ mA cm}^{-2}_{\text{metal}}$  (for  $\alpha_a + \alpha_c = 1$ ) at  $80^\circ\text{C}$ ,<sup>7,8</sup> cathode catalyst loading of  $L_{Pt}(45.8\text{wt}\% \text{ Pt}) = 0.30 \text{ mg}_{Pt}/\text{cm}^2$  or  $L_{Pt}(4.8\text{wt}\% \text{ Pt}) = 0.025 \text{ mg}_{Pt}/\text{cm}^2$ , and electrochemically active surface area of  $A_{Pt,el}(45.8\text{wt}\% \text{ Pt}) = 60 \text{ m}^2/\text{g}_{Pt}$ <sup>37</sup> or  $A_{Pt,el}(4.8\text{wt}\% \text{ Pt}) = 110 \text{ m}^2/\text{g}_{Pt}$ ,<sup>7,8</sup>  $R_{K,HER}$  amounts to  $\approx 0.7 \text{ m}\Omega \text{ cm}^2$  for the high Pt loading and  $\approx 4.4 \text{ m}\Omega \text{ cm}^2$  for the low Pt loading. This results in a difference  $\Delta R_{K,HER} = 3.7 \text{ m}\Omega \text{ cm}^2$ .

The effective proton transport resistance for the hydrogen cathode can be calculated following the approach described by Gu et al.:<sup>37</sup>

$$\frac{R_{H^+,cath}^{eff}}{R_{H^+,cath}} = \frac{1}{\beta} \cdot \left( \frac{e^\beta + e^{-\beta}}{e^\beta - e^{-\beta}} - \frac{1}{\beta} \right) \quad [A3]$$


where

$$\beta = \left( \frac{R_{H^+,cath}}{R_{K,HER}} \right)^{1/2} \quad [A4]$$

Here, the sheet resistance for proton transport in a Pt/C electrode,  $R_{H^+,cath}$ , can be calculated from the reported sheet resistivity of  $\approx 25 \text{ }\Omega \text{ cm}$  for a Pt/Vulcan electrode with an I/C-ratio of 0.6/1 at  $80^\circ\text{C}$  and a relative humidity of 122 % (i.e., in the presence of liquid water)<sup>38</sup> and the electrode thicknesses of  $\approx 8 \text{ }\mu\text{m}$  for the high-loaded and  $\approx 11 \text{ }\mu\text{m}$  for low-loaded cathode (s. Experimental Section), equating to proton conduction sheet resistances of  $R_{H^+,cath}(45.8\text{wt}\% \text{ Pt}) \approx 20 \text{ m}\Omega \text{ cm}^2$  and  $R_{H^+,cath}(4.8\text{wt}\% \text{ Pt}) \approx 27.5 \text{ m}\Omega \text{ cm}^2$ . Together with the above determined charge transfer resistances ( $R_{K,HER}(45.8\text{wt}\% \text{ Pt}) \approx 0.7 \text{ m}\Omega \text{ cm}^2$  and  $R_{K,HER}(4.8\text{wt}\% \text{ Pt}) \approx 4.4 \text{ m}\Omega \text{ cm}^2$ ), this yields  $\beta$ -values of  $\approx 5.4$  for the high-loaded and  $\approx 2.5$  for the low-loaded cathode (s. Eq. A4). Thus, the effective proton transport resistance,  $R_{H^+,cath}^{eff}$ , calculated by Eq. A3 is  $\approx 3 \text{ m}\Omega \text{ cm}^2$  for the high-loaded and  $\approx 6.8 \text{ m}\Omega \text{ cm}^2$  for the low-loaded cathode. From the sum of kinetic and proton transport resistance ( $R_{K,HER} + R_{H^+,cath}^{eff}(45.8\text{wt}\% \text{ Pt}) \approx 3.7 \text{ m}\Omega \text{ cm}^2$  and  $R_{K,HER} + R_{H^+,cath}^{eff}(4.8\text{wt}\% \text{ Pt}) \approx 11.2 \text{ m}\Omega \text{ cm}^2$ ) one can calculate a total difference of  $\approx 7.5 \text{ m}\Omega \text{ cm}^2$  between high-loaded and low-loaded cathode.

## ORCID

Maximilian Bernt  <https://orcid.org/0000-0001-8448-5532>

Armin Siebel  <https://orcid.org/0000-0001-5773-3342>

## References

- L. Bertuccioli, A. Chan, D. Hart, F. Lehner, B. Madden, and E. Standen, Study on Development of Water Electrolysis in the EU, in *Fuel Cells and Hydrogen Joint Undertaking* (2014).
- T. Smolinka, M. Günther, and J. Garche, Stand und Entwicklungspotenzial der Wasserelektrolyse zur Herstellung von Wasserstoff aus regenerativen Energien, in *Kurzfassung des Abschlussberichtes NOW-Studie* (2011).
- K. E. Ayers, J. N. Renner, N. Danilovic, J. X. Wang, Y. Zhang, R. Maric, and H. Yu, *Catalysis Today*, **262**, 121 (2016).
- U. Babic, M. Suermann, F. N. Büchi, L. Gubler, and T. J. Schmidt, *Journal of The Electrochemical Society*, **164**, F387 (2017).
- K. E. Ayers, E. B. Anderson, C. Capuano, B. Carter, L. Dalton, G. Hanlon, J. Manco, and M. Niedzwiecki, *ECS Transactions*, **33**, 3 (2010).
- M. Carmo, D. L. Fritz, J. Mergel, and D. Stolten, *International Journal of Hydrogen Energy*, **38**, 4901 (2013).
- J. Durst, A. Siebel, C. Simon, F. Hasché, J. Herranz, and H. A. Gasteiger, *Energy Environ. Sci.*, **7**, 2255 (2014).
- J. Durst, C. Simon, F. Hasche, and H. A. Gasteiger, *Journal of the Electrochemical Society*, **162**, F190 (2015).
- IEA, *Key World Energy Statistics 2016* (2017).
- C. K. Mittelsteadt, *ECS Trans.*, **69**, 205 (2015).
- L. Ma, S. Sui, and Y. Zhai, *International Journal of Hydrogen Energy*, **34**, 678 (2009).
- J. Polonský, P. Mazúr, M. Paidar, E. Christensen, and K. Bouzek, *International Journal of Hydrogen Energy*, **39**, 3072 (2014).
- P. Mazúr, J. Polonský, M. Paidar, and K. Bouzek, *International Journal of Hydrogen Energy*, **37**, 12081 (2012).
- K. A. Lewinski, D. F. v. d. Vliet, and S. M. Luopa, *ECS Transactions*, **69**, 893 (2015).
- C. Rozain, E. Mayousse, N. Guillet, and P. Millet, *Applied Catalysis B: Environmental*, **182**, 153 (2016).
- C. Rozain, E. Mayousse, N. Guillet, and P. Millet, *Applied Catalysis B: Environmental*, **182**, 123 (2016).
- G. S. Harzer, J. N. Schwämmlein, A. M. Damjanović, S. Ghosh, and H. A. Gasteiger, *Journal of The Electrochemical Society*, **165**, F3118 (2018).
- M. Bernt and H. A. Gasteiger, *Journal of The Electrochemical Society*, **163**, F3179 (2016).
- P. J. Rheinländer, M. Bernt, Y. Incedag, and H. A. Gasteiger, *Meeting Abstracts*, **MA2016-02**, 2427 (2016).
- M. Suermann, T. J. Schmidt, and F. N. Büchi, *ECS Transactions*, **69**, 1141 (2015).
- T. E. Springer, T. Zawodzinski, and S. Gottesfeld, *Journal of the Electrochemical Society*, **138**, 2334 (1991).
- S. Gottesfeld and T. A. Zawodzinski, in *Advances in Electrochemical Science and Engineering*, R. C. Alkire, H. Gerischer, D. M. Kolb and C. W. Tobias Editors, John Wiley & Sons (1997).
- M. Doyle and G. Rajendran, in *Handbook of Fuel Cells: Fundamentals, Technology, and Applications*, W. Vielstich, A. Lamm, and H. A. Gasteiger Editors, p. 18, John Wiley & Sons, New York (2003).
- M. Suermann, A. Pátru, T. J. Schmidt, and F. N. Büchi, *International Journal of Hydrogen Energy*, **42**, 12076 (2017).
- S. A. Grigoriev, P. Millet, S. V. Korobtsev, V. I. Porembskiy, M. Pepic, C. Etievant, C. Puyenchet, and V. N. Fateev, *International Journal of Hydrogen Energy*, **34**, 5986 (2009).
- M. Suermann, T. J. Schmidt, and F. N. Büchi, *Electrochimica Acta*, **211**, 989 (2016).
- M. Suermann, K. Takanohashi, A. Lamibrac, T. J. Schmidt, and F. N. Büchi, *Journal of The Electrochemical Society*, **164**, F973 (2017).
- Y. Matsumoto and E. Sato, *Materials Chemistry and Physics*, **14**, 397 (1986).
- T. Reier, D. Teschner, T. Lunkenbein, A. Bergmann, S. Selve, R. Kraehnert, R. Schlogl, and P. Strasser, *Journal of the Electrochemical Society*, **161**, F876 (2014).
- G. Lodi, E. Sivieri, A. De Battisti, and S. Trasatti, *Journal of Applied Electrochemistry*, **8**, 135 (1978).
- S. Ardizzone, G. Fregonara, and S. Trasatti, *Electrochimica Acta*, **35**, 263 (1990).
- P. Lettenmeier, S. Kolb, F. Burggraf, A. S. Gago, and K. A. Friedrich, *Journal of Power Sources*, **311**, 153 (2016).
- H.-S. Oh, H. N. Nong, T. Reier, M. Gliech, and P. Strasser, *Chemical Science*, **6**, 3321 (2015).
- G. Liu, J. Xu, Y. Wang, and X. Wang, *Journal of Materials Chemistry A*, **3**, 20791 (2015).
- A. Butler and H. Spliethoff, *Renewable and Sustainable Energy Reviews*, **82**, 2440 (2018).
- K. C. Neyerlin, W. Gu, J. Jorne, and H. A. Gasteiger, *Journal of The Electrochemical Society*, **154**, B631 (2007).
- W. Gu, D. R. Baker, Y. Liu, and H. A. Gasteiger, in *Handbook of Fuel Cells*, W. Vielstich, H. A. Gasteiger, and H. Yokokama Editors, p. 631, John Wiley & Sons, Chichester, UK (2009).
- Y. Liu, M. W. Murphy, D. R. Baker, W. Gu, C. Ji, J. Jorne, and H. A. Gasteiger, *Journal of The Electrochemical Society*, **156**, B970 (2009).



### 4.3 Impact of Intermittent Operation on Lifetime and Performance of a PEM Water Electrolyzer

This section presents the article "Impact of Intermittent Operation on Lifetime and Performance of a PEM Water Electrolyzer".<sup>[159]</sup> The article was submitted in January 2019 and accepted for publication in *The Journal of the Electrochemical Society* in April 2019 as an open access article, distributed under the terms of the Creative Commons Attribution 4.0 License (CC BY). This study was presented by Alexandra Weiß at the 234<sup>th</sup> Meeting of The Electrochemical Society (October 2018) in Cancun, Mexico (abstract number: # I01F-1598). The permanent web link to the article is <http://jes.ecsdl.org/content/166/8/F487>.

In this study, the influence of intermittent operation on the degradation of a PEM-WE is investigated. To mimic the effect of a fluctuating power supply, an AST protocol was designed comprising periods of operation at two different current densities ( $3 \text{ A cm}^{-2}$  and  $0.1 \text{ A cm}^{-2}$ ) and current interruptions where the cell is left at OCV. An initial increase in performance is observed during the first 10 cycles ( $\approx 50 \text{ mV}$ ) while prolonged cycling leads to a significant decrease in performance due to an increasing HFR (factor  $\approx 1.6$  after 700 cycles). The initial performance increase can be related to the reducing atmosphere on the anode due to  $\text{H}_2$  crossover and a resulting voltage drop during OCV periods. This leads to a reduction of the thermal  $\text{IrO}_2$  catalyst to metallic Ir at the surface of the catalyst, which is subsequently oxidized during periods of operation, leading to a transformation of the crystalline  $\text{IrO}_2$  to an amorphous  $\text{IrO}_x$  over the course of cycling. This transformation was detected by a change of the Tafel slope and by CVs showing features typical for metallic Ir and amorphous  $\text{IrO}_x$  during the test. Such an amorphous  $\text{IrO}_x$  is known to exhibit a higher activity, thus explaining the initial performance increase. However, the cycling between oxidizing conditions during operation and reducing conditions during OCV periods (i.e., the cycling between an oxidized and a metallic Ir surface) leads to the dissolution of Ir which can be proven by STEM imaging of the anode/membrane interface where dissolved Ir particles are detected in the membrane. How the dissolution of Ir and/or the transformation from a crystalline to a more amorphous  $\text{IrO}_x$  structure lead to the increasing HFR is not clear so far and further investigations will be required. Other factors which could lead to an increasing HFR, such as ionic contaminations, were

excluded, however, an increase of the PTL contact resistance during cycling was observed, which is responsible for a small fraction of the HFR increase. Since a reference experiment where the OCV period was replaced by a potential hold at 1.3 V showed no degradation over 500 cycles, the performance loss can clearly be attributed to the OCV periods. Hence, avoiding OCV periods during operation of a PEM-WE is crucial to ensure sufficient durability.

### **Author contributions**

Fabrication of membrane electrode assemblies, physical characterization and electrochemical testing was done by A.W., A.S., and M.B. Analysis of the experimental results was performed by A.S. A.W. wrote the manuscript. All authors discussed the experimental results and revised the manuscript.



## Impact of Intermittent Operation on Lifetime and Performance of a PEM Water Electrolyzer

A. Weiß,<sup>1,\*,\*z</sup> A. Siebel,<sup>1,\*,\*</sup> M. Bernt,<sup>1,2,\*</sup> T.-H. Shen,<sup>3</sup> V. Tileli,<sup>3</sup> and H. A. Gasteiger<sup>1,\*\*</sup>

<sup>1</sup>Chair of Technical Electrochemistry, Department of Chemistry and Catalysis Research Center, Technical University of Munich, 85747 Garching, Germany

<sup>2</sup>Bayerisches Zentrum für angewandte Energieforschung, 85748 Garching, Germany

<sup>3</sup>Institute of Materials, École Polytechnique Fédérale de Lausanne, CH-1015 Lausanne, Switzerland

The aim of this study is to provide a better understanding of performance degrading mechanisms occurring when a proton exchange membrane water electrolyzer (PEM-WE) is coupled with renewable energies, where times of operation and idle periods alternate. An accelerated stress test (AST) is proposed, mimicking a fluctuating power supply by operating the electrolyzer cell between high ( $3 \text{ A cm}^{-2}_{\text{geo}}$ ) and low current densities ( $0.1 \text{ A cm}^{-2}_{\text{geo}}$ ), alternating with idle periods during which no current is supplied and the cell rests at open circuit voltage (OCV). Polarization curves, periodically recorded during the OCV-AST, reveal an initial increase in activity ( $\approx 50 \text{ mV}$  after 10 cycles) followed by a significant decrease in performance during prolonged OCV cycling due to an increasing high frequency resistance (HFR) ( $\approx 1.6$ -fold after 718 cycles). These performance changes can clearly be related to the OCV periods, since they are not observed in a reference experiment where the OCV period is replaced by a potential hold at 1.3 V. The origin of the phenomena, which are responsible for the initial performance gain as well as the subsequent decay are analyzed via detailed electrochemical and physical characterization of the MEAs, and an operating strategy to prevent performance degradation is proposed.

© The Author(s) 2019. Published by ECS. This is an open access article distributed under the terms of the Creative Commons Attribution 4.0 License (CC BY, <http://creativecommons.org/licenses/by/4.0/>), which permits unrestricted reuse of the work in any medium, provided the original work is properly cited. [DOI: 10.1149/2.0421908jes]



Manuscript submitted January 3, 2019; revised manuscript received April 8, 2019. Published April 29, 2019. This was Paper 1606 presented at the Cancun, Mexico, Meeting of the Society, September 30-October 4, 2018.

In light of the fact that the energy demand is ever-increasing and that renewable energy sources, inherently intermittent in energy output, are becoming more and more important, an efficient way of storing energy is of crucial importance. One prominent example for an energy carrier meeting these requirements is gaseous hydrogen, produced in a polymer electrolyte membrane water electrolyzer (PEM-WE) via electrochemical water splitting.<sup>1,2</sup> The reliability of a PEM-WE has already been reported for  $\approx 60,000$  h of operation, showing only a marginal loss in performance.<sup>3-4</sup> In an ideal scenario, PEM-WE systems would be coupled with renewable energy sources in order to fully utilize their output by converting temporary excess energy into  $\text{H}_2$ .<sup>5</sup> This dynamic mode of operation involves frequent load changes and idle periods during which no current is supplied.<sup>2,6-8</sup> While it is well known that alkaline water electrolyzers must be operated with a so-called protective current in stand-by/idle conditions (i.e., when no power is provided by renewable energy sources) in order to avoid a substantial performance degradation,<sup>4,7,9-10</sup> very little is known about the gravity of this effect in PEM-WEs, even though it will be an important consideration for coupling PEM-WEs with renewable energy sources.<sup>6,11</sup> In this paper, we will try to further investigate this phenomenon, but first will briefly review the most common failure mechanisms of PEM-WEs.

A commonly observed failure of PEM-WEs has been related to the chemical degradation of the perfluorosulfonic acid (PFSA) based polymer electrolyte membrane, often observed as thinning of the membrane or as localized pinholes in the membrane. The concomitant increase in gas permeation ultimately leads to an unacceptably large, safety-critical  $\text{H}_2$  concentration in the  $\text{O}_2$  anode compartment, as the  $\text{H}_2$  oxidation activity of iridium based anode catalysts is very poor (contrary to the  $\text{O}_2$  reduction activity in the  $\text{H}_2$  anode). This is described in an early study by Stucki et al., who showed that the failure of a dynamically operated 100 kW PEM-WE plant after only  $\approx 15,000$  h was mostly related to thinning of the PFSA membrane, caused by chemical degradation.<sup>12</sup> Here, however, it should be noted that the chemical durability of today's PFSA membranes is dramatically better

owing to stabilization of the polymer endgroups,<sup>13</sup> so that membrane thinning is likely less of an issue when using state-of-the-art PFSA membranes.<sup>14</sup> Another membrane related degradation effect is the contamination of the ionomeric membrane with cations,<sup>11,15-16</sup> typically introduced by improperly treated feed-water which is the major cause for PEM-WE failures in the field.<sup>16-17</sup> Sun et al. showed the operation of a 9-cell PEM-WE stack for 7800 h at constant current, and recorded a gradual decrease in performance that they attributed to cationic contamination, since the initial performance was mostly recovered by boiling the degraded MEA (membrane-electrode-assembly) in sulfuric acid.<sup>18</sup>

Apart from degradation of the membrane in the membrane-electrode-assembly via chemical degradation and cationic contamination, gradual passivation of the titanium porous transport layer (PTL) at the high potentials experienced by the anode electrode of an electrolyzer increases the internal ohmic resistance and, hence, leads to a decrease of performance. This was demonstrated by Rakousky et al. after operation at  $2 \text{ A cm}^{-2}_{\text{geo}}$  for 1000 h, where the high-frequency resistance (HFR) increased by  $26 \text{ m}\Omega \text{ cm}^2_{\text{geo}}$  ( $\approx 20\%$ ) due to passivation of the Ti-PTL.<sup>19</sup> In addition, the authors observed a reduction of the anodic exchange current density, which they attribute to a contamination with titanium from either the anode catalyst itself (iridium oxide coated onto a titanium oxide support) or the anodic Ti-PTL.

With regards to the effect of dynamic PEM-WE operation, Rakousky et al. investigated the influence of different load profiles over 1000 h, namely constant current of 1 or  $2 \text{ A cm}^{-2}_{\text{geo}}$ , cycling between 1 and  $2 \text{ A cm}^{-2}_{\text{geo}}$ , or cycling between open-circuit voltage (OCV) and  $2 \text{ A cm}^{-2}_{\text{geo}}$ .<sup>20</sup> At a constant current of  $2 \text{ A cm}^{-2}_{\text{geo}}$  the authors observed an untypically high degradation rate ( $\approx 200 \mu\text{V h}^{-1}$ ) compared to that at a constant current of  $1 \text{ A cm}^{-2}_{\text{geo}}$  ( $< 1 \mu\text{V h}^{-1}$ ). When cycling between 1 and  $2 \text{ A cm}^{-2}_{\text{geo}}$  or between OCV and  $2 \text{ A cm}^{-2}_{\text{geo}}$ , the degradation rate was substantially lower than that at a constant current of  $2 \text{ A cm}^{-2}_{\text{geo}}$ , which the authors claim to be due to a not clearly defined reversible degradation effect.<sup>20</sup> Interestingly, comparing the degradation rates when cycling between OCV and  $2 \text{ A cm}^{-2}_{\text{geo}}$  at different interval times (10 min vs. 6 h per step), the degradation rate increased with the number of OCV periods over the 1000 h of test ( $\approx 16 \mu\text{V h}^{-1}$  for  $\approx 80$  OCV periods vs.  $\approx 50 \mu\text{V h}^{-1}$  for  $\approx 3000$  OCV periods over 1000 h). While the authors suggested that this might be due to cathode catalyst degradation, our data presented

<sup>z</sup>These authors contributed equally to this work.

\*Electrochemical Society Student Member.

\*\*Electrochemical Society Fellow.

<sup>z</sup>E-mail: alexandra.weiss@tum.de

below would suggest that it is related to the degradation of the anode catalyst.

To date, a detailed understanding of performance degrading phenomena associated with discontinuous operation, particularly with intermittent OCV periods, has not been established. In this work, we propose a dynamic accelerated stress test (AST) procedure, mimicking the variable power supply of renewable energy sources, where operation at low and high current densities ( $0.1$  and  $3 \text{ A cm}^{-2}_{\text{geo}}$ , respectively) alternate with idle periods, during which no current is supplied and the electrolyzer cell rests at the open circuit voltage. This test will be complemented by an experiment during which the cell voltage is not varying freely during the OCV periods but instead is potentiostated at  $1.3 \text{ V}$ , where the current density is on the order of  $1 \text{ mA cm}^{-2}_{\text{geo}}$  (i.e., significantly smaller than the  $100 \text{ mA cm}^{-2}_{\text{geo}}$ ). We will show that cycling into OCV leads to a significant performance loss, particularly at high current densities, compared to  $1.3 \text{ V}$  holds. The origin of this phenomenon will be examined via detailed electrochemical and physical characterization of the MEA before, during, and after the respective cycling test.

### Experimental

**Membrane electrode assembly (MEA) preparation and cell assembly.**—MEAs with an active area of  $5 \text{ cm}^2$  were prepared via the decal transfer method, where platinum supported on Vulcan XC72 carbon ( $45.8 \text{ wt.-% Pt/C}$ , TEC10V50E from Tanaka, Japan) served as catalyst for the hydrogen evolution reaction (HER) at the cathode electrode and  $\text{IrO}_2$  supported on  $\text{TiO}_2$  ( $\text{IrO}_2/\text{TiO}_2$  with  $75 \text{ wt.-%}$  iridium, Elyst Ir75 0480 from Umicore, Germany) as catalyst for the oxygen evolution reaction (OER) at the anode electrode. De-ionized (DI) water ( $18 \text{ M}\Omega \text{ cm}$ ), 2-Propanol (purity  $\geq 99.9\%$  from Sigma Aldrich), and Nafion ionomer solution ( $20 \text{ wt.-%}$  ionomer, D2021 from IonPower, USA) were used as solvents for the catalyst ink. The suspension was mixed for  $24 \text{ h}$  using a roller mill, where  $\text{ZrO}_2$  grinding balls ( $5 \text{ mm}$  diameter) were added to achieve a homogenous suspension. The ink was coated onto a thin decal transfer substrate (PTFE,  $50 \mu\text{m}$  thick, from Angst+Pfister, Germany) using the Mayer rod technique. Subsequently,  $5 \text{ cm}^2$  decals were punched from the coating after drying and then hot-pressed onto a Nafion 212 membrane ( $50 \mu\text{m}$  thick, from Quintech, Germany) at  $155^\circ\text{C}$  for  $3 \text{ minutes}$  at a pressure of  $2.5 \text{ MPa}$ . By weighing the decals before and after hot-pressing, the actual weight of the electrodes was determined. Throughout the study, the loading was kept constant at  $0.2 \pm 0.1 \text{ mg}_{\text{Pt}} \text{ cm}^{-2}_{\text{geo}}$  for the hydrogen cathode and  $1.75 \pm 0.15 \text{ mg}_{\text{Ir}} \text{ cm}^{-2}_{\text{geo}}$  for the oxygen anode.

At the anode, sintered titanium (from Mott Corporation, USA) with a porosity of  $\approx 50\%$ , a thickness of  $280 \pm 10 \mu\text{m}$  and a pore size of  $10\text{--}50 \mu\text{m}$  (determined by SEM) was used as a porous transport layer (PTL), whereas a carbon fiber paper (TGP-H 120T from Toray, no MPL,  $20 \text{ wt.-%}$  PTFE) with a thickness of  $370 \pm 10 \mu\text{m}$  and pore sizes of  $20\text{--}50 \mu\text{m}^{21}$  was used on the cathode. The MEA and PTLs were placed between the flow-fields of the electrolyzer cell and sealed with virgin PTFE gaskets. By choosing the right thickness of the gaskets, a compression of the carbon PTL by  $25\%$  was set, corresponding to a compressive contact pressure of  $\approx 1.7 \text{ MPa}$  at the MEA. Specific details about the cell hardware are reported elsewhere.<sup>22</sup>

**Physical characterization.**—After the electrochemical characterization and testing, a small piece of each MEA was embedded into room-temperature curing epoxy for scanning electron microscopy (SEM). Using SiC paper, the sample surface was polished in two steps (grade P320 and P1200) and afterwards polished using a  $9 \mu\text{m}$  diamond polishing agent (from Buehler, USA). The cross-sectional lamellae of the pristine and operated samples were prepared by focused ion beam milling (FIB, Zeiss NVision 40). Due to the porosity of the catalyst layer and the sensitive nature of the polymeric membrane, the area thinned for TEM analysis was kept to a minimum to keep the lamellae intact. The scanning transmission electron microscopy (STEM) was performed with a spherical aberration corrected TEM (ThermoScientific Titan Themis 60-300) equipped with a high

brightness gun source operated at  $200 \text{ kV}$ . The current was kept low to avoid possible electron beam induced damage which would cause collapse of the polymeric film. High-angle annular dark field-STEM (HAADF-STEM) images of the interface between the  $\text{IrO}_2/\text{TiO}_2$  anode catalyst layer and the Nafion membrane were acquired by collecting incoherently scattered electrons. Energy dispersive spectroscopy (STEM-EDS) elemental maps of iridium and oxygen were obtained by collecting characteristic X-ray signals via four silicon drift detectors located in close proximity to the sample at the TEM column.

**Contact resistance measurement.**—Contact resistance measurements were carried out with the test setup described by Bernt et al.<sup>22</sup> PTLs, along with an insulating Kapton foil ( $25 \mu\text{m}$ ) to ensure that the resistance is only measured along the PTL were sandwiched between two titanium flow-fields which, in turn, were sandwiched between two copper plates. A pressure of  $\approx 1.7 \text{ MPa}$  was applied to this stack in order to simulate the contact pressure in the cell. By applying different currents via the copper plates and measuring the associated voltage drops across the flow-fields, the electronic resistance (essentially equating to the contact resistance) was quantified.

**Electronic resistance measurement of the anode electrode.**—Electronic conductivities of the  $\text{IrO}_2/\text{TiO}_2$  anode catalyst layers in the size of  $5 \text{ cm}^2_{\text{geo}}$  were determined by 4-point-probe in-plane conductivity measurements (Lucas/Signatone, pin distance  $1 \text{ mm}$ ) on the electrode coated onto the membrane by applying different potentials between  $0.1\text{--}0.5 \text{ V}$  and recording the corresponding current.

**Electrochemical characterization.**—All electrochemical measurements of the MEAs were performed on an automated test station from Greenlight Innovation, using a potentiostat equipped with a current booster (BioLogic VSP 300). The anode was supplied with  $5 \text{ mL}_{\text{H}_2\text{O}} \text{ min}^{-1}$  deionized (DI) water, which was pre-heated to  $80^\circ\text{C}$ . During the measurements, the cell temperature was kept constant at  $80^\circ\text{C}$ , and the product gas exiting from the anode side was diluted with nitrogen ( $200 \text{ nccm}$ ) to avoid the formation of an explosive gas mixture due to hydrogen permeation through the membrane into the anode compartment. During warm-up, the cathode is flushed with  $\text{N}_2$  for  $300 \text{ s}$  while  $5 \text{ mL}_{\text{H}_2\text{O}} \text{ min}^{-1}$  are constantly supplied to the anode side. After reaching the desired cell temperature of  $80^\circ\text{C}$ , the cell was conditioned at  $1 \text{ A cm}^{-2}_{\text{geo}}$  for  $30 \text{ min}$ . Subsequently, polarization curves were taken at ambient pressure ( $1 \text{ bar}_a$ ) and  $10 \text{ bar}_a$ , stepwise increasing the current density from  $0.01$  to  $4 \text{ A cm}^{-2}_{\text{geo}}$  and holding at each current for  $5 \text{ min}$  to ensure a stable cell voltage reading. Finally, the last  $10 \text{ s}$  of the cell voltage at each current density were averaged. Considering the first two polarization curves as part of the conditioning, they were not included in the analysis. For the load-cycling procedure, the flow of  $\text{H}_2\text{O}$  through the anode compartment and the cell temperature were kept constant also during the open-circuit voltage (OCV) or the  $1.3 \text{ V}$ -hold periods.

Additionally, AC impedance measurements were performed at the end of each current density step in a range from  $100 \text{ kHz}$  to  $1 \text{ Hz}$ , adjusting the amplitude of the current perturbation such that it was always  $<20\%$  of the applied current, except for the smallest current density of  $10 \text{ mA cm}^{-2}_{\text{geo}}$  where it was  $40\%$ . The high-frequency resistance (HFR) was determined from the high-frequency intercept with the real axis in a Nyquist plot. At the beginning-of-test (BoT) as well as during the test and at the end-of-test (EoT), cyclic voltammograms (CVs) of the anode electrode were recorded. For this, the test procedure was stopped either after the open-circuit voltage or the  $1.3 \text{ V}$ -hold period, and the cathode counter electrode was flushed with dry  $\text{H}_2$  at  $50 \text{ nccm}$  at ambient pressure to ensure a stable reference potential, while the anode electrode was continuously fed with  $5 \text{ mL}_{\text{H}_2\text{O}} \text{ min}^{-1}$  deionized water. The CVs were recorded in a potential range of  $0.05 \text{ V}\text{--}1.3 \text{ V}$  at  $50 \text{ mV s}^{-1}$  at  $80^\circ\text{C}$ ; showing the steady-state CVs ( $2^{\text{nd}}$  one recorded).

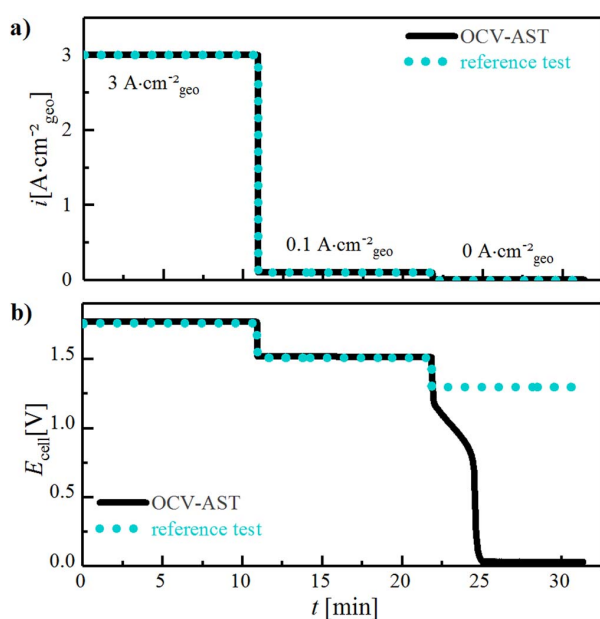


**Figure 1.** Test protocol for the accelerated stress test (AST) to mimic an intermittent power supply of a PEM-WE with periods of low and high current density followed by OCV (“OCV-AST”, black solid lines) and of a reference test avoiding OCV (“reference test”, blue dotted lines) by holding the potential at 1.3 V instead of OCV. a) Current profiles during the first cycle of the OCV-AST; b) associated potential profiles recorded at 80°C with  $p_{\text{cathode}} = 10 \text{ bar}_a$  and  $p_{\text{anode}} = 1 \text{ bar}_a$ , while feeding  $5 \text{ mL H}_2\text{O min}^{-1}$  into the anode compartment. MEA specification:  $5 \text{ cm}^2$  active-area with  $\approx 1.75 \text{ mgIr cm}^{-2}_{\text{geo}}$  anode and  $\approx 0.2 \text{ mgPt cm}^{-2}_{\text{geo}}$  cathode loading using a Nafion 212 ( $\approx 50 \mu\text{m}$  thick) membrane.

## Results and Discussion

**Degradation test protocols.**—In this section, we propose a test protocol to mimic transient operation of a PEM-WE. First a high ( $3 \text{ A cm}^{-2}_{\text{geo}}$ ) and then a low ( $0.1 \text{ A cm}^{-2}_{\text{geo}}$ ) current density are drawn from the cell, followed by a current interrupt during which the cell is left to rest at the OCV, simulating shut-off periods of a PEM-WE operated with intermittent renewable energy (denoted as “OCV-AST”). The duration of each interval was  $\approx 10 \text{ min}$ , and one cycle refers to the two current steps and the OCV period (black solid line in Figure 1a). In a second experiment, referred to as “reference test”, the OCV period at the end of each cycle was replaced by a potential hold at 1.3 V (blue dotted line in Figure 1a). During the entire operation (i.e., including the shut-off periods), the temperature was held at 80°C and  $5 \text{ mL min}^{-1}$  DI water was continuously fed into the anode compartment of the cell. During the OCV or 1.3 V-hold phase, the cathode pressure decreased by  $\approx 1 \text{ bar}_a$  (i.e., from  $10 \text{ bar}_a$  to  $\approx 9 \text{ bar}_a$ ) due to  $\text{H}_2$  permeating through the membrane into the anode compartment (the  $\text{H}_2$  partial pressure normalized permeation rate through a  $\approx 175 \mu\text{m}$  thick Nafion 117 membrane in a PEM-WE at 80°C between 10 and  $30 \text{ bar}_a$  cathode pressure was found to be  $\approx 0.24 \text{ mA cm}^{-2}_{\text{geo}} \text{ bar}_{a(\text{H}_2)}^{-1}$ ,<sup>23</sup> which if scaled to a  $\approx 50 \mu\text{m}$  thick Nafion 212 membrane equates to  $\approx 0.85 \text{ mA cm}^{-2}_{\text{geo}} \text{ bar}_{a(\text{H}_2)}^{-1}$  or  $\approx 5.9 \cdot 10^{-3} \text{ cm}_{s(\text{H}_2)}^3 \text{ cm}^{-2} \text{ bar}_{a(\text{H}_2)}^{-1} \text{ min}^{-1}$  (with  $\text{cm}_s^3$  referenced to  $1.103 \text{ bar}_a$  and 25°C)).

**Voltage and current response during the OCV-AST and the reference test.**—Figure 1b shows the cell voltage recorded during the different operation intervals in Figure 1a. During operation at constant current, the cell voltage remains essentially constant. Upon current interruption in the OCV-AST (black line), the potential drops immediately to  $\approx 1.2 \text{ V}$ , i.e., to the approximate thermodynamic cell voltage

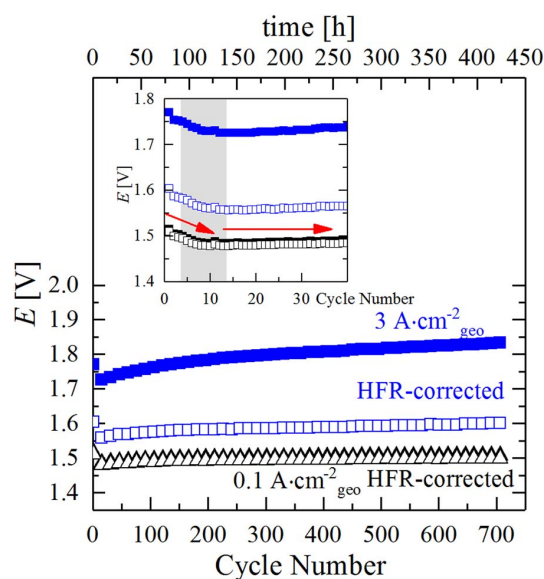


**Figure 2.** Evolution of the cell voltage and the HFR-corrected cell voltage at  $0.1 \text{ A cm}^{-2}_{\text{geo}}$  and  $3 \text{ A cm}^{-2}_{\text{geo}}$  during the OCV-AST at 80°C, cycling the cell according to the protocol shown in Figure 1 (black solid line) with  $p_{\text{cathode}} = 10 \text{ bar}_a$  and  $p_{\text{anode}} = 1 \text{ bar}_a$ , while feeding  $5 \text{ mL H}_2\text{O min}^{-1}$  into the anode compartment (same MEA specifications as in Figure 1). For better legibility, only every 15<sup>th</sup> point was plotted; the inset is a zoomed view of the initial 40 cycles including all data points.

for water electrolysis at 80°C. This is followed by a gradual decrease of the potential to  $\approx 0.8 \text{ V}$ , caused by the gradual enrichment of  $\text{H}_2$  in the anode compartment by permeation from the cathode compartment that is held at  $10 \text{ bar}_a$  (i.e., at a  $\text{H}_2$  partial pressure of  $9.5 \text{ bar}_a$ ), resulting in a  $\text{H}_2$  permeation flux of  $\approx 5.6 \cdot 10^{-2} \text{ cm}_{s(\text{H}_2)}^3 \text{ cm}^{-2} \text{ min}^{-1}$  (from the above quoted permeation rate). In this  $\text{H}_2$ -rich gas-phase at 80°C, the surface of the crystalline  $\text{IrO}_2$  on the  $\text{TiO}_2$  support undergoes a gradual partial reduction to a surface which is catalytically active for the hydrogen oxidation reaction (HOR).<sup>24</sup> Once its HOR activity is high enough (apparently at  $\approx 0.8 \text{ V}$ ), the equilibrium potential for the HOR at  $\approx 0 \text{ V}$  is being established very quickly (in less than 0.5 min), resulting in a drop of the cell voltage of the electrolyzer to  $\approx 0 \text{ V}$  vs. the reversible hydrogen electrode (RHE) potential (note that the platinum catalyzed cathode is still under a high  $\text{H}_2$  pressure, so that the  $\approx 0 \text{ V}$  cell voltage are clearly due to a drop of the anode potential to  $\approx 0 \text{ V}$  vs. RHE). When holding the cell voltage at 1.3 V instead in case of the reference test, the reduction of the  $\text{IrO}_2$  catalyst will be prevented (as will be proven later), however at the cost of applying a small bias current, as will be discussed in the last section of this work.

The evolution of the cell voltage as a function of the number of current/OCV cycles of the OCV-AST is shown in Figure 2. The cell voltage at both current densities initially decreases by  $\approx 50 \text{ mV}$  (inset of Figure 2) and above 10 cycles gradually increases, particularly at high current density. Since the HFR-corrected cell voltage also decreases during the first 10 cycles (cf. hollow blue and black symbols in Figure 2), the initially decreasing cell voltage must be due to an increase of the OER activity of the anode catalyst (note that the cathode overpotential would be  $< 10 \text{ mV}$  even if the loading of the Pt cathode catalyst would be reduced by an order of magnitude from the value of  $0.2 \text{ mgPt cm}^{-2}_{\text{geo}}$  used in this work).<sup>25</sup> As was shown previously<sup>24</sup> and as will be further discussed below, this is indeed due to an increase in the OER activity of the  $\text{IrO}_2$  based anode catalyst after extended exposure to  $\text{H}_2$  during the OCV periods. The increase in cell voltage starting after 10 cycles is largely caused by an increase in the HFR, reflected by the fact that the HFR-corrected cell voltage at  $3 \text{ A cm}^{-2}_{\text{geo}}$  rises much less significantly than the cell voltage. The nevertheless



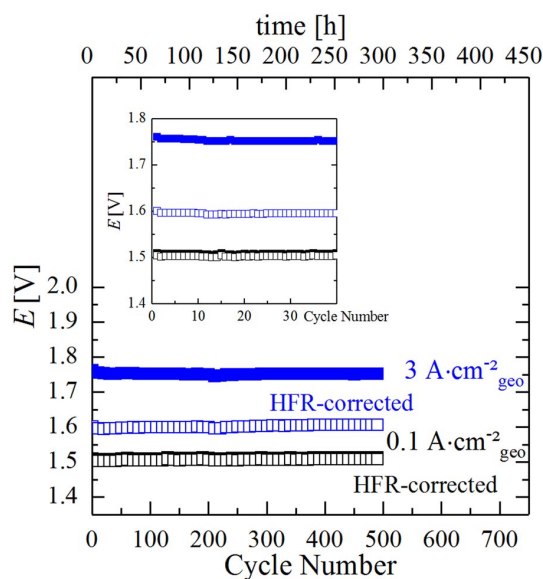


**Figure 3.** Evolution of the cell voltage and the HFR-free cell voltage at  $0.1 \text{ A cm}^{-2}_{\text{geo}}$  and  $3 \text{ A cm}^{-2}_{\text{geo}}$  during the reference test at  $80^\circ\text{C}$  with OCV periods replaced by  $1.3 \text{ V}$ -holds, cycling the cell according to the protocol shown in Figure 1 (blue dotted line) with  $p_{\text{cathode}} = 10 \text{ bar}_a$  and  $p_{\text{anode}} = 1 \text{ bar}_a$ , while feeding  $5 \text{ mL H}_2\text{O min}^{-1}$  into the anode compartment (same MEA specifications as in Figure 1). For better legibility, only every  $10^{\text{th}}$  point was plotted; the inset is a zoomed view of the initial 40 cycles including all data points.

noticeable increase of the HFR-corrected cell voltage upon extended cycling suggests the growth of a more complex mass transport resistance.

In the reference test, the potentiostatic control at  $1.3 \text{ V}$  during the shut-down period results in a constant cell as well as HFR-corrected potential at both currents over the entire cycling test (Figure 3). Interestingly, the substantial performance improvement observed over the first 10 cycles cannot be observed here, particularly not for the HFR-corrected data, as can be seen in the inset of Figure 3 ( $<10 \text{ mV}$  vs.  $\approx 50 \text{ mV}$  in Figure 2). This suggests that the (partial) reduction of the anode catalyst does not occur at  $\geq 1.3 \text{ V}$ . The comparison of both experiments proves that the performance degradation during the first experiment (Figure 2) is directly related to the OCV period at the end of each cycle, during which  $\text{H}_2$  accumulates in the anode compartment and lowers the potential of the anode catalyst to  $\approx 0 \text{ V}$  vs. RHE (Figure 1b, blue dotted line). It further proves that the degradation observed during the OCV-AST (Figure 2) is not caused by experimental artefacts (e.g., ionic contamination of the feed-water). Apparently, avoiding temporary potential excursions of the anode catalyst to below  $1.3 \text{ V}$  during intermittent shut-down mitigates parasitic processes that lead to an increasing cell voltage, which, to a large extent but not completely, can be attributed to an increase in HFR. The current/power required to hold the potential at  $1.3 \text{ V}$  during shut-down periods will be discussed in the last section of this work.

In order to gain further insights into the observed performance decay during the OCV-AST, we examine polarization curves recorded at various stages of the OCV-AST and the reference test. Figure 4 shows ambient pressure polarization curves and the corresponding HFR values recorded over the course of the OCV-AST, namely at the beginning-of-test (BoT, green squares) and after 10 (blue circles), 200 (orange triangles), and 718 cycles (end-of-test or EoT; red diamonds). It is remarkable that the performance increases by  $\approx 45 \text{ mV}$  over the entire current density range after ten cycles (blue circles) compared to BoT (green squares), which can only be rationalized by an improved OER activity of the anode catalyst. However, upon further cycling, the ambient pressure cell voltage at each current density

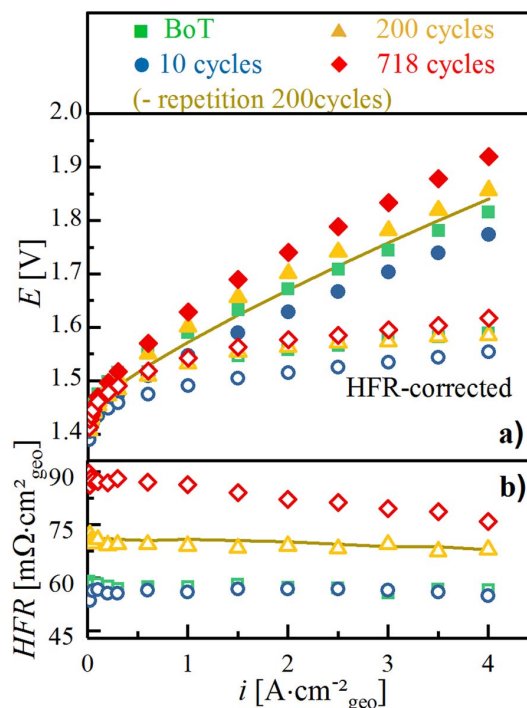


**Figure 4.** Ambient pressure PEM-WE performance data at  $80^\circ\text{C}$  recorded during the OCV-AST shown in Figure 2 a)  $E_{\text{cell}}$  vs.  $i$  performance (filled symbols) and HFR-free performance data (hollow symbols) with a cathode water-feed of  $5 \text{ mL H}_2\text{O min}^{-1}$ ; b) corresponding HFR values. The polarization curve and the HFR after 200 OCV-AST cycles for an independent repeated experiment are marked by the yellow lines.

increases continuously, consistent with the results presented above under differential pressure conditions ( $p_{\text{cathode}}/p_{\text{anode}} = 10/1 \text{ bar}_a$ , see Figure 2). This increase in cell voltage is accompanied by a substantial increase of the HFR (Figure 4b) by a factor of  $\approx 1.3$  after 200 cycles ( $\approx 71 \text{ m}\Omega \text{ cm}^2_{\text{geo}}$ ) and by a factor of  $\approx 1.6$  after 718 cycles ( $\approx 88 \text{ m}\Omega \text{ cm}^2_{\text{geo}}$ ) compared to its BoT value ( $\approx 56 \text{ m}\Omega \text{ cm}^2_{\text{geo}}$ ). Since the HFR represents the sum of the membrane ionic resistance and the electronic contact resistances at the PTL/electrode and PTL/flow field interface, one (or all) of these terms must be responsible for the performance degradation. A large fraction of the performance decrease between 10 cycles (blue circles) and EoT (red diamonds) can be ascribed to this dramatically increasing HFR, as indicated by the much smaller increase of the HFR-corrected voltage (open symbols in Figure 4a). However, the HFR increase alone cannot explain all of the performance losses over extended cycling, as the HFR-corrected voltage at each current density still increases between 10 cycles and EoT.

This analysis of the OCV-AST will be compared next to that of the reference test where OCV periods are replaced by  $1.3 \text{ V}$ -hold periods (Figure 5). Quite astoundingly, the cell voltage up to  $4 \text{ A cm}^{-2}_{\text{geo}}$  even slightly improves over 500 cycles (Figure 5a), which is related to the slightly decreasing HFR (Figure 5b), from  $\approx 54 \text{ m}\Omega \text{ cm}^2_{\text{geo}}$  initially (green squares) to  $\approx 50 \text{ m}\Omega \text{ cm}^2_{\text{geo}}$  after 500 cycles (red diamonds). The perfectly unchanged HFR-corrected cell voltage over 500 cycles signifies that the OER catalyst activity must remain unaltered. Considering the observations and conclusions from the polarization curves along with the development of the cell voltage over extended cycling, it is evident that the initial performance improvement observed after 10 cycles in the OCV-AST is not observed in the reference experiment, so that it must be linked directly to a change of the OER catalyst during the OCV periods. Quite clearly, the rather substantial performance degradation during OCV can be effectively prevented if the cell potential remains always at or above  $1.3 \text{ V}$ .

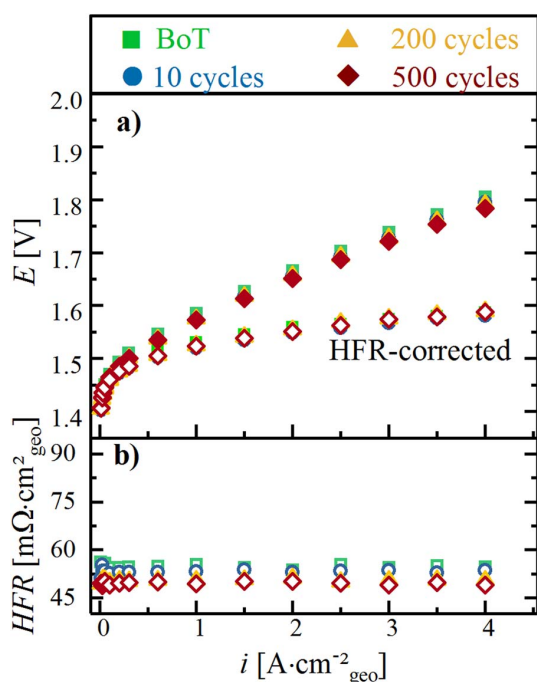


**Figure 5.** Ambient pressure PEM-WE performance data at 80°C recorded during the reference test shown in Figure 3. a)  $E_{cell}$  vs.  $i$  performance (filled symbols) and HFR-free performance data (hollow symbols) with a cathode water-feed of 5 mL<sub>H<sub>2</sub>O</sub> min<sup>-1</sup>; b) corresponding HFR values.

**Analysis of the effect of OCV periods on the OER catalyst.—**

This section will provide a detailed insight into the performance increase observed during the first ten cycles of the OCV-AST by taking a closer look at the OER kinetics. The Tafel slope, determined from the linear region (i.e., between 0.01 A cm<sup>-2</sup><sub>geo</sub> and 0.1 A cm<sup>-2</sup><sub>geo</sub>) of the ambient pressure HFR-corrected polarization curves recorded over the course of the OCV-AST (Figure 6a), decreases from 60 mV dec<sup>-1</sup> to 47 mV dec<sup>-1</sup> after the initial 10 cycles, clearly evidencing a change in the OER kinetics. Over further cycling, the Tafel slope increases slightly by  $\approx 3$  mV dec<sup>-1</sup> (50 mV dec<sup>-1</sup> after 200 cycles) and then stays constant until EoT (50 mV dec<sup>-1</sup> after 718 cycles). As one would expect, the initial Tafel slope obtained in the reference test is essentially identical with the initial value of the OCV-AST experiment (59 vs. 60 mV dec<sup>-1</sup>). However, contrary to the OCV-AST, it remained essentially constant, with a value of  $\approx 56$  mV dec<sup>-1</sup> (Figure 6b). This suggests that neither the iridium oxide surface nor the OER reaction mechanism seem to be affected during the reference experiment, while the substantial decrease of the Tafel slope in the first 10 cycles of the OCV-AST clearly suggests a change in the iridium oxide surface chemistry, induced by the OCV periods. In previous studies, we had observed a similar decrease of the Tafel slope upon in-situ reduction of the same IrO<sub>2</sub> catalyst under H<sub>2</sub> at 80°C for 15 h, accompanied by a  $\approx 40$  mV increase in OER activity and by the appearance of hydrogen underpotential deposition (H-UPD) features in the CV of the H<sub>2</sub>-exposed iridium oxide catalyst.<sup>24</sup> This was rationalized by the fact that thermally prepared, highly crystalline IrO<sub>2</sub> exhibits very different CV features than that of hydrous iridium oxide or metallic iridium.<sup>26</sup> Therefore, since the voltammetric response of the iridium oxide catalyst can provide valuable insights into the surface chemistry of the anode catalyst, we recorded the CVs of the anode catalyst before and during the OCV-AST and the reference test.

The BoT CV of the TiO<sub>2</sub> supported IrO<sub>2</sub> anode catalyst shows only capacitive currents but no well-defined features (region (1) & (2), green line Figure 7), which is characteristic of thermally treated, crystalline IrO<sub>2</sub>, and suggests that the surface of the iridium oxide corresponds

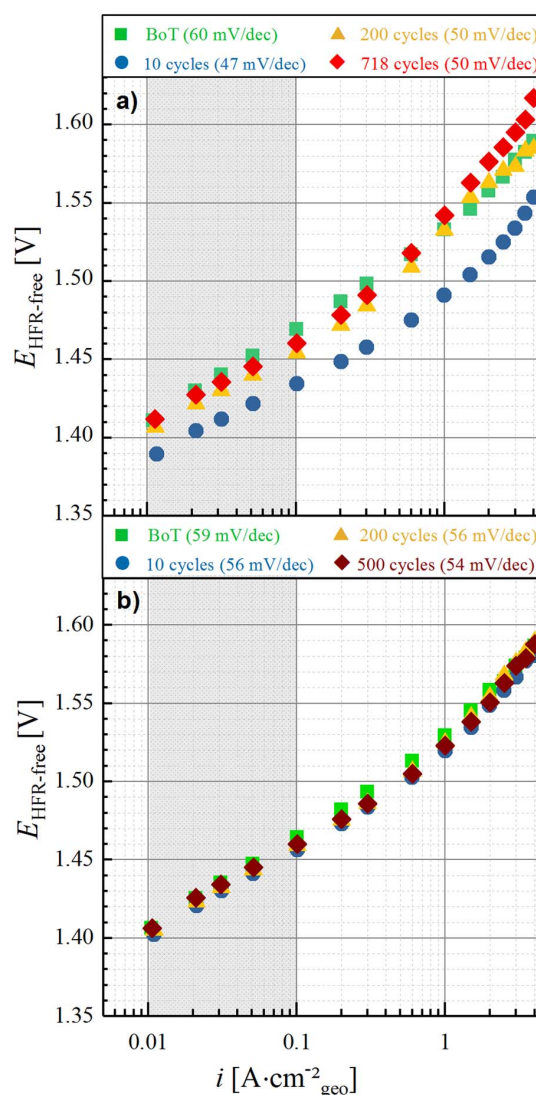


**Figure 6.** Tafel plots of  $E_{HFR-free}$  vs.  $i$  at ambient pressure and 80°C, obtained over the course of the cycling tests: a) for the OCV-AST (data from Figure 4); b) for the reference test where the OCV period was replaced by a potential hold at 1.3 V (data from Figure 5). Tafel slopes were determined between 0.01 A cm<sup>-2</sup><sub>geo</sub> and 0.1 A cm<sup>-2</sup><sub>geo</sub> (gray shaded region), and the values are given in the legend heading each of the two Tafel plots.

to that of crystalline IrO<sub>2</sub> rather than amorphous iridium oxide.<sup>26,27</sup> However, the CV changes significantly after the first 10 OCV periods of the OCV-AST (blue line): i) the capacitive currents are  $\approx 2$  times higher than at the beginning of test; ii) distinct H-UPD features can be observed at low potentials, characteristic of metallic iridium;<sup>26,28,29</sup> (see region (1) in Figure 7); and, iii) the redox features observed in region (2) can be attributed to the transition between Ir(III)/Ir(IV).<sup>26</sup> The same change in CV features was reported for the same catalyst upon its exposure to pure H<sub>2</sub> at 80°C for 15 h.<sup>24</sup> Thus, this suggests a gradual reduction of the crystalline IrO<sub>2</sub> catalyst surface into a hydrous iridium oxide during the OCV-AST (i.e., during repeated polarization of the anode catalyst to  $\approx 0$  V vs. RHE), consistent with the latter's higher OER activity,<sup>24,30-32</sup> as demonstrated in Figure 6a. Quite clearly, since thermally prepared, crystalline IrO<sub>2</sub> is not stable below  $\leq 0.8$  V,<sup>24,33</sup> its surface is reduced to metallic iridium, which will be oxidized upon extended cycling to high potentials during the OCV-AST (i.e., up to an

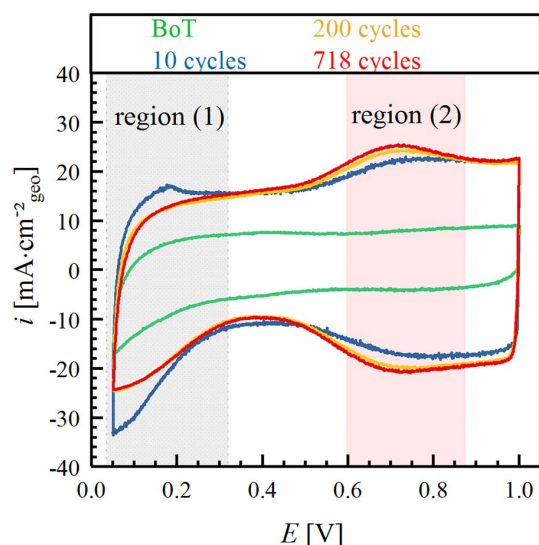


**Figure 7.** Cyclic voltammograms (CVs) recorded after different numbers of cycles of the OCV-AST (see Figure 2), recorded at 50 mV/s, 80°C, ambient pressure, and 5 mL<sub>H<sub>2</sub>O</sub> min<sup>-1</sup> (anode)/ 50 nccm H<sub>2</sub> (cathode).

anode potential of  $\approx 1.6$  V vs. RHE, as indicated by the HFR-corrected voltage at 3 A cm<sup>-2</sup><sub>geo</sub> in Figure 2), forming hydrous iridium oxide.<sup>34</sup> The fact that these hydrous iridium oxide features are still present in the CVs recorded after 200 and 718 cycles (Figure 7, yellow and red lines) indicates an irreversible change of the iridium hydration state at the anode electrode surface with respect to that at the beginning of test, because it appears impossible to electrochemically form crystalline IrO<sub>2</sub>. Instead, the surface remains a hydrous iridium oxide (no significant changes from 200 to 718 cycles). However, the well-defined H-UPD features present after the 10<sup>th</sup> cycle disappear over the course of extended cycling, showing that the initially formed metallic iridium is indeed converted into hydrous iridium oxide.<sup>34</sup> Since the electronic conductivity of hydrous iridium oxide is reported to be lower than that of crystalline IrO<sub>2</sub>,<sup>30</sup> and since the long-time stability of hydrous iridium oxide in a PEM-WE is reported to be inferior to that of crystalline IrO<sub>2</sub>,<sup>31</sup> the transformation of the initially crystalline IrO<sub>2</sub> into hydrous iridium oxide may be the cause for the large degradation over the course of the OCV-AST (Figure 2) and thus would have important consequences for the operational requirements for a PEM-WE.

If our hypothesis was true that the performance degradation observed for the OCV-AST is due to a change of the surface chemistry of the iridium based anode catalyst, we would expect that the surface chemistry of the iridium catalyst after the reference test remains unchanged compared to its initial state, as no performance degradation is observed in this case (Figure 3). Indeed, the CVs recorded over the course of the reference test (Figure 8a) only exhibit marginal differences between the BoT (green line) and the EoT after 500 cycles (red line). This minor increase of the overall capacity, mostly occurring over the first 10 cycles, is either due to a small extent of surface roughening of the IrO<sub>2</sub> catalyst or perhaps more likely to a removal of (surface) impurities, as could be inferred from the slight decrease in HFR over cycling (Figure 5b). Nevertheless, the H-UPD as well as the characteristic hydrous iridium oxide features are absent in the reference test, so that their presence in the OCV-AST is clearly related to the repetitive polarization of the anode to  $\approx 0$  V vs. RHE during the OCV periods. Although the potential is cycled close to 0 V vs. RHE during the CV measurements, the time spent at low potentials is insufficient to form metallic iridium and hence, hydrous iridium oxide, which is why no change is expected. Summarizing our observations and analysis so far, the repetitive cycling of the anode catalyst during the OCV-AST between  $\approx 0$  V vs. RHE at OCV and  $\approx 1.6$  V vs. RHE

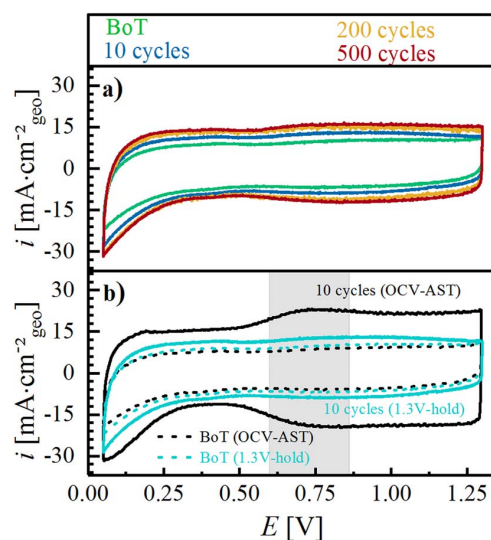


**Figure 8.** a) Cyclic voltammograms (CVs) recorded during the reference test, where the OCV periods are replaced by 1.3 V hold periods. b) Comparison between CVs recorded after 10 cycles for the OCV-AST (black line) and after 10 cycles of the reference test with 1.3 V-holds (blue line); the dotted lines represent the CVs recorded at BoT. CVs were recorded at 50 mV/s, 80°C, ambient pressure, and 5 mL<sub>H<sub>2</sub>O</sub> min<sup>-1</sup> (anode)/ 50 nccm H<sub>2</sub> (cathode).

at high current density leads to a transformation of the initially crystalline IrO<sub>2</sub> into hydrous iridium oxide, concomitant with a substantial decrease in performance and a large increase of the HFR (Figure 4). On the other hand, if the cell potential is controlled to  $\geq 1.3$  V during idle periods, the initial crystalline IrO<sub>2</sub> is retained over extended cycling, and neither a performance degradation nor an increase of the HFR is found (Figure 5).

#### Origin of the cell performance decrease during the OCV-AST.—

In this section, we will discuss possible reasons for the observed decrease in cell performance over the course of the OCV-AST, largely due to an increase of the HFR (Figure 4), contrary to the essentially constant performance and HFR when the OCV periods are replaced by potential holds at 1.3 V (Figure 5). Consequently, the increase of the HFR must be related to processes which take place during OCV periods when the anode potential was shown to decrease to  $\approx 0$  V vs. RHE or which are related to the recurring transition between high potentials (operation) and low potentials (OCV period). In general, an increase of the HFR can be ascribed to different processes occurring in the cell (see Figure 9), which will be discussed individually in the following.

At low potentials, not only can IrO<sub>2</sub> be reduced, but also parts of the cell can be corroded (e.g., flow-fields, PTL). If either of these processes were to result in the formation of metal cations (e.g., from metal impurities in titanium or cationic titanium species), these cations would be ion-exchanged into the membrane/ionomer phase and displace protons, which would not only lead to a reduction of the membrane/ionomer conductivity and to an increase of the HFR,<sup>35</sup> but it would also introduce additional mass transport resistance losses, particularly at high current densities, as described for cation-contaminated membranes in PEM fuel cells (① in Figure 9). The performance decrease and HFR increase over the course of the OCV-AST could in principle be also produced by the introduction of ionic contaminants into the feed water. However, in our test system, the deionized (DI) feed water was supplied through an ion-exchanger, and the resistivity measured between the ion-exchanger and the cell inlet was always  $> 15$  M $\Omega$ hmom during the measurements. Moreover, the DI-water was not recycled during operation and therefore we can definitely exclude the presence of ionic contaminants. Moreover, ionic contamination of



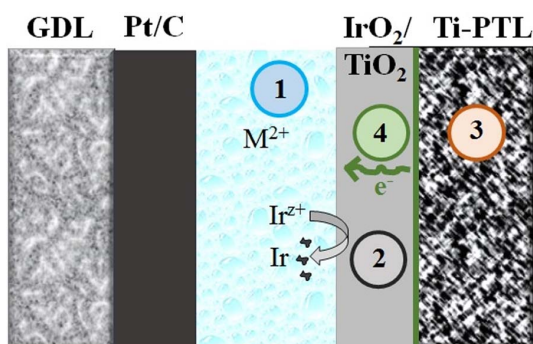


**Figure 9.** Scheme of a single cell, illustrating possible reasons for the observed HFR increase during the OCV-AST: 1) cationic contamination of the membrane; 2) dissolution of iridium from the anode catalyst and its redeposition in the membrane; 3) formation of an electronically insulating oxide film on the Ti-PTL surface; 4) additional resistance due to the low electronic conductivity of hydrous iridium oxide.

the feed water would be independent of the cell operating conditions and, hence, would have to be observed in both the OCV-AST and the reference test. If cationic contamination of the membrane from cell components were present, the HFR should be recovered upon ion-exchanging the aged MEA in 1 M  $\text{H}_2\text{SO}_4$  at  $80^\circ\text{C}$  for 2 h.<sup>18</sup> However, since the HFR after reassembling the cell with the acid treated MEA was still high ( $\approx 100 \text{ m}\Omega \text{ cm}^2_{\text{geo}}$ ) and almost identical to the one measured after the end of test ( $\approx 90 \text{ m}\Omega \text{ cm}^2_{\text{geo}}$ ), as shown in Figure 10, cationic contaminations can be ruled out as a reason for the observed performance loss. Dis- and reassembling of the MEA and PTL (which is considered incompressible) always bears the risk of a different alignment as well as the mechanical deformation of the catalyst or membrane and could be an explanation for the small discrepancy observed. However, both phenomena would most likely not be significant enough to mask the decrease in HFR due to the removal of ionic contaminations. Additionally, an experiment including a reference electrode placed in between two membranes which were subsequently laminated and processed into an MEA (unpublished data<sup>36</sup>)

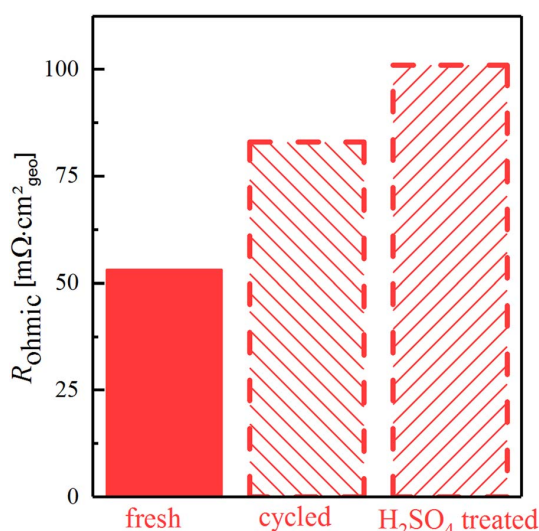


**Figure 10.** High frequency resistance of a fresh MEA at BoT, of a cycled MEA (500 OCV-AST cycles analogous to Figure 2), and of the cycled MEA cycled after 2 h in 1 M  $\text{H}_2\text{SO}_4$  at  $80^\circ\text{C}$ . The HFR was measured at OCV in the (re-assembled) electrolyzer cell at  $80^\circ\text{C}$  and ambient pressure, with a flow of  $5 \text{ mL}_{\text{H}_2\text{O}} \text{ min}^{-1}$  at the anode.

shows that the increase of the HFR during the OCV-AST can clearly be related to an increasing HFR on the anode side of the MEA. Cationic contamination, on the other hand, would lead to a lower ionic conductivity of the entire membrane and, hence, would result in an HFR increase measured between the reference electrode and the anode as well as between the reference electrode and the cathode. Thus, cationic contamination can clearly be eliminated as a possible cause of the performance decrease over the course of the OCV-AST.

Besides cationic contaminations, dissolution and re-precipitation of iridium within the membrane due to reaction with crossover hydrogen might cause an increase in HFR (② in Figure 9), if precipitated iridium were to form a barrier toward proton transport in the membrane. Geiger et al. reported that cycling iridium and thermally grown  $\text{IrO}_2$  films between 0.04 and 1.4 V vs. RHE in  $\text{H}_2\text{SO}_4$  at  $25^\circ\text{C}$  leads to the dissolution of iridium (quantified in a flow cell connected to an inductively coupled plasma mass spectrometer), whereby the dissolution rates for crystalline  $\text{IrO}_2$  were shown to be up to  $\approx 100$ -fold lower than those of iridium and hydrous iridium oxide.<sup>26,37,38</sup> This would predict that the repetitive transition of the HFR-corrected cell voltage (i.e., of the anode potential) between  $\approx 0 \text{ V}$  and  $\approx 1.6 \text{ V}$  during the OCV-AST should lead to the dissolution of iridium, which would either precipitate in the membrane and/or leave the cell with the water effluent. A similar effect involving the dissolution and the precipitation of the catalyst within the membrane due to reaction with crossover hydrogen was reported in the literature for platinum.<sup>39-41</sup> Grigoriev et al. used Pt as an OER catalyst at the anode of a PEM-WE, where they found it to dissolve and re-precipitate in the membrane during a long-term test (albeit at unrealistically high potentials exceeding 3 V vs. RHE).<sup>40</sup> On the other hand, in the case of fuel cells, voltage-cycling of the Pt-based cathode catalyst<sup>41</sup> or extended holds at OCV<sup>39</sup> lead to the precipitation of Pt in the membrane, appearing as a so-called “Pt-band”. The latter study also showed that the position of the Pt-band depends on the  $\text{H}_2/\text{O}_2$  partial pressure ratio,<sup>39</sup> from which one would predict that the deposition of dissolved iridium in a PEM-WE operated at the differential pressure conditions used in our OCV-AST ( $p_{\text{H}_2} = 9.5 \text{ bar}_a$ ,  $p_{\text{O}_2} = 0.5 \text{ bar}_a$ ) would have to occur very close to the anode/membrane interface.<sup>39</sup> To find out whether iridium is indeed being deposited within the membrane over the course of the OCV-AST, site specific TEM analysis were performed, where the membrane area close to the anode/membrane interface was closely inspected. HAADF-STEM images of the degraded MEA after EoT (718 OCV-AST cycles, Figures 11b and 11c) show a distribution of nanoparticles with particle size  $\leq 10 \text{ nm}$  (Figure 11d) for at least  $1 \mu\text{m}$  away from the interface, whereas a new MEA (Figure 11a) remains particle-free.

The STEM-EDS iridium map of a precipitated particle (Figure 11e) revealed that the particles are iridium-based with no obvious oxygen contribution as shown in the homogenous distribution of the oxygen EDS map (Figure 11f). Therefore, the precipitates are primarily composed of metallic iridium. Even though the amount of precipitated iridium is too small to cause the observed increase in HFR, the dissolution and re-precipitation results in a loss of active material in the anode electrode over time, which ultimately would lead to a lower OER activity due to a reduced electrochemically active surface area (ECSA). We believe that this effect is insignificant during the duration of the here shown experiment due to the high catalyst loadings used in this study, but would lead to a more significant performance decay for low Ir-loadings and longer test periods, which is the focus of our current studies.

Alternatively, the HFR could increase due to the formation of an electronically insulating surface film on the Ti-PTL (③ in Figure 9), leading to a higher contact resistance at the anode/PTL and/or the PTL/flow field interface. This was reported previously by Rakousky et al.<sup>19</sup> and can be easily verified by ex-situ measurements of the contact resistance between one PTL/flow-field interface for new or aged PTLs (cf. details in Experimental section).<sup>22</sup> Contact resistances measured ex-situ should be considered with caution, since temperature, contact pressure, and the exact nature of the interface (PTL/catalyst vs. PTL/flow field) during the measurement are different compared

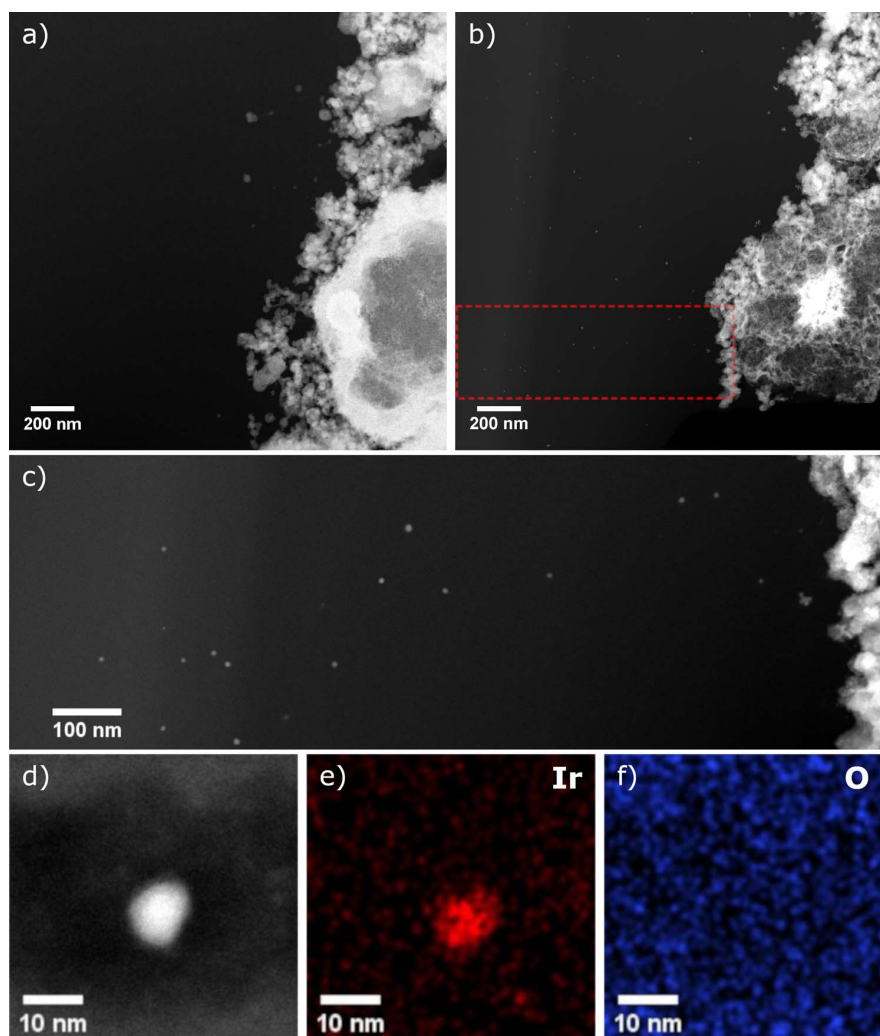


**Figure 11.** HAADF-STEM images of the interface between anode catalyst layer and membrane of (a) a new MEA and (b) an MEA after 718 cycles of the OCV-AST. (c) HAADF-STEM image of the interface of the MEA after 718 cycles of the OCV-AST (red dashed rectangular region in b). (d) HAADF-STEM image of a single particle precipitated at anode/membrane interface as well as the associated STEM-EDS elemental maps of (d) iridium and (e) oxygen.

to in-situ measurements. Nevertheless, they can be used to qualitatively judge the contribution of an additional contact resistance. For a simplified presentation, the contact resistances measured at EoT are normalized to the contact resistances measured at BoT.

The PTL/flow-field contact resistance for a PTL after 718 OCV-AST cycles measured ex-situ at  $\approx 1.7$  MPa (equivalent to the compression in the cell) is twice as high (black triangle in Figure 12) compared to BoT, while it even decreases slightly ( $-10\%$ ) after 500 cycles of the reference test with the 1.3 V-hold (black square in Figure 12). The observed decrease in contact resistance along with the HFR in case of the reference test, might be correlated to an improving alignment at the PTL/electrode interface during operation. In contrast to that, the observed increase in HFR along with the measured increase in contact resistance during the OCV-AST might be related to the passivation of the Ti-PTL. This was further investigated by repeating the OCV-AST with a Ti-PTL sputtered with a thin layer of gold, which is in the order of several micrometer (measured by SEM), on both sides, hoping that it would improve the contact resistance and serve as a protective coating.<sup>42</sup> Indeed, the contact resistance of the Au-sputtered PTL remained essentially constant after 135 OCV-AST cycles (black circle in Figure 12) and a slightly improved HFR at EoT

could be observed. This is in good agreement with the constant performance recorded during the OCV-AST when using a Au-sputtered PTL (data not shown) and thus, the recorded increase in HFR during the OCV-AST is correlated to the passivation of the Ti-PTL. However, the increase of the contact resistance over the OCV-AST ( $\approx 6 \text{ m}\Omega \text{ cm}^2_{\text{geo}}$ ) is much lower than the increase in HFR (see Figure 4) and would only account for a loss of  $\approx 20$  mV compared to the 117 mV cell voltage increase at  $3 \text{ A cm}^{-2}_{\text{geo}}$  (see Figure 2). In addition to the increasing contact resistance for a passivated Ti-PTL, the transition from the initially crystalline  $\text{IrO}_2$  to an amorphous, hydrous iridium oxide, which is known to exhibit lower conductivity,<sup>30</sup> can contribute to an increase in HFR. In this case, the observed HFR increase can be due to either an increase of the electronic through-plane resistance of the anode electrode and/or an increase of the contact resistance at the anode/PTL interface due to a lowering of the bulk conductivity of the anode catalyst as it transforms from a crystalline  $\text{IrO}_2$  to hydrous iridium oxide. Here it must be considered that the electronic through-plane resistance of an electrode does not add directly to the HFR due to coupling of ionic and electronic currents in the electrode, as was shown by a transmission-line analysis by Landesfeind et al.<sup>43</sup> For example, if the ionic and the electronic resistances in an electrode are equally large,

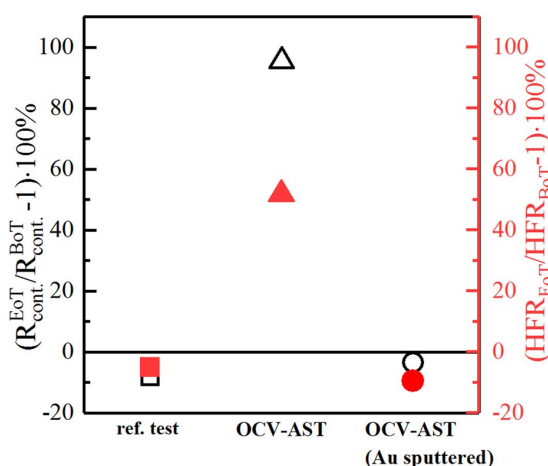


**Figure 12.** Percentage variation of the in-cell HFR (red; measured at  $0.01 \text{ A cm}^{-2}_{\text{geo}}$   $80^\circ\text{C}$ , ambient pressure, with  $5 \text{ mL}_{\text{H}_2\text{O}} \text{ min}^{-1}$ ) and the ex-situ determined contact resistances between the titanium PTL and two Ti flow-fields (black; measured at 1.7 MPa compression) for various PTLs with respect to their BoT values. Left: after 500 cycles of the reference test with the 1.3 V-hold using an uncoated PTL (“ref. test”); middle: after 718 OCV-AST cycles with an uncoated PTL (“OCV-AST”); right: after 135 OCV-AST cycles with a gold-sputtered PTL (“OCV-AST (Au-sputtered)”).

only 50% of the electronic resistance are reflected in the HFR. For the anode used here,  $R_{\text{H}^+/\text{an}}$  ranges between  $14\text{--}30 \text{ m}\Omega \text{ cm}^2_{\text{geo}}$ , depending on the tortuosity of the electrode.<sup>22</sup> In order to explain an increase of  $\approx 26 \text{ m}\Omega \text{ cm}^2_{\text{geo}}$  over the course of the OCV-AST (i.e., the observed HFR increase minus the increase of the contact resistance between the aged PTL and the flow-field), the electronic through-plane resistance of the anode electrode would have to be roughly twice as high (i.e.,  $\approx 50 \text{ m}\Omega \text{ cm}^2_{\text{geo}}$ ). For a pristine  $\text{IrO}_2/\text{TiO}_2$  electrode, the electronic through-plane resistance is  $\approx 0.04 \text{ m}\Omega \text{ cm}^2_{\text{geo}}$  and for an MEA after 200 OCV-AST cycles it was determined to be  $\approx 0.08 \text{ m}\Omega \text{ cm}^2_{\text{geo}}$ . This clearly cannot explain the increase in HFR after 200 OCV-AST cycles of  $\approx 15 \text{ m}\Omega \text{ cm}^2_{\text{geo}}$ . Thus, the only viable explanation for the HFR increase during the OCV-AST is that the lower conductivity of hydrous iridium oxide in combination with a passivated Ti-PTL leads to an increase of the interfacial contact resistance between the PTL and the anode catalyst layer (a resistance that would not be detectable with the contact resistance measurements shown in Figure 12). Due to the low contact area between the electrode and the coarse PTL structure ( $10\text{--}50 \mu\text{m}$  pores) and the poor electronic conductivity of the passivated PTL surface (see Figure 12), even a comparably small change in the electronic conductivity of the catalyst could cause a significant increase of the contact resistance. Thus, the most likely reason for the increase of the HFR and the increase of the HFR-corrected cell voltage over the course of the OCV-AST (Figure 4) is the development of a contact resistance between hydrous iridium oxide and the titanium PTL.

In summary, the repetitive transition between  $\approx 1.6 \text{ V}$  at  $3 \text{ A cm}^{-2}_{\text{geo}}$  and  $\approx 0 \text{ V}$  vs. RHE at extended OCV periods during the OCV-AST leads to the transformation of crystalline  $\text{IrO}_2$  into a hydrous iridium oxide surface. These large voltage cycles cause the dissolution of iridium and its precipitation into the membrane near the anode/membrane interface, but the overall activity loss due to this mechanism is negligible for anodes with a high iridium loading. The vast majority of the performance loss is due to an increase of the HFR, whereby the above analysis shows that the most likely reason for its increase is a parasitic contact resistance developing between hydrous iridium oxide (formed during the OCV-AST) and the passivated titanium PTL.

**Current density and energy requirement for a 1.3 V-hold during idle periods.**—In this section, an operating strategy to avoid OCV

periods and the resulting degradation phenomena will be discussed in terms of a practical application of PEM electrolyzer systems. In the reference test shown in this study, a potential hold at 1.3 V was applied to avoid a potential drop during idle periods. The current density measured during these potential hold periods was typically very low with a value of  $\approx 1 \text{ mA cm}^{-2}_{\text{geo}}$  or below toward the end of the experiment. This translates into a power density of  $\approx 1.3 \text{ mW cm}^{-2}_{\text{geo}}$  required to hold the cell potential at 1.3 V, which is only 0.025% of the maximum power density of  $\approx 5.25 \text{ W cm}^{-2}_{\text{geo}}$  obtained at a current density of  $3 \text{ A cm}^{-2}_{\text{geo}}$  and a corresponding cell voltage of  $\approx 1.75 \text{ V}$ . Consequently, the amount of energy required to avoid OCV periods by a potential hold at 1.3 V would be negligible.

In a real system, however, this operating strategy might not be practical, since it would lead to an accumulation of hydrogen in the anode compartment of the electrolyzer due to hydrogen permeation through the membrane during the potential hold at 1.3 V. This accumulation of hydrogen cannot be prevented when operated at differential pressure ( $p_{\text{cathode}} = 10 \text{ bar}_a$ ,  $p_{\text{anode}} = 1 \text{ bar}_a$ ), even when a recombination catalyst in the membrane<sup>44</sup> or the flow field is used, since almost no oxygen, which would be required for a recombination with hydrogen to water, is produced at the very low current density of  $\approx 1 \text{ mA cm}^{-2}_{\text{geo}}$  or below. The amount of oxygen which needs to be evolved to allow a full recombination of hydrogen with oxygen can be estimated based on the permeation rate of hydrogen at the applied cathode pressure, in the present case  $p_{\text{cathode}} = 10 \text{ bar}_a$ . At a temperature of  $80^\circ\text{C}$  and in the presence of liquid water, a permeation rate of  $\approx 0.85 \text{ mA cm}^{-2}_{\text{geo}} \text{ bar}_a(\text{H}_2)^{-1}$  can be assumed (see also above).<sup>23</sup> For cathode pressures of  $10 \text{ bar}_a$  or  $30 \text{ bar}_a$ , this results in current densities of  $8.1 \text{ mA cm}^{-2}_{\text{geo}}$  or  $25.1 \text{ mA cm}^{-2}_{\text{geo}}$ , respectively, which would need to be applied to produce enough oxygen to achieve a hydrogen to oxygen stoichiometry of 2:1 and, consequently, to enable a full recombination of the permeating hydrogen. Taking the corresponding cell voltage values from Figure 5, this results in power densities of  $\approx 12 \text{ mW cm}^{-2}_{\text{geo}}$  at  $10 \text{ bar}_a$  and  $\approx 36 \text{ mW cm}^{-2}_{\text{geo}}$  at  $30 \text{ bar}_a$ , respectively. This means that only 0.2% (at  $10 \text{ bar}_a$ ) and 0.7% (at  $30 \text{ bar}_a$ ) of the maximum power would need to be applied during idle periods to prevent hydrogen accumulation on the anode. Assuming an electrolyzer system which is directly coupled to a fluctuating power source and cannot obtain energy from the grid, the required energy could be supplied by, e.g., coupling a battery to the electrolyzer.<sup>45</sup> In summary, this analysis shows that operating the electrolyzer at a small current density during idle periods ( $\ll 1\%$  of maximum power required) in combination with a recombination catalyst is a promising operating strategy to avoid OCV periods and the associated performance degradation as well as safety concerns due to hydrogen permeation.

## Conclusions

In this study, the impact of intermittent power supply on the performance and lifetime of a PEM water electrolyzer was investigated. An AST protocol was designed comprising periods of operation at two current densities ( $3 \text{ A cm}^{-2}_{\text{geo}}$  and  $0.1 \text{ A cm}^{-2}_{\text{geo}}$ ), alternating with idle periods where the cell is left at the OCV in order to simulate the discontinuous power output of renewable energy sources. An initial increase in performance was observed during the first 10 cycles ( $\approx 50 \text{ mV}$ ) while prolonged cycling led to a significant decrease in performance due to an increasing HFR ( $\approx 1.6$ -fold after 700 cycles).

The initial increase in performance is related to the OCV periods during which hydrogen crossover and accumulation leads to a decrease of the cell voltage close to the HOR potential ( $\approx 0 \text{ V}$ ), leading to a reduction of the surface of the thermal  $\text{IrO}_2$  anode catalyst (coated onto a  $\text{TiO}_2$  support) to metallic Ir. The subsequent oxidation of the catalyst during periods of operation leads to the transformation of the crystalline  $\text{IrO}_2$  to an amorphous iridium oxide, which was evidenced by a lower Tafel slope (consistent with an increased activity) and the evolution of the characteristic features of metallic Ir and amorphous iridium oxide in a CV. Amorphous iridium oxide is known to exhibit a higher activity compared to crystalline  $\text{IrO}_2$ , explaining the initial performance increase.



However, the repetitive transition between oxidizing conditions during operation and reducing conditions during OCV periods (i.e., between hydrous iridium oxide and metallic iridium) causes an enhanced dissolution of Ir, which was revealed by STEM imaging of the anode/membrane interface showing Ir nanoparticles deposited in the membrane. Even though the amount of precipitated Ir is too small to have a significant impact on performance, continuous dissolution will result in a loss of active material and ultimately in a lower OER activity.

The increasing HFR, which is the major reason for the performance loss during the OCV-AST, can be partially explained by an increasing contact resistance arising from passivation of the Ti-PTL during OCV/load cycles ( $\approx 20$  mV out of 117 mV at 3 A cm<sup>-2</sup><sub>geo</sub>). However, an additional contribution is hypothesized to be the formation of hydrous iridium oxide, which has a lower electronic conductivity. Due to the low contact area between the electrode and the coarse PTL structure (10–50  $\mu$ m pores) along with a poor electronic conductivity of the passivated PTL surface, even a relatively small reduction of the electronic conductivity of the catalyst could cause a significant increase of the interfacial contact resistance between catalyst layer and PTL, thus explaining the HFR increase.

Since a reference test where the OCV period was replaced by a potential hold at 1.3 V showed no degradation over 500 cycles, the performance loss can clearly be attributed to the OCV periods. Hence, avoiding OCV periods during operation of a PEM-WE is crucial to ensure long-term stability. Based on these findings, we suggest that applying a small current density ( $\ll 1\%$  of maximum power required) during idle periods in combination with a recombination catalyst is required for a dynamically operated PEM water electrolyzer to avoid degradation and mitigate safety concerns related to hydrogen crossover.

### Acknowledgments

This work was funded by the Bavarian Ministry of Economic Affairs and Media, Energy and Technology through the project ZAE-ST (storage technologies) and by the German Ministry of Education and Research (funding number 03SFK2V0, Kopernikus-project P2X). We thank Matthias Singer for electrode preparation.

### ORCID

A. Weiß  <https://orcid.org/0000-0001-7094-5016>

A. Siebel  <https://orcid.org/0000-0001-5773-3342>

M. Bernt  <https://orcid.org/0000-0001-8448-5532>

### References

- M. Carmo, D. L. Fritz, J. Mergel, and D. Stolten, A Comprehensive Review on Pem Water Electrolysis, *International Journal of Hydrogen Energy*, **38**, 4901 (2013).
- F. Barbir, Pem Electrolysis for Production of Hydrogen from Renewable Energy Sources, *Solar Energy*, **78**, 661 (2005).
- K. E. Ayers, E. B. Anderson, K. Dreier, and K. W. Harrison, Fueling Vehicles with Sun and Water, *ECS Transactions*, **50**, 35 (2013).
- A. Buttler and H. Spliethoff, Current Status of Water Electrolysis for Energy Storage, Grid Balancing and Sector Coupling Via Power-to-Gas and Power-to-Liquids: A Review, *Renewable and Sustainable Energy Reviews*, (2017).
- A. Mohammadi and M. Mehrpooya, A Comprehensive Review on Coupling Different Types of Electrolyzer to Renewable Energy Sources, *Energy*, (2018).
- R. Clarke, S. Giddey, F. Ciacchi, S. Badwal, B. Paul, and J. Andrews, Direct Coupling of an Electrolyser to a Solar Pv System for Generating Hydrogen, *International Journal of Hydrogen Energy*, **34**, 2531 (2009).
- M. Little, M. Thomson, and D. Infield, Electrical Integration of Renewable Energy into Stand-Alone Power Supplies Incorporating Hydrogen Storage, *International Journal of Hydrogen Energy*, **32**, 1582 (2007).
- A. S. Aricò, S. Siracusano, N. Briguglio, V. Baglio, A. Di Blasi, and V. Antonucci, Polymer Electrolyte Membrane Water Electrolysis: Status of Technologies and Potential Applications in Combination with Renewable Power Sources, *Journal of Applied Electrochemistry*, **43**, 107 (2013).
- C. Schug, Operational Characteristics of High-Pressure, High-Efficiency Water-Hydrogen-Electrolysis, *International journal of hydrogen energy*, **23**, 1113 (1998).
- A. Bergen, L. Pitt, A. Rowe, P. Wild, and N. Djilali, Transient Electrolyser Response in a Renewable-Regenerative Energy System, *International Journal of Hydrogen Energy*, **34**, 64 (2009).
- U. Babic, M. Suermann, F. N. Büchi, L. Gubler, and T. J. Schmidt, Critical Review—Identifying Critical Gaps for Polymer Electrolyte Water Electrolysis Development, *Journal of The Electrochemical Society*, **164**, F387 (2017).
- S. Stucki, G. G. Scherer, S. Schlagowski, and E. Fischer, Pem Water Electrolysers: Evidence for Membrane Failure in 100kw Demonstration Plants, *Journal of Applied Electrochemistry*, **28**, 1041 (1998).
- D. E. Curtin, R. D. Lousenberg, T. J. Henry, P. C. Tangeman, and M. E. Tisack, Advanced Materials for Improved Pemfc Performance and Life, *Journal of power Sources*, **131**, 41 (2004).
- C. K. Mittelsteadt, Pem Electrolysis: Ready for Impact. *ECS Transactions*, **69**, 205 (2015).
- S. Siracusano, N. Van Dijk, R. Backhouse, L. Merlo, V. Baglio, and A. Aricò, Degradation Issues of Pem Electrolysis Meas, *Renewable Energy*, **123**, 52 (2018).
- S. A. Grigoriev, D. G. Bessarabov, and V. N. Fateev, Degradation Mechanisms of Mea Characteristics During Water Electrolysis in Solid Polymer Electrolyte Cells, *Russian Journal of Electrochemistry*, **53**, 318 (2017).
- N. Danilovic, K. E. Ayers, C. Capuano, J. N. Renner, L. Wiles, and M. Pertoso, (Plenary) Challenges in Going from Laboratory to Megawatt Scale Pem Electrolysis, *ECS Transactions*, **75**, 395 (2016).
- S. Sun, Z. Shao, H. Yu, G. Li, and B. Yi, Investigations on Degradation of the Long-Term Proton Exchange Membrane Water Electrolysis Stack, *Journal of Power Sources*, **267**, 515 (2014).
- C. Rakousky, U. Reimer, K. Wippermann, M. Carmo, W. Lueke, and D. Stolten, An Analysis of Degradation Phenomena in Polymer Electrolyte Membrane Water Electrolysis, *Journal of Power Sources*, **326**, 120 (2016).
- C. Rakousky, U. Reimer, K. Wippermann, S. Kuhri, M. Carmo, W. Lueke, and D. Stolten, Polymer Electrolyte Membrane Water Electrolysis: Restraining Degradation in the Presence of Fluctuating Power. *Journal of Power Sources*, **342**, 38 (2017).
- M. F. Mathias, J. R., J. Fleming and W. Lehnert, *Diffusion Media Materials and Characterisation*, 2003; Vol. 3.
- M. Bernt and H. A. Gasteiger, Influence of Ionomer Content in Iro2/Tio2 Electrodes on Pem Water Electrolyzer Performance, *Journal of The Electrochemical Society*, **163**, F3179 (2016).
- M. Bernt, J. Schröter, A. Weiß, A. Siebel, and H. A. Gasteiger, In *Analysis of Gas Permeation Phenomena in a Pem Water Electrolyzer Operated at High Pressure and Current Density*, Meeting Abstracts, The Electrochemical Society: 2018; pp 1598.
- P. J. Rheinländer, M. Bernt, Y. Incedag, and H. A. Gasteiger, Stability and Oer Activity of Irox in Pem Water Electrolysis, *Meeting Abstracts*, (2016), MA2016-02, 2427.
- M. Bernt, A. Siebel, and H. A. Gasteiger, Analysis of Voltage Losses in Pem Water Electrolyzers with Low Platinum Group Metal Loadings, *Journal of The Electrochemical Society*, **165**, F305 (2018).
- S. Geiger, O. Kasian, B. R. Shrestha, A. M. Mingers, K. J. J. Mayrhofer, and S. Cherevko, Activity and Stability of Electrochemically and Thermally Treated Iridium for the Oxygen Evolution Reaction, *Journal of The Electrochemical Society*, **163**, F3132 (2016).
- S. Ardizzone, A. Carugati, and S. Trasatti, Properties of Thermally Prepared Iridium Dioxide Electrodes, *Journal of Electroanalytical Chemistry and Interfacial Electrochemistry*, **126**, 287 (1981).
- R. Woods, Hydrogen Adsorption on Platinum, Iridium and Rhodium Electrodes at Reduced Temperatures and the Determination of Real Surface Area, *Journal of Electroanalytical Chemistry and Interfacial Electrochemistry*, **49**, 217 (1974).
- J. Durst, C. Simon, F. Hasché, and H. A. Gasteiger, Hydrogen Oxidation and Evolution Reaction Kinetics on Carbon Supported Pt, Ir, Rh, and Pd Electrocatalysts in Acidic Media, *Journal of The Electrochemical Society*, **162**, F190 (2015).
- E. Rasten, G. Hagen, and R. Tunold, Electrocatalysis in Water Electrolysis with Solid Polymer Electrolyte, *Electrochimica Acta*, **48**, 3945 (2003).
- S. Siracusano, V. Baglio, S. A. Grigoriev, L. Merlo, V. N. Fateev, and A. S. Aricò, The Influence of Iridium Chemical Oxidation State on the Performance and Durability of Oxygen Evolution Catalysts in Pem Electrolysis, *Journal of Power Sources*, **366**, 105 (2017).
- T. Reier, D. Teschner, T. Lunkenbein, A. Bergmann, S. Selve, R. Kraehnert, R. Schlögl, and P. Strasser, Electrocatalytic Oxygen Evolution on Iridium Oxide: Uncovering Catalyst-Substrate Interactions and Active Iridium Oxide Species, *Journal of The Electrochemical Society*, **161**, F876 (2014).
- M. Pourbaix, *Atlas of Electrochemical Equilibria in Aqueous Solutions*, 2nd. Edn. edn. ed: NACE International Cebelcor Houston, Texas, USA 1974, p 373.
- P. G. Pickup and V. I. Birss, A Model for Anodic Hydrous Oxide Growth at Iridium, *Journal of Electroanalytical Chemistry and Interfacial Electrochemistry*, **220**, 83 (1987).
- T. Okada, Effect of Ionic Contaminants, *Handbook of fuel cells*, **3**, 627 (2003).
- A. Weiß, M. Bernt, A. Siebel, and H. A. Gasteiger, A Platinum Micro-Reference Electrode for Impedance Measurements in Polymer Electrolyte Membrane Water Electrolysis, *Manuscript in preparation*.
- S. Cherevko, S. Geiger, O. Kasian, A. Mingers, and K. J. J. Mayrhofer, Oxygen Evolution Activity and Stability of Iridium in Acidic Media. Part 1. – Metallic Iridium, *Journal of Electroanalytical Chemistry*, **773**, 69 (2016).
- S. Cherevko, S. Geiger, O. Kasian, A. Mingers, and K. J. J. Mayrhofer, Oxygen Evolution Activity and Stability of Iridium in Acidic Media. Part 2. – Electrochemically Grown Hydrous Iridium Oxide, *Journal of Electroanalytical Chemistry*, **774**, 102 (2016).

39. J. Zhang, B. A. Litteer, W. Gu, H. Liu, and H. A. Gasteiger, Effect of Hydrogen and Oxygen Partial Pressure on Pt Precipitation within the Membrane of Pemfcs, *Journal of The Electrochemical Society*, **154**, B1006 (2007).
40. S. A. Grigoriev, K. A. Dzhus, D. G. Bessarabov, and P. Millet, Failure of Pem Water Electrolysis Cells: Case Study Involving Anode Dissolution and Membrane Thinning, *International Journal of Hydrogen Energy*, **39**, 20440 (2014).
41. P. Ferreira, Y. Shao-Horn, D. Morgan, R. Makharia, S. Kocha, and H. Gasteiger, Instability of Pt/ C Electrocatalysts in Proton Exchange Membrane Fuel Cells a Mechanistic Investigation, *Journal of The Electrochemical Society*, **152**, A2256 (2005).
42. H.-Y. Jung, S.-Y. Huang, P. Ganesan, and B. N. Popov, Performance of Gold-Coated Titanium Bipolar Plates in Unitized Regenerative Fuel Cell Operation, *Journal of Power Sources*, **194**, 972 (2009).
43. J. Landesfeind, M. Ebner, A. Eldiven, V. Wood, and H. A. Gasteiger, Tortuosity of Battery Electrodes: Validation of Impedance-Derived Values and Critical Comparison with 3d Tomography, *Journal of The Electrochemical Society*, **165**, A469 (2018).
44. E. Price, Durability and Degradation Issues in Pem Electrolysis Cells and Its Components, *Johnson Matthey Technology Review*, **61**, 47 (2017).
45. B. Gillessen, H. Heinrichs, P. Stenzel, and J. Linssen, Hybridization Strategies of Power-to-Gas Systems and Battery Storage Using Renewable Energy, *International Journal of Hydrogen Energy*, **42**, 13554 (2017).



## 5 Conclusion

The goal of this work was to gain a better understanding of the influence of membrane electrode assembly (MEA) properties on the performance of a proton exchange membrane water electrolyzer (PEM-WE). Additionally, accelerated stress tests were executed to study degradation mechanisms under realistic operating conditions. In order to perform tests with in-house fabricated small-scale MEAs at high current density and pressure, a cell hardware was designed which enables measurements with high reproducibility at differential pressures up to 30 bar and exhibits a performance competitive to the best results shown in literature.<sup>[15]</sup>

In the first study (section 4.1), the influence of the ionomer content in IrO<sub>2</sub>/TiO<sub>2</sub> anode electrodes with catalyst loadings of  $\approx 2 \text{ mg}_{\text{Ir}} \text{ cm}^{-2}$  was analyzed for MEAs based on a Nafion<sup>®</sup> 212 membrane. An optimum in performance was obtained for an ionomer content of 11.6 wt% corresponding to a wet-ionomer volume fraction of  $\approx 35\%$  and a remaining electrode void volume fraction of also  $\approx 35\%$ . For ionomer contents below the optimum, lower proton conductivity in the catalyst layer leads to a decrease in performance. For higher ionomer contents, on the other hand, filling of the electrode void volume with ionomer results in an additional overpotential due O<sub>2</sub> transport from the catalyst layer to the flow-field, a lower catalyst utilization, and an additional contact resistance due to the formation of an insulating ionomer film at the electrode/porous transport layer (PTL) interface. This was determined by analyzing the contributions of ohmic, kinetic, and proton transport overpotentials and it could be shown that for the optimized electrode composition losses due to mass transport account for only  $\approx 30 \text{ mV}$  at  $3 \text{ A cm}^{-2}$ . By investigating the performance at different H<sub>2</sub> pressures, it was revealed that a mass transport resistance on the hydrogen cathode, induced by a pressure gradient between catalyst layer and flow-field, caused by the capillary pressure of water in a slightly hydrophilic cathode electrode is responsible for the largest fraction ( $\approx 20 \text{ mV}$ ) of this overpotential.

In the second part (section 4.2), the impact of catalyst loading and corresponding electrode thickness on the electrolyzer performance was studied using commercially



available catalyst materials. It was shown, that, due to the fast reaction kinetics of the hydrogen evolution reaction (HER), the platinum loading on the cathode can be reduced from  $0.30 \text{ mg}_{\text{Pt}} \text{ cm}^{-2}$  to  $0.025 \text{ mg}_{\text{Pt}} \text{ cm}^{-2}$  without any negative impact on performance. On the anode, an optimum in performance at operational current densities ( $\geq 1 \text{ A cm}^{-2}$ ) was found for a catalyst loading of  $1\text{-}2 \text{ mg}_{\text{Ir}} \text{ cm}^{-2}$  corresponding to an electrode thickness of  $\approx 4\text{-}8 \text{ }\mu\text{m}$ . For thicker electrodes an increasing water transport resistance through the catalyst layer results in a reduced water content at the membrane/anode interface and, consequently, a lower membrane conductivity. This is reflected by an increase of cell voltage and high frequency resistance (HFR) at high current densities. Low catalyst loadings, on the other hand, lead to very thin ( $< 2 \text{ }\mu\text{m}$ ) and, consequently, inhomogeneous catalyst layers resulting in a drastic performance decrease due to a poor anode catalyst utilization and an associated higher HFR. However, this effect could potentially be mitigated by incorporation of a PTL modified with a microporous layer (MPL). Finally, the requirements for catalyst materials to enable a large-scale application of PEM electrolysis were discussed. It was shown that the defined target for Ir-specific power density of  $0.01 \text{ g}_{\text{Ir}} \text{ kW}^{-1}$  cannot be reached with today's commercial catalyst materials due to significant performance losses at low catalyst loadings or, more precisely, for thin electrodes. Consequently, catalyst materials with a lower packing density need to be developed to allow the fabrication of catalyst layers with a reasonable thickness ( $\approx 4\text{-}8 \text{ }\mu\text{m}$ ) at low Ir loadings.

Finally, the influence of a fluctuating power supply on the performance and degradation of a PEM-WE was investigated (section 4.3). For this purpose, an accelerated stress test (AST) was designed comprising periods of operation (at  $3 \text{ A cm}^{-2}$  and  $0.1 \text{ A cm}^{-2}$ ) and current interruptions where the cell is left at open circuit voltage (OCV). An initial performance increase was observed which can be attributed to the reduction of the thermal  $\text{IrO}_2$  catalyst on the anode during OCV periods and the subsequent transformation to an amorphous  $\text{IrO}_x$  in the course of cycling. However, the recurring transition between an oxidized (during operation) and a metallic (during OCV period) Ir surface results in the dissolution and subsequent deposition of Ir in the membrane during the test. This is accompanied by a significant performance decrease due to an increasing HFR, which can partially be explained by an increasing contact resistance between PTL and flow-field, but which must also be related to the transformation of the crystalline  $\text{IrO}_2$  to amorphous  $\text{IrO}_x$ . The observed degradation is clearly caused by the OCV periods since a reference experiment where OCV periods

were replaced by potential holds at 1.3 V showed no decrease in performance. Consequently, avoiding current interruptions and resulting OCV periods is crucial to ensure long-term stability of PEM-WEs.

In summary, the detailed analysis of voltage losses in PEM-WEs presented in this work illustrates how MEAs can be optimized to achieve maximum efficiency at high current densities and low catalyst loadings. Additionally, the results can be used to define requirements for material development and optimized operating strategies to enable a cost-competitive, large-scale application of PEM electrolysis in the future.



# Bibliography

- [1] International Energy Agency, “Key world energy statistics 2017”, <https://www.iea.org/publications/freepublications/publication/KeyWorld2017.pdf>, accessed on November 8<sup>th</sup> 2018.
- [2] “The Paris Agreement”, <https://unfccc.int/process-and-meetings/the-paris-agreement/the-paris-agreement>, accessed on November 1<sup>st</sup> 2018.
- [3] J. Rogelj, G. Luderer, R. C. Pietzcker, E. Kriegler, M. Schaeffer, V. Krey and K. Riahi, “Energy system transformations for limiting end-of-century warming to below 1.5°C”, *Nature Climate Change* **5**, 519, (2015).
- [4] J. Rockström, O. Gaffney, J. Rogelj, M. Meinshausen, N. Nakicenovic and H. J. Schellnhuber, “A roadmap for rapid decarbonization”, *Science* **355**, 1269–1271, (2017).
- [5] M. Sterner and I. Stadler, “Energiespeicher - Bedarf, Technologien, Integration”, Springer-Verlag, Berlin-Heidelberg, (2014).
- [6] Bundesnetzagentur, “Monitoringbericht 2017”, [https://www.bundesnetzagentur.de/SharedDocs/Downloads/DE/Allgemeines/Bundesnetzagentur/Publikationen/Berichte/2017/Monitoringbericht\\_2017.pdf?\\_\\_blob=publicationFile&v=3](https://www.bundesnetzagentur.de/SharedDocs/Downloads/DE/Allgemeines/Bundesnetzagentur/Publikationen/Berichte/2017/Monitoringbericht_2017.pdf?__blob=publicationFile&v=3), accessed on November 8<sup>th</sup> 2018.
- [7] “Integration fluktuierender erneuerbarer Energien durch konvergente Nutzung von Strom- und Gasnetzen - Konvergenz Strom- und Gasnetze (KonStGas) - Abschlussbericht”, (2017), [http://www.dbi-gruppe.de/files/PDFs/Projekte/00\\\_Abschlussbericht\\\_KonStGas\\\_2017.pdf](http://www.dbi-gruppe.de/files/PDFs/Projekte/00\_Abschlussbericht\_KonStGas\_2017.pdf), accessed on November 8<sup>th</sup> 2018.
- [8] P. E. Dodds, I. Staffell, A. D. Hawkes, F. Li, P. Grünewald, W. McDowall and P. Ekins, “Hydrogen and fuel cell technologies for heating: A review”, *International Journal of Hydrogen Energy* **40**, 2065–2083, (2015).

## Bibliography

---

- [9] H.-M. Groscurth and S. Bode, “Discussion Paper Nr. 9 “Power-to-heat” oder “Power-to-gas”?”, (2013), [https://www.arrhenius.de/uploads/media/arrhenius\\_DP\\_9\\_-\\_Power-to-heat.pdf](https://www.arrhenius.de/uploads/media/arrhenius_DP_9_-_Power-to-heat.pdf), accessed on November 8<sup>th</sup> 2018.
- [10] “H2FUTURE project - Technology”, <https://h2future-project.eu/technology>, accessed on November 17<sup>th</sup> 2018.
- [11] International Energy Agency, “CO<sub>2</sub> Emissions from Fuel Combustion: Overview”, (2018), [https://webstore.iea.org/download/direct/1082?fileName=CO2\\_Emissions\\_from\\_Fuel\\_Combustion\\_2018\\_Overview.pdf](https://webstore.iea.org/download/direct/1082?fileName=CO2_Emissions_from_Fuel_Combustion_2018_Overview.pdf), accessed on November 8<sup>th</sup> 2018.
- [12] O. Gröger, H. A. Gasteiger and J.-P. Suchsland, “Electromobility: Batteries or fuel cells?”, *Journal of The Electrochemical Society* **162**, A2605–A2622, (2015).
- [13] M. Carmo, D. L. Fritz, J. Mergel and D. Stolten, “A comprehensive review on PEM water electrolysis”, *International Journal of Hydrogen Energy* **38**, 4901–4934, (2013).
- [14] T. Smolinka, M. Günther and J. Garche, “Stand und Entwicklungspotenzial der Wasserelektrolyse zur Herstellung von Wasserstoff aus regenerativen Energien”, *Kurzfassung des Abschlussberichtes NOW-Studie*, (2011).
- [15] A. Buttler and H. Spliethoff, “Current status of water electrolysis for energy storage, grid balancing and sector coupling via power-to-gas and power-to-liquids: A review”, *Renewable and Sustainable Energy Reviews* **82**, 2440–2454, (2018).
- [16] J. Polonský, P. Mazúr, M. Paidar, E. Christensen and K. Bouzek, “Performance of a PEM water electrolyser using a TaC-supported iridium oxide electrocatalyst”, *International Journal of Hydrogen Energy* **39**, 3072–3078, (2014).
- [17] D. Bessarabov, A. Kruger, S. M. Luopa, J. Park, A. A. Molnar and K. A. Lewinski, “Gas crossover mitigation in PEM water electrolysis: hydrogen crossover benchmark study of 3M’s Ir-NSTF based electrolysis catalyst-coated membranes”, *ECS Transactions* **75**, 1165–1173, (2016).
- [18] T. E. Springer, T. Zawodzinski and S. Gottesfeld, “Polymer electrolyte fuel cell model”, *Journal of the Electrochemical Society* **138**, 2334–2342, (1991).

- 
- [19] S. Gottesfeld and T. A. Zawodzinski, “Polymer electrolyte fuel cells”, *Advances in Electrochemical Science and Engineering* **5**, 195–301, (1997).
- [20] F. N. Büchi and G. G. Scherer, “Investigation of the transversal water profile in Nafion membranes in polymer electrolyte fuel cells”, *Journal of the Electrochemical Society* **148**, A183–A188, (2001).
- [21] W. Zhang, R. Wycisk, D. L. Kish and P. N. Pintauro, “Pre-Stretched Low Equivalent Weight PFSA Membranes with Improved Fuel Cell Performance”, *Journal of The Electrochemical Society* **161**, F770–F777, (2014).
- [22] Y. Liu, M. W. Murphy, D. R. Baker, W. Gu, C. Ji, J. Jorne and H. A. Gasteiger, “Proton conduction and oxygen reduction kinetics in PEM fuel cell cathodes: effects of ionomer-to-carbon ratio and relative humidity”, *Journal of The Electrochemical Society* **156**, B970–B980, (2009).
- [23] M. Doyle and G. Rajendran, “Perfluorinated Membranes” in *Handbook of Fuel Cells*, Vol. 3, Chapter 30, pp. 351–395, edited by W. Vielstich, H. A. Gasteiger, and A. Lamm, John Wiley & Sons, New York, (2003).
- [24] J. T. Hinatsu, M. Mizuhata and H. Takenaka, “Water uptake of perfluoro-sulfonic acid membranes from liquid water and water vapor”, *Journal of the Electrochemical Society* **141**, 1493–1498, (1994).
- [25] T. A. Zawodzinski, T. E. Springer, J. Davey, R. Jestel, C. Lopez, J. Valerio and S. Gottesfeld, “A comparative study of water uptake by and transport through ionomeric fuel cell membranes”, *Journal of the Electrochemical Society* **140**, 1981–1985, (1993).
- [26] P. von Schroeder, “Über Erstarrungs- und Quellungserscheinungen von Gelatine”, *Zeitschrift für physikalische Chemie* **45**, 75–117, (1903).
- [27] H. Ito, T. Maeda, A. Nakano and H. Takenaka, “Properties of Nafion membranes under PEM water electrolysis conditions”, *International Journal of Hydrogen Energy* **36**, 10527–10540, (2011).
- [28] G. Alberti, R. Narducci and M. Sganappa, “Effects of hydrothermal/thermal treatments on the water-uptake of Nafion membranes and relations with changes of conformation, counter-elastic force and tensile modulus of the matrix”, *Journal of Power Sources* **178**, 575–583, (2008).

- [29] R. W. Kopitzke, C. A. Linkous, H. R. Anderson and G. L. Nelson, “Conductivity and water uptake of aromatic-based proton exchange membrane electrolytes”, *Journal of the Electrochemical Society* **147**, 1677–1681, (2000).
- [30] F. Marangio, M. Pagani, M. Santarelli and M. Cali, “Concept of a high pressure PEM electrolyser prototype”, *International Journal of Hydrogen Energy* **36**, 7807–7815, (2011).
- [31] H. Janssen, J. C. Bringmann, B. Emonts and V. Schroeder, “Safety-related studies on hydrogen production in high-pressure electrolyzers”, *International Journal of Hydrogen Energy* **29**, 759–770, (2004).
- [32] T. Sakai, H. Takenaka, N. Wakabayashi, Y. Kawami and E. Torikai, “Gas Permeation Properties of Solid Polymer Electrolyte (SPE) Membranes”, *Journal of The Electrochemical Society* **132**, 1328–1332, (1985).
- [33] M. Schalenbach, M. Carmo, D. L. Fritz, J. Mergel and D. Stolten, “Pressurized PEM water electrolysis: Efficiency and gas crossover”, *International Journal of Hydrogen Energy* **38**, 14921–14933, (2013).
- [34] F. Barbir, “PEM electrolysis for production of hydrogen from renewable energy sources”, *Solar Energy* **78**, 661–669, (2005).
- [35] S. S. Kocha, J. D. Yang and J. S. Yi, “Characterization of gas crossover and its implications in PEM fuel cells”, *AIChE Journal* **52**, 1916–1925, (2006).
- [36] J. Zhang, H. A. Gasteiger and W. Gu, “Electrochemical measurement of the oxygen permeation rate through polymer electrolyte membranes”, *Journal of The Electrochemical Society* **160**, F616–F622, (2013).
- [37] C. K. Mittelsteadt and H. Liu, “Conductivity, permeability, and ohmic shorting of ionomeric membranes”, in *Handbook of Fuel Cells*, Vol. 5, Chap. 23, pp. 345–358, edited by W. Vielstich, H. A. Gasteiger, and H. Yokokama, John Wiley & Sons, New York, (2009).
- [38] M. Schalenbach, M. A. Hoeh, J. T. Gostick, W. Lueke and D. Stolten, “Gas permeation through nafion. Part 2: resistor network model”, *The Journal of Physical Chemistry C* **119**, 25156–25169, (2015).



- 
- [39] M. Schalenbach, T. Hoefner, P. Paciok, M. Carmo, W. Lueke and D. Stolten, “Gas permeation through nafion. Part 1: measurements”, *The Journal of Physical Chemistry C* **119**, 25145–25155, (2015).
- [40] H. Ito, N. Miyazaki, M. Ishida and A. Nakano, “Cross-permeation and consumption of hydrogen during proton exchange membrane electrolysis”, *International Journal of Hydrogen Energy* **41**, 20439–20446, (2016).
- [41] P. Trinke, B. Bensmann and R. Hanke-Rauschenbach, “Current density effect on hydrogen permeation in PEM water electrolyzers”, *International Journal of Hydrogen Energy* **42**, 14355–14366, (2017).
- [42] P. Trinke, B. Bensmann and R. Hanke-Rauschenbach, “Experimental evidence of increasing oxygen crossover with increasing current density during PEM water electrolysis”, *Electrochemistry Communications* **82**, 98–102, (2017).
- [43] U. Babic, M. Suermann, F. N. Büchi, L. Gubler and T. J. Schmidt, “Critical Review - Identifying Critical Gaps for Polymer Electrolyte Water Electrolysis Development”, *Journal of The Electrochemical Society* **164**, F387–F399, (2017).
- [44] E. Price, “Durability and Degradation Issues in PEM Electrolysis Cells and its Components”, *Johnson Matthey Technology Review* **61**, 47–51, (2017).
- [45] A. Albert, A. O. Barnett, M. S. Thomassen, T. J. Schmidt and L. Gubler, “Radiation-grafted polymer electrolyte membranes for water electrolysis cells: evaluation of key membrane properties”, *ACS Applied Materials & Interfaces* **7**, 22203–22212, (2015).
- [46] A. Albert, T. Lochner, T. J. Schmidt and L. Gubler, “Stability and degradation mechanisms of radiation-grafted polymer electrolyte membranes for water electrolysis”, *ACS Applied Materials & Interfaces* **8**, 15297–15306, (2016).
- [47] E. Fabbri, A. Haberer, K. Waltar, R. Kötz and T. J. Schmidt, “Developments and perspectives of oxide-based catalysts for the oxygen evolution reaction”, *Catalysis Science & Technology* **4**, 3800–3821, (2014).
- [48] J. Russell, L. Nuttall and A. Fickett, “Hydrogen generation by solid polymer electrolyte water electrolysis”, *American Chemical Society Division of Fuel Chemistry Preprints* **18**, 24–40, (1973).

- [49] K. Neyerlin, W. Gu, J. Jorne, A. Clark and H. A. Gasteiger, “Cathode catalyst utilization for the ORR in a PEMFC analytical model and experimental validation”, *Journal of The Electrochemical Society* **154**, B279–B287, (2007).
- [50] J. Durst, A. Siebel, C. Simon, F. Hasché, J. Herranz and H. A. Gasteiger, “New insights into the electrochemical hydrogen oxidation and evolution reaction mechanism”, *Energy & Environmental Science* **7**, 2255–2260, (2014).
- [51] J. Durst, C. Simon, F. Hasché and H. A. Gasteiger, “Hydrogen oxidation and evolution reaction kinetics on carbon supported Pt, Ir, Rh, and Pd electrocatalysts in acidic media”, *Journal of The Electrochemical Society* **162**, F190–F203, (2015).
- [52] P. Strasser, S. Koh, T. Anniyev, J. Greeley, K. More, C. Yu, Z. Liu, S. Kaya, D. Nordlund and H. Ogasawara, “Lattice-strain control of the activity in dealloyed core–shell fuel cell catalysts”, *Nature Chemistry* **2**, 454, (2010).
- [53] J. Tymoczko, F. Calle-Vallejo, W. Schuhmann and A. S. Bandarenka, “Making the hydrogen evolution reaction in polymer electrolyte membrane electrolyzers even faster”, *Nature Communications* **7**, 10990, (2016).
- [54] M. Miles and M. Thomason, “Periodic variations of overvoltages for water electrolysis in acid solutions from cyclic voltammetric studies”, *Journal of The Electrochemical Society* **123**, 1459–1461, (1976).
- [55] M. H. Miles, E. A. Klaus, B. P. Gunn, J. R. Locker, W. E. Serafin and S. Srinivasan, “The oxygen evolution reaction on platinum, iridium, ruthenium and their alloys at 80°C in acid solutions”, *Electrochimica Acta* **23**, 521–526, (1978).
- [56] I. C. Man, H. Su, F. Calle-Vallejo, H. A. Hansen, J. I. Martínez, N. G. Inoglu, J. Kitchin, T. F. Jaramillo, J. K. Nørskov and J. Rossmeisl, “Universality in oxygen evolution electrocatalysis on oxide surfaces”, *ChemCatChem* **3**, 1159–1165, (2011).
- [57] S. Cherevko, S. Geiger, O. Kasian, N. Kulyk, J.-P. Grote, A. Savan, B. R. Shrestha, S. Merzlikin, B. Breitbach and A. Ludwig, “Oxygen and hydrogen evolution reactions on Ru, RuO<sub>2</sub>, Ir, and IrO<sub>2</sub> thin film electrodes in acidic and alkaline electrolytes: A comparative study on activity and stability”, *Catalysis Today* **262**, 170–180, (2016).

- [58] S. Siracusano, N. Van Dijk, E. Payne-Johnson, V. Baglio and A. S. Aricò, “Nanosized IrO<sub>x</sub> and IrRuO<sub>x</sub> electrocatalysts for the O<sub>2</sub> evolution reaction in PEM water electrolyzers”, *Applied Catalysis B: Environmental* **164**, 488–495, (2015).
- [59] A. T. Marshall, S. Sunde, M. Tsytkin and R. Tunold, “Performance of a PEM water electrolysis cell using Ir<sub>x</sub>Ru<sub>y</sub>Ta<sub>z</sub>O<sub>2</sub> electrocatalysts for the oxygen evolution electrode”, *International Journal of Hydrogen Energy* **32**, 2320–2324, (2007).
- [60] O. Kasian, S. Geiger, P. Stock, G. Polymeros, B. Breitbach, A. Savan, A. Ludwig, S. Cherevko and K. J. Mayrhofer, “On the Origin of the Improved Ruthenium Stability in RuO<sub>2</sub>–IrO<sub>2</sub> Mixed Oxides”, *Journal of The Electrochemical Society* **163**, F3099–F3104, (2016).
- [61] S. Siracusano, V. Baglio, N. Van Dijk, L. Merlo and A. S. Aricò, “Enhanced performance and durability of low catalyst loading PEM water electrolyser based on a short-side chain perfluorosulfonic ionomer”, *Applied Energy* **192**, 477–489, (2017).
- [62] T. Reier, D. Teschner, T. Lunkenbein, A. Bergmann, S. Selve, R. Kraehnert, R. Schlögl and P. Strasser, “Electrocatalytic oxygen evolution on iridium oxide: uncovering catalyst-substrate interactions and active iridium oxide species”, *Journal of The Electrochemical Society* **161**, F876–F882, (2014).
- [63] S. Geiger, O. Kasian, B. R. Shrestha, A. M. Mingers, K. J. Mayrhofer and S. Cherevko, “Activity and stability of electrochemically and thermally treated iridium for the oxygen evolution reaction”, *Journal of The Electrochemical Society* **163**, F3132–F3138, (2016).
- [64] T. Y. Paul, W. Gu, J. Zhang, R. Makharia, F. T. Wagner and H. A. Gasteiger, “Carbon-Support Requirements for Highly Durable Fuel Cell Operation”, in *Polymer Electrolyte Fuel Cell Durability*, pp. 29–53, edited by F. N. Büchi, M. Inaba, and T. J. Schmidt, Springer, New York, (2009).
- [65] F. T. Wagner, S. G. Yan and P. T. Yu, “Catalyst and catalyst-support durability”, in *Handbook of Fuel Cells*, Vol. 5, Chap. 16, pp. 250–263, edited by W. Vielstich, H. A. Gasteiger, and H. Yokokama, John Wiley & Sons, New York, (2009).

- [66] P. Mazúr, J. Polonský, M. Paidar and K. Bouzek, “Non-conductive TiO<sub>2</sub> as the anode catalyst support for PEM water electrolysis”, *International Journal of Hydrogen Energy* **37**, 12081–12088, (2012).
- [67] E. Oakton, D. Lebedev, M. Povia, D. F. Abbott, E. Fabbri, A. Fedorov, M. Nachtegaal, C. Coperet and T. J. Schmidt, “IrO<sub>2</sub>-TiO<sub>2</sub>: A high-surface-area, active, and stable electrocatalyst for the oxygen evolution reaction”, *ACS Catalysis* **7**, 2346–2352, (2017).
- [68] G. Auer, P. Woditsch, A. Westerhaus, J. Kischkewitz, W. Griebler, M. Rohe and M. Liedekerke, “Pigments, inorganic, 2. White pigments” in *Ullmann’s Encyclopedia of Industrial Chemistry*, pp. 1–36, Wiley–VCH, Weinheim, (2000).
- [69] R. E. Fuentes, J. Farrell and J. W. Weidner, “Multimetallic electrocatalysts of Pt, Ru, and Ir supported on anatase and rutile TiO<sub>2</sub> for oxygen evolution in an acid environment”, *Electrochemical and Solid-State Letters* **14**, E5–E7, (2011).
- [70] E. Oakton, D. Lebedev, A. Fedorov, F. Krumeich, J. Tillier, O. Sereda, T. J. Schmidt and C. Copéret, “A simple one-pot Adams method route to conductive high surface area IrO<sub>2</sub>-TiO<sub>2</sub> materials”, *New Journal of Chemistry* **40**, 1834–1838, (2016).
- [71] L. Ma, S. Sui and Y. Zhai, “Investigations on high performance proton exchange membrane water electrolyzer”, *International Journal of Hydrogen Energy* **34**, 678–684, (2009).
- [72] J. Polonský, I. M. Petrushina, E. Christensen, K. Bouzek, C. B. Prag, J. E. T. Andersen and N. J. Bjerrum, “Tantalum carbide as a novel support material for anode electrocatalysts in polymer electrolyte membrane water electrolyzers”, *International Journal of Hydrogen Energy* **37**, 2173–2181, (2012).
- [73] H. Oh, H. N. Nong and P. Strasser, “Preparation of mesoporous Sb-, F-, and In-doped SnO<sub>2</sub> bulk powder with high surface area for use as catalyst supports in electrolytic cells”, *Advanced Functional Materials* **25**, 1074–1081, (2015).
- [74] H. N. Nong, H. Oh, T. Reier, E. Willinger, M. Willinger, V. Petkov, D. Teschner and P. Strasser, “Oxide-Supported IrNiO<sub>x</sub> Core-Shell Particles as Efficient, Cost-Effective, and Stable Catalysts for Electrochemical Water Splitting”, *Angewandte Chemie International Edition* **54**, 2975–2979, (2015).

- [75] S. Siracusano, V. Baglio, C. D'Urso, V. Antonucci and A. S. Aricò, "Preparation and characterization of titanium suboxides as conductive supports of IrO<sub>2</sub> electrocatalysts for application in SPE electrolyzers", *Electrochimica Acta* **54**, 6292–6299, (2009).
- [76] L. Wang, P. Lettenmeier, U. Golla-Schindler, P. Gazdzicki, N. A. Cañas, T. Morawietz, R. Hiesgen, S. S. Hosseiny, A. S. Gago and K. A. Friedrich, "Nanostructured Ir-supported on Ti<sub>4</sub>O<sub>7</sub> as a cost-effective anode for proton exchange membrane (PEM) electrolyzers", *Physical Chemistry Chemical Physics* **18**, 4487–4495, (2016).
- [77] S. M. Alia, S. Shulda, C. Ngo, S. Pylypenko and B. S. Pivovar, "Iridium-Based Nanowires as Highly Active, Oxygen Evolution Reaction Electrocatalysts", *ACS Catalysis* **8**, 2111–2120, (2018).
- [78] K. A. Lewinski, D. van der Vliet and S. M. Luopa, "NSTF advances for PEM electrolysis - the effect of alloying on activity of NSTF electrolyzer catalysts and performance of NSTF based PEM electrolyzers", *ECS Transactions* **69**, 893–917, (2015).
- [79] K. E. Ayers, J. N. Renner, N. Danilovic, J. X. Wang, Y. Zhang, R. Maric and H. Yu, "Pathways to ultra-low platinum group metal catalyst loading in proton exchange membrane electrolyzers", *Catalysis Today* **262**, 121–132, (2016).
- [80] E. Borgardt, O. Panchenko, F. J. Hackemüller, J. Giffin, M. Bram, M. Müller, W. Lehnert and D. Stolten, "Mechanical characterization and durability of sintered porous transport layers for polymer electrolyte membrane electrolysis", *Journal of Power Sources* **374**, 84–91, (2018).
- [81] H. Ito, T. Maeda, A. Nakano, C. M. Hwang, M. Ishida, A. Kato and T. Yoshida, "Experimental study on porous current collectors of PEM electrolyzers", *International Journal of Hydrogen Energy* **37**, 7418–7428, (2012).
- [82] J. Mo, Z. Kang, G. Yang, S. T. Retterer, D. A. Cullen, T. J. Toops, J. B. Green and F.-Y. Zhang, "Thin liquid/gas diffusion layers for high-efficiency hydrogen production from water splitting", *Applied Energy* **177**, 817–822, (2016).

- [83] J. Mo, R. R. Dehoff, W. H. Peter, T. J. Toops, J. B. Green and F.-Y. Zhang, “Additive manufacturing of liquid/gas diffusion layers for low-cost and high-efficiency hydrogen production”, *International Journal of Hydrogen Energy* **41**, 3128–3135, (2016).
- [84] S. A. Grigoriev, P. Millet, S. A. Volobuev and V. N. Fateev, “Optimization of porous current collectors for PEM water electrolyzers”, *International Journal of Hydrogen Energy* **34**, 4968–4973, (2009).
- [85] L. Zielke, A. Fallisch, R. Paust, N. and Zengerle and S. Thiele, “Tomography based screening of flow field/current collector combinations for PEM water electrolysis”, *RSC Advances* **4**, 58888–58894, (2014).
- [86] C. H. Lee, R. Banerjee, F. Arbabi, J. Hinebaugh and A. Bazylak, “Porous Transport Layer Related Mass Transport Losses in Polymer Electrolyte Membrane Electrolysis - A Review”, *Proceedings of the ASME 14th International Conference on Nanochannels, Microchannels, and Minichannels*, (2016).
- [87] K. Bromberger, J. Ghinaiya, T. Lickert, A. Fallisch and T. Smolinka, “Hydraulic ex situ through-plane characterization of porous transport layers in PEM water electrolysis cells”, *International Journal of Hydrogen Energy* **43**, 2556–2569, (2018).
- [88] C. M. Hwang, M. Ishida, H. Ito, T. Maeda, A. Nakano, Y. Hasegawa, N. Yokoi, A. Kato and T. Yoshida, “Influence of properties of gas diffusion layers on the performance of polymer electrolyte-based unitized reversible fuel cells”, *International Journal of Hydrogen Energy* **36**, 1740–1753, (2011).
- [89] C. M. Hwang, M. Ishida, H. Ito, T. Maeda, A. Nakano, A. Kato and T. Yoshida, “Effect of titanium powder loading in gas diffusion layer of a polymer electrolyte unitized reversible fuel cell”, *Journal of Power Sources* **202**, 108–113, (2012).
- [90] M. Suermann, “Pressurized Polymer Electrolyte Water Electrolysis: Electrochemical Characterization and Energetic Evaluation”, PhD thesis, ETH Zürich, (2017).
- [91] P. Lettenmeier, S. Kolb, F. Burggraf, A. S. Gago and K. A. Friedrich, “Towards developing a backing layer for proton exchange membrane electrolyzers”, *Journal of Power Sources* **311**, 153–158, (2016).

- 
- [92] P. Lettenmeier, S. Kolb, N. Sata, A. Fallisch, L. Zielke, S. Thiele, A. S. Gago and K. A. Friedrich, “Comprehensive investigation of novel pore-graded gas diffusion layers for high-performance and cost-effective proton exchange membrane electrolyzers”, *Energy & Environmental Science* **10**, 2521–2533, (2017).
- [93] S. S. Dhrab, K. Sopian, M. Alghoul and M. Sulaiman, “Review of the membrane and bipolar plates materials for conventional and unitized regenerative fuel cells”, *Renewable and Sustainable Energy Reviews* **13**, 1663–1668, (2009).
- [94] H. Tawfik, Y. Hung and D. Mahajan, “Metal bipolar plates for PEM fuel cell — A review”, *Journal of Power Sources* **163**, 755–767, (2007).
- [95] H.-Y. Jung, S.-Y. Huang, P. Ganesan and B. N. Popov, “Performance of gold-coated titanium bipolar plates in unitized regenerative fuel cell operation”, *Journal of Power Sources* **194**, 972–975, (2009).
- [96] M. Langemann, D. L. Fritz, M. Müller and D. Stolten, “Validation and characterization of suitable materials for bipolar plates in PEM water electrolysis”, *International Journal of Hydrogen Energy* **40**, 11385–11391, (2015).
- [97] H.-Y. Jung, S.-Y. Huang and B. N. Popov, “High-durability titanium bipolar plate modified by electrochemical deposition of platinum for unitized regenerative fuel cell (URFC)”, *Journal of Power Sources* **195**, 1950–1956, (2010).
- [98] K. E. Ayers, E. B. Anderson, C. Capuano, B. Carter, L. Dalton, G. Hanlon, J. Manco and M. Niedzwiecki, “Research advances towards low cost, high efficiency PEM electrolysis”, *ECS Transactions* **33**, 3–15, (2010).
- [99] A. S. Gago, A. S. Ansar, N. Wagner, J. Arnold and K. A. Friedrich, “Titanium coatings deposited by thermal spraying for bipolar plates of PEM electrolyzers”, *4<sup>th</sup> European PEFC and H<sub>2</sub> Forum*, Lucerne, Switzerland, (2013).
- [100] A. S. Gago, S. A. Ansar, B. Saruhan, U. Schulz, P. Lettenmeier, N. A. Cañas, P. Gazdzicki, T. Morawietz, R. Hiesgen and J. Arnold, “Protective coatings on stainless steel bipolar plates for proton exchange membrane (PEM) electrolyzers”, *Journal of Power Sources* **307**, 815–825, (2016).
- [101] G. Chisholm, P. J. Kitson, N. D. Kirkaldy, L. G. Bloor and L. Cronin, “3D printed flow plates for the electrolysis of water: an economic and adaptable approach to device manufacture”, *Energy & Environmental Science* **7**, 3026–3032, (2014).



- [102] H. Ito, T. Maeda, A. Nakano, Y. Hasegawa, N. Yokoi, C. M. Hwang, M. Ishida, A. Kato and T. Yoshida, “Effect of flow regime of circulating water on a proton exchange membrane electrolyzer”, *International Journal of Hydrogen Energy* **35**, 9550–9560, (2010).
- [103] J. Nie, S. Cohen, Y. Chen, B. Carter and R. F. Boehm, “Velocity and temperature distributions in bipolar plate of PEM electrolysis cell”, *Proceedings of the International Mechanical Engineering Congress and Exposition*, 197–204, (2007).
- [104] J. Nie, Y. Chen, S. Cohen, B. D. Carter and R. F. Boehm, “Numerical and experimental study of three-dimensional fluid flow in the bipolar plate of a PEM electrolysis cell”, *International Journal of Thermal Sciences* **48**, 1914–1922, (2009).
- [105] J. Nie and Y. Chen, “Numerical modeling of three-dimensional two-phase gas-liquid flow in the flow field plate of a PEM electrolysis cell”, *International Journal of Hydrogen Energy* **35**, 3183–3197, (2010).
- [106] J. Nie, Y. T. Chen, J. F. Wu and K. M. Veepuri, “Explorations of Improving Flow Uniformity in the Bipolar Plate of a PEM Electrolysis Cell Using Different Designs”, *Proceedings of Fluids Engineering Division Summer Meeting*, 725–732, (2008).
- [107] M. Bernt and H. A. Gasteiger, “Influence of Ionomer Content in IrO<sub>2</sub>/TiO<sub>2</sub> Electrodes on PEM Water Electrolyzer Performance”, *Journal of The Electrochemical Society* **163**, F3179–F3189, (2016).
- [108] S. G. Bratsch, “Standard electrode potentials and temperature coefficients in water at 298.15 K”, *Journal of Physical and Chemical Reference Data* **18**, 1–21, (1989).
- [109] W. Gu, D. R. Baker, Y. Liu and H. A. Gasteiger, “Proton exchange membrane fuel cell (PEMFC) down-the-channel performance model”, in *Handbook of Fuel Cells*, Vol. 6, Chap. 43, pp. 631–657, edited by W. Vielstich, H. Yokokawa, and H. A. Gasteiger, John Wiley & Sons, New York, (2009).

- 
- [110] H. A. Gasteiger, Y. Liu, D. Baker and W. Gu, “Kinetics and Kinetically Limited Performance in PEMFCs and DMFCs with State-of-the-Art Catalysts”, in *Mini-Micro Fuel Cells*, pp. 209–224, edited by S. Kakaç, A. Pramuanjaroenkij, and L. Vasiliev, Springer, Dordrecht, (2008).
- [111] Y. Matsumoto and E. Sato, “Electrocatalytic properties of transition metal oxides for oxygen evolution reaction”, *Materials Chemistry and Physics* **14**, 397–426, (1986).
- [112] M. Suermann, T. J. Schmidt and F. N. Büchi, “Cell performance determining parameters in high pressure water electrolysis”, *Electrochimica Acta* **211**, 989–997, (2016).
- [113] P. J. Rheinländer, P. Peitl, M. Bernt and H. A. Gasteiger, “H<sub>2</sub>-Transport Limitations in the Hydrogen Electrode in PEM Water Electrolysis”, *The Electrochemical Society - Meeting Abstracts* **MA2017-01**, 1513–1513, (2017).
- [114] E. L. Thompson, J. Jorne, W. Gu and H. A. Gasteiger, “PEM fuel cell operation at -20°C. II. Ice formation dynamics, current distribution, and voltage losses within electrodes”, *Journal of The Electrochemical Society* **155**, B887–B896, (2008).
- [115] R. Makharia, M. F. Mathias and D. R. Baker, “Measurement of catalyst layer electrolyte resistance in PEFCs using electrochemical impedance spectroscopy”, *Journal of The Electrochemical Society* **152**, A970–A977, (2005).
- [116] Y. Liu, C. Ji, W. Gu, D. R. Baker, J. Jorne and H. A. Gasteiger, “Proton conduction in PEM fuel cell cathodes: effects of electrode thickness and ionomer equivalent weight”, *Journal of The Electrochemical Society* **157**, B1154–B1162, (2010).
- [117] Y. Liu, C. Ji, W. Gu, J. Jorne and H. A. Gasteiger, “Effects of catalyst carbon support on proton conduction and cathode performance in PEM fuel cells”, *Journal of The Electrochemical Society* **158**, B614–B621, (2011).
- [118] K. Neyerlin, W. Gu, J. Jorne and H. A. Gasteiger, “Study of the exchange current density for the hydrogen oxidation and evolution reactions”, *Journal of The Electrochemical Society* **154**, B631–B635, (2007).

- [119] U. Babic, T. J. Schmidt and L. Gubler, “Communication - Contribution of Catalyst Layer Proton Transport Resistance to Voltage Loss in Polymer Electrolyte Water Electrolyzers”, *Journal of The Electrochemical Society* **165**, J3016–J3018, (2018).
- [120] M. Suermann, T. J. Schmidt and F. N. Büchi, “Investigation of mass transport losses in polymer electrolyte electrolysis cells”, *ECS Transactions* **69**, 1141–1148, (2015).
- [121] A. Skulimowska, M. Dupont, M. Zaton, S. Sunde, L. Merlo, D. J. Jones and J. Rozière, “Proton exchange membrane water electrolysis with short-side-chain Aquivion<sup>®</sup> membrane and IrO<sub>2</sub> anode catalyst”, *International Journal of Hydrogen Energy* **39**, 6307–6316, (2014).
- [122] A. Ghielmi, P. Vaccarono, C. Troglia and V. Arcella, “Proton exchange membranes based on the short-side-chain perfluorinated ionomer”, *Journal of Power Sources* **145**, 108–115, (2005).
- [123] N. Briguglio and V. Antonucci, “Overview of PEM Electrolysis for Hydrogen Production”, in *PEM Electrolysis for Hydrogen Production: Principles and Applications*, Chap. 1, pp. 1–9, edited by D. Bessarabov, H. Wang, H. Li and N. Zhao, CRC Press, Boca Raton, (2015).
- [124] B. Benschmann, R. Hanke-Rauschenbach, G. Müller-Syring, M. Henel and K. Sundmacher, “Optimal configuration and pressure levels of electrolyzer plants in context of power-to-gas applications”, *Applied Energy* **167**, 107–124, (2016).
- [125] B. Benschmann, R. Hanke-Rauschenbach, I. P. Arias and K. Sundmacher, “Energetic evaluation of high pressure PEM electrolyzer systems for intermediate storage of renewable energies”, *Electrochimica Acta* **110**, 570–580, (2013).
- [126] G. Tjarks, A. Gibelhaus, F. Lanzerath, M. Müller, A. Bardow and D. Stolten, “Energetically-optimal PEM electrolyzer pressure in power-to-gas plants”, *Applied Energy* **218**, 192–198, (2018).
- [127] S. A. Grigoriev, M. M. Khaliullin, N. V. Kuleshov and V. N. Fateev, “Electrolysis of water in a system with a solid polymer electrolyte at elevated pressure”, *Russian Journal of Electrochemistry* **37**, 819–822, (2001).

- 
- [128] S. A. Grigoriev, V. I. Porembsky and V. N. Fateev, “Pure hydrogen production by PEM electrolysis for hydrogen energy”, *International Journal of Hydrogen Energy* **31**, 171–175, (2006).
- [129] A. Nouri-Khorasani, E. T. Ojong, T. Smolinka and D. P. Wilkinson, “Model of oxygen bubbles and performance impact in the porous transport layer of PEM water electrolysis cells”, *International Journal of Hydrogen Energy* **42**, 28665–28680, (2017).
- [130] Department of Energy, “Fuel Cell Technologies Office Multi-Year Research, Development, and Demonstration Plan”, (2015), <http://energy.gov/eere/fuelcells/downloads/fuel-cell-technologies-office-multi-year-research-development-and-22>, accessed on November 1<sup>st</sup> 2018.
- [131] K. E. Ayers, E. B. Anderson, K. Dreier and K. W. Harrison, “Fueling Vehicles with Sun and Water”, *ECS Transactions* **50**, 35–46, (2013).
- [132] W. N. Arkilander and T. M. Molter, “Oxygen generator cell design for future submarines”, Report 0148–7191, SAE Technical Paper, (1996).
- [133] A. B. LaConti, M. Hamdan and R. C. McDonald, “Mechanisms of membrane degradation”, in *Handbook of Fuel Cells*, Vol. 3, Chap. 49, pp. 647–662, edited by W. Vielstich, H. A. Gasteiger, and A. Lamm, John Wiley & Sons, New York, (2003).
- [134] H. Liu, H. A. Gasteiger, A. Laconti and J. Zhang, “Factors impacting chemical degradation of perfluorinated sulfonic acid ionomers”, *ECS Transactions* **1**, 283–293, (2006).
- [135] H. Liu, F. D. Coms, J. Zhang, H. A. Gasteiger and A. B. LaConti, “Chemical Degradation: Correlations Between Electrolyzer and Fuel Cell Findings”, in *Polymer Electrolyte Fuel Cell Durability*, Chap. 3, pp. 71–118, edited by F. N. Büchi, M. Inaba, and T. J. Schmidt, Springer, New York, (2009).
- [136] E. Endoh, “Development of highly durable PFSA membrane and MEA for PEMFC under high temperature and low humidity conditions”, *ECS Transactions* **16**, 1229–1240, (2008).
- [137] D. E. Curtin, R. D. Lousenberg, T. J. Henry, P. C. Tangeman and M. E. Tisack, “Advanced materials for improved PEMFC performance and life”, *Journal of Power Sources* **131**, 41–48, (2004).

- [138] M. Chandesris, V. Médeau, N. Guillet, S. Chelghoum, D. Thoby and F. Fouda-Onana, “Membrane degradation in PEM water electrolyzer: Numerical modeling and experimental evidence of the influence of temperature and current density”, *International Journal of Hydrogen Energy* **40**, 1353–1366, (2015).
- [139] F. Fouda-Onana, M. Chandesris, V. Médeau, S. Chelghoum, D. Thoby and N. Guillet, “Investigation on the degradation of MEAs for PEM water electrolyzers part I: Effects of testing conditions on MEA performances and membrane properties”, *International Journal of Hydrogen Energy* **41**, 16627–16636, (2016).
- [140] P. Millet, A. Ranjbari, F. De Guglielmo, S. A. Grigoriev and F. Auprêtre, “Cell failure mechanisms in PEM water electrolyzers”, *International Journal of Hydrogen Energy* **37**, 17478–17487, (2012).
- [141] S. Sun, Z. Shao, H. Yu, G. Li and B. Yi, “Investigations on degradation of the long-term proton exchange membrane water electrolysis stack”, *Journal of Power Sources* **267**, 515–520, (2014).
- [142] Q. Feng, G. Liu, B. Wei, Z. Zhang, H. Li and H. Wang, “A review of proton exchange membrane water electrolysis on degradation mechanisms and mitigation strategies”, *Journal of Power Sources* **366**, 33–55, (2017).
- [143] A. B. LaConti, H. Liu, C. K. Mittelsteadt and R. C. McDonald, “Polymer electrolyte membrane degradation mechanisms in fuel cells-findings over the past 30 years and comparison with electrolyzers”, *ECS Transactions* **1**, 199–219, (2006).
- [144] O. Kasian, J. Grote, S. Geiger, S. Cherevko and K. J. Mayrhofer, “The common intermediates of oxygen evolution and dissolution reactions during water electrolysis on iridium”, *Angewandte Chemie International Edition* **57**, 2488–2491, (2018).
- [145] P. Lettenmeier, R. Wang, R. Abouatallah, S. Helmly, T. Morawietz, R. Hiesgen, S. Kolb, F. Burggraf, J. Kallo and A. S. Gago, “Durable membrane electrode assemblies for proton exchange membrane electrolyzer systems operating at high current densities”, *Electrochimica Acta* **210**, 502–511, (2016).
- [146] H. Xu, “High-Performance, Long-Lifetime Catalysts for Proton Exchange Membrane Electrolysis”, DOE Hydrogen and Fuel Cells Program, Annual Progress Report, (2016).

- [147] S. M. Alia, B. Rasimick, C. Ngo, K. C. Neyerlin, S. S. Kocha, S. Pylypenko, H. Xu and B. S. Pivovar, “Activity and durability of iridium nanoparticles in the oxygen evolution reaction”, *Journal of The Electrochemical Society* **163**, F3105–F3112, (2016).
- [148] S. Siracusano, V. Baglio, S. A. Grigoriev, L. Merlo, V. N. Fateev and A. S. Aricò, “The influence of iridium chemical oxidation state on the performance and durability of oxygen evolution catalysts in PEM electrolysis”, *Journal of Power Sources* **366**, 105–114, (2017).
- [149] C. Rakousky, U. Reimer, K. Wippermann, M. Carmo, W. Lueke and D. Stolten, “An analysis of degradation phenomena in polymer electrolyte membrane water electrolysis”, *Journal of Power Sources* **326**, 120–128, (2016).
- [150] P. Paciok, M. Schalenbach, M. Carmo and D. Stolten, “On the mobility of carbon-supported platinum nanoparticles towards unveiling cathode degradation in water electrolysis”, *Journal of Power Sources* **365**, 53–60, (2017).
- [151] “Technical data about the Energiepark Mainz”, <http://www.energiepark-mainz.de/en/technology/technical-data>, accessed on November 1<sup>st</sup> 2018.
- [152] A. Ursua, L. M. Gandia and P. Sanchis, “Hydrogen production from water electrolysis: current status and future trends”, *Proceedings of the IEEE* **100**, 410–426, (2012).
- [153] M. Schalenbach, G. Tjarks, M. Carmo, W. Lueke, M. Mueller and D. Stolten, “Acidic or Alkaline? Towards a New Perspective on the Efficiency of Water Electrolysis”, *Journal of The Electrochemical Society* **163**, F3197–F3208, (2016).
- [154] M. Schalenbach, O. Kasian and K. J. J. Mayrhofer, “An alkaline water electrolyzer with nickel electrodes enables efficient high current density operation”, *International Journal of Hydrogen Energy* **43**, 11932–11938, (2018).
- [155] L. Bertuccioli, A. Chan, D. Hart, F. Lehner, B. Madden and E. Standen, “Study on development of water electrolysis in the EU”, *Final report in fuel cells and hydrogen joint undertaking*, (2014).
- [156] O. Schmidt, A. Gambhir, I. Staffell, A. Hawkes, J. Nelson and S. Few, “Future cost and performance of water electrolysis: An expert elicitation study”, *International Journal of Hydrogen Energy* **42**, 30470–30492, (2017).

## Bibliography

---

- [157] S. Roohparvarzadeh, “Experimental characterization of the compressive behaviour of gas diffusion layers in PEM fuel cells”, PhD thesis, University of Waterloo, (2014).
- [158] M. Bernt, A. Siebel and H. A. Gasteiger, “Analysis of Voltage Losses in PEM Water Electrolyzers with Low Platinum Group Metal Loadings”, *Journal of The Electrochemical Society* **165**, F305–F314, (2018).
- [159] A. Weiß, A. Siebel, M. Bernt, T.-H. Shen, V. Tileli and H. A. Gasteiger, “Impact of Intermittent Operation on Lifetime and Performance of a PEM Water Electrolyzer”, *Journal of The Electrochemical Society* **166**, F487–F497, (2019).



# Acknowledgements

I would like to thank my supervisor **Prof. Hubert Gasteiger** for his exceptional support during my PhD project. Your extraordinary commitment for all your students as well as your passion for science have been an enormous motivation. Thank you for providing the best possible environment for me to succeed with my PhD project.

I would also like to thank my colleagues in the electrolysis team, **Alexandra Weiß**, **Maximilian Möckl**, and **Armin Siebel**. Having started as the first PhD student working on electrolysis it is amazing to see how the group has developed over the last years. Thank you all for contributing to that and making it an exciting and memorable time. Big thanks go to all student researchers which I had the pleasure to supervise. Thank you for your excellent work, **Matthias Singer**, **Deepa Pandit**, **Philip Petzoldt**, and **Jonas Schröter**. Additionally, I would like to acknowledge some colleagues who helped me to get familiar with electrochemistry at the beginning of my PhD project. Thank you, **Frédéric Hasché**, **Julien Durst**, and **Yelena Gorlin** for your introductions to electrochemistry, MEA fabrication, and lab work in general.

I further thank **Katia Rodewald** for SEM images, **Svetoslav Koynov** for his help with gold-coating, and **Cortney Mittelsteadt** for advise on how to build an electrolyzer cell and test station. Support by the mechanical workshop, especially by **Marcel Schmidt**, and by the electrical workshop is also gratefully acknowledged.

**Veronika Pichler** and **Heiko Juranowitsch** as well as **Barbara Friese**, **Rebecca Steiner**, **Susanne Wegertseder**, and **Friederike Kennett** are acknowledged for their help with all administrative issues and lab maintenance.

Of course, I also want to thank my colleagues at the Chair of Technical Electrochemistry and ZAE Bayern (especially all the people I shared the office with over the years) for the great working atmosphere and all the leisure activities. Here, a special thanks goes to **Armin Siebel**, **Christoph Simon**, and **Gregor Harzer** for exciting dart games, to the TEC badminton/squash crew for the early morning exercise, and to all the mountain bike enthusiasts for great biking trips.

Finally, I would like to thank my family, with my parents **Inga** and **Rainer** and my sister **Tina** as well as my girlfriend **Anne** for being part of my life and for always supporting me. Thank you for everything!